New nanomaterials:
Amyloid fibrils from waste proteins

A thesis submitted in partial fulfilment of the requirements for the

Degree of Doctor of Philosophy in Biochemistry

2012

Laura J. Domigan

University of Canterbury

UNIVERSITY OF CANTERBURY
Te Whare Wānanga o Waitaha
CHRISTCHURCH NEW ZEALAND

Acknowledgements

My first thanks must go to my supervisor Juliet Gerrard, for always being there with support, enthusiasm, and something to make me laugh. I have learnt so much from you, least of all how to use commas, and you have made my time as a PhD student incredibly enjoyable. Djellabas and dodgy food in Morocco will never be forgotten. Big thanks also to my co-supervisor Richard Blaikie for being brave enough to take on a biologist, and providing much needed advice and guidance through the nano-world. Thank you also to Susie Meade, for all of the chats, the coffees, and the always excellent advice.

Thank you to Jackie Healy for your kindness and your svelte technical assistance. Thanks to Helen Devereaux and Gary Turner for their help in the nanofabrication lab (plus lab members), to Matt Walters for help with posters, and to Mike Flaws for SEM assistance. Thanks to Keith Baronian and Alison Downard for assistance with the electrochemistry.

Thank you to all of the members of Juliet's lab group; it has been an awesome group to be a part of. Particular thanks to Clem, Madhu, and Grant for your help in the lab, as well as ex-lab members Ren, Andy, Sean and Sophie. Thanks to Jared, for being a great and supportive friend. It was great to have someone to keep me company on this journey, and make it a good one too! Thank you also to Davon, for always being there for coffee and chats.

Thank you to the collaborators that have assisted with various parts of this thesis: Margie Sunde at the University of Sydney; Cosmin Laslau and Jadranka Travas-Sejdic at the University of Auckland; and to the NaBIS group at Denmark Technical University for giving me a wonderful spring in Copenhagan.

Thanks must also go to Mum and Dad and all the rest of my family (including Joan, Margaret and Mr B); thank you for your support over all of these years and for always loving and believing in me. And finally lots of love and thanks to Hamish, you have made these years a lot less stressful, and a lot more fun than I would have ever thought they would be.

Table of Contents

Abbreviations

A	Amperes
Å	Ångstroms
A_{280}	absorbance at 280 nm
A_{570}	absorbance at 570 nm
AC	alternating current
ACN	acetonitrile
AFM	atomic force microscopy
A_n	depolarising factor, for the axis *n*
°C	degrees Celsius
CA	current amplification
CAD	computer-aided design
CD	circular dichroism
cm	centimetres
CNT	carbon nanotubes
CP	conducting polymer
CR	Congo red
Da	Daltons
DNA	deoxyribose nucleic acid
DEP	dielectrophoresis
dH_2O	distilled water
DMF	*N,N*-dimethylformamide
DMSO	dimethyl sulfoxide
dsDNA	double-stranded deoxyribose nucleic acid
DTT	dithiothreitol
e	eccentricity of particle

ε_0	permittivity of vacuum
E	electric field
ε_m	permittivity of medium
E_{pa}	electrochemical anodic peak potential
EAS	*easily*-wettable hydrophobin from *Neurospora crassa*
EDTA	ethylenediaminetetraacetic acid
EDX	energy-dispersive X-ray spectroscopy
EG	electrode gap
EM	electron microscopy
EP	electrode pairs
ES	electrode spacing
EW	electrode width
FcOH	ferrocene methanol
F	force
F-actin	filamentous actin
FAD/$FADH_2$	flavin adenine dinucleotide (oxidised/reduced form)
FcOH	ferrocene methanol
FET	field-effect transistor
FF	diphenylalanine
FTIR	Fourier transform infrared spectroscopy
f_{to}	turnover frequency
Γ	geometry factor
g	grams
GA	glutaraldehyde
G-actin	globular actin
GOx	glucose oxidase
GOx:IF	glucose oxidase functionalised insulin fibrils
H_2O	water
HCl	hydrochloric acid

HDMS	hexamethyldisilazane
HMW	high molecular weight
HPLC	high performance liquid chromatography
hr	hour
HRP	horseradish peroxidase
Hz	Hertz
I-V	current-voltage
K_f	Claussius-Mossotti factor
kDa	kiloDaltons
kHz	kiloHertz
L	litre
LDS	lithium dodecyl sulfate
LED	light emitting diode
LS	landing space
µg	micrograms
µL	microlitres
µM	micromolar
µm	micrometres
µS	microSiemens
M	molar
m	metre
mA	milliAmperes
MG	methylglyoxal
mg	milligrams
MHz	megaHertz
MIF	metal ion free
min	minute
mL	millilitres
mM	millimolar

mm	millimetres
MOPS	3-morpholinopropanesulfonic acid
mV	milliVolts
MW	molecular weight
NaCl	sodium chloride
NADH	nicotinamide adenine dinucleotide (reduced form)
NB	nanobelt
ND	nanodisk
NF	nanofibre
nm	nanometres
NMR	nuclear magnetic resonance
NP	nanoparticle
NT	nanotube
Ω	Ohms
OPA	*o*-phthaldialdehyde
%	percent
p	dipole movement
pA	picoAmps
PAGE	polyacrylamide gel electrophoresis
PANI	polyaniline
PB	phosphate buffer
PCR	polymerase chain reaction
PDB	Protein Data Bank
PDB	Protein Data Bank
PEDOT-S	alkosulfonate poly(3,4-ethylenedioxythiophene)
PNF	protein/peptide nanofibre
PNT	protein/peptide nanotube
PPF	polypropylene fumarate
PPS	poly(sulfonated styrene)

PPY	polypyrrole
RFU	relative fluorescence units
RNA	ribose nucleic acid
rpm	revolutions per minute
σ	variance
S	Siemens
SDS	sodium dodecyl sulphate
SEB	standard electrolyte buffer
SEC	size exclusion chromatography
sec	second
SEM	scanning electron microscope
SiNW	silicon nanowire
ssDNA	single-stranded deoxyribose nucleic acid
ssNMR	solid state nuclear magnetic resonance
SWNT	single walled carbon nanotube
TEM	transmission electron microscopy
ThT	thioflavin T
TMAH	tetramethyl ammonium hydroxide
TMV	tobacco mosaic virus
TPU	thermoplastic polyurethane
Tris	tris(hydroxymethyl)aminomethane
UV	ultraviolet
V	Volts
Vpp	Volts peak-peak
v/v	unit volume per unit volume
wt	weight
w/v	unit weight per unit volume
w/w	unit weight per unit weight

This thesis has contributed to the following publications:

Domigan L. J, Healy J. P, Meade S. J, Blaikie R. J, Gerrard J. A. 2011. Controlling the dimensions of amyloid fibrils: Towards homogenous components for bionanotechnology. Biopolymers 97(2): 123-133

Domigan L. J. 2012. Proteins and peptides as biological nanowires: Towards biosensing devices. In: Gerrard J. A. (Ed.), Protein Nanotechnology. Humana Press. *Accepted.*

Healy J. P, Wong K, Roux C. L, **Domigan L. J.**, Sunde M, Sawyer E. B, Gras S. L, Larsen N. G, Gerrard J. A, Vasudevamurthy M, K. 2012. Polymorphism and higher ordered structures of protein nanofibers from crude mixtures of fish lens crystallins: Towards useful materials. Biopolymers. *Accepted.*

Abstract

The current landscape of nanotechnology has focussed attention on materials that self-assemble. The search for such materials has unsurprisingly led to the biological world, where functional nanoscale biomolecular assemblies are in abundance. Amyloid fibrils are one such self-assembling biological structure, formed when native proteins misfold into insoluble fibrous quaternary structures. This research has explored the use of amyloid fibrils formed from waste proteins, namely crude crystallin proteins from fish eye lenses, as biological nanowires.

The use of amyloid fibrils as nanowires was investigated by examining the ability to control their dimensions and arrangement, along with analysis of their properties, such as stability and conductivity. TEM and AFM studies on the model amyloid forming protein, bovine insulin, showed that a number of fibril length distributions can be achieved, by systematically altering fibril growth and storage conditions. Although the same set of conditions cannot be directly applied to crystallin fibrils, these fibrils can also be produced on a range of length scales. Amyloid fibrils can be manipulated and aligned in a controlled manner by dielectrophoresis; this tool could later be used to incorporate amyloid fibrils into a biosensing or bioelectronics device.

Dielectrophoresis was also used to immobilise crystallin fibrils between electrode pairs, in order to investigate the conductivity of small numbers of fibrils. These experiments complemented work carried out on the conductivity of amyloid fibril networks, using fabricated interdigitated electrodes. In the unmodified state, amyloid fibrils formed from bovine insulin, fungal hydrophobins, and crude crystallins were all shown to have low conductivity, with current values in the range of 10^{-8}–10^{-10} A recorded at bias voltages of 0–2 V. Amyloid fibrils were used as a template for the synthesis of conductive nanowires, by modification with the conducting polymers polyaniline and polypyrrole, increasing conductivity by one and four orders of magnitude respectively.

The functionalisation of fibrils with glucose oxidase enabled the creation of a very simple glucose sensing device. This device, consisting of a gold electrode modified with the glucose oxidase functionalised fibrils, showed an electrochemical response in the presence of glucose and the mediator FcOH. Future work is necessary to optimise the use of amyloid fibrils in this way; however, this study confirms a role for amyloid fibrils from a low cost source in bionanotechnology.

1. Chapter One

Introduction

1.1. Context

A role has been recognised for a number of biomolecules and biomolecular assemblies in the fast emerging field of bionanotechnology, where they may be used in a number of ways; for example, as nanowires. Amyloid fibrils, a highly ordered misfolded protein state, are one such biomolecular assembly that has been identified with potential in this area. However, the majority of work in the literature has focused on the use of amyloid-like fibrils formed from engineered peptides. This thesis aims to investigate the use of amyloid fibrils, formed from native proteins, as biological nanowires – with a focus on those formed from cheap, readily available proteins.

This chapter provides a background on amyloid fibril structure and their formation, along with how these unique structures may fit into the field of bionanotechnology.

1.2. Bionanotechnology

The term bionanotechnology refers to the interaction between the fields of biology and nanotechnology, with nanotechnology being defined as the creation, design, and manipulation of structures or particles with dimensions smaller than 100 nm (Chan, 2006). Once a field solely utilised by engineers and physical scientists, nanotechnology is now being used by the biological and medical research communities, and is drawing inspiration, and in some cases raw materials, from the biological world.

In the search for new nanomaterials and components, a focus has been placed on those that self-assemble, with this "bottom-up" approach to manufacturing being recognised as one of the ways of manufacturing in the future (Gras, 2007a). Traditional "top-down" fabrication of nanomaterials and components involves processes like lithography to produce such structures by patterning; by contrast, "bottom-up" assembly refers to the creation of nanostructures *via* self-assembly from relatively simple building blocks, and biology can aid in the provision of these building blocks (**Figure 1.1**).

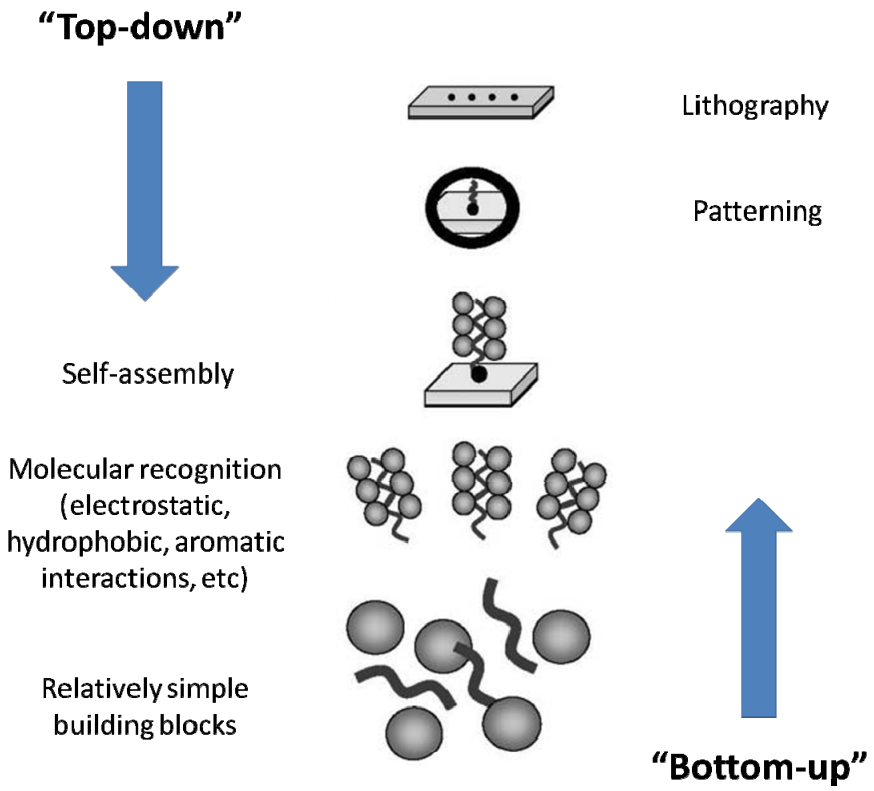

Figure 1.1. *A comparison of the "top-down" and "bottom-up" approaches to manufacturing of nanomaterials. The top-down fabrication process is based on the patterning of assemblies using lithography. The bottom-up approach is based on the interaction of simple building blocks to form a well-ordered assembly by molecular recognition and self-assembly. Schematic taken from Gazit (2007).*

Nanostructures include nanotubes (NT), nanofibres (NF), nanobelts (NB), nanodisks (ND), and nanoparticles (NP), as shown in **Figure 1.2**. The smallest dimensions of these structures are usually less than 100 nm, for example, platinum nanoparticles are usually in the 6-10 nm diameter size range (El-Sayed, 2001), and carbon nanotubes (CNTs) can vary from 0.4-100 nm diameter, with variable lengths (Ding *et al*., 2001; Tang *et al*., 2001).

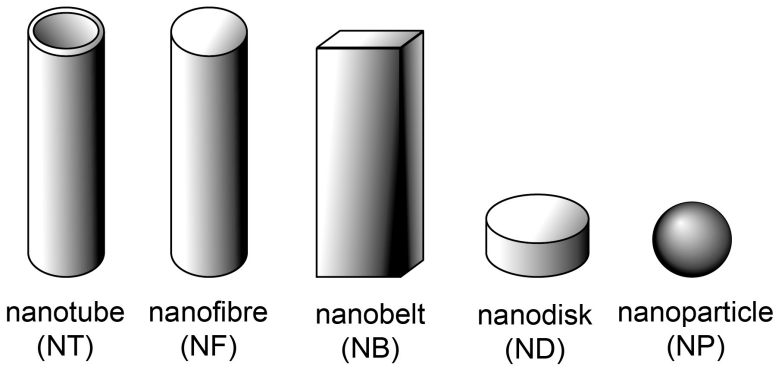

Figure 1.2. *A schematic representation of common nanostructures. Adapted from Chopra* et al. *(2007).*

The shift to a "bottom-up" approach has unsurprisingly led to the wide use of biological molecules and macromolecular assemblies, as these biological species are similar in size to nanostructures. Some typical sizes of proteins and biological species are given in **Table 1.1** (Vo-Dinh, 2005). Potential has been seen for a number of these assemblies to be translated into functional nanomaterials.

Table 1.1. *Typical sizes of biological species. Adapted from Vo-Dinh (2005).*

Biological species	Example	Typical size
Small proteins	Chymotrypsin	4 nm sphere
Large proteins	Aspartate transcarbamoylases	7 nm sphere
Small assemblies	Ribosome	20 nm sphere
Large assemblies	Viruses	100 nm sphere

1.3. Amyloid fibrils

Amyloid fibril is the name given to the insoluble fibrous quaternary structure formed by the assembly of normally soluble protein or peptide monomers into intermolecularly hydrogen bonded β-sheets (Chiti and Dobson, 2006). The structure of amyloid fibrils is discussed in greater detail below (Section 1.3.1.). The name "amyloid" was given based on the first identification of these insoluble deposits (Virchow, 1854), where they were stained with iodine, making them amylose-like. In later years, protein components were identified (Friedreich and Kekulé, 1859), but the name amyloid has remained.

Amyloid fibrils are best known for their role in a number of diseases, such as Alzheimer's disease, Type II diabetes, Parkinson's disease and Creutzfeld-Jacob disease (Chiti and Dobson, 2006). In these diseases, commonly occurring proteins misfold forming insoluble fibrillar aggregates. Functional amyloid assemblies also exist (Otzen and Nielsen, 2008), and these are discussed in Section 1.3.1. It is now known that amyloid fibrils can form from a variety of different protein and peptide solutions, and this, as well as a number of other desirable properties (Gras, 2007a), has shifted research into amyloid fibrils from being solely into their involvement in disease, to include their use as novel bionanomaterials.

1.3.1. Amyloid fibril structure

A number of different techniques, including electron microscopy (EM), atomic force microscopy (AFM), X-ray fibre diffraction, and solid-state nuclear magnetic resonance (ssNMR), have been employed to fully characterise both the macromolecular and internal structure of amyloid fibrils (Makin and Serpell, 2005).

There is a wide range of different morphologies of fibrils: straight and twisted fibrils, linear assemblies with several laterally associated fibrils (Kowalewski and Holtzman, 1999), rings (Hatters *et al*., 2003), and large spherical clusters of fibrils called spherulites (Krebs *et al*., 2004). Solution conditions can favour a particular morphology as was observed by Petkova *et al*. (2005), in their work on β-amyloid fibrils, where the predominant structure present was controlled by subtle variations in fibril growth conditions. The basic unit of amyloid fibrils is known as a protofilament, and amyloid fibrils consist of a number of these, typically 2-6, each of which is about 2-5 nm in diameter (Serpell *et al*., 2000). This protofilament structure of amyloid fibrils is seen to be conserved across a range of proteins (Serpell *et al*., 2000), although the way the protofilaments associate with each other can differ. Different numbers and arrangements of protofilaments have even been observed under the same experimental conditions (Jiménez *et al*., 1999; Makin and Serpell, 2004). **Figure 1.3** shows the 3-D reconstruction of insulin fibrils and depicts fibrils formed with two, four, and six protofilaments (Jimenez *et al*., 2002). In some cases, the protofilaments twist together to form rope-like fibrils 7-13 nm wide (Goeden-Wood *et al*., 2003; Serpell *et al*., 2000), while in other cases, the protofilaments associate laterally to form long ribbons that are 2-5 nm thick and up to 30 nm wide (Saiki *et al*., 2005).

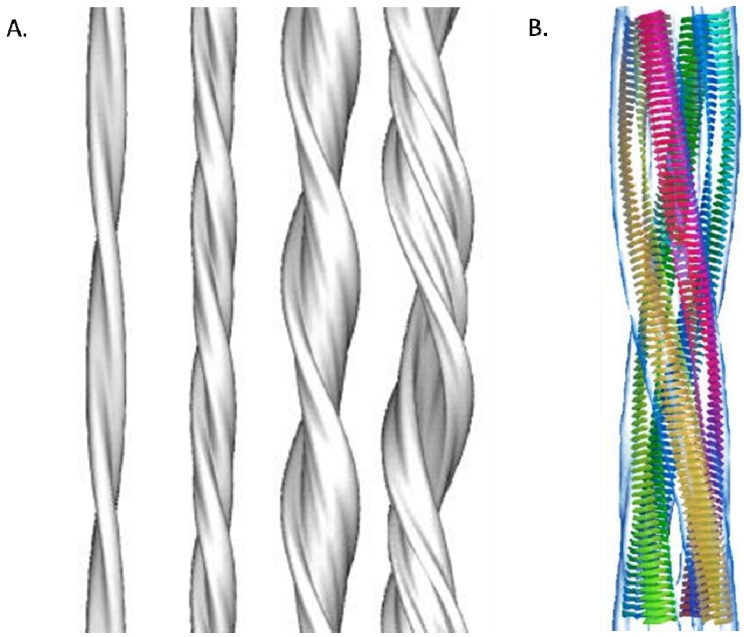

Figure 1.3. *The protofilament structure of amyloid fibrils. Often a variety of different protofilament structures exist for amyloid fibrils from a protein. A) Surface representation of 3-D maps of the four insulin fibril structures. From left to right: A pair of protofilaments, the four protofilament compact fibril, the six protofilament fibril, the twisted ribbon. B) Molecular model of an amyloid fibril derived from cryo-EM analysis of SH3 domain fibrils. This model shows the β-sheet structure of amyloid fibrils within the protofilaments. Figures taken from Jimenez* et al. *(2002).*

Amyloid fibrils have a cross-β structure (**Figure 1.4**), which was first observed by X-ray fibre diffraction from the egg stalk of the lacewing *Chrysopa* (Geddes *et al*., 1968), and consists of β-strands, approximately 4.7 Å apart, arranged perpendicular to the fibril axis, and β-sheets, approximately 10 Å apart, running parallel to the axis of the fibril (Makin and Serpell, 2005; Serpell *et al*., 2000). Other proposed models for the internal structure of amyloid fibrils include a β-helical structure, that of hollow nanotubes, and also a model where the native structure of the monomeric protein is largely retained (Makin and Serpell, 2005).

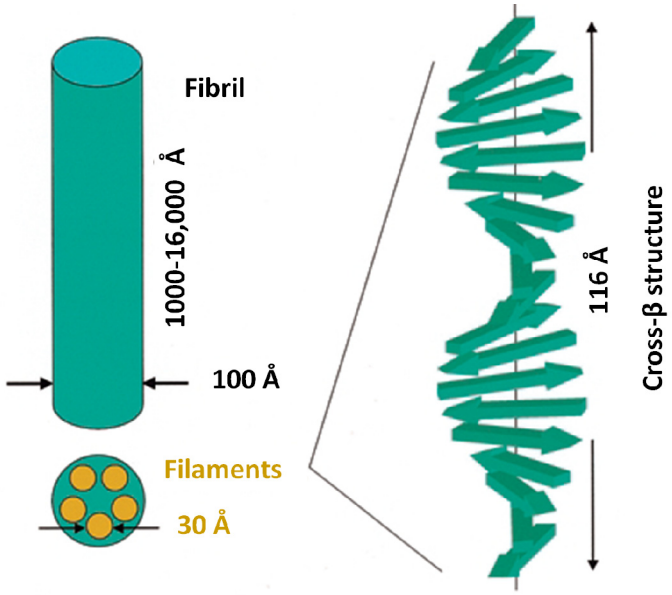

Figure 1.4. *Schematic of the hierarchies of amyloid fibril structure, from fibril, to protofilament, to the internal cross-β structure. Schematic taken from Jaskolski (2001).*

1.3.2. Amyloid fibril formation

When a polypeptide chain comes off the ribosome there are a number of different structures that can be formed: the native state of the protein, which is reached through the formation of intermediate structures, and degraded and aggregated structures as shown in **Figure 1.5** (Dobson, 2003a).

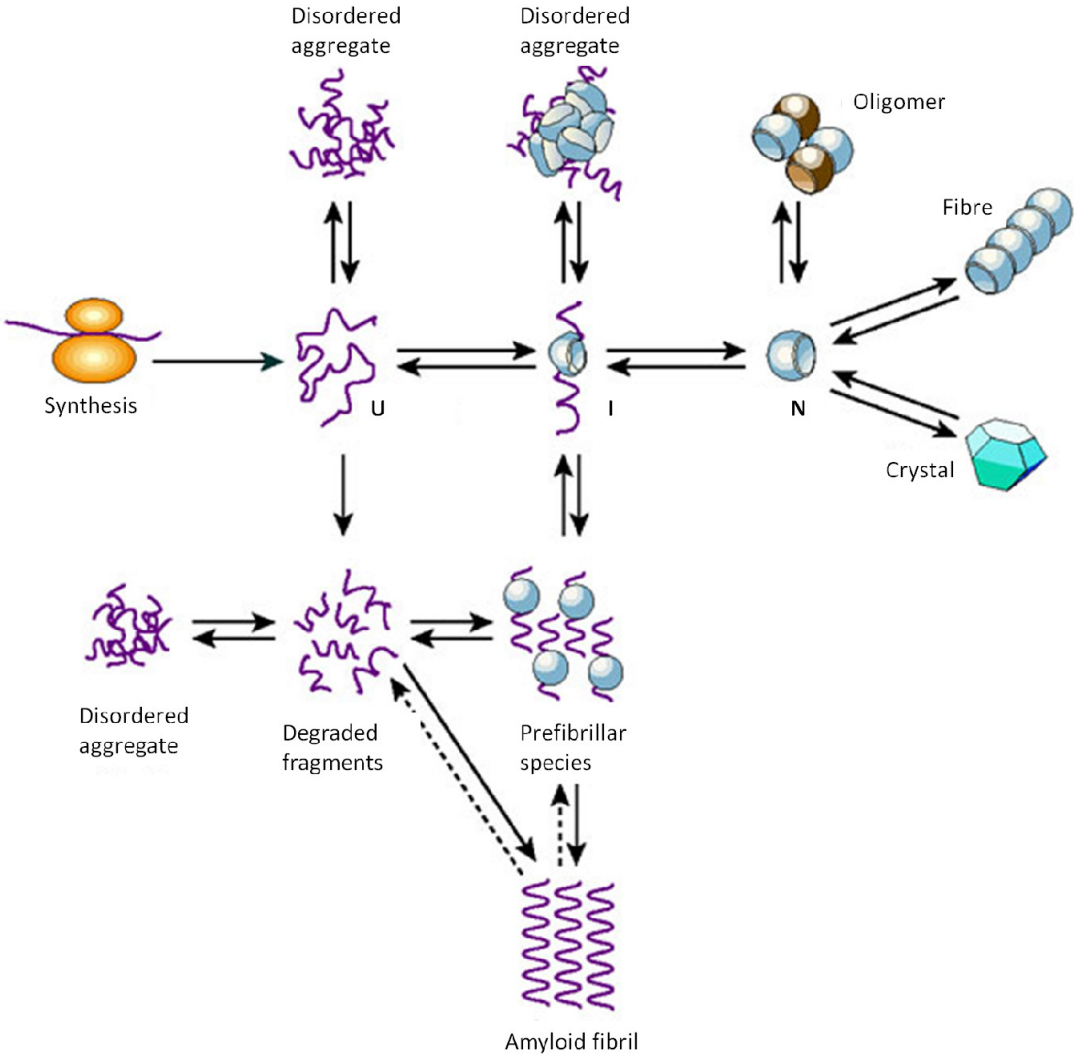

Figure 1.5. *Schematic of the different states that may be adopted by a protein molecule following synthesis at the ribosome. U = Unfolded, I = Intermediate, N = Native. The arrows show the transitions from state to state, with the dotted arrows representing transitions which sometimes occur. Schematic taken from Dobson (2003a).*

The state a protein adopts under specific conditions depends on the relative thermodynamic and kinetic stabilities of the various states (Dobson, 2003b). Amyloid fibrils are just one type of aggregated state that can be adopted by a protein, but are unique in having such a highly ordered 'misfolded' structure (Dobson, 2003a). This highly ordered amyloid structure is also stable, as shown by the diagram in **Figure 1.6** (Jahn and Radford, 2008). The kinetics of protein folding have been explained through the concept of an energy landscape, with a rough energy landscape showing the various other states the protein may exist in and their relative stabilities (Jahn and Radford, 2008).

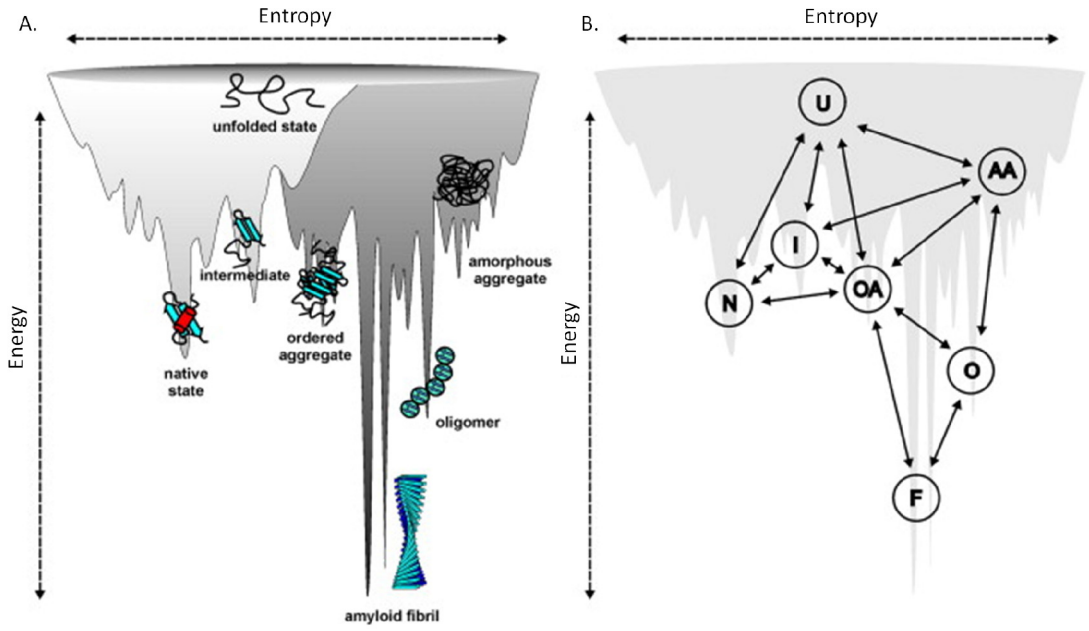

Figure 1.6. *Schematic showing a combined energy landscape for protein folding and aggregation, taken from Jahn and Radford (2008). A) There are a number of conformational states which are available to a polypeptide chain, each differing in energy and entropy. The surface represents the roughness of the energy landscape. Shown in light grey, is from polypeptide chain to the native monomeric state, and in dark grey, where there is an increase in roughness, intermolecular protein association. B) There are a number of proposed pathways between the different conformational states; unfolded (U), intermediate (I), native (N), ordered aggregate (OA), amorphous aggregate (AA), oligomer (O), and fibril (F).*

Amyloid fibril formation is shown schematically in **Figure 1.7**. The native monomeric state of the protein is disrupted in some way, by a change in physical and/or chemical conditions, causing the formation of partially folded intermediate species. These intermediates then self-assemble into ladders of β-strands which then aggregate to form amyloid fibrils (Cherny and Gazit, 2008).

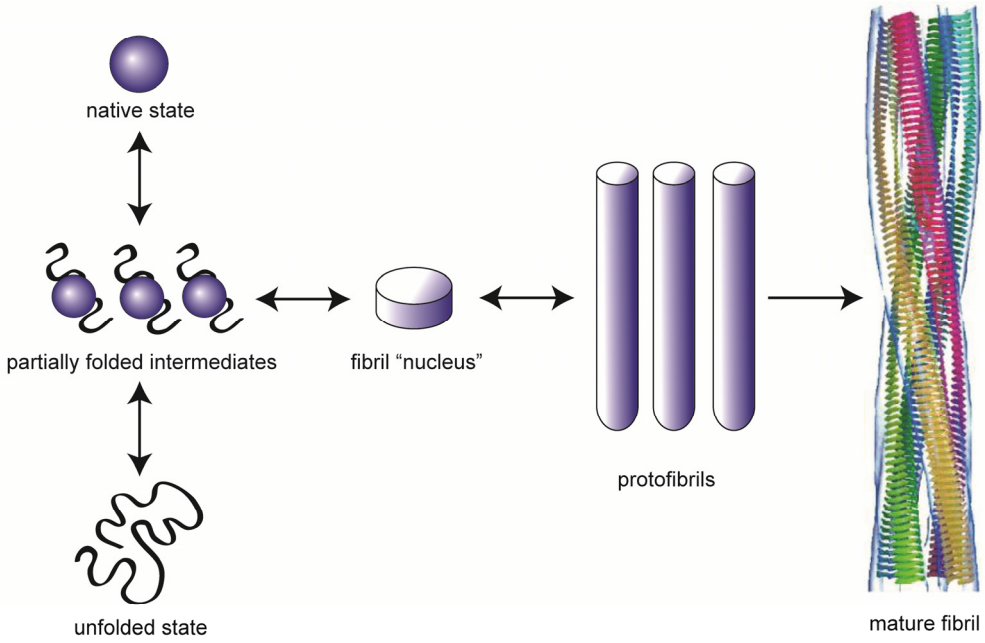

Figure 1.7. *The formation of amyloid fibrils. The folded monomer undergoes a conformational transformation from the native state to form a partially unfolded intermediate species. These intermediates then self-assemble to form a fibril "nucleus", from which protofilaments are formed by elongation of the nuclear unit. These protofilaments then come together to form a mature fibril (Jimenez* et al.*, 2002).*

Amyloid fibril formation has been shown to have many characteristics of a nucleated growth mechanism (Chiti and Dobson, 2006). The kinetics and formation of amyloid fibrils is discussed in greater detail in Chapter 3.

1.3.3. Sources of amyloid fibrils

Amyloidogenic proteins are diverse in sequence and share few characteristics, which reinforces the idea that the amyloid structure can be generated by many polypeptide sequences (Fowler *et al*., 2007). It has been shown that many proteins can be induced to form fibrils under appropriate physical and chemical conditions, such as temperature and pH extremes, solvents and chaotropic agents (Gras, 2007a). In addition to the more than 25 different proteins associated with different amyloid pathologies (Krishnan and Lindquist, 2005), a number of different proteins/peptides form amyloid fibrils, both in nature and *in vitro* (Stefani and Dobson, 2003).

Functional amyloid structures also exist. It has been identified that nature uses the cross-β mode of self-organisation in many structural contexts (Otzen and Nielsen, 2008). Functional amyloid proteins have been found across varied domains of life including humans, invertebrates, fungi, and bacteria. Some examples of these functional amyloid proteins include those playing roles in human melanosomes (Berson *et al*., 2003; Fowler *et al*., 2005), spider and moth silk (Iconomidou *et al*., 2000; Kenney *et al*., 2002), the termination factor Sup35 in yeast (True and Lindquist, 2000), coatings of fungal spores (Kwan *et al*., 2006), and in bacteria, curli protein and inclusion bodies (Carrio *et al*., 2005; Chapman *et al*., 2002).

It has been proposed that, if the correct conditions are found, amyloid fibril formation is a generic property of all proteins (Chiti and Dobson, 2006). So far, a number of proteins that are not known to form fibrils in disease or nature have been induced to form fibrils *in vitro*, these include bovine insulin (Nielsen *et al*., 2001b), wheat proteins (Mackintosh *et al*., 2009), hen egg lysozyme (Krebs *et al*., 2000), α-lactoglobulin (Graveland-Bikker and de Kruif, 2006), milk proteins (Thorn *et al*., 2005), ovalbumin, and bovine serum albumin (Pearce *et al*., 2007).

In this thesis, three different amyloid-forming proteins are used, bovine insulin, crude crystallin proteins, and fungal hydrophobins, each possessing unique and interesting properties. Bovine insulin is used as the model amyloid-forming protein in this study, since it is very well characterised (Brange *et al*., 1997; Jimenez *et al*., 2002; Nielsen *et al*., 2001a; Nielsen *et al*., 2001b; Podesta *et al*., 2006; Whittingham *et al*., 2002), and forms defined fibrils very rapidly from the native structure.

The other amyloid-forming proteins used are fungal hydrophobins, mentioned previously as one of many proteins that form functional amyloids (Kwan *et al*., 2006), and fish eye crystallin proteins. Amyloid fibrils formed from crude fish eye crystallin proteins are the main focus of this study, since if amyloid fibrils are to be used successfully in bionanotechnology, there is a need for production of amyloid fibrils from a readily available and inexpensively sourced protein (Waterhouse and Gerrard, 2004). Crude fish crystallins meet this requirement, as we have shown in our lab that they can be produced in large quantities from low value waste products (Healy *et al*., 2011).

Each of these amyloid fibril sources are discussed in more detail in Chapter 2.

1.3.4. Characterisation of amyloid fibrils

A number of techniques exist for the characterisation of amyloid fibrils, with the main ones being the recognition of a fibrillar structure, either by microscopy or by X-ray scattering, as well as the ability to bind and shift the spectral properties of certain hydrophobic dyes. Circular dichroism (CD) and Fourier Transform Infrared spectroscopy (FTIR) can also reveal the high β-sheet content of amyloid fibrils.

Transmission electron microscopy (TEM) is commonly used to recognise fibrillar morphology in *in vitro* protein aggregation (Nilsson, 2004). As well as confirming the presence of amyloid fibrils, it also provides useful structural information as the latest TEMs can operate at close to one Å resolution (Smith, 2008). TEM generally shows amyloid fibrils to be straight, unbranching fibres, with 70-120 Å diameters, and of variable lengths (Cohen *et al*., 1982).

AFM can also be used for visual characterisation of fibrils. Due to the nature and limitations of AFM, it is most useful and reliable for topographic measurements. AFM has been used previously in a number of cases to study self-assembly and the surface structure of amyloid fibrils (Dong *et al*., 2006; Morris *et al*., 1999; Podesta *et al*., 2006).

As detailed in Section 1.3.2, amyloid fibrils have a "cross-β" structure, with β-sheets arranged parallel to the fibril axis with their constituent β-strands perpendicular to the axis. This cross-β structure is recognised by X-ray fibre diffraction, with the resulting diffraction pattern having two characteristic signals, a sharp reflection at 4.7 Å along the same direction as the fibril axis and a more diffuse reflection at between 10 and 11 Å perpendicular to the fibril direction, arising from the molecular spacings between the β-strands and β-sheets respectively (Eanes and Glenner, 1968) (**Figure 1.8**).

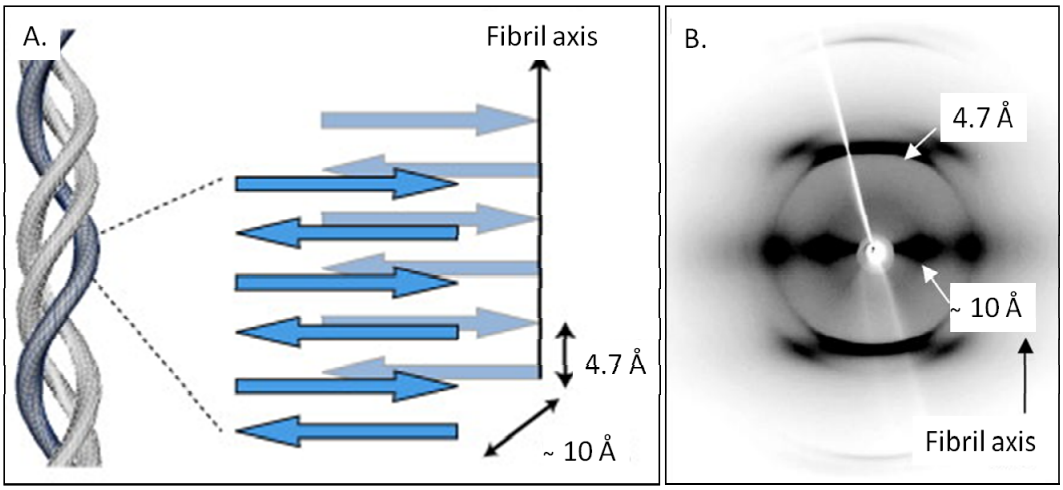

Figure 1.8. *X-ray fibre diffraction is a common method for recognising the cross-β structure of amyloid fibrils (A). The resulting diffraction pattern (B) has two characteristic signals, a sharp reflection at 4.7 Å along the same direction as the fibril axis and a more diffuse reflection at between 10 and 11 Å perpendicular to the fibril direction, arising from the molecular spacings between the β-strands and β-sheets respectively. Figure adapted from (Biancalana and Koide, 2010; Makin and Serpell, 2005).*

Amyloid fibrils may also be characterised by specific chemical staining, such as with the dyes Congo red and Thioflavin T (ThT). When stained with Congo red, amyloid fibrils show an apple-green colour when viewed in a light microscope under cross-polarised light. ThT is a benzothiazole dye that binds to amyloid fibrils, and while much research has been done, the mechanism of this binding is yet to be fully understood (Khurana *et al*., 2005; Krebs *et al*., 2005; Wolfe *et al*., 2010). It was first introduced in 1959 as a dye that shows enhanced fluorescence upon binding to amyloid fibrils in tissue sections (Vassar and Culling, 1959). It is now commonly used for amyloid fibril detection with the dye being added to samples and a characteristic ThT fluorescence emission at approximately 480 nm detected when excited at 450 nm. ThT binding of amyloid fibrils can be used in a number of ways such as diagnosis of amyloid fibrils in tissue sections using fluorescence microscopy (Vassar and Culling, 1959), to directly observe amyloid fibril growth using total internal reflection fluorescence spectroscopy (Ban *et al*., 2006), and for monitoring of extracted amyloid fibrils and *in vitro* amyloid fibril formation using fluorescence spectroscopy (LeVine III, 1993; Naiki *et al*., 1989). The ThT assay measures the change in fluorescence intensity of ThT upon binding to amyloid fibrils (Nilsson, 2004).

In this thesis TEM, AFM, X-ray fibre diffraction, and the ThT assay have been used for characterisation of amyloid fibril structures.

1.4. Amyloid fibrils in bionanotechnology

Over the past decade, there has been an increasing interest in the use of amyloid fibrils in bionanotechnology for a range of different applications due to them possessing a number of desirable properties that recommends their use in this field (Cherny and Gazit, 2008; Gras, 2007b; Gras, 2009; Hamada *et al*., 2004; Mankar *et al*., 2011; Waterhouse and Gerrard, 2004). Some of these properties are generic characteristics of proteins, whereas others are specific to the amyloid fibril structure.

1.4.1. Properties of amyloid fibrils

In addition to self-assembly, the topography of amyloid fibrils also recommends their use as nanomaterials. They naturally exist in the nanometre scale, with widths of generally 7-10 nm and lengths of up to several microns (Gras, 2007a). These lengths are usually highly heterogeneous, and this is addressed in Chapter 3. When using biological molecules in the assembly of nanostructures it is important to have a high level of longevity in the structure formed (Gras, 2007a). Because of their highly ordered β-sheet structure, amyloid fibrils are stable at pH and temperature extremes (Scheibel, 2005), as well as at high pressure (Dirix *et al*., 2005). This observed stability is particularly relevant, due to the similarities in these conditions to those likely to be encountered in an industrial setting, where these nanostructures may be manufactured or used (Scheibel *et al*., 2003).

The mechanical properties of amyloid fibrils are also of interest. Amyloid fibrils have been shown to have a strength comparable to steel and are flexible, with a stiffness similar to that of silk (Smith *et al*., 2006). These mechanical properties are overall similar to those seen in spider silk, which could be expected as both are β-sheet rich protein fibrils (Smith *et al*., 2006). The major difference is that while spider silk requires complex biological machinery to reach its final form, amyloid fibrils self-assemble in solution.

As amyloid fibrils can be formed from a vast number of different proteins and peptides (Fowler *et al*., 2007), there is huge sequence versatility available (Gras, 2007a). It is also possible to target specific amino acids to be exposed on the fibril surface so that additional functionality can be introduced to fibrils through the attachment of bioactive groups, enzymes and other non-protein groups (Hartgerink, 2004). Functionality can also be added to fibrils through the formation of “cofibrils” as demonstrated by MacPhee and Dobson with the incorporation of fluorescence into fibrils by the formation of mixed fibrils of insulin and a fluorescent peptide (MacPhee and Dobson, 2000).

The favourable surface interactions of amyloid fibrils are another feature that recommends their use in bionanotechnology. Amyloid fibrils can interact with and bind to non-biological solid surfaces while remaining intact, unlike globular proteins (Gras, 2007a).

1.4.2. Applications in bionanotechnology

A number of different applications for amyloid fibrils in bionanotechnology have been identified, in medicine, health and nutrition, catalysis, electronics, plastics and structural materials (Waterhouse and Gerrard, 2004). Significant steps have already been taken towards the use of amyloid fibrils in various applications. Amyloid fibrils may be used as functional templates, where by modification *via* enzyme immobilisation, metal coating, or other chemical modifications, they may be used as nanowires, or as enzyme scaffolds for biosensing, bioremediation, or other applications. Many polymers, either synthetic or natural, may form gels and/or liquid crystal phases (Cherny and Gazit, 2008). Amyloid fibril hydrogels have applications in both tissue engineering and drug delivery.

Amyloid fibrils have been used as nanoscaffolds for enzyme immobilisation, with the dimensions of amyloid fibrils offering a large surface area, which increases the active enzyme area, in addition to the other known benefits of enzyme immobilisation such as reusability and increased stability (Brady and Jordaan, 2009). The chemistry of the different amino acid side chains can be exploited to add functionality to fibrils (Hartgerink, 2004) *via* the formation of cross-links between mature fibrils and enzymes of interest. Organophosphate hydrolase and glucose oxidase have both been covalently attached to amyloid fibrils in this manner, making active fibrils that could be used in bioremediation, antimicrobial films and biosensing (Pilkington *et al*., 2010; Raynes *et al*., 2011; Yemini *et al*., 2005a).

Another mode of enzyme immobilisation to fibrils is the creation of fusion proteins, where the protein of interest is fused to an amyloid-forming protein monomer prior to fibril formation, resulting in decorated fibrils. By this method green fluorescent protein, barnase bacterial protein, carbonic anhydrase, glutathione-S-transferase, and cytochrome$_{b562}$ have been attached to fibrils (Baldwin *et al*., 2006; Baxa *et al*., 2002).

Amyloid fibrils also show promise in tissue engineering, with functionalised amyloid fibril scaffolds promoting cell growth and adhesion. For example, it was seen that designed amyloidogenic peptide sequences that had been functionalised with an integrin recognition motif, produced fibrils that interacted specifically with cells (Bongiovanni *et al*., 2011; Gras *et al*., 2008). A number of amyloid forming proteins and peptides have been shown to form hydrogels (Aggeli *et al*., 2003; Bhak *et al*., 2010; Maity *et al*., 2011). For example, Aggeli *et al* showed that a peptide derived from hen lysozyme forms pH dependent gels, which may be used in scenarios where a responsive material is desirable (Aggeli *et al*., 2003). Responsive materials such as these have potential biomedical applications, where biocompatibility and/or biodegradability is sought after (Waterhouse and Gerrard, 2004).

1.5. Nanowires

Nanowires, along with nanotubes, nanobelts, and nanosprings, are a type of 1-D nanostructure, which have been the subject of increasing research focus due to their unique properties, as when materials are reduced to the nanometre scale, new electrical, optical, and mechanical properties are often displayed. The high aspect ratio of 1-D nanostructures also provides a large surface-to-volume ratio, which can be beneficial to a number of applications, for example, the immobilisation of enzymes for biosensing. There are also other properties that enhance these materials' desirability and applicability, such as control over dimensions and arrangement, and stability under a range of conditions, particularly those conditions that may be encountered in potential applications.

In general, 1-D nanostructures are formed by promoting the crystallisation of solid-state structures along one dimesion, and this process can be carried out by a range of different mechanisms, with the main ones identified by Wanekaya *et al*. (2006) as:

1) The use of 1-D template structures to direct the formation of the nanostructure.
2) The use of the intrinsically anisotropic crystallographic structure of a solid to achieve 1-D growth.
3) The use of a liquid/solid interface to reduce the symmetry of a seed.
4) The use of appropriate capping agents to kinetically control the growth rates of various facets of a seed.

Nanowires can be formed from a number of different materials, with CNTs and crystalline nanowires such as silicon nanowires (SiNW) gaining the most attention since their discovery in 1991 and 1998 respectively (Iijima, 1991; Yu *et al*., 1998). Nanowires are also often formed from other metals, semiconductors, and inorganic compounds. Of interest to this thesis are nanowires formed from biological materials.

1.5.1. Biological nanowires

Not only are the dimensions of many biological macromolecules comparable to nanoscale building blocks, the presence of high-aspect ratio elongated structures in biology means that a number of biological macromolecules and macromolecular assemblies have been investigated as nanowires. With most of the biological structures investigated having low conductivity in the native state, the use of biomolecules, such as nucleic acids, viruses, proteins, and peptides, as templates for the formation of metallic and semiconductor nanowires has been explored. The different biomolecules that have been investigated for use as nanowires, along with their dimensions, sources, and with what they have been modified, are summarised in **Table 1.2**.

Table 1.2. *Summary of the variety of different biomolecules and biomolecular assemblies that have been investigated as nanowires, or as templates for nanowire formation.*

Biomolecule/ Biomolecular assembly	Dimensions (diameter/length)	Source	Modified nanowires (biomolecule as a template)	References
A) Nucleic acids				
DNA	1-2 nm/tunable in micron range	PCR	Au, Ag, Pt, Pd, Cu	(Braun *et al*., 1998; Ford *et al*., 2001; Kim *et al*., 2010; Monson and Woolley, 2003; Patolsky *et al*., 2002; Richter *et al*., 2000; Richter *et al*., 2001; Seidel *et al*., 2004)
B) Viruses				
Tobacco mosaic virus (TMV)	18 nm, 4 nm (central channel)/300 nm		CdS, PbS, Pd, FeO, Si, Ni, Co, Ag, Au, Pt, CoPt, $FePt_3$	(Dujardin *et al*., 2003; Knez *et al*., 2003; Lim *et al*., 2010; Shenton *et al*., 1999; Tsukamoto *et al*., 2007)
C) Proteins				
Collagen	1.5 nm/300 nm	Self-assembly from proteins produced by recombinant expression	Au, ZnO	(Bai *et al*., 2007; Bai *et al*., 2009; Orza *et al*., 2011)
Actin	8 nm/up to 10 μm		Au	(Patolsky *et al*., 2004)
Microtubules	25 nm/several microns	Isolated from porcine brain tissue	Ag, Au, Co, FeO, Ni, Pd,	(Behrens *et al*., 2004; Zhou *et al*., 2008; Zhou *et al*., 2010)
Amyloid fibrils	10-20 nm/up to several microns	Self-assembly from proteins produced by recombinant expression, and from crude waste materials	Conducting polymers (PEDOT-S, PTAA, PPF), H_2PtCl_6, Ag, Fe^{3+}	(Choi *et al*., 2011; Hamedi *et al*., 2008; Herland *et al*., 2007; Hsieh and Hsieh, 2010; Leroux *et al*., 2010; Malisauskas *et al*., 2008; Scheibel *et al*., 2003; Tanaka *et al*., 2008; Tang *et al*., 2010)
D) Peptides				
Peptide nanotubes	1-100 nm/	Self-assembly from engineered peptide solutions	Au, Ag, Cu, Pt, Zns	(Banerjee *et al*., 2003; Banerjee *et al*., 2005; Djalali *et al*., 2002; Djalali *et al*., 2003; Kasotakis *et al*., 2009; Song *et al*., 2004)
Amyloid-like peptide nanotubes Eg. FF peptide	1-100 nm/		Au, Ag, Co_3O_4	(Carny *et al*., 2006; Reches and Gazit, 2003; Ryu *et al*., 2009)

1.5.2. Nucleic acids

DNA molecules have been identified as interesting building blocks for nanotechnology due to their size, chemical robustness, and the ability to synthesise large amounts for relatively low costs. In terms of size, the diameters of ssDNA and dsDNA are approximately 1 and 2 nm respectively, and the length of DNA can be easily tuned, from nanometres to microns, using a range of techniques such as PCR, DNA ligation and enzymatic digestion, with the length per nucleoside subunit 0.34 nm (Gu *et al*., 2006).

In regards to using the DNA molecule itself as a nanowire, the inherent conductivity of DNA is in debate, with current values in the nanoAmp range recorded under applied potentials up to 6 V recorded for DNA networks of 100 nm wires (Cai *et al*., 2000), and studies also reporting that DNA is insulating at lengths greater than 40 nm, where currents remained below the noise level of approximately 1 pA under applied potentials up to 10 V for bundles of approximately 10 DNA molecules (Storm *et al*., 2001).

What has been of more interest, due to these poor electrical characteristics, is the use of DNA molecules as templates for self-assembly of metallic nanowires. This work began in 1998, when Braun created the first conductive nanowire using DNA as a template for the formation of conductive silver nanowires (Braun *et al*., 1998). Since this pioneering study, DNA nanowires have been formed *via* modification with silver (Braun *et al*., 1998), gold (Kim *et al*., 2006; Patolsky *et al*., 2002), platinum (Ford *et al*., 2001; Seidel *et al*., 2004), palladium (Richter *et al*., 2000; Richter *et al*., 2001), and copper (Monson and Woolley, 2003).

1.5.3. Viruses

Whole biological organisms have also attracted attention as nanowires, such as the Tobacco Mosaic Virus (TMV). TMV is a rod shaped RNA virus, which is formed from the self assembly of 2130 coat protein subunits which are arranged helically with a coil of RNA that spans the length of the virus (Shenton *et al*., 1999). The TMV is uniform in diameter and length, existing with dimensions of 18 nm and 300 nm respectively. The TMV also has a 4 nm hollow core, and has chemically distinct internal and external surfaces, meaning that it may be modified on both its internal and external surfaces (Dujardin *et al*., 2003; Tsukamoto *et al*., 2007).

Nanowires have been formed using TMV as a template with surface modification of the TMV by cadmium sulfide, lead sulfide, iron oxide, silica (Shenton *et al*., 1999), platinum, palladium, and gold (Dujardin *et al*., 2003; Lim *et al*., 2010). The central channel of TMV has also been used as a template, with 3 nm nickel and cobalt nanowires being produced this way (Knez *et al*., 2003), as well as a variety of other nanowires (Dujardin *et al*., 2003; Tsukamoto *et al*., 2007).

Other viruses have also been used for this purpose, such as the M13 bacteriophage, which was used as a scaffold for the synthesis of ZnS, CdS, CoPt, and FePt nanowires (Mao *et al*., 2004).

1.5.4. Proteins

There are a number of naturally occurring fibrous protein structures, and globular proteins can also be induced to form fibrous structures, as in the case of amyloid fibrils. The morphology and dimensions of these protein structures make them excellent candidates for the formation of self assembling 1-D nanostructures.

Protein structures have the advantage of chemical and biological diversity, providing building blocks with heterogeneity. The amino acid building blocks also give the opportunity to exploit the chemistry of the various side chains for derivitisation and functionalisation, be it for metallic modification or the immobilisation of enzymes. The option for genetic control of the primary sequence further enhances this property, and *via* recombinant expression it is possible to easily generate large amounts of a protein of interest, making them a readily available source. Additionally, typically fibrous proteins have a higher relative stability than globular proteins, and unique mechanical properties (Wong Po Foo and Kaplan, 2002).

The use of proteins as biological nanowires has been explored in some detail, with a variety of different protein structures used. These protein/peptide nanotubes (PNTs), and nanofibres (PNFs), have been used as template molecules in a number of different ways. **Figure 1.9** shows a schematic representation of the three most common ways; by modification with metallic nanoparticles (NPs), conducting polymers (CPs), and metal ions.

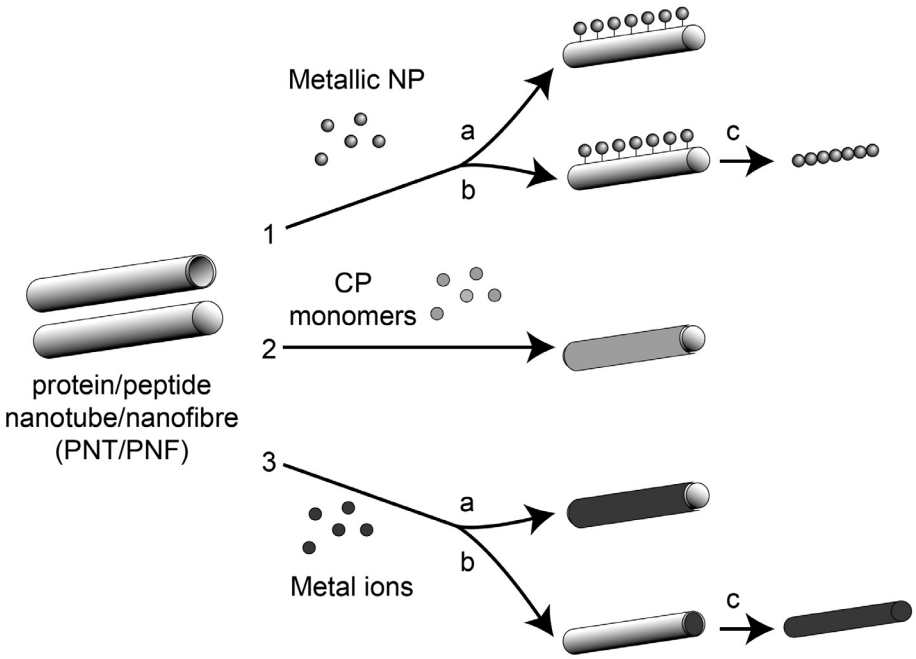

Figure 1.9. *Schematic showing the most common ways in which protein/peptide nanotubes/nanofibres (PNTs/PNFs) are used for the templating of conductive nanowires. 1) The PNT/PNF is modified with metallic nanoparticles (NPs). This may occur such that the PNT/PNF itself is decorated with metallic NPs (a), or with the PNT/PNF being used as a "sacrificial" template for the formation of a chain of metallic NPs (b). 2) The PNT/PNF is modified with conducting polymer (CP) monomers, with the polymerisation reaction being carried out in the presence of the PNT/PNF, forming a coating of conducting polymer on the surface of the PNT/PNF. 3) The PNT/PNF is modified with metal ions. a) A coating of metal may be formed on the exterior of the PNT/PNF, or b) on the interior of a PNT. In some cases, c), the PNT can then be removed, leaving a thin metallic nanowire.*

1.5.5. Collagen

As the major component of the extracellular matrix of bone, cartilage, skin, blood vessels and corneas, collagen is one of the most abundant proteins in higher organisms. The collagen triple helix is approximately 300 nm long and 1.5 nm in diameter, and collagens consist of one or more of these triple helices (Kadler *et al*., 1996). It is this hierarchical design, along with the relative dimensions of the building molecules, that give collagen its superior mechanical properties, creating a tough and robust material (Buehler, 2006).

Collagen has been modified to form both gold and zinc oxide nanowires (Bai *et al*., 2007; Bai *et al*., 2009; Orza *et al*., 2011). Bai *et al*. (2007) used a collagen-like triple helix, which is formed from a polypeptide that was genetically engineered and contains a fragment from the natural collagen sequence. With collagen being using largely in tissue engineering applications, the application of metallically modified collagen has also been investigated here. Orza *et al*. (2011) constructed a matrix of gold coated collagen nanofibres and demonstrated how these could be used for the growth and differentiation of human adult stem cells.

1.5.6. Actin

Filamentous actin (F-actin), formed by the polymerisation of monomers of globular actin (G-actin), has a diameter of 8 nm and exists in lengths up to 10 μm (Kabsch and Vandekerckhove, 1992). *In vivo*, the polymerisation and depolymerisation of actin is a dynamic equilibrium; however, *in vitro*, actin can be stabilised against depolymerisation (Cooper, 1987), and this is essential for the use of actin as a filamentous building block, or as a nanowire. Protein-metal nanowires have been formed based on the use of G-actin as a molecular building block, with the filaments being coated with gold nanoparticles (Patolsky *et al*., 2004), the process shown in **Figure 1.9**, 1a.

1.5.7. Microtubules

Microtubules are proteinaceous cylindrical structures which are assembled from tubulin protofilaments, resulting in a structure with an external diameter of 25 nm and several microns in length (Nogales, 2001). *In vivo,* they are part of the cytoskeleton, and are involved in processes such as motility and intracellular transport. Tubulin, from which microtubules are formed, can also form other structures, such as sheets, spirals, and rings. Nanowires of nickel, cobalt, silver, gold, and iron oxide have all been formed around the microtubule template (Behrens *et al*., 2004; Zhou *et al*., 2008; Zhou *et al*., 2010).

1.5.8. Peptides

Peptides have been identified as excellent building blocks for nanotechnology, due to chemical variety, biocompatibility, and their ability to spontaneously associate into a range of structures such as nanofibrils, nanotapes, nanoribbons, nanospheres, and nanotubes (Valéry *et al*., 2011). The elongated structures achievable have variable dimensions, some with diameters as small as 1 nm, and others up to hundreds of nanometres (Valéry *et al*., 2011). Self-assembling peptides have also been investigated as nanowires, mainly as template molecules. Like proteins, peptides offer surfaces which can be functionalised, which has seen the creation of nanowires of gold (Djalali *et al*., 2002; Djalali *et al*., 2003; Kasotakis *et al*., 2009), silver (Kasotakis *et al*., 2009; Reches and Gazit, 2003), copper (Banerjee *et al*., 2003), cobalt oxide (Ryu *et al*., 2009), platinum (Kasotakis *et al*., 2009; Song *et al*., 2004), zinc sulfide (Banerjee *et al*., 2005), and even trilayered metal-insulator-metal coaxial cables (Carny *et al*., 2006).

1.5.9. Amyloid inspired peptides

Peptide design is based on the predicted interactions between the side chains, which has resulted in inspiration from amyloid fibrils, with a number of self-assembling peptides being fragments of amyloid-forming proteins (Cherny and Gazit, 2008). The peptide that has attracted the most attention in this field over the last few years is the dipeptide diphenylalanine (FF). This short aromatic peptide is the key recognition sequence of the Alzheimer's disease β-amyloid peptide and forms discrete and hollow nanotubes in solution (Reches and Gazit, 2003). Aside from being modified with metals, Gazit and co-workers have also shown the ability to control arrangement of these peptide nanotubes, with vertical arrays created by vapour deposition (Adler-Abramovich *et al*., 2009), and alignment of nanotubes in a magnetic field (Hill *et al*., 2007). Some investigation has also been made into their conductive properties in the unmodified state. By immobilising FF peptide nanotubes between electrodes using dielectrophoresis, Castillo *et al*. created current-voltage (I-V) curves for small bundles of nanotubes (Castillo *et al*., 2008). The current transmitted through the immobilised nanotubes after an applied potential of 0-3 V was in the pA range, confirming that the peptide nanotubes had high resistance.

1.6. Amyloid fibrils as nanowires

Amyloid inspired peptide nanotubes have gained a large amount of attention as nanowires. Less research has involved amyloid fibrils formed from whole amyloid forming proteins, although there are some previous investigations that have looked at amyloid fibrils as both unmodified and modified nanowires, beginning with the work of Schiebel *et al*. in 2003, where amyloid-like fibres formed from the N-terminal and middle region (NM region) of Sup25p, a prion determinant from *Saccharomyces cerevisiae*, were shown to act as insulators with high resistance and, after modification *via* gold toning, to conduct with low resistance (Scheibel *et al*., 2003). Another study on unmodified fibrils formed from an elastin-related polypeptide showed these amyloid fibrils to be able to sustain electrical conduction, with current values in the range of several nanoAmps at 0-2 Volts (del Mercato *et al*., 2007) these, however, are still low current values in comparison to other nanowires such as CNTs.

Amyloid fibril nanowires have also been investigated with the fibrils undergoing modification by conducting polymers as well as other metallic modifications. Insulin amyloid fibrils have been used as scaffolds for the formation of conducting polymer nanowires, with insulin amyloid fibrils being modified with the conducting polymers poly(thiophene acetic acid) (PTAA), alkoxysulfonate PEDOT (PEDOT-S), and poly(propylene fumarate) (PPF) (Hamedi *et al*., 2008; Herland *et al*., 2008; Tanaka *et al*., 2008). Insulin amyloid fibrils have also been modified with the platinum complex, hexachloroplatanic acid (Tang *et al*., 2010), and silver nanoparticles (Leroux *et al*., 2010), as well as being used as a sacrificial template for the formation of gold nanowires (Hsieh and Hsieh, 2010). Amyloid fibrils formed from α-synuclein and lysozyme have also been used in this way, with fibrils modified with iron (Choi *et al*., 2011) and silver (Malisauskas *et al*., 2008) respectively.

1.7. Nanowire applications

Nanowires, be they biological, metallic, or semiconducting, have a range of different applications in the fields of electronics, optics, magnetic medium, thermoelectronics, and sensing. In this thesis, biosensing was used as a model nanowire application.

1.8. Biosensing

Biosensing is the detection and quantification of biological and chemical species, and is critical to many areas of health care and life science. It involves the transduction of a signal that is associated with the selective recognition of a species of interest (Patolsky *et al*., 2006). As efficient biosensing requires direct interaction with biomolecules of dimensions in the nanoscale, it is predictable that this field requires techniques and probing tools that exist on a similar scale (Li *et al*., 2005) and so nanostructures, such as nanowires, offer the opportunity to develop novel sensors.

The four most commonly used types of biosensing devices based on nanowires are nanowire-modified microtips, single nanowire field-effect transistors (FETs), porous nanowire films, and nanoelectrode arrays (Li *et al*., 2005). These are shown schematically in **Figure 1.10**.

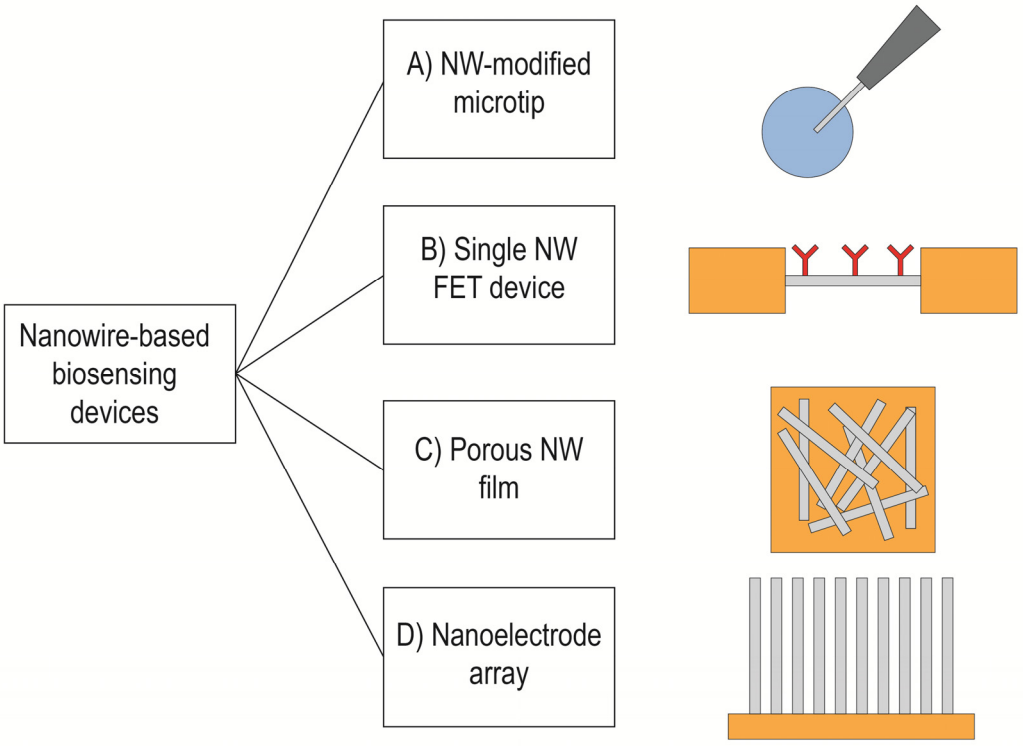

Figure 1.10. *Schematic representations of the four most common types of biosensing devices based on nanowires. A) Nanowire-modified microtips, B) Single nanowire field-effect transistors (FETs) C) Porous nanowire films, and D) Nanoelectrode arrays.*

Nanowire-modified microtips (**Figure 1.10**, A) have a single nanowire extended from a microtip, and this can be used to probe a single cell or single molecules (Li *et al.*, 2005). Depending on the detection technique, the nanowire may either be attached to an optical fibre for optical detection, or to an electrode for electrical or electrochemical detection. Single nanowire FETs (**Figure 1.10**, B) function by exhibiting a conductivity change along the nanowire in response to variations in the electric field or potential at the surface (Patolsky *et al.*, 2006). The standard set-up involves a semiconductor nanowire connected to a metal source and drain electrodes through which current flows. This current flow between the source and drain electrodes, *via* the nanowire, is switched on and off by a third electrode, the gate. The surface of the nanowire is often modified with receptor groups that recognise specific molecules, i.e., the analyte of interest. The binding of the analyte of interest results in an increase/decrease in the conductance of the nanowire and this is the signal that is associated with the presence of this analyte.

Porous nanowire films (**Figure 1.10**, C) can exist as a thin film which is cast on a conventional electrode, or as a 3-D porous film (Li *et al*., 2005), most often in the creation of an enzyme-based electrochemical sensor (described in Section 1.8.1). CNTs have been used in this way, with the large surface-to-volume ratio and good electrical conductance of carbon nanotubes allowing them to act as both the immobilisation matrix for the enzyme, and also the mediator molecules, which are present to improve the electron transport between the active site of the enzyme and the electrode. Nanoelectrode arrays (**Figure 1.10**, D) are usually comprised of arrays of vertically aligned CNTs. The electrochemical signal is a characteristic of the oxidation-reduction reaction of the analyte, as opposed to non-specific charges sensed by FETs, which results in high specificity (Li *et al*., 2005).

There have been some previous investigations in the use of PNTs/PNFs as immobilisation scaffolds for the creation of enzyme electrode sensors, specifically using PNTs/PNFs formed from the FF peptide, a collagen-type peptide, and the ionic complementary peptide EFK16-11 (Qian *et al*., 2009; Yemini *et al*., 2005a; Yemini *et al*., 2005b; Yemini *et al*., 2006). In this thesis, amyloid fibrils are used as an immobilisation matrix for glucose oxidase (GOx), creating a porous nanowire film-type biosensor. This is discussed in detail in Chapter 5.

1.8.1. Glucose sensing

Glucose sensing has a very important role in both the diagnosis and management of diabetes, as well as in the food industry. In diabetes, careful monitoring of blood and urine glucose levels is necessary to correctly diagnose and manage the disease. Glucose monitoring is used in the food industry during fermentation processes, as the amount of glucose greatly influences the quality of food products.

Since the creation of the first glucose monitor in 1971, this field has grown rapidly due to high demand, with glucose sensors dominating the biosensor market (Oliver *et al*., 2009). There are a number of different types of glucose sensors, with detection methods based on fluorescence, electrochemistry, and spectroscopy, among many others. For the purpose of this thesis, the focus is on those sensors which use enzyme electrodes, a mode of detection which was first created in 1962 (Clark Jr and Lyons, 1962).

Enzyme electrodes function by using enzymes that catalyse oxidation-reduction reactions, and so donate and accept electrons. This electron movement from the enzyme may then be used to produce a concentration-dependent current or voltage, which may be measured using electrodes. In glucose sensing, the enzyme GOx is widely used. GOx catalyses the conversion of glucose to gluconolactone; detail of this reaction and the GOx enzyme can be found in Section 5.2. GOx modified electrodes can be used in glucose sensing either by measuring oxidation and reduction of a mediator molecule, eg. ferrocene, or by measuring peroxide amperometrically using a platinum electrode. The schematic in **Figure 1.11** shows how these two scenarios work.

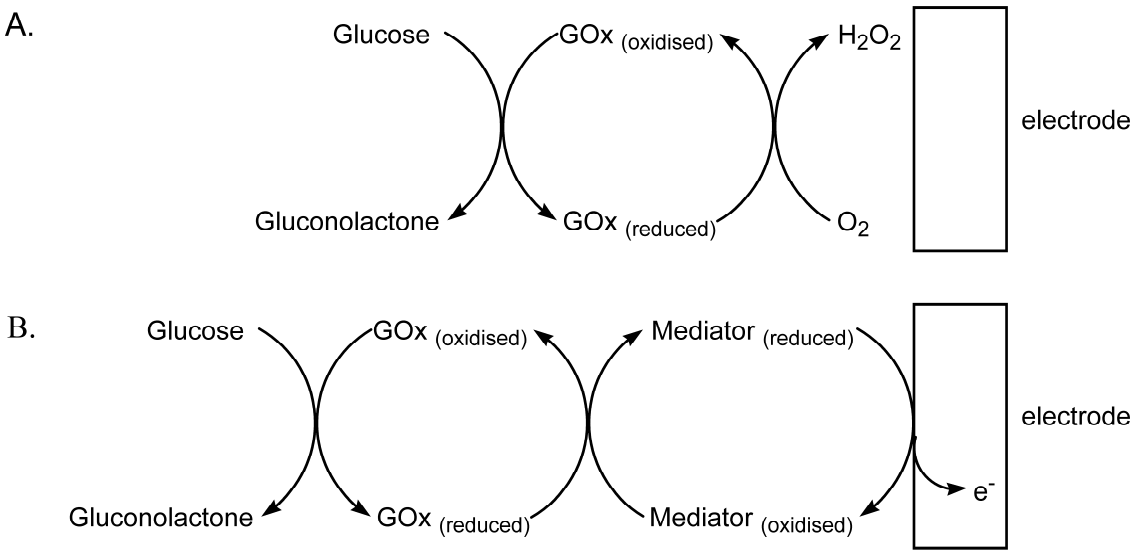

Figure 1.11. *Schematic showing the functioning of glucose oxidase (GOx) enzyme electrodes as glucose sensors. These can work in one of two ways; A) Through the amperometric detection of hydrogen peroxide using a platinum electrode, and B) By measuring the oxidation and reduction of a mediator molecule.*

1.9. Thesis objectives

This introduction has provided background information regarding the structure, formation, and sources of amyloid fibrils, as well as how amyloid fibrils may be used in the field of bionanotechnology.

Amyloid fibrils formed from three different protein systems were used throughout this thesis. Bovine insulin was used as a model amyloid forming protein due to it being very well characterised. Fungal hydrophobins were used due to their formation of well aligned rodlets, making it an interesting system. Finally, crude fish crystallin proteins were used as a readily available protein source, due to the proteins being able to be extracted from waste products. The early part of this study involved formation and characterisation of amyloid fibrils from these three protein sources. Due to gaps in the current knowledge on amyloid fibrils formed from crude fish crystallins, these were characterised in greater detail.

There are a number of favourable properties in a nanowire, and the ability of amyloid fibrils, particularly those formed from crude crystallin proteins, to realise these led to a focus on this protein. As such, the stability in solution of crystallin fibrils was examined. This is particularly relevant in light of what has been shown regarding the stability in solution of a leading amyloid-like peptide nanotube, and also potential end-point applications, such as their use in biosensing.

A systematic study was then conducted in order to investigate the ability to control the dimensions of amyloid fibrils. Given what is known about amyloid fibril formation (Brange *et al*., 1997), it was hypothesised that altering the growth and storage conditions used for the formation of amyloid fibrils would influence the dimensions of the resulting fibrils. Control over fibril dimensions enhances their desirability as nanomaterials, as well as being necessary for the experimental set-up in Chapter 4.

Although there have been previous studies that have utilised modified amyloid fibrils as nanowires, less is known about the intrinsic conductivity of amyloid fibrils formed from native proteins in the unmodified state. This was investigated by examining the conductive properties of amyloid fibril networks formed from three different native protein sources, with direct comparison to literature values for amyloid-like fibrils formed from peptides. Conductivity measurements on individual, or small bundles of fibrils were also carried out; in order to do this crystallin fibrils were manipulated and immobilised between electrodes by dielectrophoresis. The ability to control the arrangement of amyloid fibrils on a microchip would open up new opportunities for their use in bionanotechnology.

It was then of interest to investigate the use of amyloid fibrils in a model nanowire application. Other nanowires, including biological ones, have been used in the construction of glucose sensors, and the use of amyloid fibrils was investigated. Methods already existed for enzyme immobilisation onto bovine insulin fibrils, and the aim was to also immobilise enzymes, in this case glucose oxidase, to amyloid fibrils formed from crude fish crystallins. The use of these functionalised fibrils in glucose sensing was explored.

1.10. Thesis overview

Chapter 2 details the formation and characterisation of amyloid fibrils formed from the three protein sources used in this thesis; bovine insulin, fungal hydrophobins, and crude fish crystallins. An investigation into the stability of amyloid fibrils formed from crude crystallin proteins is also detailed in this chapter.

Chapter 3 focuses on the use of growth and storage conditions to control the length of amyloid fibrils formed from bovine insulin and crude fish crystallins.

Chapter 4 presents the conductive properties of networks of amyloid fibrils formed from bovine insulin, fungal hydrophobins, and crude fish crystallins; along with the modification of bovine insulin with conducting polymers. Amyloid fibrils formed from crude crystallin proteins were also manipulated and isolated using dielectrophoresis.

Chapter 5 details an investigation into the use of amyloid fibrils in the construction of a glucose sensor, chosen as a model nanowire application. This entails the creation of glucose oxidase functionalised fibrils, electrochemical characterisation of amyloid fibrils, and the glucose sensing capabilities of an electrode modified with functionalised fibrils.

Chapter 6 summarises the major findings of this thesis, and future directions to be pursued from this work.

Chapter 7 outlines the experimental procedures used throughout this body of work.

1.11. References

Adler-Abramovich L, Aronov D, Beker P, Yevnin M, Stempler S, Buzhansky L, Rosenman G, Gazit E. 2009. Self-assembled arrays of peptide nanotubes by vapour deposition. *Nature Nanotechnology* **4**:849–854.

Aggeli A, Bell M, Carrick L, Fishwick C, Harding R, Mawer P, Radford S, Strong A, Boden N. 2003. pH as a trigger of peptide β-sheet self-assembly and reversible switching between nematic and isotropic phases. *Journal of the American Chemical Society* **125**:9619–9628.

Bai H, Xu F, Anjia L, Matsui H. 2009. Low temperature synthesis of ZnO nanowires by using a genetically-modified collagen-like triple helix as a catalytic template. *Soft Matter* **5**:966–969.

Bai H, Xu K, Xu Y, Matsui H. 2007. Fabrication of Au nanowires of uniform length and diameter using a monodisperse and rigid biomolecular template: Collagen-like triple helix. *Angewandte Chemie International Edition* **46**:3319–3322.

Baldwin A, Bader R, Christodoulou J, MacPhee C, Dobson C, Barker P. 2006. Cytochrome display on amyloid fibrils. *Journal of the American Chemical Society* **128**:2162–2163.

Ban T, Yamaguchi K, Goto Y. 2006. Direct observation of amyloid fibril growth, propagation, and adaptation. *Accounts of Chemical Research* **39**:663–670.

Banerjee I, Yu L, Matsui H. 2003. Cu nanocrystal growth on peptide nanotubes by biomineralization: size control of Cu nanocrystals by tuning peptide conformation. *Proceedings of the National Academy of Sciences of the United States of America* **100**:14678.

Banerjee I, Yu L, Matsui H. 2005. Room-temperature wurtzite ZnS nanocrystal growth on Zn finger-like peptide nanotubes by controlling their unfolding peptide structures. *Journal of the American Chemical Society* **127**:16002–16003.

Baxa U, Speransky V, Steven A, Wickner R. 2002. Mechanism of inactivation on prion conversion of the Saccharomyces cerevisiae Ure2 protein. *Proceedings of the National Academy of Sciences of the United States of America* **99**:5253.

Behrens S, Wu J, Habicht W, Unger E. 2004. Silver nanoparticle and nanowire formation by microtubule templates. *Chemistry of Materials* **16**:3085–3090.

Berson J, Theos A, Harper D, Tenza D, Raposo G, Marks M. 2003. Proprotein convertase cleavage liberates a fibrillogenic fragment of a resident glycoprotein to initiate melanosome biogenesis. *The Journal of Cell Biology* **161**:521.

Bhak G, Lee S, Park J, Cho S, Paik S. 2010. Amyloid hydrogel derived from curly protein fibrils of α-synuclein. *Biomaterials* **31**:5986–5995.

Biancalana M, Koide S. 2010. Molecular mechanism of thioflavin-T binding to amyloid fibrils. *Biochimica et Biophysica Acta (BBA)-Proteins & Proteomics* **1804**:1405–1412.

Bongiovanni M, Scanlon D, Gras S. 2011. Functional fibrils derived from the peptide TTR1-cycloRGDfK that target cell adhesion and spreading. *Biomaterials* **32**:6099–6110.

Brady D, Jordaan J. 2009. Advances in enzyme immobilisation. *Biotechnology Letters* **31**:1639–1650.

Brange J, Andersen L, Laursen ED, Meyn G, Rasmussen E. 1997. Toward understanding insulin fibrillation. *Journal of Pharmaceutical Sciences* **86**:517–525.

Braun E, Eichen Y, Sivan U, Ben-Yoseph G. 1998. DNA-templated assembly and electrode attachment of a conducting silver wire. *Nature* **391**:775–778.

Buehler M. 2006. Nature designs tough collagen: Explaining the nanostructure of collagen fibrils. *Proceedings of the National Academy of Sciences of the United States of America* **103**:12285–12290.

Cai L, Tabata H, Kawai T. 2000. Self-assembled DNA networks and their electrical conductivity. *Applied Physics Letters* **77**:3105–3106.

Carny O, Shalev D, Gazit E. 2006. Fabrication of coaxial metal nanocables using a self-assembled peptide nanotube scaffold. *Nano Letters* **6**:1594–1597.

Carrio M, Gonzalez-Montalban N, Vera A, Villaverde A, Ventura S. 2005. Amyloid-like properties of bacterial inclusion bodies. *Journal of Molecular Biology* **347**:1025–1037.

Castillo J, Tanzi S, Dimaki M, Svendsen W. 2008. Manipulation of self-assembly amyloid peptide nanotubes by dielectrophoresis. *Electrophoresis* **29**:5026–5032.

Chan W. 2006. Bionanotechnology progress and advances. *Biology of Blood and Marrow Transplantation: Journal of the American Society for Blood and Marrow Transplantation* **12**:87–91.

Chapman M, Robinson L, Pinkner J, Roth R, Heuser J, Hammar M, Normark S, Hultgren S. 2002. Role of *Escherichia coli* curli operons in directing amyloid fiber formation. *Science* **295**:851.

Cherny I, Gazit E. 2008. Amyloids: Not only pathological agents but also ordered nanomaterials. *Angewandte Chemie - International Edition* **47**:4062–4069.

Chiti F, Dobson. 2006. Protein misfolding, functional amyloid, and human disease. *Annual Review of Biochemistry* **75**:333–366.

Choi Y, Kim J, Bhak G, Lee D, Paik S. 2011. Photoelectric protein nanofibrils of α-synuclein with embedded iron and phthalocyanine tetrasulfonate. *Angewandte Chemie* **123**:6194–6198.

Chopra N, Gavalas V, Bachas L, Hinds B, Bachas L. 2007. Functional one-dimensional nanomaterials: Applications in nanoscale biosensors. *Analytical Letters* **40**:2067–2096.

Clark Jr L, Lyons C. 1962. Electrode systems for continuous monitoring in cardiovascular surgery. *Annals of the New York Academy of Sciences* **102**:29–45.

Cohen A, Shirahama T, Skinner M. 1982. Electron microscopy of amyloid. *Electron Microscopy of Proteins* **3**:165–206.

Cooper J. 1987. Effects of cytochalasin and phalloidin on actin. *The Journal of Cell Biology* **105**:1473 –1478.

Ding R, Lu G, Yan Z, Wilson M. 2001. Recent advances in the preparation and utilization of carbon nanotubes for hydrogen storage. *Journal of Nanoscience and Nanotechnology* **1**:7–29.

Dirix C, Meersman F, MacPhee C, Dobson C, Heremans K. 2005. High hydrostatic pressure dissociates early aggregates of TTR 105-115, but not the mature amyloid fibrils. *Journal of Molecular Biology* **347**:903–909.

Djalali R, Chen Y, Matsui H. 2002. Au nanowire fabrication from sequenced histidine-rich peptide. *Journal of the American Chemical Society* **124**:13660–13661.

Djalali R, Chen Y, Matsui H. 2003. Au nanocrystal growth on nanotubes controlled by conformations and charges of sequenced peptide templates. *Journal of the American Chemical Society* **125**:5873–5879.

Dobson C. 2003a. Protein folding and misfolding. *Nature* **426**:884–890.

Dobson C. 2003b. Protein folding and disease: A view from the first Horizon Symposium. *Nature Reviews Drug Discovery* **2**:154–160.

Dong M, Hovgaard M, Xu S, Otzen D, Besenbacher F. 2006. AFM study of glucagon fibrillation via oligomeric structures resulting in interwoven fibrils. *Nanotechnology* **17**:4003.

Dujardin E, Peet C, Stubbs G, Culver J, Mann S. 2003. Organization of metallic nanoparticles using tobacco mosaic virus templates. *Nano Letters* **3**:413–417.

Eanes E, Glenner G. 1968. X-ray diffraction studies on amyloid filaments. *Journal of Histochemistry & Cytochemistry* **16**:673.

El-Sayed M. 2001. Some interesting properties of metals confined in time and nanometer space of different shapes. *Accounts of Chemical Research* **34**:257–264.

Ford W, Harnack O, Yasuda A, Wessels J. 2001. Platinated DNA as precursors to templated chains of metal nanoparticles. *Advanced Materials* **13**:1793–1797.

Fowler D, Koulov A, Alory-Jost C, Marks M, Balch W, Kelly J. 2005. Functional amyloid formation within mammalian tissue. *PLoS Biology* **4**:6.

Fowler D, Koulov A, Balch W, Kelly J. 2007. Functional amyloid - from bacteria to humans. *Trends in Biochemical Sciences* **32**:217–224.

Friedreich N, Kekulé A. 1859. Zur amyloidfrage. *Virchows Archiv* **16**:50–65.

Gazit E. 2007. Self-assembled peptide nanostructures: the design of molecular building blocks and their technological utilization. *Chemical Society Reviews* **36**:1263–1269.

Geddes A, Parker K, Atkins E, Beighton E. 1968. "Cross-beta" conformation in proteins. *Journal of Molecular Biology* **32**:343–358.

Goeden-Wood N, Keasling J, Muller S. 2003. Self-assembly of a designed protein polymer into β-sheet fibrils and responsive gels. *Macromolecules* **36**:2932–2938.

Gras S. 2007a. Amyloid fibrils: From disease to design. New biomaterial applications for self-assembling cross-β fibrils. *Australian Journal of Chemistry* **60**:333–342.

Gras S. 2007b. Protein misfolding: A route to new nanomaterials. *Advanced Powder Technology* **18**:699–705.

Gras S. 2009. Surface- and solution- based assembly of amyloid fibrils for biomedical and nanotechnology applications. In: . *Advances in Chemical Engineering*. Elsevier, Vol. 35, pp. 161–209.

Gras S, Tickler A, Squires A, Devlin G, Horton M, Dobson C, MacPhee C. 2008. Functionalised amyloid fibrils for roles in cell adhesion. *Biomaterials* **29**:1553–1562.

Graveland-Bikker J, de Kruif C. 2006. Unique milk protein based nanotubes: Food and nanotechnology meet. *Trends in Food Science and Technology* **17**:196–203.

Gu Q, Cheng C, Gonela R, Suryanarayanan S, Anabathula S, Dai K, Haynie DT. 2006. DNA nanowire fabrication. *Nanotechnology* **17**:R14.

Hamada D, Yanagihara I, Tsumoto K. 2004. Engineering amyloidogenicity towards the development of nanofibrillar materials. *Trends in Biotechnology* **22**:93–97.

Hamedi M, Herland A, Karlsson R, Inganas O. 2008. Electrochemical devices made from conducting nanowire networks self-assembled from amyloid fibrils and alkoxysulfonate PEDOT. *Nano Letters* **8**:1736–1740.

Hartgerink J. 2004. Covalent capture: A natural complement to self-assembly. *Current Opinion in Chemical Biology* **8**:604–609.

Hatters D, MacRaild C, Daniels R, Gosal W, Thomson N, Jones J, Davis J, MacPhee C, Dobson C, Howlett G. 2003. The circularization of amyloid fibrils formed by apolipoprotein C-II. *Biophysical Journal* **85**:3979–3990.

Healy J, Wong K, Roux C, Domigan L, Sunde M, Sawyer E, Gras S, Gerrard J, Vadudevamurthy M. 2012. Polymorphism and higher ordered structures of protein nanofibers from crude mixtures of fish lens crystallins: Towards useful materials. *Biopolymers*:Accepted.

Herland A, Thomsson D, Mirzov O, Scheblykin I, Inganäs O. 2008. Decoration of amyloid fibrils with luminescent conjugated polymers. *Journal of Materials Chemistry* **18**:126–132.

Herland A, Björk P, Hania PR, Scheblykin I, Inganäs O. 2007. Alignment of a conjugated polymer onto amyloid-like protein fibrils. *Small* **3**:318–25.

Hill R, Sedman V, Allen S, Williams P, Paoli M, Adler-Abramovich L, Gazit E, Eaves L, Tendler S. 2007. Alignment of aromatic peptide tubes in strong magnetic fields. *Advanced Materials* **19**:4474–4479.

Hsieh S, Hsieh C. 2010. Alignment of gold nanoparticles using insulin fibrils as a sacrificial biotemplate. *Chemical Communications* **46**:7355–7357.

Iconomidou V, Vriend G, Hamodrakas S. 2000. Amyloids protect the silkmoth oocyte and embryo. *FEBS Letters* **479**:141–145.

Iijima S. 1991. Helical microtubules of graphitic carbon. *Nature* **354**:56–58.

Jahn T, Radford S. 2008. Folding versus aggregation: Polypeptide conformations on competing pathways. *Archives of Biochemistry and Biophysics* **469**:100–117.

Jaskolski M. 2001. 3D domain swapping, protein oligomerization, and amyloid formation. *Acta Biochimica Polonica* **48**:807–827.

Jiménez J, naki Guijarro J, Orlova E, Zurdo J, Dobson C, Sunde M, Saibil H. 1999. Cryo-electron microscopy structure of an SH3 amyloid fibril and model of the molecular packing. *The EMBO Journal* **18**:815–821.

Jimenez J, Nettleton E, Bouchard M, Robinson C, Dobson C, Saibil H. 2002. The protofilament structure of insulin amyloid fibrils. *Proceedings of the National Academy of Sciences of the United States of America* **99**:9196–9201.

Kabsch W, Vandekerckhove J. 1992. Structure and function of actin. *Annual Review of Biophysics and Biomolecular Structure* **21**:49–76.

Kadler K, Holmes D, Trotter J, Chapman J. 1996. Collagen fibril formation. *Biochemical Journal* **316**:1.

Kasotakis E, Mossou E, Adler-Abramovich L, Mitchell E, Forsyth V, Gazit E, Mitraki A. 2009. Design of metal-binding sites onto self-assembled peptide fibrils. *Biopolymers* **92**:164–172.

Kenney J, Knight D, Wise M, Vollrath F. 2002. Amyloidogenic nature of spider silk. *European Journal of Biochemistry* **269**:4159–4163.

Khurana R, Coleman C, Ionescu-Zanetti C, Carter S, Krishna V, Grover R, Roy R, Singh S. 2005. Mechanism of thioflavin T binding to amyloid fibrils. *Journal of Structural Biology* **151**:229–238.

Kim H, Roh Y, Hong B. 2006. Controlled gold nanoparticle assembly on DNA molecule as template for nanowire formation. *Journal of Vacuum Science & Technology A: Vacuum, Surfaces, and Films* **24**:1327.

Kim H, Roh Y, Hong B. 2010. Selective alignment of gold nanowires synthesized with DNA as template by surface-patterning technique. *IEEE Transactions on Nanotechnology* **9**:254–257.

Knez M, Bittner A, Boes F, Wege C, Jeske H, Mai E, Kern K. 2003. Biotemplate synthesis of 3-nm nickel and cobalt nanowires. *Nano Letters* **3**:1079–1082.

Kowalewski T, Holtzman D. 1999. In situ atomic force microscopy study of Alzheimer's β-amyloid peptide on different substrates: New insights into

mechanism of β-sheet formation. *Proceedings of the National Academy of Sciences of the United States of America* **96**:3688–3693.

Krebs M, Bromley E, Donald A. 2005. The binding of thioflavin-T to amyloid fibrils: Localisation and implications. *Journal of Structural Biology* **149**:30–37.

Krebs M, MacPhee C, Miller A, Dunlop I, Dobson C, Donald A. 2004. The formation of spherulites by amyloid fibrils of bovine insulin. *Proceedings of the National Academy of Sciences of the United States of America* **101**:14420–14424.

Krebs M, Wilkins D, Chung E, Pitkeathly M, Chamberlain A, Zurdo J, Robinson C, Dobson C. 2000. Formation and seeding of amyloid fibrils from wild-type hen lysozyme and a peptide fragment from the β-domain. *Journal of Molecular Biology* **300**:541–549.

Krishnan R, Lindquist S. 2005. Structural insights into a yeast prion illuminate nucleation and strain diversity. *Nature* **435**:765–772.

Kwan A, Winefield R, Sunde M, Matthews J, Haverkamp R, Templeton M, Mackay J. 2006. Structural basis for rodlet assembly in fungal hydrophobins. *Proceedings of the National Academy of Sciences of the United States of America* **103**:3621.

Leroux F, Gysemans M, Bals S, Batenburg K, Snauwaert J, Verbiest T, Van Haesendonck C, Van Tendeloo G. 2010. Three-dimensional characterization of helical silver nanochains mediated by protein assemblies. *Advanced Materials* **22**:2193–2197.

LeVine III H. 1993. Thioflavin T interaction with synthetic Alzheimer's disease β-amyloid peptides: Detection of amyloid aggregation in solution. *Protein Science* **2**:404–410.

Li J, Ng H, Chen H. 2005. Carbon nanotubes and nanowires for biological sensing. *Methods in Molecular Biology* **300**:191–224.

Lim J, Kim S, Lee S, Stach E, Culver J, Harris M. 2010. Quantitative study of Au (III) and Pd (II) ion biosorption on genetically engineered tobacco mosaic virus. *Journal of Colloid and Interface Science* **342**:455–461.

Mackintosh S, Meade S, Healy J, Sutton K, Larsen N, Squires A, Gerrard A. 2009. Wheat glutenin proteins assemble into a nanostructure with unusual structural features. *Journal of Cereal Science* **49**:157–162.

MacPhee C, Dobson C. 2000. Formation of mixed fibrils demonstrates the generic nature and potential utility of amyloid nanostructures. *Journal of the American Chemical Society* **122**:12707–12713.

Maity S, Kumar P, Haldar D. 2011. Sonication-induced instant amyloid-like fibril formation and organogelation by a tripeptide. *Soft Matter* **7**:5239–5245.

Makin O, Serpell L. 2005. Structures for amyloid fibrils. *FEBS Journal* **272**:5950–5961.

Makin O, Serpell L. 2004. Structural characterisation of islet amyloid polypeptide fibrils. *Journal of Molecular Biology* **335**:1279–1288.

Malisauskas M, Meskys R, Morozova-Roche L. 2008. Ultrathin silver nanowires produced by amyloid biotemplating. *Biotechnology Progress* **24**:1166–1170.

Mankar S, Anoop A, Sen S, Maji S. 2011. Nanomaterials: Amyloids reflect their brighter side. *Nano Reviews* **2**:6032–6044.

Mao C, Solis D, Reiss B, Kottmann S, Sweeney R, Hayhurst A, Georgiou G, Iverson B, Belcher A. 2004. Virus-based toolkit for the directed synthesis of magnetic and semiconducting nanowires. *Science* **303**:213.

del Mercato L, Pompa P, Maruccio G, Torre A, Sabella S, Tamburro A, Cingolani R, Rinaldi R. 2007. Charge transport and intrinsic fluorescence in amyloid-like

fibrils. *Proceedings of the National Academy of Sciences of the United States of America* **104**:18019–18024.

Monson C, Woolley A. 2003. DNA-templated construction of copper nanowires. *Nano Letters* **3**:359–363.

Morris V, Kirby A, Gunning A. 1999. Atomic force microscopy for biologists. London: Imperial College Press.

Naiki H, Higuchi K, Hosokawa M, Takeda T. 1989. Fluorometric determination of amyloid fibrils in vitro using the fluorescent dye, thioflavin T. *Analytical Biochemistry* **177**:244–249.

Nielsen L, Frokjaer S, Carpenter J, Brange J. 2001a. Studies of the structure of insulin fibrils by Fourier transform infrared (FTIR) spectroscopy and electron microscopy. *Journal of Pharmaceutical Sciences* **90**:29–37.

Nielsen L, Khurana R, Coats A, Frokjaer S, Brange J, Vyas S, Uversky V, Fink A. 2001b. Effect of environmental factors on the kinetics of insulin fibril formation: Elucidation of the molecular mechanism. *Biochemistry* **40**:6036–6046.

Nilsson M. 2004. Techniques to study amyloid fibril formation in vitro. *Methods* **34**:151–160.

Nogales E. 2001. Structural insights into microtubule function. *Annual Review of Biophysics and Biomolecular Structure* **30**:397–420.

Oliver N, Toumazou C, Cass A, Johnston D. 2009. Glucose sensors: A review of current and emerging technology. *Diabetic Medicine* **26**:197–210.

Orza A, Soritau O, Olenic L, Diudea M, Florea A, Ciuca D, Mihu C, Casciano D, Biris A. 2011. Electrically conductive gold-coated collagen nanofibers for placental-derived mesenchymal stem cells enhanced differentiation and proliferation. *ACS Nano* **5**:4490–4503.

Otzen D, Nielsen P. 2008. We find them here, we find them there: Functional bacterial amyloid. *Cellular and Molecular Life Sciences* **65**:910–927.

Patolsky F, Weizmann Y, Lioubashevski O, Willner I. 2002. Au-nanoparticle nanowires based on DNA and polylysine templates. *Angewandte Chemie - International Edition* **41**:2323–2327.

Patolsky F, Zheng G, Lieber C. 2006. Nanowire-based biosensors. *Analytical Chemistry* **78**:4260–4269.

Patolsky F, Weizmann Y, Willner I. 2004. Actin-based metallic nanowires as bio-nanotransporters. *Nature Materials* **3**:692–695.

Pearce F, Mackintosh S, Gerrard J. 2007. Formation of amyloid-like fibrils by ovalbumin and related proteins under conditions relevant to food processing. *Journal of Agricultural and Food Chemistry* **55**:318–322.

Petkova A, Leapman R, Guo Z, Yau W-M, Mattson M, Tycko R. 2005. Self-propagating, molecular-level polymorphism in Alzheimer's β-amyloid fibrils. *Science* **307**:262–265.

Pilkington S, Roberts S, Meade S, Gerrard J. 2010. Amyloid fibrils as a nanoscaffold for enzyme immobilisation. *Biotechnology Progress* **26**:93–100.

Podesta A, Tiana G, Milani P, Manno M. 2006. Early events in insulin fibrillization studied by time-lapse atomic force microscopy. *Biophysical Journal* **90**:589–597.

Qian Z, Khan M, Mikkelsen S, Chen P. 2009. Improved enzyme immobilization on an ionic-complementary peptide-modified electrode for biomolecular sensing. *Langmuir* **26**:2176–2180.

Raynes J, Pearce F, Meade S, Gerrard J. 2011. Immobilization of organophosphate hydrolase on an amyloid fibril nanoscaffold: Towards bioremediation and chemical detoxification. *Biotechnology Progress* **27**:360–367.

Reches M, Gazit E. 2003. Casting metal nanowires within discrete self-assembled peptide nanotubes. *Science* **300**:625–627.

Richter J, Seidel R, Kirsch R, Mertig M, Pompe W, Plaschke J, Schackert H. 2000. Nanoscale palladium metallization of DNA. *Advanced Materials* **12**:507–510.

Richter J, Mertig M, Pompe W, Monch I, Schackert H. 2001. Construction of highly conductive nanowires on a DNA template. *Applied Physics Letters* **78**:536.

Ryu J, Kim S, Kang K, Park C. 2009. Synthesis of diphenylalanine/cobalt oxide hybrid nanowires and their application to energy storage. *ACS Nano* **4**:159–164.

Saiki M, Honda S, Kawasaki K, Zhou D, Kaito A, Konakahara T, Morii H. 2005. Higher-order molecular packing in amyloid-like fibrils constructed with linear arrangements of hydrophobic and hydrogen-bonding side-chains. *Journal of Molecular Biology* **348**:983–998.

Scheibel T. 2005. Protein fibers as performance proteins: New technologies and applications. *Current Opinion in Biotechnology* **16**:427–433.

Scheibel T, Parthasarathy R, Sawicki G, Lin X-M, Jaeger H, Lindquist S. 2003. Conducting nanowires built by controlled self-assembly of amyloid fibers and selective metal deposition. *Proceedings of the National Academy of Sciences of the United States of America* **100**:4527–4532.

Seidel R, Ciacchi L, Weigel M, Pompe W, Mertig M. 2004. Synthesis of platinum cluster chains on DNA templates: Conditions for a template-controlled cluster growth. *The Journal of Physical Chemistry B* **108**:10801–10811.

Serpell L, Sunde M, Benson M, Tennent G, Pepys M, Fraser P. 2000. The protofilament substructure of amyloid fibrils. *Journal of Molecular Biology* **300**:1033–1039.

Shenton W, Douglas T, Young M, Stubbs G, Mann S. 1999. Inorganic–organic nanotube composites from template mineralization of tobacco mosaic virus. *Advanced Materials* **11**:253–256.

Smith D. 2008. Progress and perspectives for atomic-resolution electron microscopy. *Ultramicroscopy* **108**:159–166.

Smith J, Knowles T, Dobson C, MacPhee C, Welland M. 2006. Characterization of the nanoscale properties of individual amyloid fibrils. *Proceedings of the National Academy of Sciences of the United States of America* **103**:15806–15811.

Song Y, Challa S, Medforth C, Qiu Y, Watt R, Peña D, Miller J, van Swol F, Shelnutt J. 2004. Synthesis of peptide-nanotube platinum-nanoparticle composites. *Chemical Communications* **9**:1044–1045.

Stefani M, Dobson C. 2003. Protein aggregation and aggregate toxicity: New insights into protein folding, misfolding diseases and biological evolution. *Journal of Molecular Medicine* **81**:678–699.

Storm A, van Noort J, de Vries S, Dekker C. 2001. Insulating behavior for DNA molecules between nanoelectrodes at the 100 nm length scale. *Applied Physics Letters* **79**:3881–3883.

Tanaka H, Herland A, Lindgren L, Tsutsui T, Andersson M. 2008. Enhanced current efficiency from bio-organic light-emitting diodes using decorated amyloid fibrils with conjugated polymer. *Nano Letters* **8**:2858–2861.

Tang Q, Solin N, Lu J, Inganäs O. 2010. Hybrid bioinorganic insulin amyloid fibrils. *Chemical Communications* **46**:4157–4159.

Tang Z, Zhang L, Wang N, Zhang X, Wen G, Li G, Wang J, Chan C, Sheng P. 2001. Superconductivity in 4 Å single-walled carbon nanotubes. *Science* **292**:2462 – 2465.

Thorn D, Meehan S, Sunde M, Rekas A, Gras S, MacPhee C, Dobson C, Wilson M, Carver J. 2005. Amyloid fibril formation by bovine milk κ-casein and its inhibition by the molecular chaperones α3- and β-casein. *Biochemistry* **44**:17027–17036.

True H, Lindquist S. 2000. A yeast prion provides a mechanism for genetic variation and phenotypic diversity. *Nature* **407**:477–484.

Tsukamoto R, Muraoka M, Seki M, Tabata H, Yamashita I. 2007. Synthesis of CoPt and $FePt_3$ nanowires using the central channel of tobacco mosaic virus as a biotemplate. *Chemistry of Materials* **19**:2389–2391.

Valéry C, Artzner F, Paternostre M. 2011. Peptide nanotubes: molecular organisations, self-assembly mechanisms and applications. *Soft Matter* **7**:9583–9594.

Vassar P, Culling C. 1959. Fluorescent stains, with special reference to amyloid and connective tissues. *Archives of Pathology* **68**:487–494.

Virchow R. 1854. Weitere Mittheilungen über das Vorkommen der pflanzlichen Cellulose beim Menschen. *Virchows Archiv* **6**:268–271.

Vo-Dinh T. 2005. Protein nanotechnology: The new frontier in biosciences. In: . *Protein Nanotechnology: Protocols, Instrumentation, and Applications*. Totowa, NJ: Humana Press Inc. Methods in Molecular Biology, Vol. 300, pp. 1–13.

Wanekaya A, Chen W, Myung N, Mulchandani A. 2006. Nanowire-based electrochemical biosensors. *Electroanalysis* **18**:533–550.

Waterhouse S, Gerrard J. 2004. Amyloid fibrils in bionanotechnology. *Australian Journal of Chemistry* **57**:519–523.

Whittingham J, Scott D, Chance K, Wilson A, Finch J, Brange J, Dodson G. 2002. Insulin at pH 2: Structural analysis of the conditions promoting insulin fibre formation. *Journal of Molecular Biology* **318**:479–490.

Wolfe L, Calabrese M, Nath A, Blaho D, Miranker A, Xiong Y. 2010. Protein-induced photophysical changes to the amyloid indicator dye thioflavin T. *Proceedings of the National Academy of Sciences of the United States of America* **107**:16863–16868.

Wong Po Foo C, Kaplan D. 2002. Genetic engineering of fibrous proteins: Spider dragline silk and collagen. *Advanced Drug Delivery Reviews* **54**:1131–1143.

Yemini M, Reches M, Gazit E, Rishpon J. 2005a. Peptide nanotube-modified electrodes for enzyme-biosensor applications. *Analytical Chemistry* **77**:5155–5159.

Yemini M, Reches M, Rishpon J, Gazit E. 2005b. Novel electrochemical biosensing platform using self-assembled peptide nanotubes. *Nano Letters* **5**:183–186.

Yemini M, Xu P, Kaplan D, Rishpon J. 2006. Collagen-like peptide as a matrix for enzyme immobilization in electrochemical biosensors. *Electroanalysis* **18**:2049–2054.

Yu D, Bai Z, Ding Y, Hang Q, Zhang H, Wang J, Zou Y, Qian W, Xiong G, Zhou HT.1998. Nanoscale silicon wires synthesized using simple physical evaporation. *Applied Physics Letters* **72**:3458.

Zhou J, Gao Y, Martinez-Molares A, Jing X, Yan D, Lau J, Hamasaki T, Ozkan C, Ozkan M, Hu E, others. 2008. Microtubule-based gold nanowires and nanowire arrays. *Small* **4**:1507–1515.

Zhou J, Wang X, Xue M, Xu Z, Hamasaki T, Yang Y, Wang K, Dunn B. 2010. Characterization of gold nanoparticle binding to microtubule filaments. *Materials Science and Engineering: C* **30**:20–26.

2. Chapter Two

Formation and characterisation of amyloid fibrils

2.1. Introduction

In this thesis, three different amyloid-forming proteins are used: bovine insulin, fungal hydrophobins, and crude crystallin proteins. Fibrils formed from each of these different proteins differ in morphology, and each has unique and interesting properties. This thesis focuses mainly on those fibrils formed from crude crystallin proteins, which were extracted from fish eye lenses. If these fibrils, or protein nanofibres (PNFs), are able to be used in bionanotechnology, this will add value to a low cost waste product.

This chapter demonstrates the formation of amyloid fibrils from these three protein sources. The amyloid fibrils formed were characterised by microscopy and the ThT assay, with crystallin fibrils also being characterised by X-ray fibre diffraction. X-ray fibre diffraction is one of the main techniques used to ascertain the presence of the characteristic "cross-β" amyloid fibril structure and diffraction patterns for amyloid fibrils formed from crude fish crystallins have not previously been obtained.

If amyloid fibrils formed from crude crystallin proteins are to be used as building blocks for bionanotechnology, as nanowires or as a nanoscaffold, there are a number of issues that need to be addressed in order to make them more attractive for commercial applications, one of these being stability. This chapter also investigates the stability in solution of crystallin amyloid fibrils.

2.2. Amyloid fibrils formed from bovine insulin

As less is known about fibrils formed from crude fish crystallins, amyloid fibrils from bovine insulin were also used extensively in this study, as a model amyloid fibril system. Bovine insulin forms amyloid fibrils very rapidly, and this fibril system has been very well characterised. There is a large amount of literature available on insulin amyloid fibrils, including detail of their morphology (Jimenez *et al*., 2002; Nielsen *et al*., 2001a), and mechanism and kinetics of their formation (Bouchard *et al*., 2000; Brange *et al*., 1997; Devlin *et al*., 2006; Nielsen *et al*., 2001b). There have also been studies that have investigated their use in bionanotechnology, as scaffolds for enzyme immobilisation (Pilkington *et al*., 2010; Raynes *et al*., 2011), and as nanowire templates (Herland *et al*., 2007; Herland *et al*., 2008; Hsieh and Hsieh, 2010; Hsieh and Hsieh, 2011).

2.2.1. Bovine insulin

Bovine insulin is a globular protein with a molecular weight of approximately 5.7 kDa. In its native state, the polypeptide hormone has a mainly helical structure with two polypeptide chains, linked by two inter-chain and one intra-chain disulfide bonds (**Figure 2.1**) (Blundell *et al*., 1971). Bovine insulin consists of 51 amino acids, 20 in the A chain, shown in **Figure 2.1** in orange, and 31 in the B chain, shown in blue. In solution, insulin exists as an equilibrium mixture of monomers, dimers, tetramers, hexamers, and possibly higher order states (Nielsen *et al*., 2001b). It is accepted in the literature that it is the monomeric form of insulin that forms amyloid fibrils (Brange *et al*., 1997). Bovine insulin used throughout this study was obtained commercially.

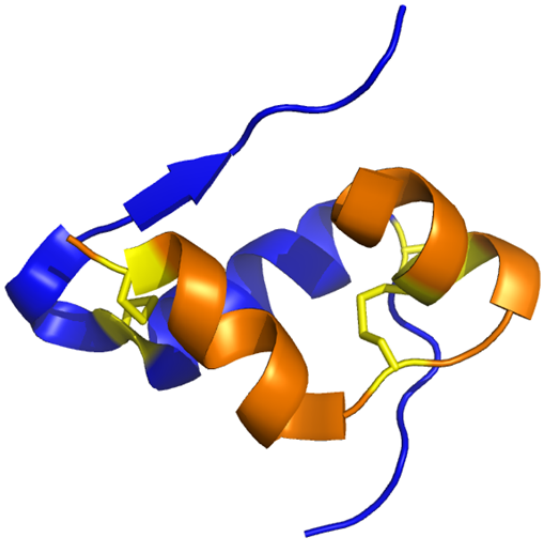

Figure 2.1. *PyMOL image of the native structure of bovine insulin. In this ribbon representation, the A chain is shown in orange, and the B chain is shown in blue. The three disulfide bonds are shown in stick representation and are coloured yellow. This image was constructed using PyMOL from PDB file 2A3G (Delano, 2002).*

2.2.2. Bovine insulin fibrillation

Bovine insulin is often used in studies of amyloid formation as it forms fibrils very rapidly from disruption of the natively hexameric structure, into monomers that then progress through the fibril formation pathway (Brange *et al*., 1997). More detail of the mechanism of fibril formation from bovine insulin is given in Chapter 3. *In vitro,* insulin can be converted from this native structure to the fibrillar form by incubation at high insulin concentrations, low pH and high temperature, with fibrillation occurring under these conditions within hours (Krebs *et al*., 2004; Nielsen *et al*., 2001b; Waugh, 1946). Other studies have also used denaturants such as guanidine hydrochloride and urea to form amyloid-like aggregates from insulin (Ahmad *et al*., 2003; Ahmad *et al*., 2004)

For this study, insulin amyloid fibrils were formed by subjecting bovine insulin to low pH, high temperatures, and the presence of salt. The standard conditions used were those developed in-house to optimise fibril formation, and involved incubation of insulin at 5.8 mg/mL, in buffer containing 100 mM NaCl, 25 mM HCl, pH 1.6, at 60 °C for 24 hours (Section 7.2.1). The presence of fibrils was then confirmed using ThT (Section 7.2.2), a fluorescent dye that is frequently used to detect amyloid formation *in vitro* (LeVine III, 1993), and visually, by the appearance of fibrillar structures under TEM (Section 7.5).

In situ ThT fluorescent measurements were carried out in a 96 well plate reader, with fibrillation monitored by measuring fluorescence over four hours of incubation, with measurements taken every five minutes (Section 7.2.1). **Figure 2.2** shows the increase in ThT fluorescence over the period of incubation. The observed ThT fluorescence intensity had a classic sigmoidal pattern (Nielsen *et al*., 2001b), with a lag phase, here of approximately 40 minutes, followed by a rapid increase in fibril formation (**Figure 2.2**). A plateau is then reached, indicating that most soluble protein has been converted into fibrils.

Figure 2.3 shows a representative TEM image of amyloid fibrils formed from bovine insulin. When amyloid fibrils are viewed by TEM they generally share an elongated, unbranched, fibrillar appearance, as visible in the network of fibrils shown in **Figure 2.3** .

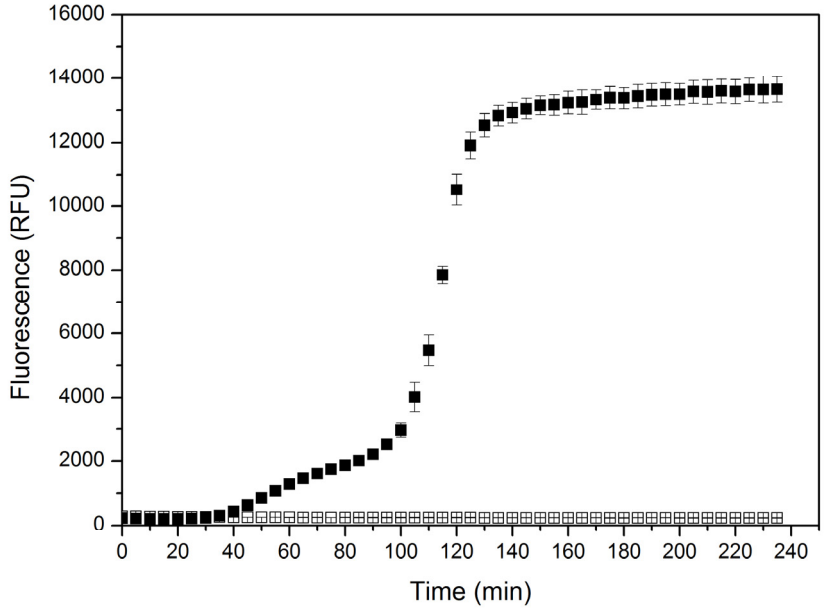

Figure 2.2. *Time profiles for ThT induced fluorescence of bovine insulin incubated at a concentration of 5.8 mg/mL in fibril buffer (closed square), and control sample containing no insulin (open square), at 60 °C. Each reading represents an average of triplicate well readings, with the error bars representing standard error.*

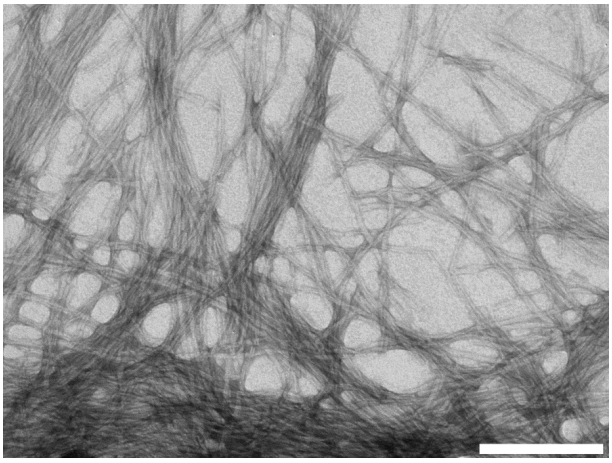

Figure 2.3. *Representative TEM image with negative staining of amyloid fibrils formed from bovine insulin. Scale bar is 0.2 μm.*

2.3. Amyloid fibrils formed from fungal hydrophobins

Amyloid fibrils formed from fungal hydrophobins are unique in that the fibrils formed are part of a spontaneously forming monolayer of amyloid fibril "rodlets" (Sunde *et al*., 2008). The formation of this rodlet monolayer with unique amphipathic properties has lead to investigations into the use of hydrophobins in bionanotechnology (Gras, 2007; Hou *et al*., 2009; Wang *et al*., 2010; Zampieri *et al*., 2010; Zhao *et al*., 2007).

2.3.1. Fungal hydrophobins

Hydrophobins are a family of low molecular weight (7-9 kDa) proteins with a characteristic pattern of cysteine residues that form four disulfide bonds. Other than these conserved cysteine residues, the family shares little amino acid sequence homology, but have very similar hydrophobicity plots (Sunde *et al*., 2008). This protein family is unique to fungi, where *in vivo*, they are secreted as soluble monomers and upon reaching an interface, aggregate spontaneously to form robust polymeric monolayers that are highly amphipathic (Linder *et al*., 2005). A TEM image showing a hydrophobin monolyer formed *in vitro* is shown in **Figure 2.4** (Morris *et al*., 2011). These monolayers act as natural surfactants, reducing the surface tension of the medium and allowing fungi to breach the air/water interface and to produce hyphae (Wösten *et al*., 1999).

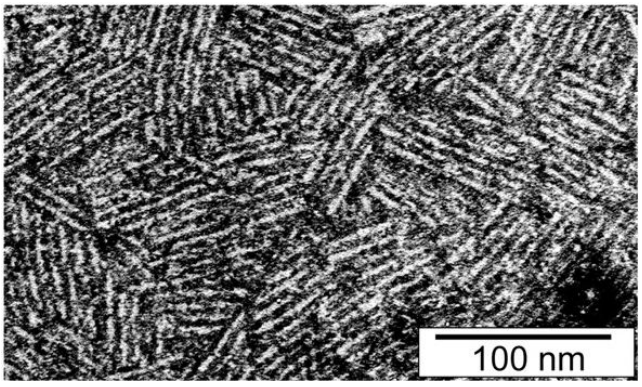

Figure 2.4. *Negatively stained TEM micrograph of an in vitro formed rodlet monolayer. From Morris* et al. *(2011).*

There are two classes of hydrophobins, referred to as Class I, and Class II. Class I hydrophobins form insoluble polymer rodlets, Class II hydrophobins form polymers that are soluble in some organic solvents – with no rodlet appearance (Sunde *et al*., 2008). For this study, the hydrophobin protein used was the Class I hydrophobin EAS, named so as it is the protein encoded by the *easily*-wettable gene from *Neurospora crassa*, which was obtained from Margie Sunde at the University of Sydney. A NMR solution structure of this protein is shown in **Figure 2.5**. EAS has a β-barrel fold comprised of four antiparallel β-sheets, with an additional two-stranded β-sheet, and two sizeable disordered regions (**Figure 2.5**) (Kwan *et al*., 2006).

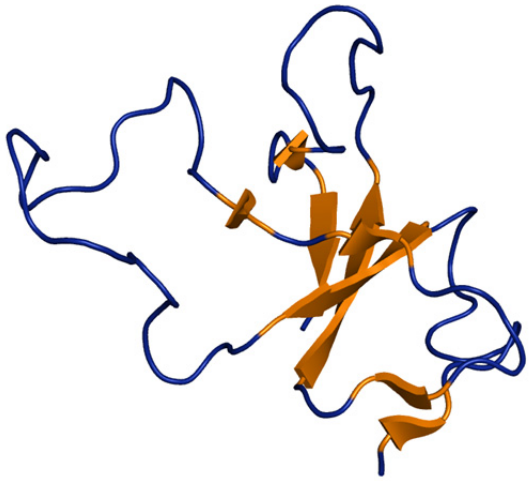

Figure 2.5. *PyMOL image of the native solution structure of the Class I hydrophobin EAS. In this ribbon representation, the β-sheets are shown in orange, and the disordered loops are shown in blue. This image was constructed using PyMOL from PDB file 2FMC (Delano, 2002; Kwan* et al.*, 2006).*

2.3.2. Hydrophobin fibrillation

The rodlets formed by Class I hydrophobins have been shown to have many structural and morphological similarities with amyloid fibrils. EAS rodlets have been previously shown to bind Congo red and ThT (Mackay *et al*., 2001). All that is required for the formation of rodlets is the creation of a hydrophobic:hydrophilic interface, which triggers rodlet assembly (Wösten and de Vocht, 2000). A model for rodlet assembly is shown in **Figure 2.6**.

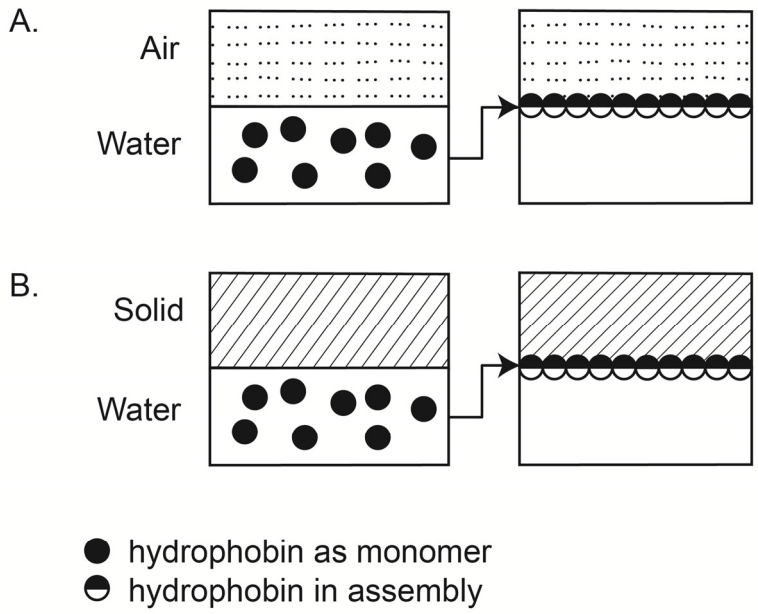

Figure 2.6. *Model for assembly of hydrophobin rodlet monolayer. Monomers diffuse to the hydrophilic-hydrophobic interface, where they assemble into the rodlet monolayer. This interface may be A), an air/water interface, or B), a solid/water interface. Schematic adapted from Wösten and de Vocht (2000).*

The effect of a number of different conditions, namely protein concentration, the presence/absence of agitation (shaking), and of 5 mm glass beads, on the formation of hydrophobin rodlets was investigated. Shaking was used to provide air pockets in the solution, creating additional air/water interfaces. The presence of glass beads was used to increase the available surface area on which the rodlets could form, and therefore the number of solid/water interfaces. The different conditions under which rodlets were formed are summarised in **Table 2.1**. Rodlet formation was monitored for each of the samples using the ThT assay in a plate reader. ThT was included in the nanopure H_2O, and rodlet formation monitored in real time. Rodlet formation was monitored by measuring fluorescence at 482 nm over three hours of incubation (Section 7.3.2). Replicates were carried out in a single plate, the typical variation seen between plates was less than 10 %.

Table 2.1. *Details of the different conditions used to form EAS hydrophobin rodlets.*

Sample	Native protein concentration (mg/mL)	Solvent	Temperature	Shaking (Y/N)	Glass beads (Y/N)
1	0	Nanopure H_2O	60 °C	N	N
2	0.1				
3	0.5				
4	1.0				
5	0			Y	N
6	0.1				
7	0.5				
8	1.0				
9	0			N	Y
10	0.1				
11	0.5				
12	1.0				

Figure 2.7 compares fibrillation patterns of EAS rodlet formation at 0, 0.1, 0.5, and 1.0 mg/mL, with all samples incubated at 60 °C in nanopure H_2O (**Table 2.1**, 1-4). Of the concentrations examined, 0.5 mg/mL was the lowest at which an increased ThT fluorescence was observed, with no increase in fluorescence seen for the 0.1 mg/mL sample. As fibril formation is known to be a nucleation dependent polymerisation mechanism, there exists a critical concentration, below which fibrillation does not occur. It is unlikely in this case that this is the true critical concentration of EAS for rodlet formation, as previous work has shown rodlet formation to occur at concentrations lower than 1 μg/mL (Wösten and de Vocht, 2000). However, large variations in critical concentration have been observed previously in amyloid fibril systems, such as in the case of β-lactoglobulin fibrillation, where critical concentrations ranging from 0.33 wt % to 2.5 wt % have been reported (Kroes-Nijboer *et al*., 2009). This type of discrepancy has lead to the need to clarify the definition of critical concentration to the concentration of native protein where the conversion from protein to fibrils is too low to be determined by the method in question (Arnaudov and De Vries, 2005).

Of interest is also the lack of the characteristic sigmoidal shaped curve for fibrillation kinetics, as observed in the formation of insulin fibrils (**Figure 2.2**). No distinct lag phase was observed for EAS rodlet formation. This is likely due to the fact that the amyloid like structure is functional *in vivo* for hydrophobins, with fast kinetics being a functional feature of the system (Kwan *et al*., 2006). The rate of rodlet formation was seen to increase with increasing concentration (**Figure 2.7**).

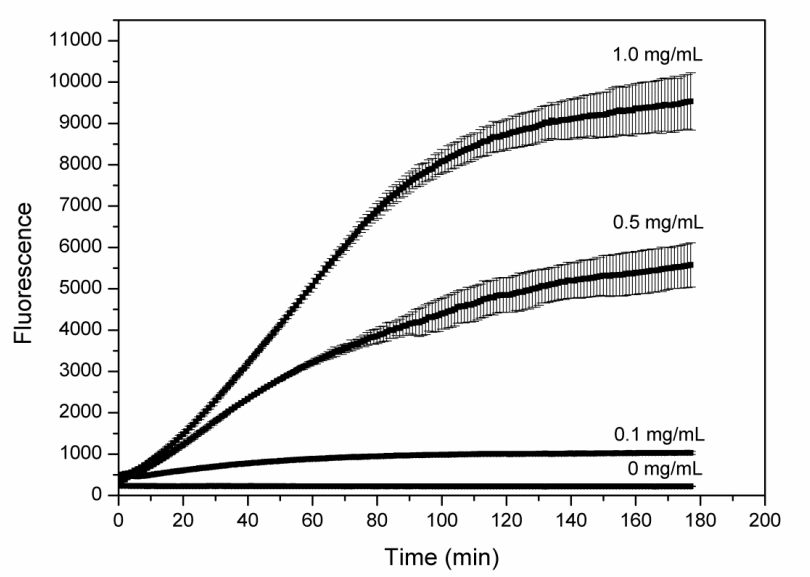

Figure 2.7. *Time profiles for ThT induced fluorescence of hydrophobins incubated at 60 °C. Samples were prepared at 0 mg/mL, 0.1 mg/mL, 0.5 mg/mL, and 1.0 mg/mL in nanopure water (Samples 1-4,* ***Table 2.1****). Each reading represents an average of triplicate well readings, with the error bars representing standard error.*

When EAS rodlets were formed as per the conditions established above, with the addition of shaking (**Table 2.1**, 5-8), the same trend was seen as in **Figure 2.7**, with no increased fluorescence for the sample formed at 0.1 mg/mL, and above this the rate of rodlet formation increasing with increased concentration (**Figure 2.8**). When EAS rodlets were formed in the presence of glass beads (**Table 2.1**, 9-12), this trend was again repeated, although in this instance there was a slight increase in fluorescence observed for the 0.1 mg/mL sample (**Figure 2.9**).

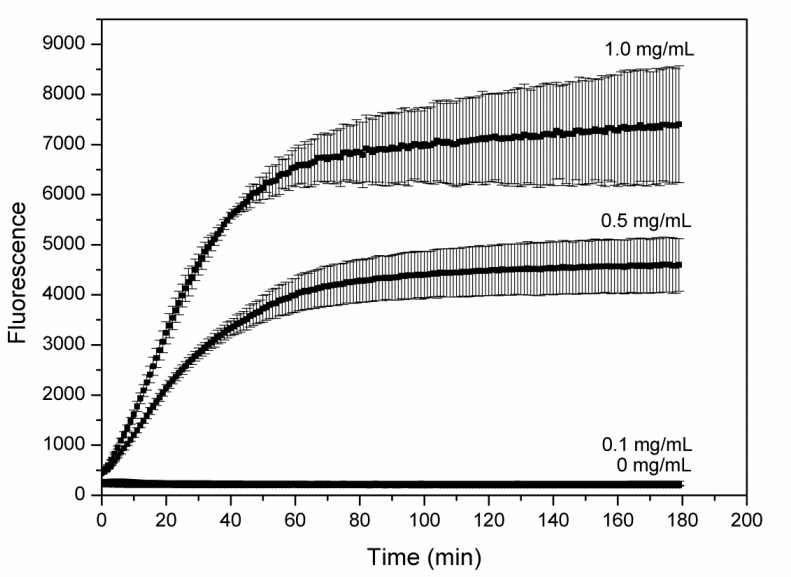

Figure 2.8. *Time profiles for ThT induced fluorescence of hydrophobins incubated at 60 °C with shaking. Samples were prepared at 0 mg/mL, 0.1 mg/mL, 0.5 mg/mL, and 1.0 mg/mL in nanopure water (Samples 5-8,* ***Table 2.1****). Each reading represents an average of triplicate well readings, with the error bars representing standard error.*

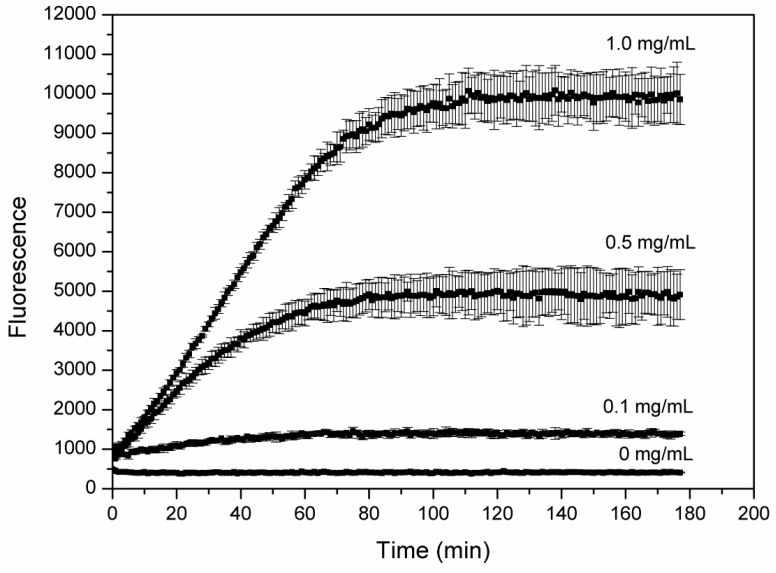

Figure 2.9. *Time profiles for ThT induced fluorescence of hydrophobins incubated at 60 °C in the presence of beads. Samples were prepared at 0 mg/mL, 0.1 mg/mL, 0.5 mg/mL, and 1.0 mg/mL in nanopure water (Samples 9-12,* ***Table 2.1****). Each reading represents an average of triplicate well readings, with the error bars representing standard error.*

When the time profiles for ThT induced fluorescence of hydrophobins incubated at 1 mg/mL in each of the three conditions are plotted together (**Figure 2.10**), a difference in the rate of rodlet formation is observed. The rate of rodlet formation was calculated from the linear region of the curve, with the fastest rate observed for the sample that was incubated with glass beads (127.67 ± 5.31 RFU/min) (**Table 2.2**). An elevated rate was also seen for the shaken sample when compared to the sample with elevated temperature only, with calculated rates of 116.83 ± 7.31 RFU/min and 85.52 ± 1.13 RFU/min respectively (**Table 2.2**). This is an expected result, as the bead provides an additional solid/liquid interface on which the rodlet monolayer may form, as depicted in **Figure 2.6**, B, and shaking provides a dynamic air/water interface, as depicted in **Figure 2.6**, A. Unusually, a lower maximum fluorescence was reached with the sample that was shaken (**Figure 2.10**).

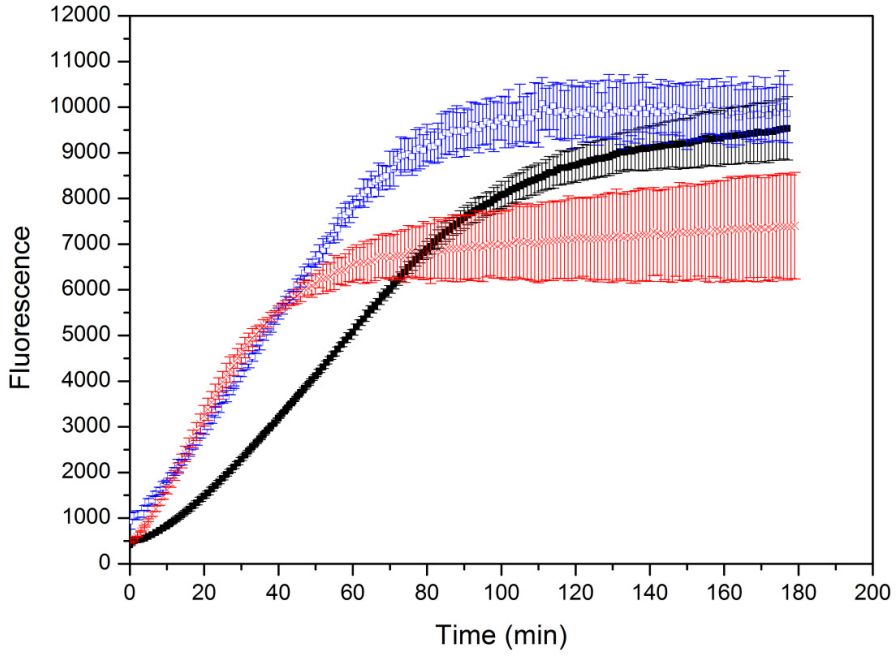

Figure 2.10. *Time profiles for ThT induced fluorescence of: hydrophobins formed at 60 °C (black), hydrophobins formed at 60 °C with shaking (red), and hydrophobins formed at 60 °C in the presence of beads. All samples were prepared at 1 mg/mL in nanopure water. Each reading represents an average of triplicate well readings, with the error bars representing standard error.*

Table 2.2. *Rate of increase in ThT fluorescence, indicative of rodlet formation, for EAS hydophobin rodlets formed under different conditions. All rodlets were formed at a concentration of 1 mg/mL in nanopure H_2O.*

Condition	Rate (RFU/min)
Heating 60 °C	85.52 ± 1.13
Heating 60 °C + shaking	116.83 ± 7.31
Heating 60 °C + beads	127.67 ± 5.31

The presence of rodlets was confirmed for all samples by TEM. **Figure 2.11** shows a representative TEM image of the rodlet monolayer, with unfortunately poor resolution due to staining technique. AFM imaging was more effective for these structures and a high resolution AFM image is shown in Chapter 4.

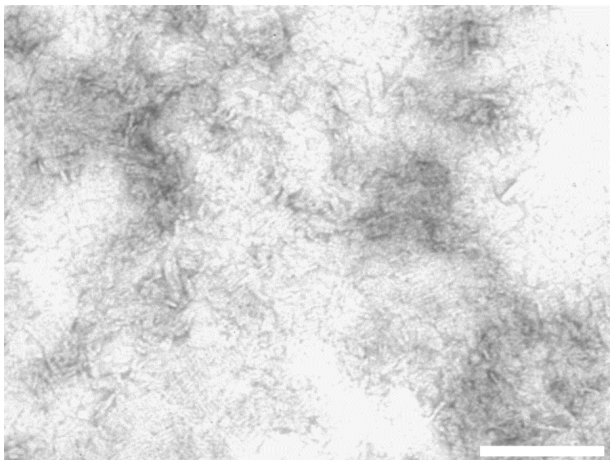

Figure 2.11. *Representative TEM image with negative staining of amyloid fibrils formed from fungal hydrophobins. Scale bar is 0.2 μm.*

2.4. Amyloid fibrils formed from crude fish crystallins

The nanomaterials that are the main focus of this study are amyloid fibrils formed from mixtures of crude crystallin proteins from fish eye lenses. The PNTs/PNFs that have previously been investigated as having a potential role in bionanotechnology are typically formed from purified proteins and engineered peptides (Gazit, 2007; Hamedi *et al*., 2008; Pilkington *et al*., 2010), which makes their manufacture a time-consuming and often expensive process. If PNTs/PNFs are to be used commercially as nanomaterials, a large scale and low cost manufacturing process needs to be established (Waterhouse and Gerrard, 2004). Previous work has reported the synthesis of amyloid fibrils from crude crystallin protein mixtures, extracted from bovine lenses obtained from the abattoir (Garvey *et al*., 2009). Recently, fish eye lenses have been used in our lab for amyloid fibril manufacture (Healy *et al*., 2012), due to their ready availability from the seafood industry, and the fact that they are perceived as safer than bovine products in the wake of bovine spongiform encephalopathy outbreaks. Our lab has shown that the fibril manufacture process from fish eye crystallins can be scaled up to produce large quantities of fibrils (Wong, 2012); however, these fibrils are yet to be fully characterised, both structurally, and in terms of their applicability to bionanotechnological applications.

2.4.1. Crystallins

In vivo, crystallin proteins are the predominant protein in the eye lense, where their role is to maintain lens stability and transparency (Harding, 1991). Crystallins are highly stable proteins, which within the lens are organised in a supramolecular β-sheet structure (Harding, 1991). There are three distinct classes of crystallin proteins, referred to as α, β, and γ, with each of these classes having distinct subunits. α-Crystallin is a molecular chaperone and the principal lens protein, and is a member of the small heat shock protein family (Harding, 1991). There are two subunits, αA and αB, which are closely related. The α-crystallin complex is a highly heterogenous aggregate of 20 kDa subunits, resulting in multimers of approximately 300 to 1000 kDa. β-Crystallin exists as smaller complexes of approximately 50-200 kDa, formed from 20-30 kDa subunits, and γ-crystallins exist as monomers of approximately 20 kDa. Further details of the different classes of crystallin proteins are shown in **Table 2.3**.

Table 2.3. *Details of the different classes of crystallin proteins. Adapted from (Ecroyd and Carver, 2009; Kiss and Cheng, 2008; Posner* et al.*, 2008).*

Class	**Protein sequences identified**		
	Mammalian	**Antarctic toothfish *(Dissostichus mawsoni)***	**Zebrafish *(Danio rerio)***
α-crystallins	αA, αB	αA, αB	αA, αB
β-crystallins	βA (βA1, βA2, βA3, βA4) βB (βB1, βB2, βB3)	βA (βA1, βA2, βA4) βB (βB1, βB2, βB3)	βA (βA1, βA2, βA4) βB (βB1, βB2, βB3)
γ-crystallins	γS, γA, γB, γC, γD, γE, γF	γM1, γM3, γM4, γM5, γM7, γM8a, γM8b, γM8c, γ8d, γM8e, γM9, γN, γS1, γS2	γM1, γM2a, γM2b, γM2c, γM2d1, γM2d2, γM3, γM4, γM5, γM6, γM7, γMx, γN1, γN2, γS1, γS2, γS3, γS4

The crystallin proteins used in this study were extracted from eye lenses from *Macruronus novaezelandiae* (Hoki), with fish heads obtained from local fish markets, and the eye lenses extracted in the lab. No sequence or structural data exists for crystallin proteins from *M. Novaezelandiae*, and so where required, sequences from *Danio rerio* (zebrafish) are used in this thesis. **Figure 2.12** shows representative crystal structures of proteins from each of the three classes of crystallin proteins. The zebrafish structure was chosen where available, and if not available, the structure shown is that with the highest sequence similarity to the zebrafish sequence (see Appendix A). Within each class, the proteins are closely sequence and structurally related (Ecroyd and Carver, 2009), as is evident in **Figure 2.12**, A-E. The high β-sheet content of native crystallins is also apparent (**Figure 2.12**), with β-crystallins and γ-crystallins homologous β-sheet proteins (Ecroyd and Carver, 2009).

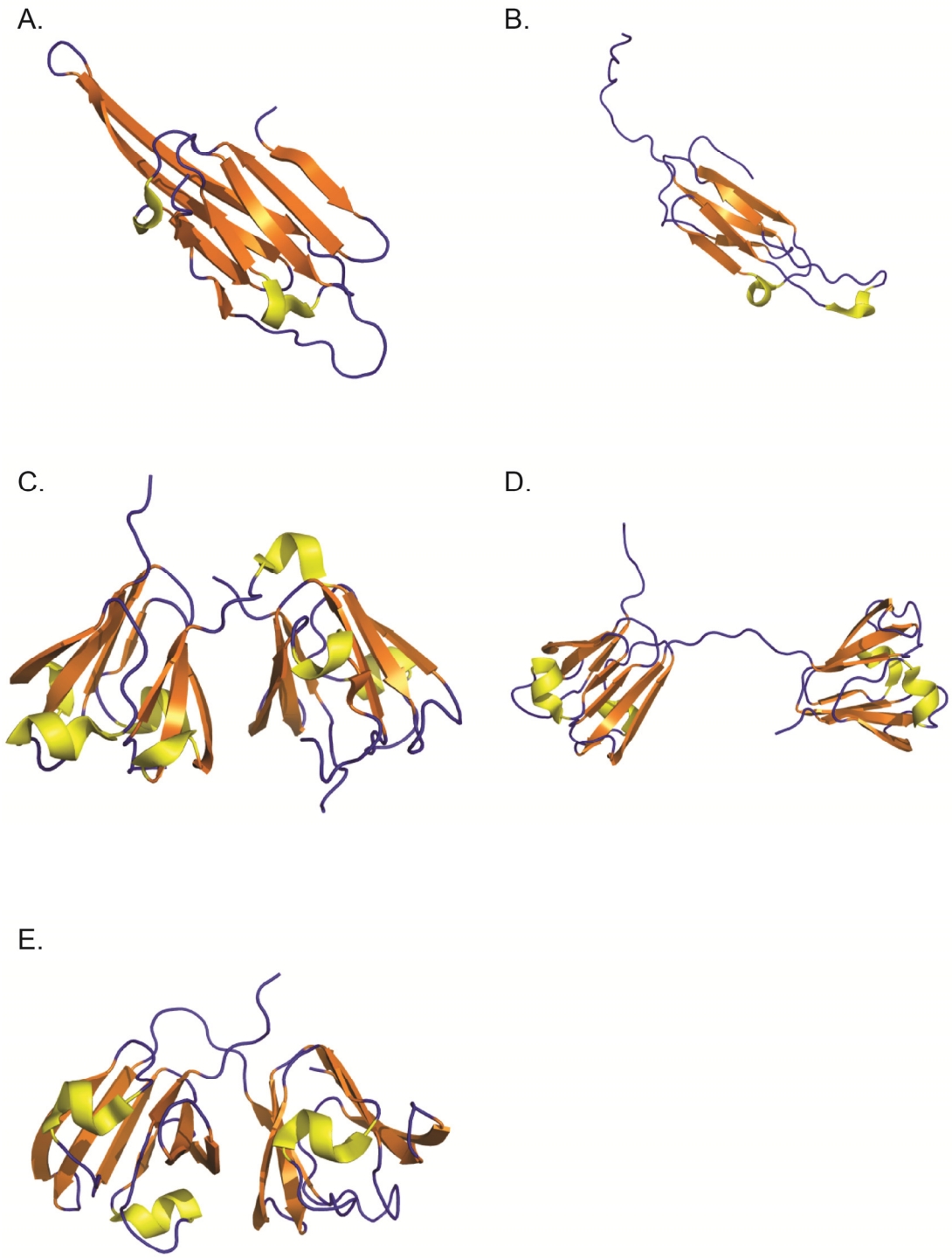

Figure 2.12. *Representative structures of crystallin proteins generated using PyMOL (Delano, 2002). A) αA crystallin from D. rerio (PDB 3N3E), B) αB crystallin from H. sapien (PDB 3L1G), C) βA-4 crystallin from H. sapien (PDB 3LWK), D) βB-2 crystallin from B. taurus, and E) γB crystallin from H. sapien (PDB 2JDF).*

2.4.2. Crystallin fibrillation

The disease cataract, defined as the opacity of the eye lens, which results in 48 % of global blindness (World Health Organisation (WHO), 2011) is caused by crystallin aggregation and precipitation. One proposed mechanism for this is the formation of amyloid fibrils by crystallin proteins, although to date, crystallin amyloid fibrils have not been found *in vivo* (Meehan *et al*., 2004). *In vitro* however, all three classes of crystallins, from bovine eye lenses, have been shown to form amyloid fibrils, when subjected to denaturing solvents, pH extremes, and high temperatures (Meehan *et al*., 2004).

Amyloid fibrils were formed from mixtures of crude crystallin proteins using in-house methods based on those of Garvey *et al*. (2009), developed to optimise fibril formation. These methods involved subjecting the protein to denaturing solvents, low pH, and elevated temperatures (Section 7.4.2). This process differs from some other fibril formation processes in that after one hour under these conditions, large amorphous aggregate is removed, and fibril formation then takes place. In previous studies using crystallins from bovine lens, where this step is not present, a large amount of amorphous aggregate is present in the final fibril product (Garvey *et al*., 2009). This is not desirable if these fibrils are to be used in bionanotechnology, and this additional step prevents the need for later purification of fibrils by proteases (Garvey *et al*., 2009). The presence of amyloid fibrils was confirmed by the ThT assay (**Figure 2.13**) (Section 7.4.3). Native crystallin proteins have a high background ThT reading due to their predominantly β-sheet structure (**Figure 2.12**); however, the use of the assay is still valid under carefully controlled conditions. TEM was also used, with a representative TEM image shown in **Figure 2.14**.

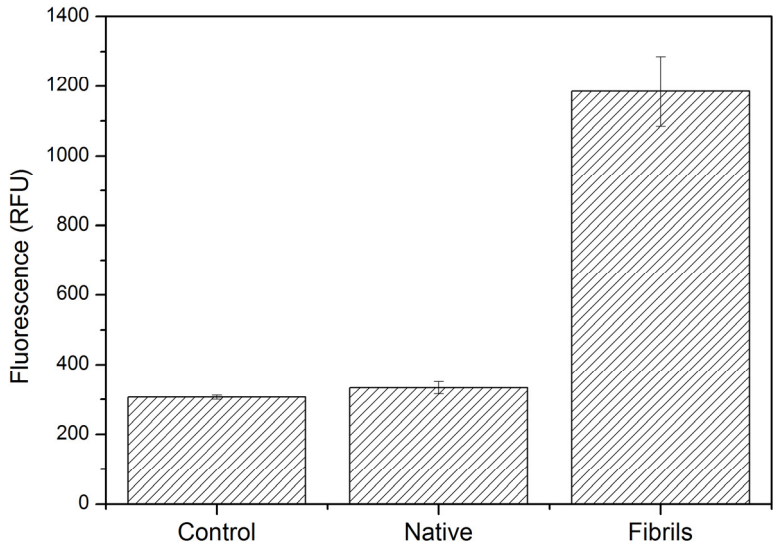

Figure 2.13. *ThT induced fluorescence for control (fibril formation buffer only), native (unfibrilised crystallins), and fibrils (fibrilised crystallins). Each reading represents an average of triplicate well readings, with the error bars representing the standard deviation.*

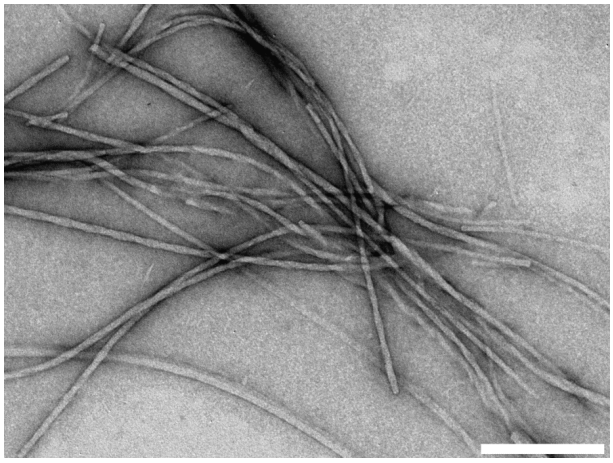

Figure 2.14. *Representative TEM image with negative staining of amyloid fibrils formed from crude fish crystallins. Scale bar is 0.2 μm.*

2.5. X-ray fibre diffraction of amyloid fibrils formed from crude crystallins

One of the key identifying features of amyloid fibrils is the characteristic cross-β structure (Pauling and Corey, 1951), with β-strands arranged in β-sheets and these β-sheets then stacked perpendicular to the axis of the fibril. X-ray fibre diffraction can be used to examine this structure *via* the spacing of the isotropic reflections. Although X-ray fibre diffraction has been used to examine the intermolecular structure of amyloid fibrils formed from bovine crystallins (Garvey *et al*., 2009), it had not previously been done on fibrils formed from crude fish crystallins.[1]

When X-ray fibre diffraction was carried out on crude fish crystallin fibrils, isotropic reflections were observed at 4.6 Å and 10.3 Å (**Figure 2.15**) (Section 7.7). These reflections correspond to the spacing between hydrogen bonded β-strands within a β-sheet and the spacing between multiple β-sheets respectively (Serpell *et al*. 1999).

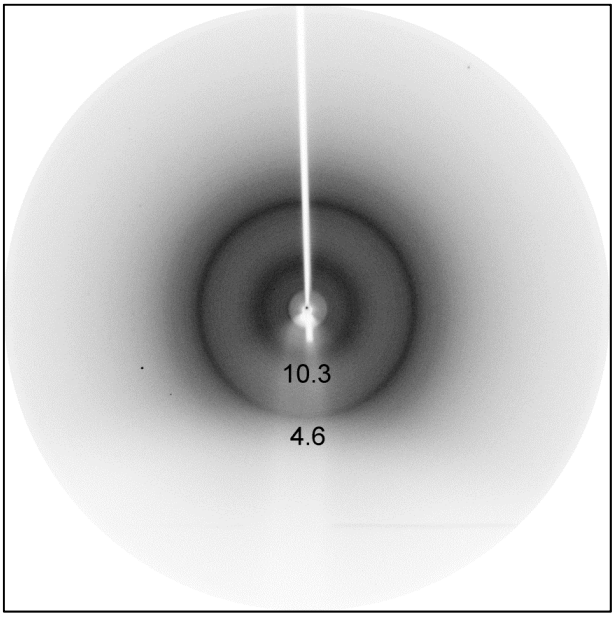

Figure 2.15. *X-ray fibre diffraction pattern of amyloid fibrils formed from crude fish crystallins showing the characteristic isotropic reflections at 4.6 Å and 10.3 Å.*

[1] This work is published in (Healy *et al*., 2012)

TEM images were taken of the resuspended pellet which was used for the X-ray fibre diffraction. As shown in **Figure 2.16**, fibrils were present, with no visible unfibrilised protein, meaning that the observed diffraction pattern can be confidently attributed to the presence of amyloid fibrils.

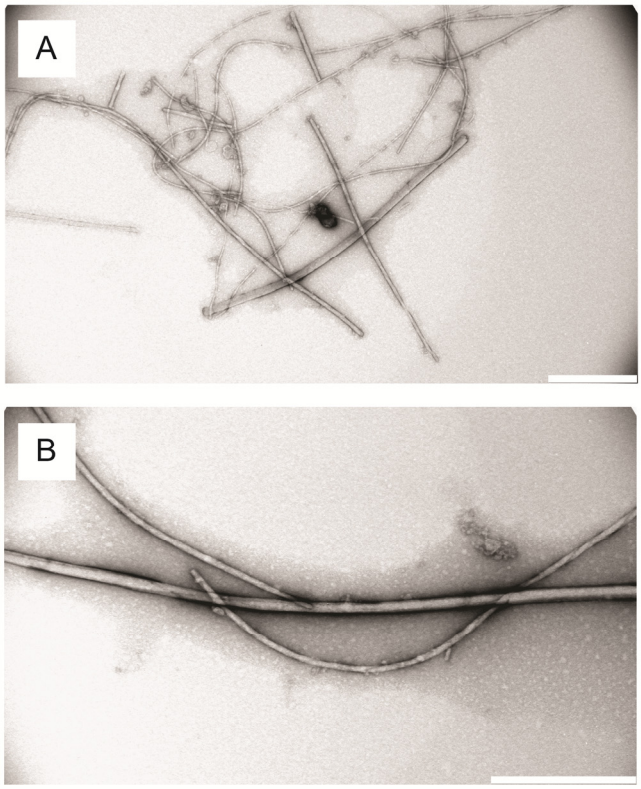

Figure 2.16. *TEM images of resuspended pellet of crystallin fibrils that was used for the X-ray fibre diffraction experiments. Scale bar is 0.5 μm.*

2.6. Fibril formation from semi-purified crystallin proteins

In addition to being able to form amyloid fibrils from crude crystallin protein mixtures (Garvey *et al*., 2009), it has also been shown for bovine crystallins that each of the three classes of crystallin proteins (α, β, and γ) can be induced to form fibrils (Meehan *et al*., 2004), indicating that the fibrils formed from the crude protein mixture are likely to have been contributed to by all three crystallin classes. This has not previously been demonstrated for fish crystallins. In order to examine whether all three classes of fish crystallin proteins are able to form fibrils under the same conditions that crude mixtures form fibrils, the crude protein extract was separated into the three classes using size exclusion chromatography (SEC), and each semi-purified fraction then subjected to the fibril formation conditions previously established (Section 7.8).

2.6.1. Separation of crystallin proteins

Aliquots of the crude crystallin protein extract, were separated into individual classes of crystallin proteins (α_T, β_T, and γ_T) using SEC, using methods based of those of (Garvey *et al*., 2009), with proteins eluted using 20 mM Tris, pH 8.0 (Section 7.8.1). The elution profile is shown in **Figure 2.17**.

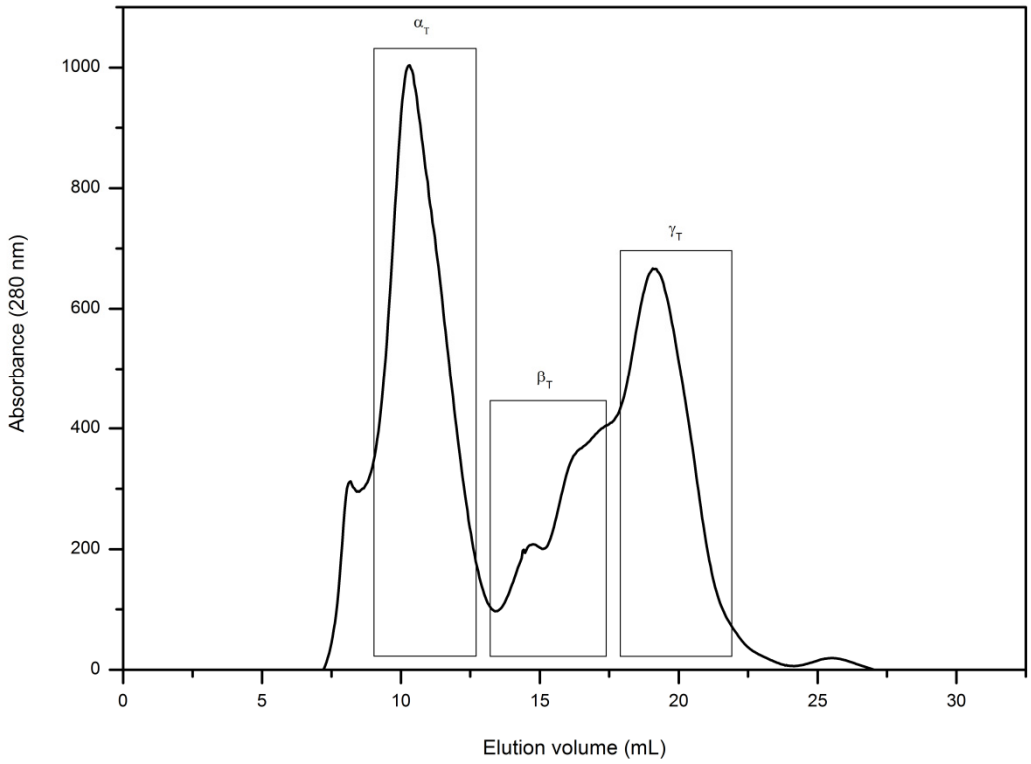

Figure 2.17. *Size exclusion separation of crystallin proteins extracted from fish eye lenses. Peak fractions corresponding to total α, β, and γ crystallins (labelled α_T, β_T, and γ_T) were collected to form semi-pure crystallin preparations. Protein eluting before the α-crystallin peak was also collected and is referred to as the high molecular weight (HMW) fraction.*

By comparison with previous separations of crystallin proteins (Garvey *et al*., 2009; Pilkington, 2009), including studies which separated crystallins from barracuda (*Sphyraena novaehollandiae*) and the Antarctic toothfish (*Dissostichus mawsoni*) (Healy *et al*., 2012; Kiss *et al*., 2010), the major peaks were able to be identified. The first peak (unlabelled) is HMW aggregate, the second peak, labelled α_T, consists of the two closely related subunits αA and αB (**Table 2.3**). The third peak, labelled β_T, consists of high, or octomeric, and low, or dimeric and trimeric, molecular weight β-crystallins. The fourth peak, labelled γ_T, consists of total γ-crystallins (**Figure 2.17**). When compared to elution profiles for bovine crystallins (Garvey *et al*., 2009; Pilkington, 2009), the elution profile for hoki crystallins shows there to be lower amounts of β-crystallins present. This appears to be a common feature of fish crystallin proteins, as is also seen for barracuda and the Antarctic toothfish (Healy *et al*., 2012; Kiss *et al*., 2004), and in a comparative analysis of crystallin proteins from Antarctic toothfish and bovine lenses (Kiss *et al*., 2010). The hoki elution profile also shows γ-crystallins to be more abundant in fish than mammals, a result that is supported by the literature (Greiling *et al*., 2009; Kiss *et al*., 2004; Kiss *et al*., 2010; Kiss and Cheng, 2008). Estimations of relative protein abundance based on peak areas were made, and are compared to literature values for crystallins from other fish in **Table 2.4**.

Table 2.4. *Estimations of relative protein abundance based on peak areas.*

Fish species	Crystallin class	Relative protein abundance (%)	Reference
Hoki	α	45	This study. Peak areas were calculated using OriginPro 8.
	β	2	
	γ	53	
Toothfish	α	52	(Kiss *et al*., 2004)
	β	5	
	γ	43	
Big eye tuna	α	47	(Kiss *et al*., 2004)
	β	12	
	γ	41	

The fractions for the first and second halves of each crystallin peak were pooled, resulting in six different fractions: α_T1, α_T2, β_T1, β_T2, γ_T1, and γ_T2. These fractions were then run on an SDS-PAGE gel to assess purity (**Figure 2.18**) (Section 7.1). The crude sample produced a number of bands (Lane 1). The α_T1 and α_T2 bands appear similar, each with a number of bands ranging from ~ 20-35 kDa (Lanes 2 and 3). Comparison with SDS-PAGE gels of bovine crystallin proteins reveals a higher heterogeneity on SDS-PAGE for α-crystallins from hoki, this was also seen for Antarctic toothfish and big eye tuna (Kiss *et al*., 2004). Those bands present at ~ 20 kDa correspond with α-crystallin subunits, although there are also some higher molecular weight bands, ~ 30-35 kDa, which are consistent with reported values for β_H crystallins ((Kiss *et al*., 2004)). This indicates that β_H coeluted with α-crystallins, this was also seen for Antarctic toothfish and big eye tuna (Kiss *et al*., 2004). The β_T1 and β_T2 bands correspond with β-crystallins seen previously (Lanes 4 and 5), although the low molecular weight band seen in the β_T2 fraction is perhaps some slight γ-crystallin contamination (Kiss *et al*., 2010). The γ_T1, and γ_T2 bands are consistent with those reported in the literature for other γ-crystallins from fish (Kiss *et al*., 2010). The SDS-PAGE gel confirms that the three crystallin classes were semi-purified (Kiss *et al*., 2004; Kiss *et al*., 2010).

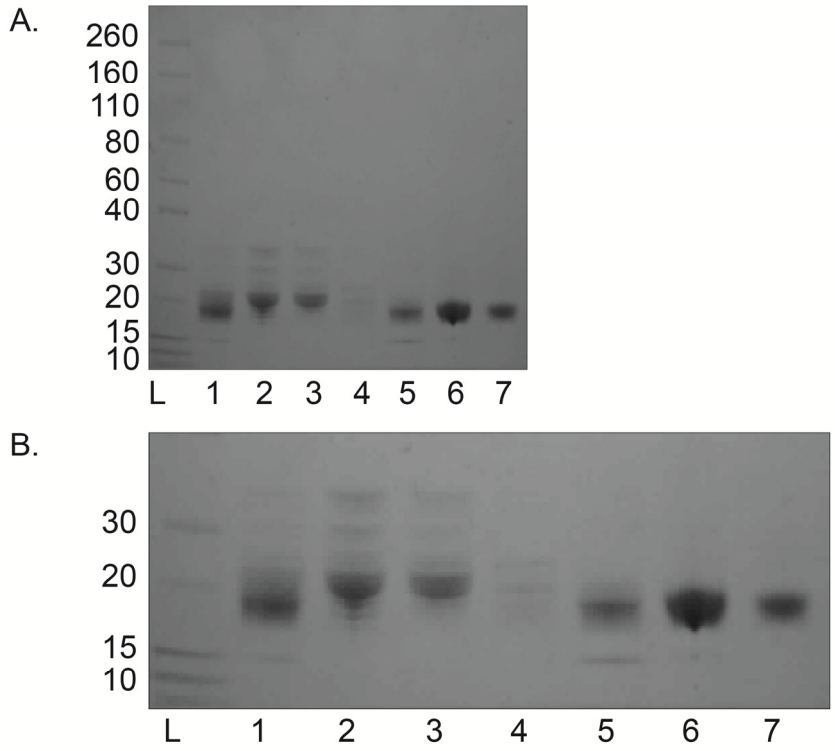

Figure 2.18. *A) SDS-PAGE gel of semi-purified crystallin samples, and B), an enlargement of the bands of interest. L = ladder (molecular weights indicated in kDa on the left-hand side), 1 = crude, 2 = α_T1, 3 = α_T2, 4 = β_T1, 5 = β_T2, 6 = γ_T1, and 7 = γ_T2.*

2.6.2. Formation of fibrils from semi-pure crystallins

When amyloid fibrils are formed from crude crystallin mixtures, it is not known which classes of crystallin proteins are being converted into a fibrillar form. The ability of the different classes of hoki crystallin proteins to form fibrils was assessed by subjecting the semi-purified crystallin proteins obtained from the separation detailed in Section 2.6.1 to the conditions established for the formation of fibrils from crude crystallin protein mixtures (Section 7.8.2). Details of the different crystallin protein solutions used for fibril formation are shown in **Table 2.5**.

Table 2.5. *Crystallin protein solutions used for amyloid fibril formation*

Protein solution		Components
Crude crystallin mixture		All high molecular weight crystallins, all α, β, and γ crystallins, 20 mM Tris, plus trace amounts of protein extraction buffer
Semi-pure crystallin fractions	• α_T-crystallins	All α crystallins, 20 mM Tris, plus trace amounts of protein extraction buffer
	• β_T-crystallins	All β crystallins, 20 mM Tris, plus trace amounts of protein extraction buffer
	• γ_T-crystallins	All γ crystallins, 20 mM Tris, plus trace amounts of protein extraction buffer

In order to form amyloid fibrils at the same protein concentration used to form fibrils from crude crystallin protein mixtures, each of the samples detailed in **Table 2.5** were freeze-dried, and then re-constituted in minimal nanopure H_2O (Section 7.8.2). The concentration of this protein concentrate was determing by NanoDrop (A_{280}) (Section 7.1), and fibrils then formed as per the in-house methods (Section 7.4.2). It must be noted that the fractions were not dialysed following purification, and therefore contained a high concentration of Tris buffer (and therefore salt). This is why the crude crystallin mixture control (**Table 2.5**) was included, to ensure the freeze-drying process and/or the presence of Tris buffer did not affect the fibril formation process. TEM images were then taken to ascertain the level of amyloid fibril formation in all samples (Section 7.5). **Figure 2.19** shows representative TEM images of amyloid fibrils formed from the semi-purified crystallin protein samples detailed in **Table 2.5**.

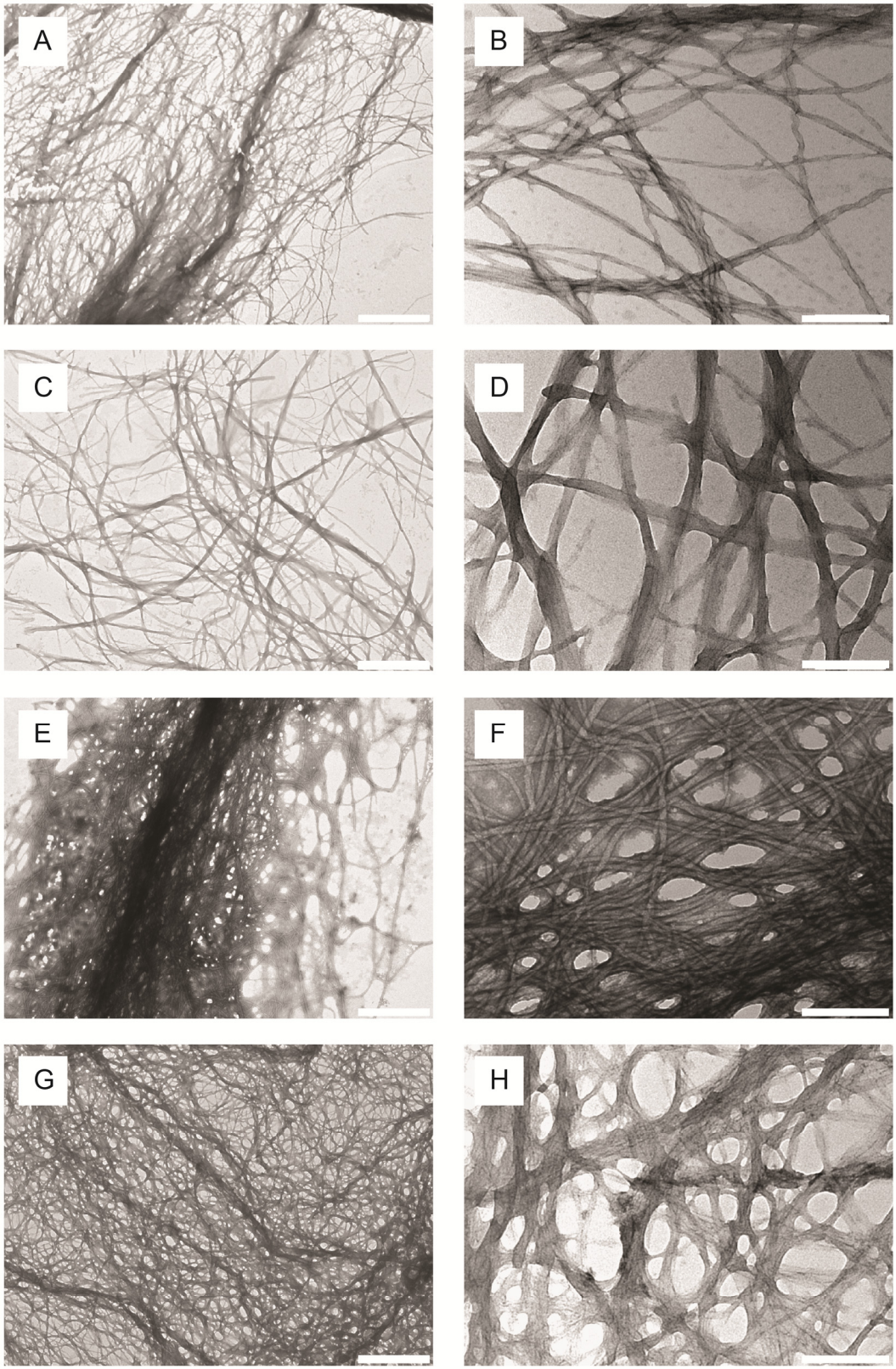

Figure 2.19. *TEM images of amyloid fibrils formed from crude crystallins (A & B), α_T fraction (C & D), β_T fraction (E & F), and γ_T fraction (G & H). Scale bars are 1 μm (A, C, E, G) and 0.2 μm (B, D, F, H).*

The crude crystallin sample formed amyloid fibrils as expected (**Figure 2.19**, A and B), with no difference in morphology to those shown in **Figure 2.14**, confirming that the freeze-drying process and the presence of Tris had not affected fibril formation. Fibrils also formed from all of the semi-purified crystallin fractions (**Figure 2.19**, C-H), with no noticeable differences in morphology between fractions, other than an increase in the density of the fibril network in those formed from the γ_T sample (**Figure 2.19**, G and H). This result confirms that all classes of crystallins are able to form amyloid fibrils (Garvey *et al*., 2009). It also shows that there is no loss in "quality" of fibrils formed from crude crystallin mixtures, and that further purification steps are unnecessary in the creation of quality nanofibres.

2.7. Stability of crystallin fibrils

It has previously been noted that the observed stability of other PNTs/PNFs, namely those formed from the FF peptide, differs significantly when the nanotubes are in solution (Andersen *et al*., 2011). An investigation into the stability in solution of FF peptide nanotubes tested their stability in various solutions ranging from organic solvents to buffer liquids, and demonstrated that the nanotubes could be dissolved in most solvents, including water and phosphate buffer (Andersen *et al*., 2011). Many of the applications in which these, and other PNTs/PNFs, are planned to play a central role involve their submersion in solvents, for example the creation of a biosensing device (Yemini *et al*., 2005a; Yemini *et al*., 2005b). This finding of instability in solution raises some doubts regarding the effectiveness of these nanotubes when used in this type of platform.

In order for crystallin fibrils to have a role in bionanotechnology, stability in a range of solvents is an issue that must be addressed. In the investigation into the stability of FF nanotubes, the size of the nanotubes, being greater than a micron in diameter and tens of microns in length, meant that optical microscopy could be used to observe the dissolution in real-time, with HPLC and mass spectrometry then used to identify the dissolved dipeptide in solution (Andersen *et al*., 2011). These same methods could not be used for crystallin fibrils, as the size of crystallin fibrils is outside the resolution of optical microscopy, and the nature of the crude protein source prevents simple identification by HPLC or mass spectrometry. Instead, the ThT assay was used to indicate the presence of fibrils in solution, and TEM was then used to visually confirm the presence of fibrils.

The different solvents used, and the relevance of each solvent is detailed in **Table 2.6**, with common biological solvents and cleanroom solvents chosen due the likeliness of these solvents being encountered in future applications, as well as allowing for direct comparison with the results obtained for the FF nanotubes (Andersen *et al*., 2011). Amyloid fibrils were formed from crude crystallin proteins as per standard in-house techniques (Section 7.4.2), and the growth buffer then exchanged with the desired solvent by centrifugation (Section 7.9).

Table 2.6. *Details of the different solvents for which the stability of crystallin fibrils was investigated, and the relevance of each solvent selected.*

	Solvent	**Relevance**
A	25 % *n*-propanol, pH 3.8	Crystallin fibril buffer (control)
B	25 % *n*-propanol, pH 7.0	To test the effect of biological pH
C	Nanopure H_2O	Biological relevance
D	100 mM phosphate buffer (PB), pH 7.4	Commonly used biological buffer solution
E	Ethanol	Common cleanroom solvent
F	Isopropanol	Common cleanroom solvent
G	Methanol	Common cleanroom solvent
H	Acetonitrile	Common cleanroom solvent

2.7.1. ThT assay of crystallin fibrils in different solvents

The ThT assay was used as an indicator of the presence of amyloid fibrils in solution. As the ThT assay is known to be sensitive to pH and viscosity (Sabaté *et al*., 2008; Sulatskaya *et al*., 2010), care was taken to have appropriate ThT control measurements in each of the solvents of interest (**Figure 2.20**). Some variation was seen and so the appropriate control value was subtracted from each ThT assay result.

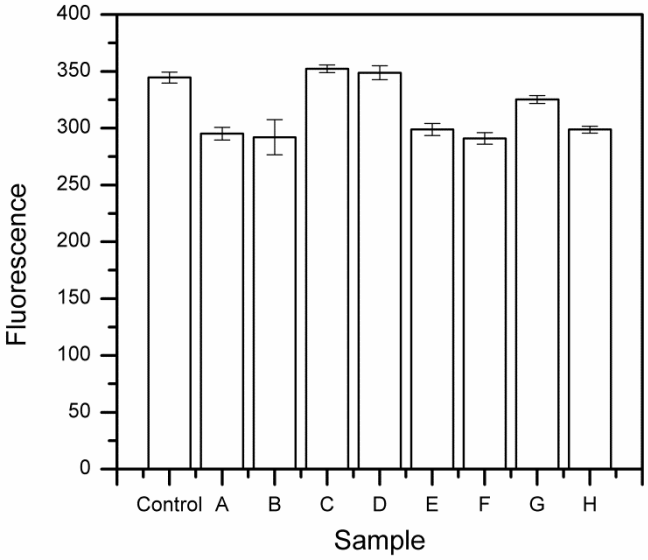

Figure 2.20. *Control measurements of ThT fluorescence in the presence of different solvents. From left to right: Control) ThT buffer solution, A) Crystallin fibril buffer, B) Crystallin fibril buffer pH 7, C) Nanopure H_2O, D) 100 mM PB pH 7.4, E) Ethanol, F) Isopropanol, G) Methanol, and H) Acetonitrile. Error bars represent the standard deviation of three replicates.*

Upon resuspension of crystallin fibrils in the solvents detailed in **Table 2.6**, an aliquot was taken at time zero, and then again after three hours. The ThT assay was then carried out on these samples (**Figure 2.21**). At time zero, when compared to the control sample which was resuspended again in the fibril formation buffer, slight decreases were seen in the sample resuspended in nanopure H_2O, isopropanol, methanol, and acetonitrile. However, after three hours in the solvents of interest, significant decreases in ThT fluorescence were only seen in the samples resuspended in methanol and acetonitrile, with the ThT fluorescence for fibrils in acetonitrile showing the largest decrease (**Figure 2.21**). There was also a slight drop in fluorescence observed for the control sample, this is most likely due to the difficulty associated with resuspending the pelleted fibrils due to their tendency to clump. This is also likely to be responsible for the increased error bars on some samples.

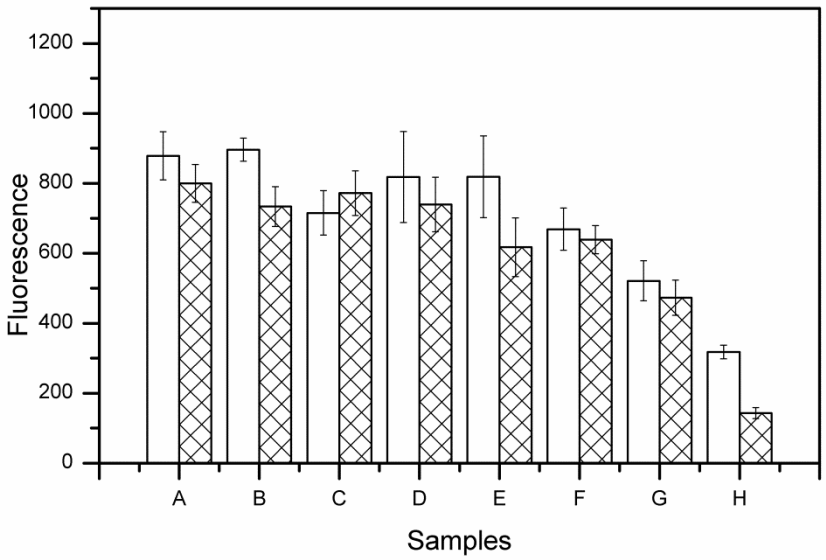

Figure 2.21. *ThT fluorescence of crystallin fibrils resuspended in various solvents at T =0 (white fill), and at T = 3 hours (patterned fill). Samples from left to right: A) Crystallin fibril buffer, B) Crystallin fibril buffer pH 7, C) Nanopure H_2O, D) 100 mM PB pH 7.4, E) Ethanol, F) Isopropanol, G)Methanol, and H) Acetonitrile. Fluorescence values have all had the appropriate control value subtracted (see* ***Figure 2.20****). Error bars represent the standard deviation of three replicates.*

2.7.2. TEM study of crystallin fibrils in different solvents

After several hours of incubation in the solvent of interest, TEM images were taken to confirm the presence or absence of fibrils in each of the samples. These images are shown in **Figure 2.22**. The sample that was resuspended in crystallin fibril buffer showed amyloid fibrils typical of a crystallin fibril preparation (**Figure 2.22**, A), showing that the centrifugation and resuspension procedure had not damaged the fibrils. For the sample that was resuspended in crystallin fibril buffer at pH 7 there are fibrils present; however, they seem to be of a slightly different morphology, appearing shorter and more discrete (**Figure 2.22**, B). This was not an unexpected result, as morphological differences have been seen previously with elevated pH in fibrils formed from bovine insulin (Rao, 2008), and from crude bovine crystallins (Pilkington, 2009). The fibrils in the sample resuspended in nanopure H_2O appear unchanged (**Figure 2.22**, C).

TEM images of the sample that was resuspended in phosphate buffer show amyloid fibrils, but they are very difficult to make out due to the presence of some larger, dark aggregate on top of the fibrils (**Figure 2.22**, D). The dark aggregate observed in the sample resuspended in phosphate buffer was determined to be due to the presence of the phosphate buffer, not the fibrils dissolving. The phosphate buffer is perhaps interacting with the stain used for TEM, as this was present in the sample with a lower concentration of phosphate buffer and in a phosphate buffer only control (**Figure 2.23**).

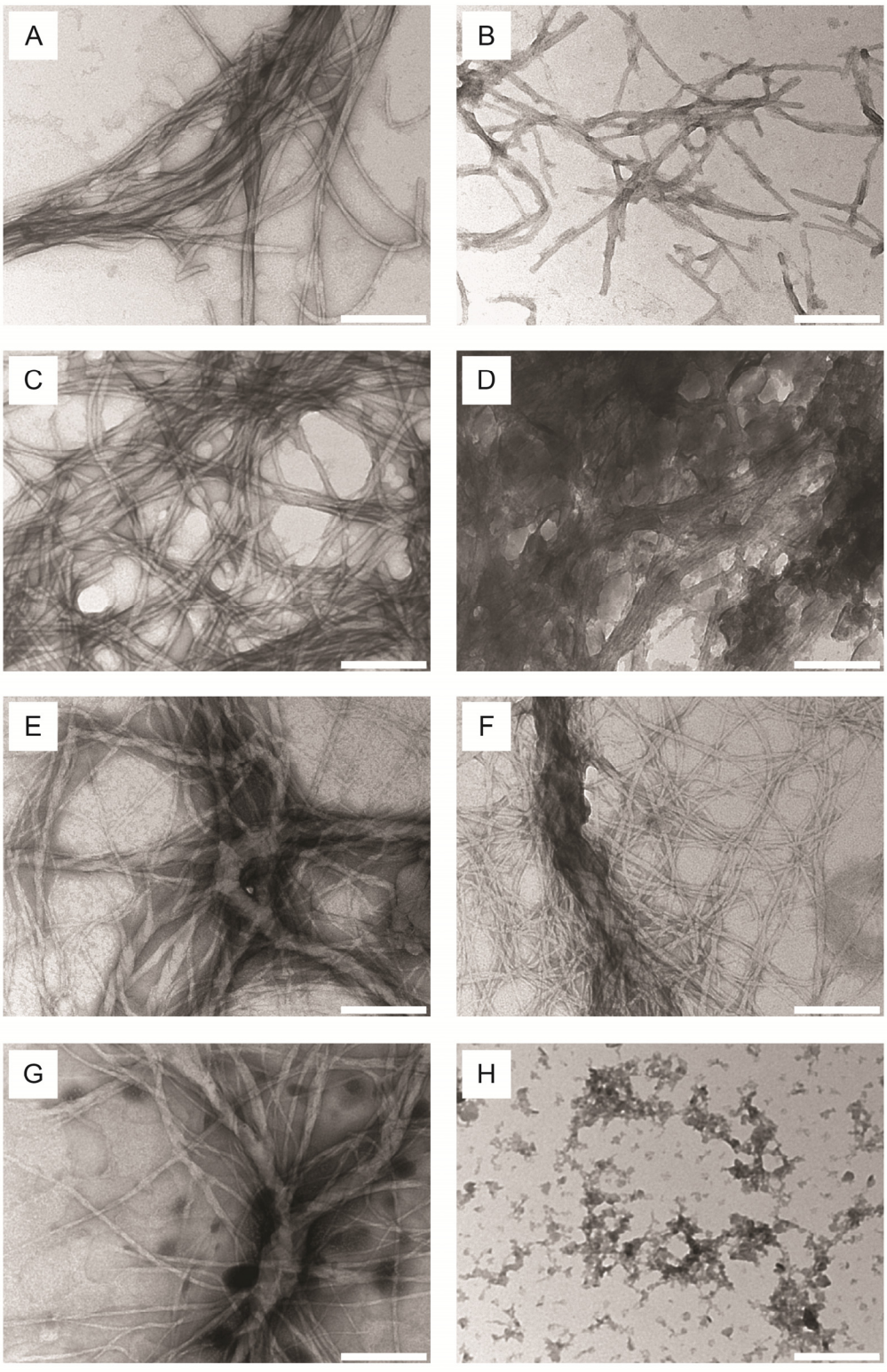

Figure 2.22. *Representative TEM images of crystallin fibrils resuspended in: A) Crystallin fibril buffer, B) Crystallin fibril buffer adjusted to pH 7, C) Nanopure H2O, D) 100 mM PB pH 7.4, E) Ethanol, F) Isopropanol, G) Methanol, and H) Acetonitrile. Scale bar is 0.2 µm.*

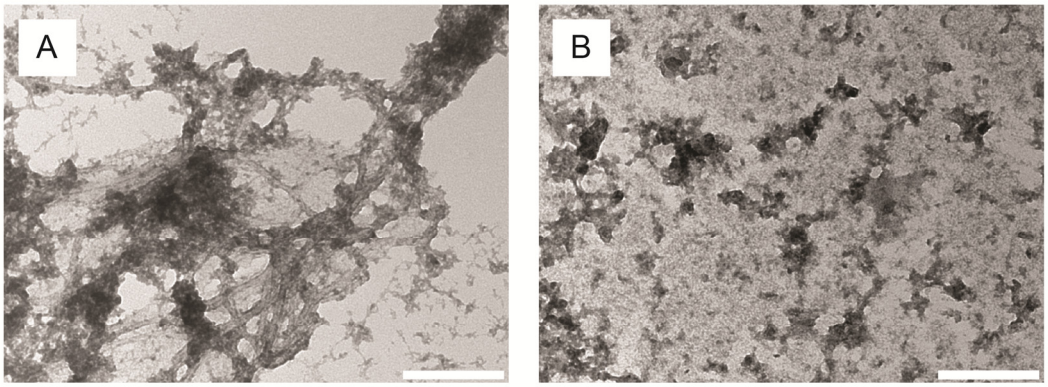

Figure 2.23. *Representative TEM images of A) Crystallin fibrils resuspended in 50 mM PB pH 7.4, and B) Control PB grid. Scale bar is 0.2 μm.*

TEM images for the samples resuspended in ethanol, isopropanol, and methanol all show clear fibrils (**Figure 2.22**, E-H). In the case of the methanol sample this result is somewhat contradictory to what was observed by the ThT assay (**Figure 2.21**), which suggests that although fibrils are present, they may exist in much lower quantities. TEM images of the sample that was resuspended in acetonitrile show no fibrils to be present (**Figure 2.22**, H), in agreement with the ThT assay. The effect of acetonitrile on crystallin fibrils was further investigated by resuspending fibrils in 50 % acetonitrile. With a lower concentration of acetonitrile fibrils remain present; however, there were a large number of circular fibril assemblies visible by TEM (**Figure 2.24**). Organic solvents, including ACN, have previously been shown to dissolve amyloid fibrils (Hirota-Nakaoka *et al*., 2003). Circular fibril assemblies have also previously been observed, in fibrils formed from α-crystallins (Meehan *et al*., 2004). With further characterisation, this circular morphology may prove interesting for bionanotechnology.

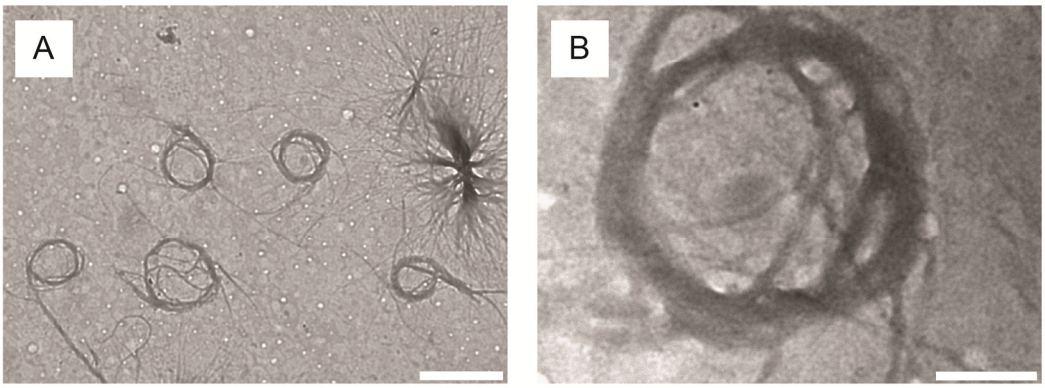

Figure 2.24. *TEM images of crystallin fibrils resuspended in 50 % acetonitrile. Scale bar is 1 μm (A), and 0.2 μm (B).*

The stability of crystallin amyloid fibrils in various solvents is summarised in ***Table 2.7***, and compared to results previously obtained for FF nanotubes (Andersen *et al*., 2011). It can be confirmed that crystallin amyloid fibrils are significantly more stable in solution than FF nanotubes, and therefore could be a more appropriate choice for a PNT/PNF to be used in applications where solvent contact is involved, such as biosensing. Their solubility in ACN was not an unexpected result, with ACN having been used previously in the literature to resolubilise amyloid fibrils (Kaplan and Pras, 1987). This solubility in ACN could also give rise to further applications, such as sacrificial templates for metallic nanowire formation (Hsieh and Hsieh, 2010).

Table 2.7. *Summary of stability of FF nanotubes, according to (Andersen et al., 2011), and crystallin amyloid fibrils in various solvents.*

	Solvent	FF nanotubes stable? (Y/N)	Crystallin amyloid fibrils stable? (Y/N)	
			ThT assay	TEM
A	25 % n-propanol, pH 3.8	N/A	Y	Y
B	25 % n-propanol, pH 7.0	N/A	Y	Y
C	Nanopure H_2O	N	Y	Y
D	100 mM phosphate buffer, pH 7.4	N	Y	Y
E	Ethanol	N	Y	Y
F	Isopropanol	N	Y	Y
G	Methanol	N	N	Y
H	Acetonitrile	N	N	N

2.8. Summary

This chapter has demonstrated the formation of amyloid fibrils from bovine insulin, fungal hydrophobins, and mixtures of crude fish crystallins. The amyloid fibrils formed from bovine insulin were consistent with those observed in the literature, as were those from fungal hydrophobins. The impact of the creation of hydrophobic:hydrophilic interfaces on hydrophobin rodlet formation was demonstrated *via* the use of real-time ThT assaying. The internal structure of amyloid fibrils formed from crude fish crystallins was investigated with X-ray fibre diffraction, and the characteristic cross-β diffraction pattern was observed, confirming that the amyloid-like structures seen are in fact true amyloid fibrils. It was also shown that amyloid fibrils are able to be formed from all three classes of fish crystallins, with no morphological difference observed between those fibrils formed from the crude and semi-purified proteins. This finding affirms the use of crude fish crystallins as a source of amyloid fibrils for bionanotechnology.

Also in support of the use of crystallin fibrils as nanomaterials, is their stability in solution in a range of relevant solvents. Crystallin fibrils showed superior stability to another commonly used fibril source, the FF peptide, suggesting that they may be a more desirable source, dependent on the application, of PNTs/PNFs for bionanotechnology.

2.9. References

Ahmad A, Millett I, Doniach S, Uversky V, Fink A. 2003. Partially folded intermediates in insulin fibrillation. *Biochemistry* **42**:11404–11416.

Ahmad A, Millett I, Doniach S, Uversky V, Fink A. 2004. Stimulation of insulin fibrillation by urea-induced intermediates. *Journal of Biological Chemistry* **279**:14999–15013.

Andersen K, Castillo-Leon J, Hedström M, Svendsen W. 2011. Stability of diphenylalanine peptide nanotubes in solution. *Nanoscale* **3**:994–998.

Arnaudov L, De Vries R. 2005. Thermally induced fibrillar aggregation of hen egg white lysozyme. *Biophysical Journal* **88**:515–526.

Blundell T, Cutfield J, Cutfield S, Dodson E, Dodson G, Hodgkin D, Mercola D, Vijayan M. 1971. Atomic positions in rhombohedral 2-zinc insulin crystals. *Nature* **231**:506–511.

Bouchard M, Zurdo J, Nettleton E, Dobson C, Robinson C. 2000. Formation of insulin amyloid fibrils followed by FTIR simultaneously with CD and electron microscopy. *Protein Science* **9**:1960–1967.

Brange J, Andersen L, Laursen E, Meyn G, Rasmussen E. 1997. Toward understanding insulin fibrillation. *Journal of Pharmaceutical Sciences* **86**:517–525.

Delano W. 2002. The PyMOL Molecular Graphics System.

Devlin G, Knowles T, Squires A, McCammon M, Gras S, Nilsson M, Robinson C, MacPhee C. 2006. The component polypeptide chains of bovine insulin nucleate or inhibit aggregation of the parent protein in a conformation-dependent manner. *Journal of Molecular Biology* **360**:497–509.

Ecroyd H, Carver J. 2009. Crystallin proteins and amyloid fibrils. *Cellular and Molecular Life Sciences* **66**:62–81.

Garvey M, Gras S, Meehan S, Meade S, Carver J, Gerrard J. 2009. Protein nanofibres of defined morphology prepared from mixtures of crude crystallins. *International Journal of Nanotechnology* **6**:258–273.

Gazit E. 2007. Use of biomolecular templates for the fabrication of metal nanowires. *FEBS Journal* **274**:317–322.

Gras S. 2007. Amyloid fibrils: From disease to design. New biomaterial applications for self-assembling cross-β fibrils. *Australian Journal of Chemistry* **60**:333–342.

Greiling T, Houck S, Clark J. 2009. The zebrafish lens proteome during development and aging. *Molecular Vision* **15**:2313–2325.

Hamedi M, Herland A, Karlsson R, Inganas O. 2008. Electrochemical devices made from conducting nanowire networks self-assembled from amyloid fibrils and alkoxysulfonate PEDOT. *Nano Letters* **8**:1736–1740.

Harding J. 1991. Cataract: biochemistry, epidemiology and pharmacology. Chapman and Hall London.

Healy J, Wong K, Roux C, Domigan L, Sunde M, Sawyer E, Gras S, Gerrard J, Vadudevamurthy M. 2012. Polymorphism and higher ordered structures of protein nanofibers from crude mixtures of fish lens crystallins: Towards useful materials. *Biopolymers*:Accepted.

Herland A, Thomsson D, Mirzov O, Scheblykin I, Inganäs O. 2008. Decoration of amyloid fibrils with luminescent conjugated polymers. *Journal of Materials Chemistry* **18**:126–132.

Herland A, Björk P, Hania P, Scheblykin I, Inganäs O. 2007. Alignment of a conjugated polymer onto amyloid-like protein fibrils. *Small* **3**:318–25.

Hirota-Nakaoka N, Hasegawa K, Naiki H, Goto Y. 2003. Dissolution of β2-microglobulin amyloid fibrils by dimethylsulfoxide. *Journal of Biochemistry* **134**:159–164.

Hou S, Li X, Li X, Feng X. 2009. Coating of hydrophobins on three-dimensional electrospun poly (lactic-co-glycolic acid) scaffolds for cell adhesion. *Biofabrication* **1**:035004.

Hsieh C, Hsieh S. 2011. Nanoparticle chain formation on functional surfaces using insulin fibrils as a structure directing agent. *Journal of Materials Chemistry*:16900–16904.

Hsieh S, Hsieh C. 2010. Alignment of gold nanoparticles using insulin fibrils as a sacrificial biotemplate. *Chemical Communications* **46**:7355–7357.

Jimenez J, Nettleton E, Bouchard M, Robinson C, Dobson C, Saibil H. 2002. The protofilament structure of insulin amyloid fibrils. *Proceedings of the National Academy of Sciences of the United States of America* **99**:9196–9201.

Kaplan B, Pras M. 1987. Preparative fractionation of amyloid proteins on a microgram scale by high-performance liquid chromatography and polyacrylamide gel electrophoresis. *Clinica Chimica Acta* **163**:199–205.

Kiss A, Cheng C. 2008. Molecular diversity and genomic organisation of the α, β, and γ eye lens crystallins from the Antarctic toothfish *Dissostichus mawsoni*. *Comparative Biochemistry and Physiology Part D: Genomics and Proteomics* **3**:155–171.

Kiss A, Devries A, Morgan-Kiss R. 2010. Comparative analysis of crystallins and lipids from the lens of Antarctic toothfish and cow. *Journal of Comparative Physiology B: Biochemical, Systemic, and Environmental Physiology* **180**:1019–1032.

Kiss AJ Mirarefi A, Ramakrishnan S, Zukoski C, DeVries A, Cheng C. 2004. Cold-stable eye lens crystallins of the Antarctic nototheniid toothfish *Dissostichus mawsoni* Norman. *Journal of Experimental Biology* **207**:4633.

Krebs M, MacPhee C, Miller A, Dunlop I, Dobson C, Donald A. 2004. The formation of spherulites by amyloid fibrils of bovine insulin. *Proceedings of the National Academy of Sciences of the United States of America* **101**:14420–14424.

Kroes-Nijboer A, Venema P, Bouman J, van der Linden E. 2009. The critical aggregation concentration of β-lactoglobulin-based fibril formation. *Food Biophysics* **4**:59–63.

Kwan A, Winefield R, Sunde M, Matthews J, Haverkamp R, Templeton M, Mackay J. 2006. Structural basis for rodlet assembly in fungal hydrophobins. *Proceedings of the National Academy of Sciences of the United States of America* **103**:3621–3626.

LeVine III H. 1993. Thioflavin T interaction with synthetic Alzheimer's disease β-amyloid peptides: Detection of amyloid aggregation in solution. *Protein Science* **2**:404–410.

Linder M, Szilvay G, Nakari-Setälä T, Penttilä M. 2005. Hydrophobins: the protein-amphiphiles of filamentous fungi. *FEMS Microbiology Reviews* **29**:877–896.

Mackay J, Matthews J, Winefield R, Mackay L, Haverkamp R, Templeton M. 2001. The hydrophobin EAS is largely unstructured in solution and functions by forming amyloid-like structures. *Structure* **9**:83–91.

Meehan S, Berry Y, Luisi B, Dobson C, Carver J, MacPhee C. 2004. Amyloid fibril formation by lens crystallin proteins and its implications for cataract formation. *Journal of Biological Chemistry* **279**:3413–3419.

Morris V, Ren Q, Macindoe I, Kwan A, Byrne N, Sunde M. 2011. Recruitment of class I hydrophobins to the air: water interface initiates a multi-step process of functional amyloid formation. *Journal of Biological Chemistry* **286**:15955–15963.

Nielsen L, Frokjaer S, Carpenter J, Brange J. 2001a. Studies of the structure of insulin fibrils by Fourier transform infrared (FTIR) spectroscopy and electron microscopy. *Journal of Pharmaceutical Sciences* **90**:29–37.

Nielsen L, Khurana R, Coats A, Frokjaer S, Brange J, Vyas S, Uversky V, Fink A. 2001b. Effect of environmental factors on the kinetics of insulin fibril formation: elucidation of the molecular mechanism. *Biochemistry* **40**:6036–6046.

Pauling L, Corey R. 1951. Configuration of polypeptide chains. *Nature* **168**:550–551.

Pilkington S. 2009. Incorporating glucose oxidase activity into amyloid fibrils. Masters Thesis; University of Canterbury.

Pilkington S, Roberts S, Meade S, Gerrard J. 2010. Amyloid fibrils as a nanoscaffold for enzyme immobilisation. *Biotechnology Progress* **26**:93–100.

Posner M, Hawke M, LaCava C, Prince C, Bellanco N, Corbin R. 2008. A proteome map of the zebrafish (Danio rerio) lens reveals similarities between zebrafish and mammalian crystallin expression. *Molecular Vision* **14**:806.

Rao S. 2008. Amyloid fibrils in bionanomaterials. PhD Thesis; University of Canterbury.

Raynes J, Pearce F, Meade S, Gerrard J. 2011. Immobilization of organophosphate hydrolase on an amyloid fibril nanoscaffold: Towards bioremediation and chemical detoxification. *Biotechnology Progress* **27**:360–367.

Sabaté R, Lascu I, Saupe SJ. 2008. On the binding of thioflavin-T to HET-s amyloid fibrils assembled at pH 2. *Journal of Structural Biology* **162**:387–396.

Sulatskaya AI, Maskevich A, Kuznetsova I, Uversky V, Turoverov K. 2010. Fluorescence quantum yield of thioflavin T in rigid isotropic solution and incorporated into the amyloid fibrils. *PLoS One* **5**:e15385.

Sunde M, Kwan A., Templeton M, Beever R, Mackay J. 2008. Structural analysis of hydrophobins. *Micron* **39**:773–784.

Wang Z, Wang Y, Huang Y, Li S, Feng S, Xu H, Qiao M. 2010. Characterization and application of hydrophobin-dispersed multi-walled carbon nanotubes. *Carbon* **48**:2890–2898.

Waterhouse S, Gerrard J. 2004. Amyloid fibrils in bionanotechnology. *Australian Journal of Chemistry* **57**:519–523.

Waugh D. 1946. A fibrous modification of insulin. I. The heat precipitate of insulin. *Journal of the American Chemical Society* **68**:247–250.

Wong K. 2012. Scaling up the production of protein nanotubes. Masters Thesis; University of Canterbury.

World Health Organisation (WHO). 2011. World Health Statistics.

Wösten H, Richter M, Willey J. 1999. Structural proteins involved in emergence of microbial aerial hyphae. *Fungal Genetics and Biology* **27**:153–160.

Wösten H, de Vocht M. 2000. Hydrophobins, the fungal coat unravelled. *Biochimica et Biophysica Acta (BBA)-Reviews on Biomembranes* **1469**:79–86.

Yemini M, Reches M, Gazit E, Rishpon J. 2005a. Peptide nanotube-modified electrodes for enzyme-biosensor applications. *Analytical Chemistry* **77**:5155–5159.

Yemini M, Reches M, Rishpon J, Gazit E. 2005b. Novel electrochemical biosensing platform using self-assembled peptide nanotubes. *Nano Letters* **5**:183–186.

Zampieri F, Wösten H, Scholtmeijer K. 2010. Creating surface properties using a palette of hydrophobins. *Materials* **3**:4607–4625.

Zhao Z, Qiao M, Yin F, Shao B, Wu B, Wang Y, Wang X, Qin X, Li S, Yu L. 2007. Amperometric glucose biosensor based on self-assembly hydrophobin with high efficiency of enzyme utilization. *Biosensors and Bioelectronics* **22**:3021–3027.

3. Chapter Three

Controlling dimensions of amyloid fibrils

3.1. Introduction

Amyloid fibrils have the potential to be used in a range of applications, such as bioelectronics and biosensing (Waterhouse and Gerrard, 2004). In these applications, as well as in others, the ability to have some degree of control over the fibrils formed is desirable. Length control is also a way of reducing the cytotoxic potential of amyloid fibril based nanomaterials. Xue *et al*. (2009a) have shown that fibril length correlates with the ability of amyloid fibrils to disrupt membranes and reduce cell viability, with shorter fibrils showing increased cytotoxic potential. For this thesis, an additional motivation to control the length of amyloid fibrils was the experimental setup used in Chapter 4, as in order to gain information about their conductive properties, fibrils needed to be long enough to bridge pairs of electrodes.

The nature of the fibrillation process is such that a large number of structural species of highly diverging sizes may exist simultaneously (Langkilde and Vestergaard, 2009), making control over this process difficult. Amyloid fibrils also exist in a range of morphologies, and solution conditions have previously been shown to favour a particular fibril morphology (Petkova *et al*., 2005). Amyloid fibrils described in the literature vary in size depending on the native protein/peptide, with diameters ranging from a few nanometres to greater than 30 nanometres and lengths of up to several microns (Gras, 2007).

Although the accepted mechanism for fibrillation has been applied to a range of fibril forming proteins/peptides, there are differences observed between the fibrils formed from different proteins/peptides (Gras, 2007). There have been a small number of studies on amyloid fibril length carried out on other protein systems (Humblet-Hua *et al*., 2008; van Raaij *et al*., 2008; Rogers *et al*., 2005a; Rogers *et al*., 2005b; Xue *et al*., 2009b) This study focuses on the fibrils formed from bovine insulin, with the aim of optimising the formation process, in order to improve homogeneity in samples of these novel nanomaterials.[1]

3.2. Controlling the dimensions of bovine insulin amyloid fibrils

Bovine insulin amyloid fibrils have diameters of 7-10 nm, and are up to several microns long, although morphological variations are often seen in fibrils from the same preparation (Jimenez *et al*., 2002). Bovine insulin is often used in studies of amyloid formation as it forms fibrils very rapidly after disruption of the natively hexameric structure. *In vitro,* insulin can be converted from this native structure to the fibrillar form by incubation at high insulin concentrations, low pH and high temperature, with fibrillation occurring under these conditions within hours (Krebs *et al*., 2004; Nielsen *et al*., 2001a; Waugh, 1946). However, most studies have tended to focus more on the kinetics of insulin amyloid fibril formation rather than the dimensions of fibrils formed (Jansen *et al*., 2005; Jimenez *et al*., 2002; Mauro *et al*., 2007; Nielsen *et al*., 2001b). Mauro *et al.* (2007) observed some differences in the lengths of fibrils formed under various conditions, but were more concerned with the aggregation kinetics, and Jimenez *et al*. (2002) have observed different insulin fibril morphologies.

[1] This work is published in (Domigan *et al*., 2011)

The mechanism of insulin amyloid fibril formation is shown schematically in **Figure 3.1**. Amyloid fibril formation has been shown to have many characteristics of a nucleated growth mechanism (Chiti and Dobson, 2006). When the time course of the change of a peptide or protein from its native state into a fibrillar form is measured, a lag phase is generally observed, followed by a rapid exponential growth phase (Naiki *et al*., 1989). This lag phase is assumed to be the time needed for 'nuclei' to form (**Figure 3.1**, Steps 1-3), and from here fibril growth proceeds rapidly by elongation of the fibrils **Figure 3.1**, Step 4), from association of monomers or oligomers with this nucleus (Chiti and Dobson, 2006). This nucleation-polymerisation mechanism of growth has been likened to that observed in crystallisation (Thirumalai *et al*., 2003).

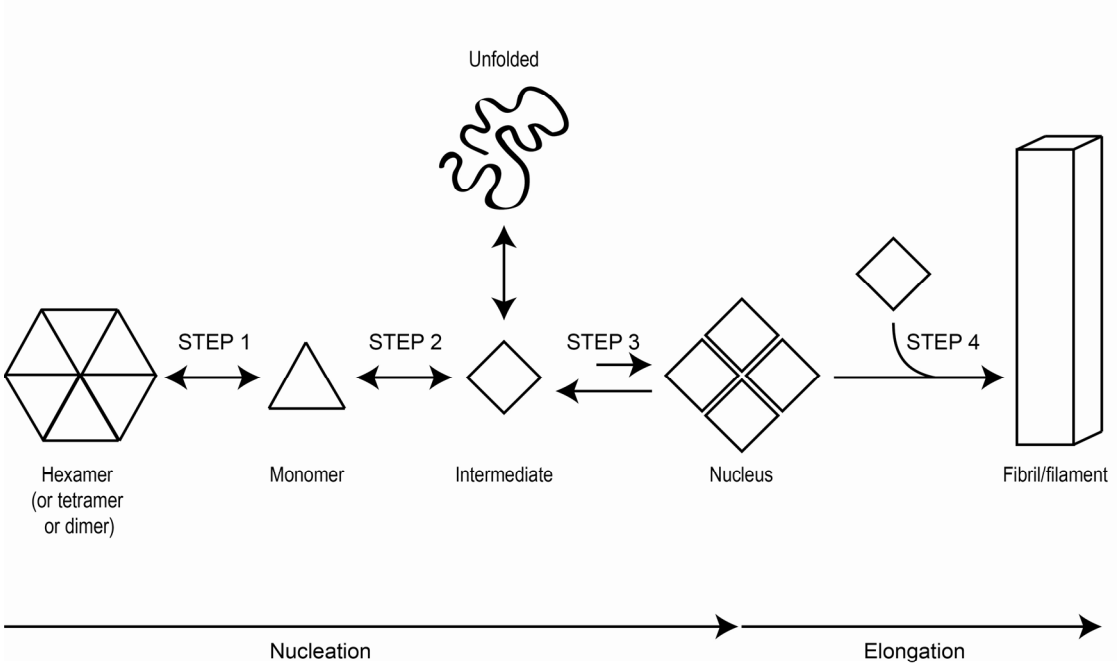

Figure 3.1. *Schematic showing the nucleation-elongation mechanism for insulin fibril formation, adapted from Nielsen* et al. (2001b). ***Step 1:*** *The first thing that must occur is a change in quarternary structure from the oligomeric state to the monomer.* ***Step 2:*** *This involves destabilisation of the monomer to produce a partially folded intermediate which exists in equilibrium with unfolded structures.* ***Step 3:*** *This is the formation of the nucleus from the assembly of a few partially folded monomeric species. These first 3 steps make up the nucleation component of insulin fibril formation. The next step* ***(Step 4)*** *is elongation of the nucleus into a fibril/filament by addition of partially folded intermediate monomeric insulin species.*

This chapter presents a systematic study of the use of growth and storage conditions to control the length of amyloid fibrils formed from bovine insulin, with length distributions constructed from TEM images. Growth temperature, pH, protein concentration, and storage conditions were examined, and were seen to offer a range of conditions that favour different length distributions.

3.3. Effect of growth and storage conditions on bovine insulin amyloid fibril length distribution

Amyloid fibrils were formed from bovine insulin under a range of growth and storage conditions, as detailed in **Table 3.1** (Section 7.10.1). For each of these samples, unless stated otherwise, fibril lengths were measured from TEM images, and length distributions constructed (Section 7.10.2). The assumption was made that the appearance of fibrils on the TEM grid was representative of the bulk sample. Investigation into the effect of growth temperature and pH led to the establishment of initial growth conditions. Alterations were then made to these conditions to show the effect of native protein concentration and storage conditions on length distribution.

3.3.1. Effect of growth temperature

The effect of growth temperature on fibril dimensions was examined with the native insulin subjected to temperatures ranging from room temperature through to 60 °C. 60 °C was chosen as the maximum temperature, as it has been shown that this yields insulin fibrils with a predominantly compact morphology, whereas above this a variety of morphologies are seen (Jimenez *et al*., 2002). When examining the effect of growth temperature, a protein concentration of 5.8 mg/mL was used, as this is the standard concentration used in-house for insulin fibril formation. Room temperature and 30 °C (**Table 3.1**, Conditions 1 and 2) were insufficient to cause fibril formation, with Thioflavin T (ThT) readings indicative of negligible amyloid fibril formation even after 3 weeks of growth. Fibrils were seen to form more slowly at 40 °C than at the higher temperatures, with fibril formation confirmed after three and one days respectively.

A decrease in the rate of aggregation was seen with a decrease in temperature, which is supported by previous work that saw the same relationship between temperature and aggregation rate. The previous study saw that the time to increase viscosity 4-fold of a bovine insulin solution, taken as being indicative of aggregation, increased from 35 °C to 55 °C and above this temperature little difference was observed (Brange *et al*., 1997).

For those fibril samples formed at 40 and 50 °C, although some fibrils formed, a large amount of unfibrilised protein remained (**Figure 3.2**, B-D). Thus, 60 °C (**Figure 3.2**, A), was used for the remainder of the experiments, following previous studies (Brange *et al*., 1997; Mauro *et al*., 2007; Nielsen *et al*., 2001a).

Table 3.1. *Detail of the different growth and storage conditions used for the insulin amyloid fibril samples.*

Sample number	Growth concentration (mg/mL)	Growth temperature (°C)	Buffer		Growth time	Storage conditions
			pH	Salt		
1	5.8	Room temp.	1.5	100 mM NaCl	24 hrs	Room temp.
2		30				
3		40				
4		50				
5		60				
6	5.8	60	1.0	100 mM NaCl	24 hrs	Room temp.
7			2.0			
8			2.5			
9	0.5	60	1.5	100 mM NaCl	24 hrs	Room temp.
10	1.0					
11	2.0					
12	3.0					
13	4.0					
14	5.0					
15	5.8	60	1.5	100 mM NaCl	24 hrs	Refrigeration
16						Freeze/thaw x1
17						Freeze/thaw x2

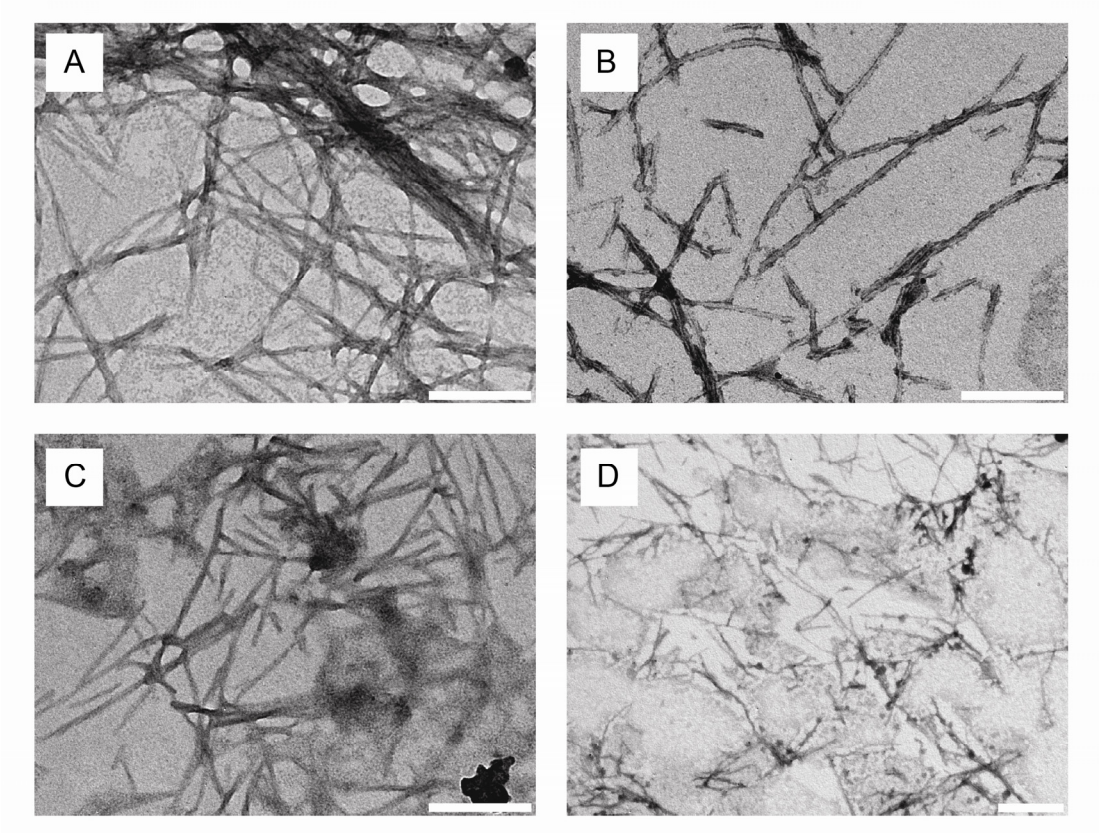

Figure 3.2. *TEM images of fibrils formed at A) 60 °C, B) 50 °C and C) 40 °C. Scale bar is 0.5 μm. D) A representative image of the large amount of unfibrilised protein which exists at the lower temperatures. Scale bar is 0.2 μm.*

The lengths of fibrils formed were analysed for samples formed at 40, 50 and 60 °C, and it was seen that there was an increase in length with increasing growth temperature, with the mean fibril length 0.52, 0.59 and 0.68 μm respectively (**Table 3.2**). The length distribution **(Figure 3.3)**, shows the average fibril length is heavily skewed by a population of small fibril fragments being observed no matter what the condition. This bias has previously been noted by Xue *et al*. (2009b), who commented that the distribution of lengths is biased towards shorter fibrils, due to longer fibrils being more likely to be cut off by image boundaries, by overlap with other fibrils, and by length dependent effects on the surface deposition efficiency of fibrils. The small range in length seen here between the different temperatures reflects the small temperature range examined, due to the lack of fibril formation at the lowest temperatures.

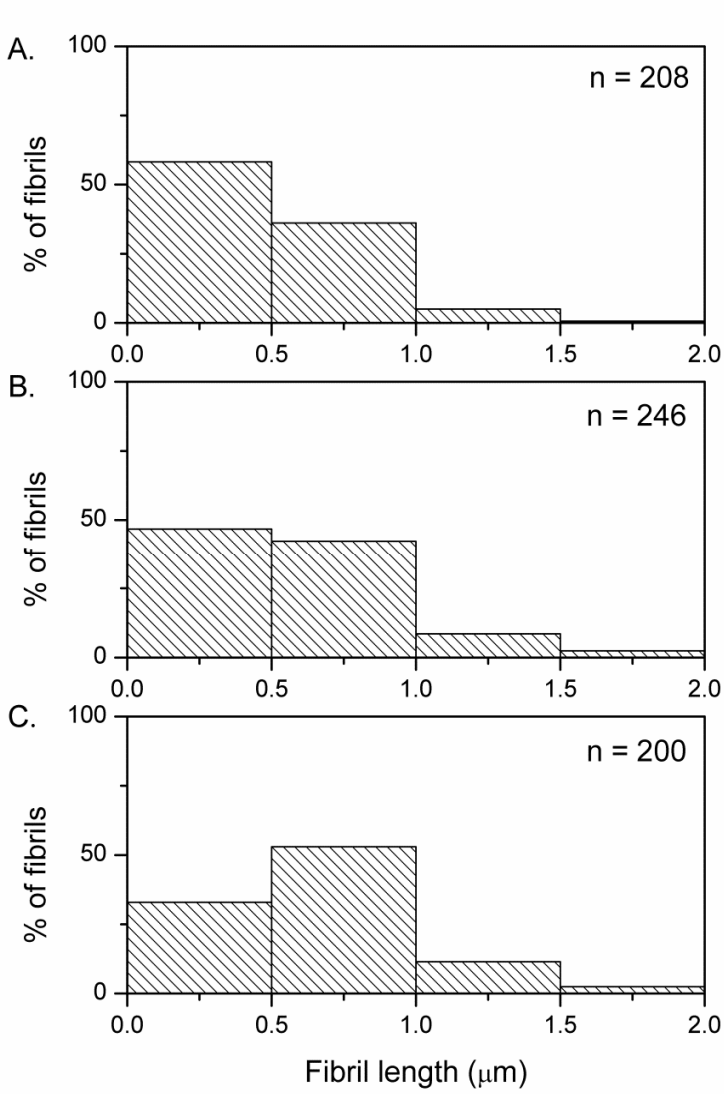

Figure 3.3. *Length distribution of insulin amyloid fibrils formed at A) 40 °C, B) 50 °C, and C) 60 °C*

The differences in length that were observed at the different temperatures reiterates previous observations that increased temperature accelerates the elongation stage of fibrillation (Jansen *et al*., 2005), therefore, longer fibrils were observed to form at the higher temperature.

Table 3.2. *Average fibril length and range for bovine insulin fibrils formed under different growth conditions*[*].

Sample number**	Average fibril length (µm)	Range (µm)
3	0.52	0.14-1.61
4	0.59	0.13-1.94
5	0.68	0.10-1.82
9	1.32	0.08-6.32
10	1.11	0.11-4.68
11	1.33	0.19-4.22
12	1.12	0.19-3.95
13	0.56	0.08-2.04
14	0.75	0.14-2.09
15	0.57	0.10-3.31
16	0.29	0.07-0.91
17	0.15	0.01-0.36

** Average lengths and ranges only calculated where possible, see detail in text.*

*** See Table 3.1 for details of sample conditions*

3.3.2. Effect of pH

Fibrils were formed in 100 mM NaCl adjusted to pH 1.0, 1.5, 2.0, and 2.5 with HCl in order to investigate the effect of pH on the length of insulin fibrils (Conditions 5-8, Table 3.1). No fibrils formed at pH 1.0 (**Figure 3.6**, A).

Fibril formation at the different pH values was monitored by the increase in ThT fluorescence. As pH has been shown previously to have an effect on the ThT assay (Sabaté *et al*., 2008), ThT control measurements were taken at each of the pH values in the absence of insulin. As shown in **Figure 3.4**, no difference in fluorescence was observed across the pH range used, and so the control measurement at pH 1.5 was used when monitoring fibril formation.

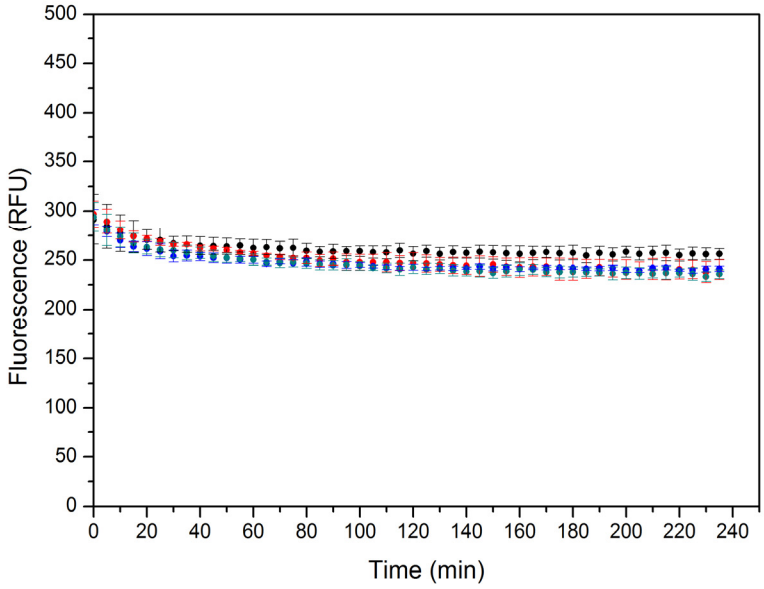

***Figure 3.4**. ThT control measurements in the presence of fibril buffer at pH 1.0 (black), 1.5 (red), 2.0 (blue), and 2.5 (green). Each reading represents an average of triplicate well readings, with the error bars representing standard error.*

The increase in ThT fluorescence at pH 1.5 and pH 2.0 followed the characteristic sigmoidal increase in fluorescence (**Figure 3.5**, red and blue traces), commonly observed in amyloid formation (Brange *et al*., 1997). At pH 2.5, the sigmoidal increase in fluorescence was also observed (**Figure 3.5**, green trace), although a much lower plateau was reached, demonstrating that less fibrillation was occurring at this pH. At pH 1.0, an increase in fluorescence was observed; however, it was not typical of fibril formation, and is likely due the formation of an amorphous, but β-sheet containing, aggregate. This reiterates the need for the formation of fibrils to be confirmed by TEM (**Figure 3.6**).

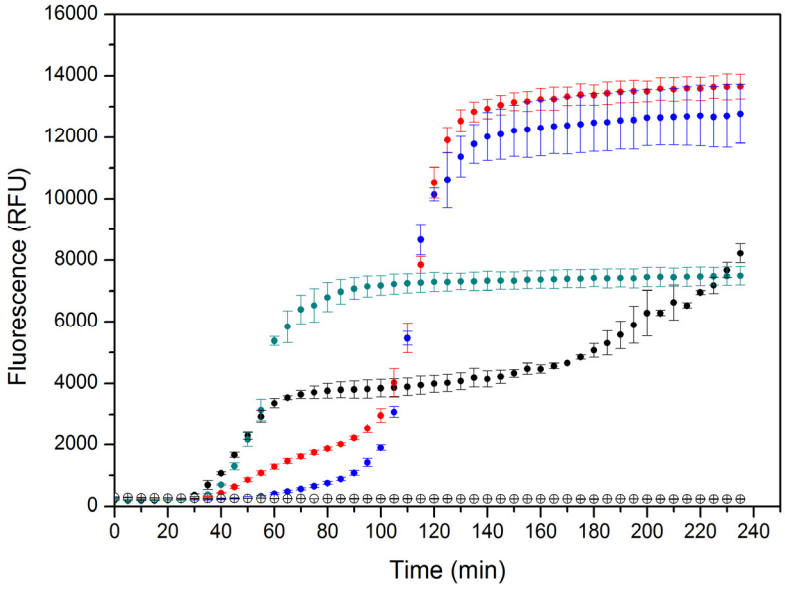

Figure 3.5. *Time profile of ThT fluorescence for bovine insulin incubated at 60 °C in fibril buffer adjusted to pH 1.0 (black), 1.5 (red), 2.0 (blue), and 2.5 (green). Control measurement (pH 1.5), with no insulin present, is shown in white. Each reading represents an average of triplicate well readings, with the error bars representing standard error.*

At the higher pH values, where fibrils did form, the change in pH changed the association between the fibrils. With increase in pH there was an increase in fibril-fibril interactions, with more clumping of fibrils observed (**Figure 3.6**, B-D). This is consistent with previous work, where fibrils formed at pH 1.6 were dialysed into buffers of higher pH, clumping of fibrils was also observed (Rao, 2008). Our findings showed that although fibrils would form at the higher pH values, pH 1.5 was optimum and so this was the pH used for all other experiments. Length distributions were not measured due to the clumping of fibrils at pH 2.0 and 2.5, making it impossible to clearly identify individual fibrils.

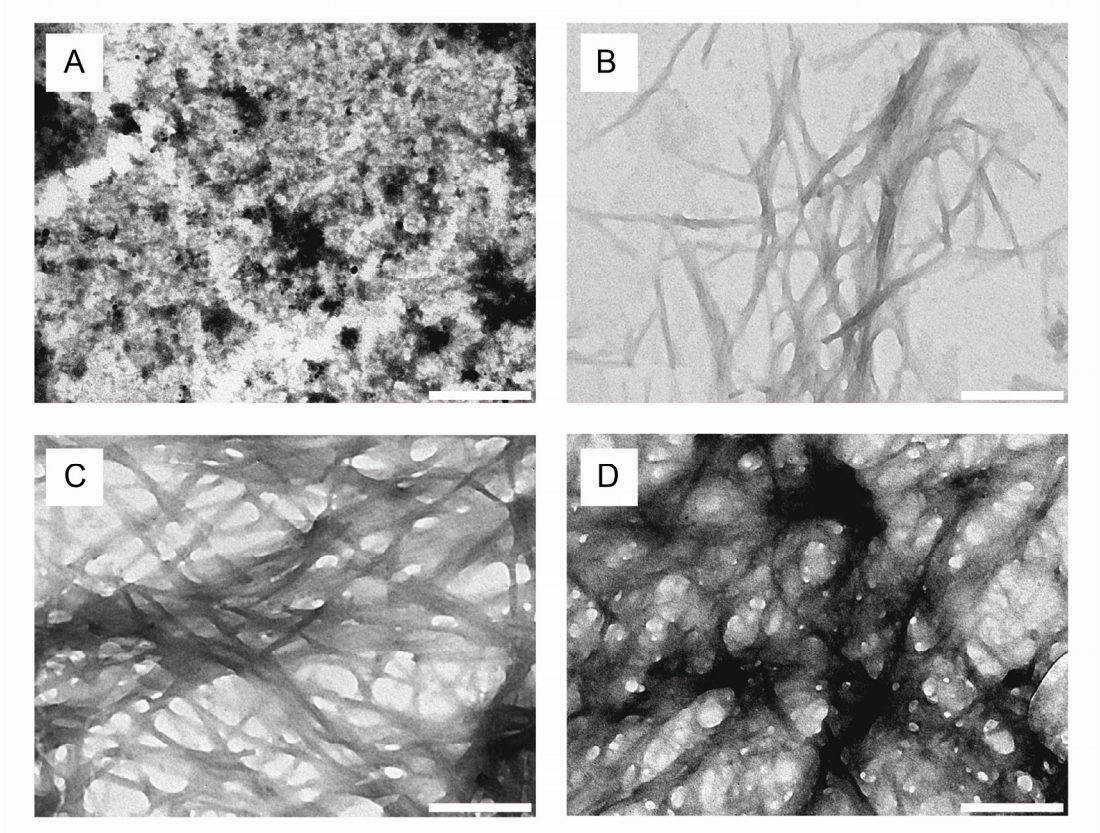

Figure 3.6. *TEM images of fibrils formed at A) pH 1.0, B) pH 1.5, C) pH 2.0, and D) pH 2.5. Scale bar is 0.5 μm.*

With regards to the effect of pH on fibril formation, Blundell *et al.* observed that below pH 2.0, insulin is mainly in its monomeric form, with increase in pH from here increasing the population of dimers (Blundell *et al*., 1971). It was seen that this increase in the population of dimers was coupled to a decrease in the tendency for fibrils to form, supporting the idea that fibril formation requires interaction between monomers (Whittingham *et al*., 2002). This is perhaps an explanation for the observed loss of the defined fibrillar structure at pH values above 2.0. Nielsen *et al*. formed insulin fibrils at pH 1.6, 3.0, and 7.4, and saw shorter lag times and faster growth at the more acidic pH values, although did not comment on the effect on fibril structure (Nielsen *et al*., 2001b).

3.3.3. Effect of native protein concentration

The effect of native protein concentration on fibril dimensions was investigated using concentrations of bovine insulin ranging from 0.5 mg/mL (87 μM) through to 5.8 mg/mL (1012 μM), (Conditions 5 and 9-14, **Table 3.1**). Fibril formation at each concentration was monitored by the ThT assay (**Figure 3.7**).

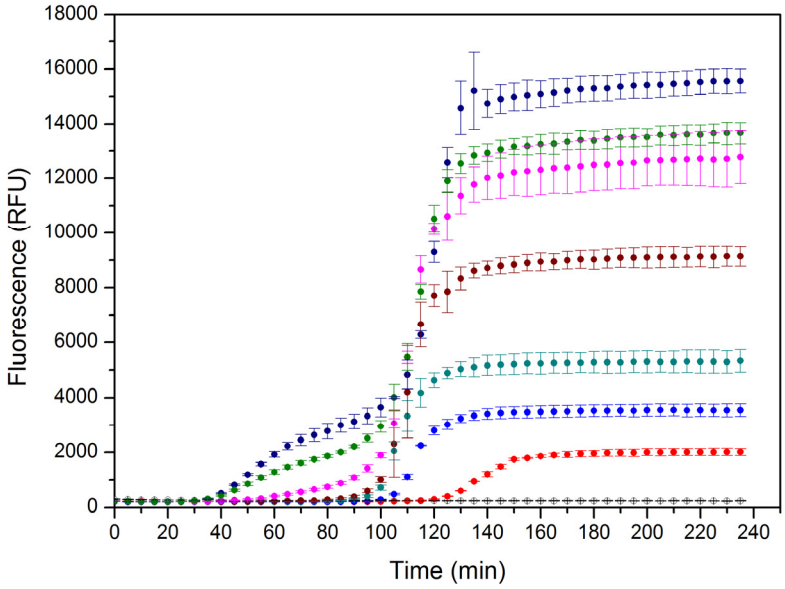

Figure 3.7. *Time profile of ThT fluorescence for bovine insulin at various concentrations incubated at 60 °C in fibril buffer, pH 1.6. The samples were: Control (black), 0.5 mg/mL (red), 1.0 mg/mL (blue), 2.0 mg/mL (cyan), 3.0 mg/mL (brown), 4.0 mg/mL (pink), 5.0 mg/mL (green), and 5.8 mg/mL (navy). Each reading represents an average of triplicate well readings, with the error bars representing standard error.*

Fibrils formed at all concentrations (**Figure 3.8**), with the ThT fluorescence values **(Figure 3.7** and **Figure 3.9)** showing more fibrils formed at the higher concentrations, an expected result based on previous work (Brange *et al*., 1997; Khurana *et al*., 2003; Mauro *et al*., 2007; Nielsen *et al*., 2001b).

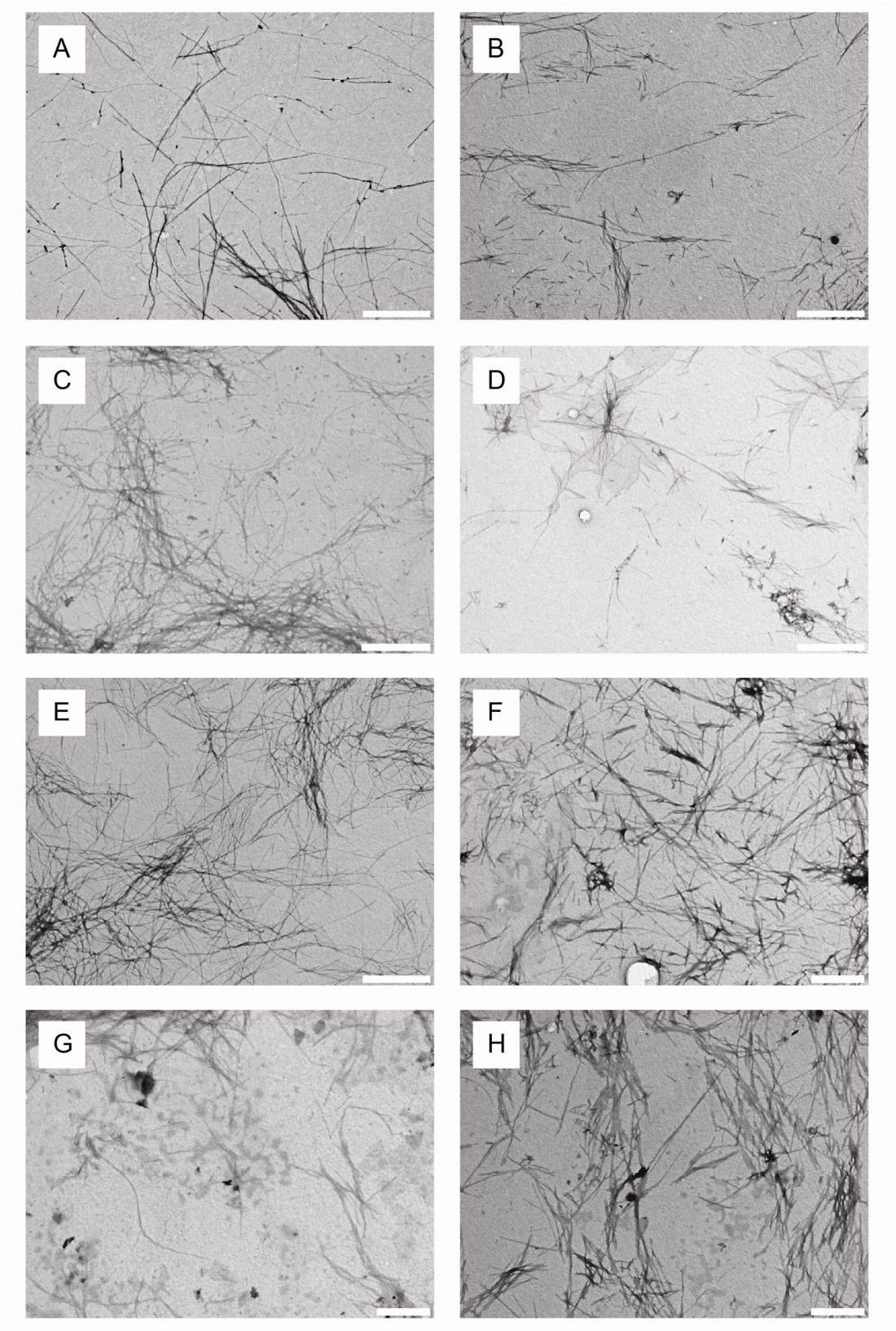

Figure 3.8. *TEM images of fibrils formed at: A) 0.5 mg/mL, B) 1.0 mg/mL, C) and D) 2.0 mg/mL, E) 3.0 mg/mL, F) 4.0 mg/mL, G) 5.0 mg/mL, and H) 5.8 mg/mL. Scale bars are 1 μm (A-E) and 0.5 μm (F-H).*

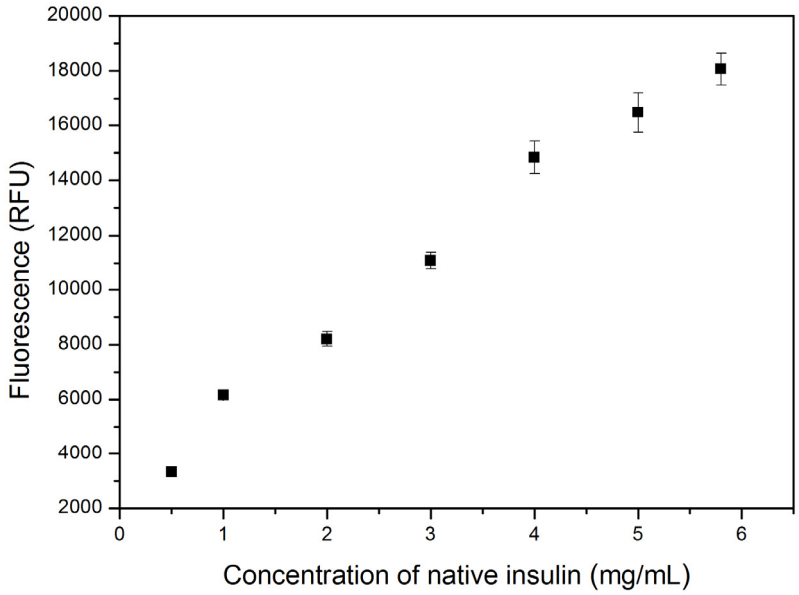

Figure 3.9. *Final ThT fluorescence (RFU) of insulin amyloid fibril samples formed at varying concentrations. Error bars show standard deviation of the mean from triplicate samples.*

It was observed that fibril length increased with decreasing native protein concentration, with fibrils formed at 0.5 mg/mL existing up to 6 μm in length (**Figure 3.10**, A), as opposed to those formed at 5.8 mg/mL, where the entire population of fibrils formed was under 2 μm in length (**Figure 3.10**, G). A plot of the average fibril length at differing native protein concentrations also reflects this trend, with a plateau reached around 2 mg/mL **(Figure 3.11)**, although with less variation observed than for range calculations, due to the previously mentioned existence of a large number of shorter species present at all growth concentrations which biases average length calculations.

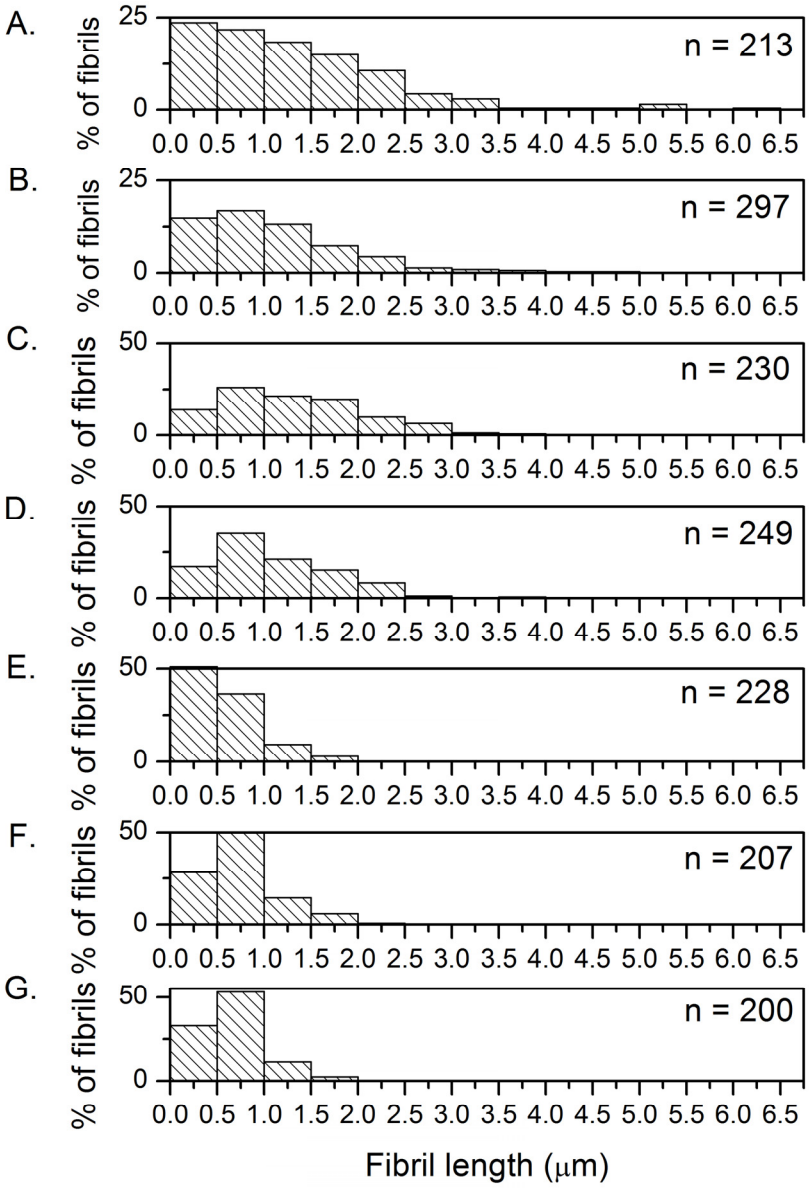

Figure 3.10. *Length distribution of insulin amyloid fibrils formed at A) 0.5 mg/mL, B) 1.0 mg/mL, C) 2.0 mg/mL, D) 3.0 mg/mL, E) 4.0 mg/mL, F) 5.0 mg/mL, and G) 5.8 mg/mL.*

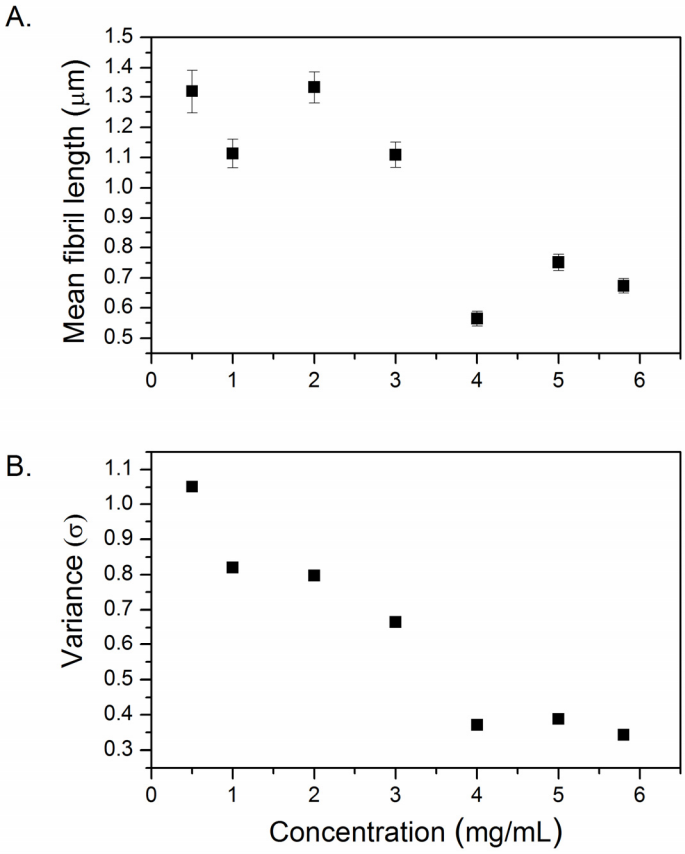

Figure 3.11. *A) Average lengths of insulin amyloid fibrils formed at varying concentrations. Error bars show uncertainty in the mean length (σ/√(n)) calculated from n samples. B) Variance of fibril samples formed at varying concentrations.*

The observation of increasing length with decreasing native protein concentration from the concentrations 5.8 mg/mL through to 0.5 mg/mL can be explained by the growth mechanism for insulin fibril formation. It has previously been observed that at low temperatures and concentrations, fibril nucleation (**Figure 3.1**, Steps 1-3) is inhibited while elongation (**Figure 3.1**, Step 4) continues on preformed fibrils (Mauro *et al*., 2007; Waugh, 1946), and this observation can be applied to these results. In terms of the native insulin that is to be converted to amyloid fibrils, a proportion forms fibril nuclei, a process thought to require the nearly simultaneous interaction of 3-4 insulin molecules (Waugh, 1957), and a proportion is added to the nuclei to elongate the fibrils. What appears to be occurring at the lower concentrations is that, because nuclei formation is less favourable (Waugh, 1946), the ratio of "nuclei forming insulin" to "elongating insulin" is in favour of elongating insulin, therefore longer fibrils are formed. This is also supported by **Figure 3.7**, which shows a longer lag time, the time in which nuclei are forming, for the low concentrations of native insulin. This has been well documented in the literature; for example, Brange *et al.* saw an increase in the rate of fibrillation with increasing insulin concentration (Brange *et al*., 1997). Nuclei formation is the slowest phase of fibrillation (Waugh, 1957), and this, therefore, supports the theory that at high concentration more nuclei are being formed and less elongation is occurring.

As previously stated, insulin fibrillation requires interaction between monomers and it has been shown that low protein concentration shifts the equilibrium of insulin toward smaller oligomers (Whittingham *et al*., 2002). This is another contributing factor for the observed length distribution.

Differences are observed in fibrils formed from different polypeptides (Gras, 2007), and other length studies of amyloid fibrils involving different native proteins corroborate this. Van Raaij *et al.,* in their study of α-synuclein fibrils, saw that fibril length increased with increasing native protein concentration (van Raaij *et al*., 2008), a study that was in agreement with a proposed statistical model by Van Gestel and De Leeuw (2006). The statistical model stated that two conditions must be met in order for the model to be applied: that the solution is dilute enough that the effects of interaggregate interactions may be neglected, and that the processes described by the model are reversible. The α-synuclein study met both of these conditions, with much lower concentrations used than our study (5-250 μM as opposed to the 174-1012 μM used in our study), and the knowledge that the different stages in the fibrillation process are reversible, whereas insulin fibrillation is normally not reversible without dramatic changes in the solvent environment (Brange *et al*., 1997).

The conflicting results observed with different native proteins demonstrate that it does not appear to be possible to apply results of length studies on fibrils formed from one protein to those formed from another.

3.3.4. Effect of storage conditions

Fibrils were formed using the standard conditions that had been adopted and then stored at room temperature, in refrigeration and frozen (Conditions 5, 15 and 16, **Table 3.1**). The effect of freezing on fibril dimensions was further examined by increasing the freeze/thaw cycles to which the fibrils were subjected (Condition 17, **Table 3.1**).

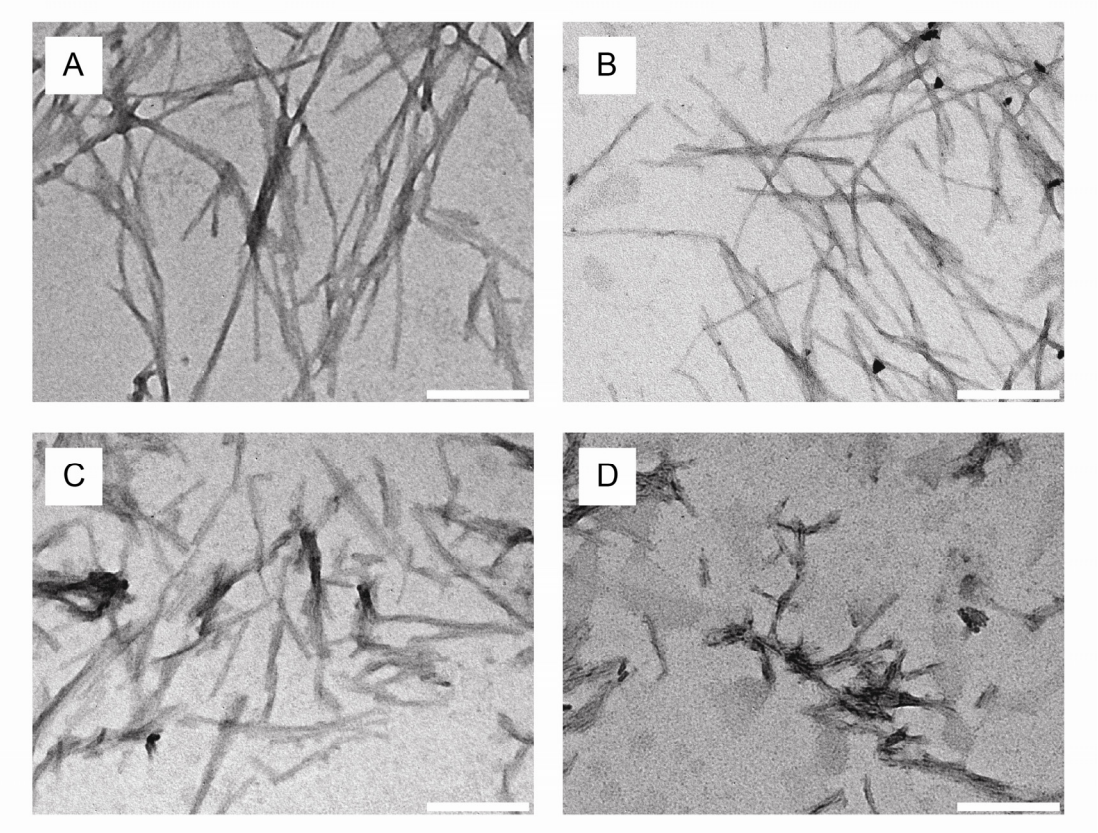

Figure 3.12. *TEM images of fibrils subjected to various storage conditions. A) Room temperature, B) Refrigeration, C) Freeze/thaw x 1, and D) Freeze/thaw x 2. Scale bar is 0.2 μm.*

Fibrils stored at room temperature had a longer average length (0.68 μm) than both those that were refrigerated (0.57 μm) and frozen (0.29 μm), with freezing and then thawing resulting in fibrils of less than half the average length (**Table 3.2**). This decrease in length upon freezing is also evident from the histograms constructed from these samples **(Figure 3.13)**. When the number of freeze thaw cycles was increased to two, the fibrils became even shorter (0.15 μm).

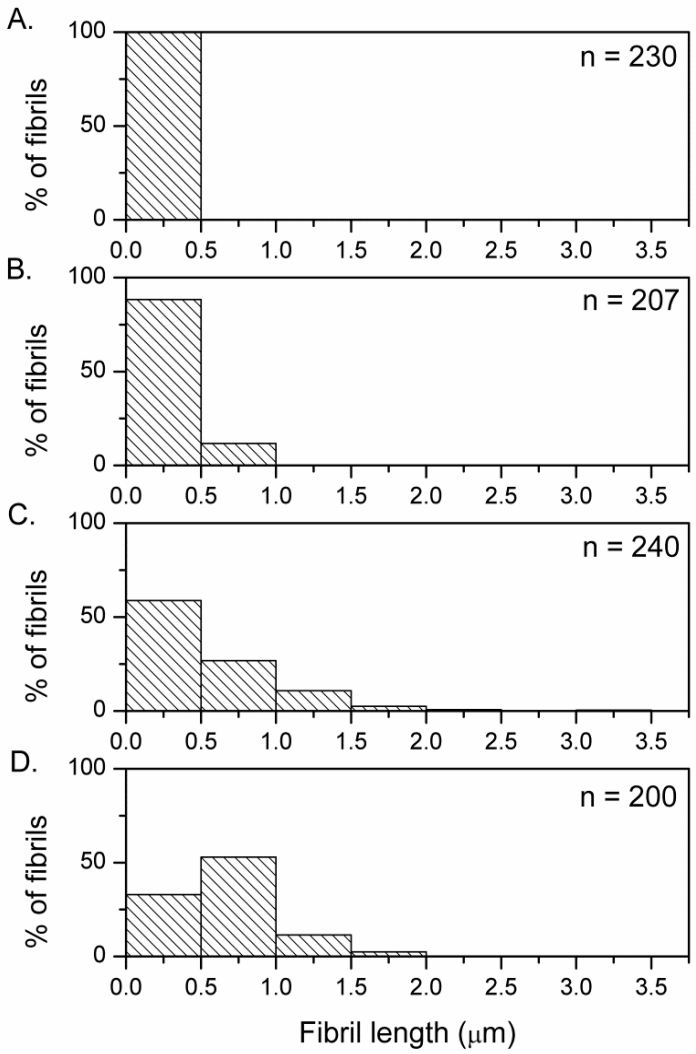

Figure 3.13. *Length distribution of insulin amyloid fibrils stored at A) Freeze/thaw x2, B) Freeze/thaw x1, C) Refrigeration, and D) Room temperature.*

ThT readings were taken of all samples to ensure that the β-sheet structure of the fibrils was still intact and that the freeze thawing had not degraded the fibrils **(Figure 3.14)**. The ThT values in fact increased with successive freeze thaw cycles, presumably due to the smaller fragments being more soluble and therefore resulting in a higher measurable concentration of bound dye in solution.

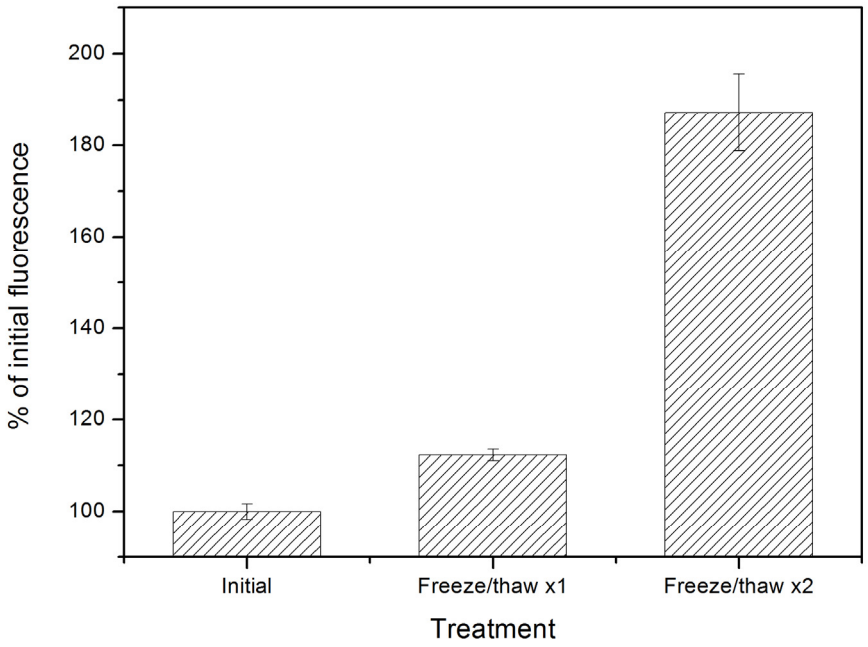

Figure 3.14. *ThT fluorescence of insulin amyloid fibril sample before and after freeze/thaw cycles. Fluorescence is shown as a percent of the initial fluorescence of the sample. Error bars show standard deviation of the mean from triplicate samples.*

Storage condition was seen to influence the resulting length of preformed fibrils, with room temperature being the ideal storage temperature to maintain fibril integrity, as refrigeration and freezing caused a decrease in fibril length due to fracturing. This decrease in length seen with altered storage conditions is also interesting in light of recent literature where these fragmented fibrils have been identified to have different behaviour than the intact mature fibril. Fibril fragments may have increased cytotoxicity, but have been shown to increase the efficiency of new fibril growth by seeding as well as having increased ability to disrupt liposome membranes – offering potentially new or enhanced biological properties (Xue *et al*., 2009a). It is also known that the presence of fibril fragments increases the rate of new fibrillogenesis (Xue *et al*., 2009a), meaning that fibril fragments produced through freeze-thaw cycles could be used as fibril seeds.

3.4. Effect of growth and storage conditions on bovine insulin amyloid fibril diameter

The effect of growth/storage conditions on the diameter of amyloid fibrils formed from bovine insulin was examined using AFM (Section 7.10.3). AFM measures the topography of a sample, and so it is height that is being measured. For this study it was assumed that fibril height is equivalent to diameter. Measurements were taken for samples formed under Conditions 5, 9, and 17 (**Table 3.1**), chosen as they were the "standard" growth condition, and conditions that gave the longest and shortest fibrils respectively. The change in growth and storage condition had no effect on the diameter of fibrils formed, with fibrils from all three conditions having an average diameter of 7.9 ± 2.2 nm (**Table 3.3**). A representative AFM image is shown in **Figure 3.15**.

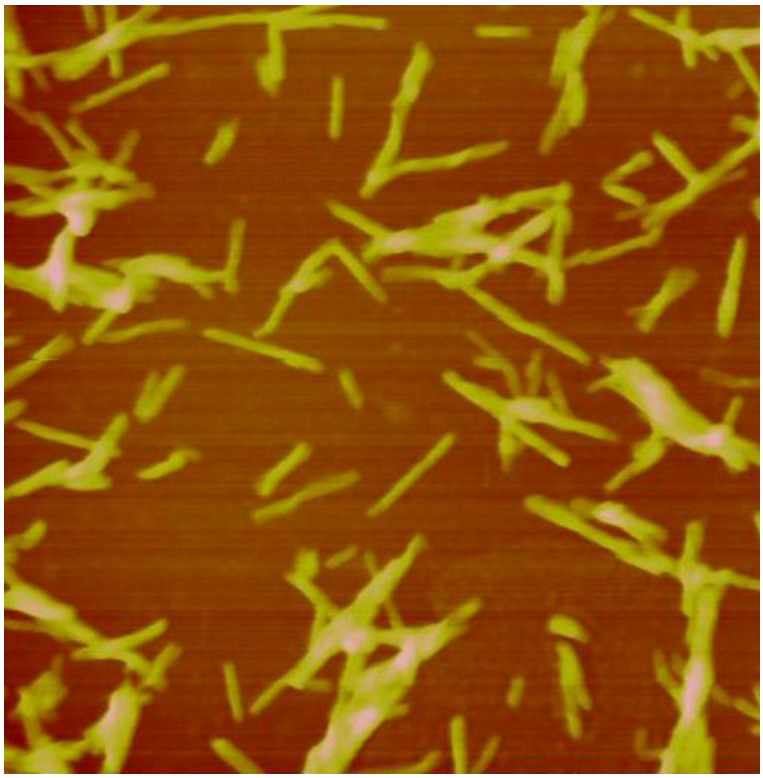

Figure 3.15. *Representative AFM image, as used for measurement of fibril diameter. AFM was operating in tapping mode. Scan size is 1 μm by 1 μm.*

The fibril diameters measured by AFM were shown not to be effected by growth or storage condition, with diameters of all fibrils formed within the expected diameter of insulin amyloid fibrils of 7-10 nm (Jimenez *et al*., 2002). This result was also seen in the study by Xue *et al*., (2009b), where they showed there to be no significant length dependence of fibril diameter.

Table 3.3. *Average fibril diameter and range for bovine insulin fibrils formed under different growth conditions*[*].

Sample number**	**Fibril diameter**	
	Mean (µm)	**Range (µm)**
5 ("standard")	7.5 ± 1.4	4.3-8.9
9 (longest)	8.4 ± 3.1	2.9-14.4
17 (shortest)	7.8 ± 1.5	5.6-11.9

** Average diameters and ranges only calculated for three samples, see detail in text. For each sample diameters of at least 50 fibrils were measured, with three diameter measurements taken along the length of each fibril.*

*** See Table 3.1 for details of sample conditions*

3.5. Effect of growth and storage conditions on dimensions of crystallin amyloid fibrils

The conditions that gave the shortest and longest fibrils, namely, freeze-thaw cycles and low concentration respectively, were then applied to the crystallin fibril system, to investigate whether the same trend in fibril length was observed. Amyloid fibrils were formed from crude crystallin proteins using the "standard" conditions established in-house to maximise fibril yield (Section 7.4.2) (Garvey *et al*., 2009) (Condition 18, **Table 3.4**), and also with the native protein concentration lowered by the same amount, relative to the "standard" protein concentration, as the concentration which resulted in the longest bovine insulin fibrils (Condition 9, Table 3.1). This meant that crystallin fibrils were then formed at 0.9 mg/mL (Condition 19, **Table 3.4**). Crystallin amyloid fibrils, formed under the "standard" conditions were also subjected to freeze/thaw cycles, after exchanging the solvent for water to allow freezing (Condition 20, **Table 3.4**). These conditions are detailed in **Table 3.4**.

Table 3.4. *Detail of the different growth and storage conditions used for the crystallin amyloid fibril samples.*

Sample #	Growth concentration (mg/mL)	Growth temperature (°C)	Buffer	Growth time	Storage conditions
18	10	60	25 % n-propanol, pH 3.8	3 days	Room temp.
19	0.9				Room temp.
20	10				Freeze/thaw x2
21*	10				Sonicated
22*	10			5 months	Room temp.

* These conditions were carried out by J. Raynes and J. Healy (21 and 22 respectively with TEM images kindly provided (Healy *et al*., 2012; Raynes, 2012).

The fibrils formed from each of these conditions were then visualised by TEM (Section 7.5). Representative TEM images are shown in **Figure 3.16**. Fibrils formed from the standard conditions existed in a very dense network (**Figure 3.16**, A and B), which meant that it was not possible to accurately construct full length distributions, as it was too difficult to discern individual fibrils. The same was true for the fibrils formed at the lower concentration, although a less dense network was observed (**Figure 3.16**, C and D). Subjecting crystallin fibrils to freeze/thaw cycles did seem to have some effect on fibril length, with a number of fragmented fibrils observed (**Figure 3.16**, E); however, this process was not nearly as efficient for crystallin fibrils as it was for insulin fibrils, as a proportion of the fibrils in the sample remained unchanged (**Figure 3.16**, F).

Previous work carried out in our lab by Jared Raynes has shown sonication of crystallin fibrils to be an effective method of producing fibril fragments (**Figure 3.17**, A and B). Compared with freeze-thaw cycles, sonication appears to give the most homogenous distribution. These fragments can then be used as seeds to promote fibril formation or in other applications where short fibrils are desirable. Other work by Jackie Healy has shown that over time association between individual crystallin fibrils increases, resulting in the formation of higher order structures (**Figure 3.17**, C and D). **Figure 3.17**, C shows a representative image of crystallin fibrils after 3 days of growth, which are approximately 10-20 nm wide, and then when imaged again after five months of growth 200 nm thick bundles were observed (**Figure 3.17**, D) (Healy *et al*., 2012).

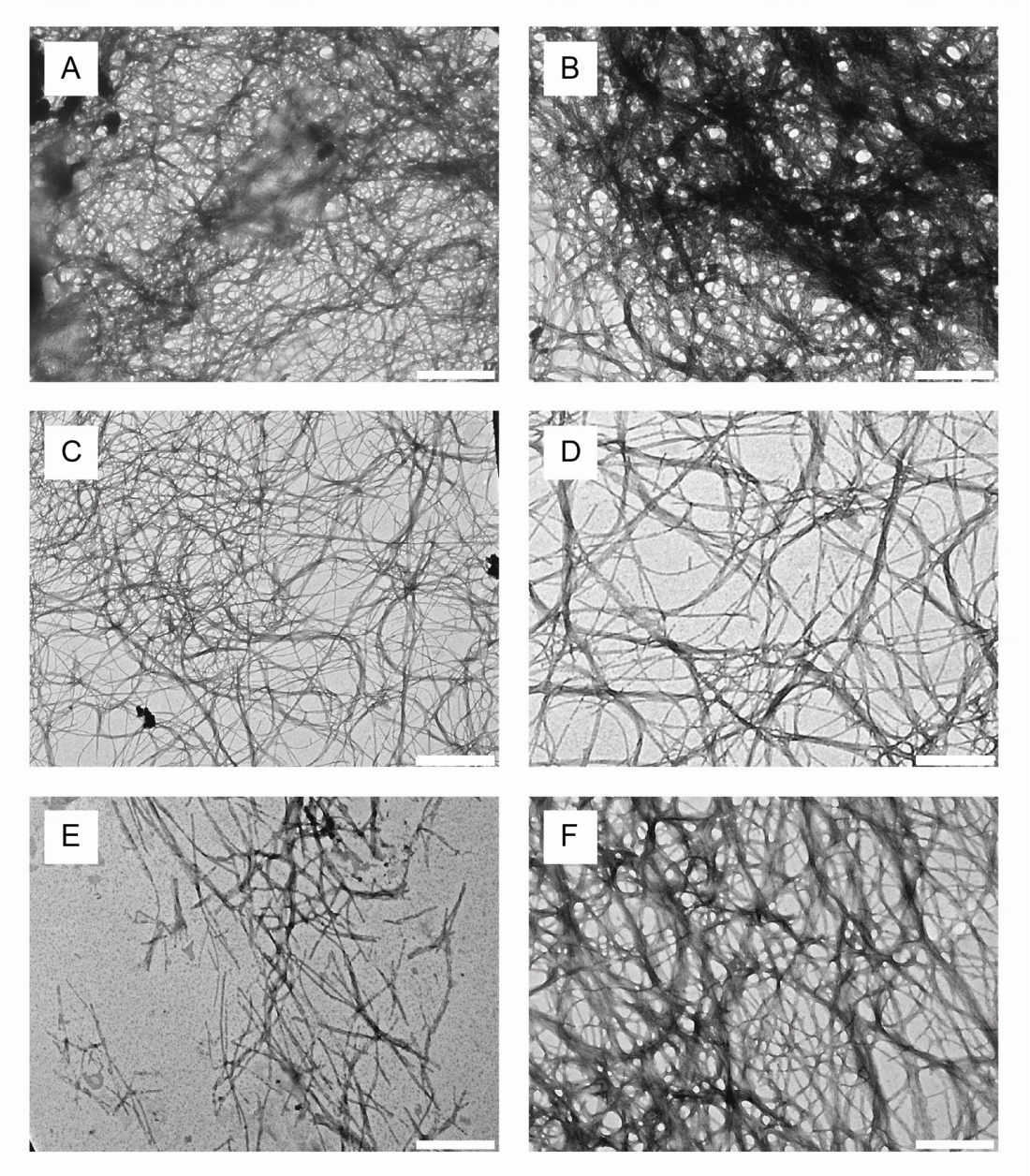

Figure 3.16. *Representative TEM images of crystallin fibrils formed under standard conditions (A & B), low concentration (C & D), and those subjected to freeze/thaw cycles (E & F). Scale bars are 1 μm (A & C) and 0.5 μm (B, D, E & F).*

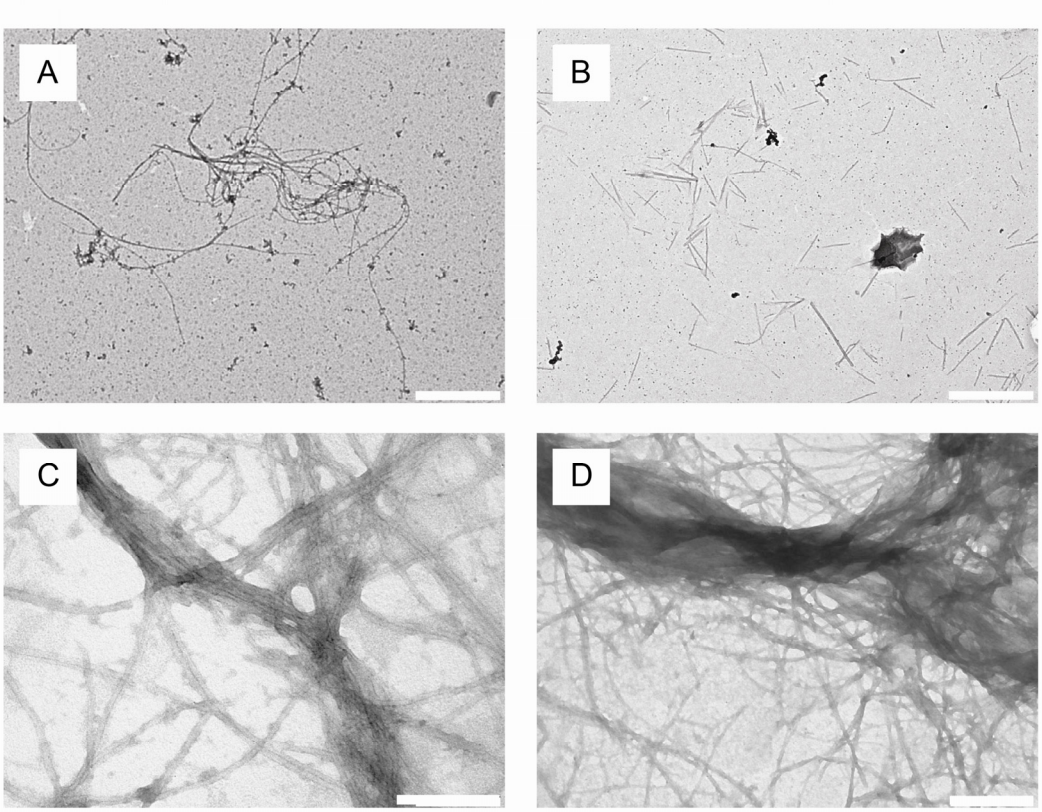

3.6.

Figure 3.17. *A & B) Representative TEM images of crystallin fibrils before (A) and after (B), sonication (Raynes, 2012). C & D) Representative TEM images of crystallin fibrils taken after 3 days of growth (C), and after 5 months (D) (Healy et al., 2012). Scale bars*

These results indicated that it is unlikely to be possible to apply the same "length-controlling" conditions to different fibril systems, as was touched on previously when discussing the discrepancies seen when comparing results from the control of insulin fibril length in this study, to literature studies involving other fibril systems. It also raises the issue of the methods used to investigate fibril length. The majority of studies on fibril length use microscopy, such as TEM and AFM, to construct length distributions. As well as difficulties encountered such as those in this study, where the density of the network did not allow full length characterisation, there are other disadvantages associated with the use of these techniques in this way. AFM and TEM are often time consuming, and as the fibrils are in the dry state on a solid support, are not necessarily representative of the dispersion of fibrils in a suspension.

Preliminary work has been carried out using the qNano particle analyser (Izon, NZ) to construct length distributions of crystallin fibrils using resistive pulse sensing (Appendix B). Further work using this tool will hopefully result not only in characterisation of fibril length, but also of the concentration of fibrils in solution. With the right fibril system, it may also be possible to monitor the formation of fibrils in real time.

3.7. Summary

Length distributions of amyloid fibrils formed from bovine insulin were examined under different growth temperatures, pH, protein concentrations, and storage conditions. A range of fibril lengths were achieved, from very small fibril fragments resulting from freeze thaw cycles, through to fibrils of several microns long formed by lowering the growth concentration. At all of the conditions examined a range of fibril lengths still exist, due to the nature of the fibrillation mechanism. However, it has been shown that a range of average lengths and length distributions are achievable, by simply altering growth and storage conditions, and this finding takes us a step further towards control over dimensions. When the same set of conditions were applied to amyloid fibrils formed from crude fish crystallins, the same trends in fibril length were not necessarily observed, indicating that although there is a common fibril formation pathway, the resulting structures have properties that differ between fibril systems. However, other methods have shown to be effective in producing a range of crystallin fibril sizes. The ability to provide some degree of homogeneity in these structures offers the opportunity to explore length dependent properties, as well as providing guidelines where fibrils of particular length distribution are wanted.

3.8. References

Blundell T, Cutfield J, Cutfield S, Dodson E, Dodson G, Hodgkin D, Mercola D, Vijayan M. 1971. Atomic positions in rhombohedral 2-zinc insulin crystals. *Nature* **231**:506–511.

Brange J, Andersen L, Laursen E, Meyn G, Rasmussen E. 1997. Toward understanding insulin fibrillation. *Journal of Pharmaceutical Sciences* **86**:517–525.

Chiti F, Dobson C. 2006. Protein misfolding, functional amyloid, and human disease. *Annual Review of Biochemistry* **75**:333–366.

Domigan L, Healy J, Meade S, Blaikie R, Gerrard J. 2011. Controlling the dimensions of amyloid fibrils: Towards homogenous components for bionanotechnology. *Biopolymers* **97**:123–133.

Garvey M, Gras S, Meehan S, Meade S, Carver J, Gerrard J. 2009. Protein nanofibres of defined morphology prepared from mixtures of crude crystallins. *International Journal of Nanotechnology* **6**:258–273.

Van Gestel J, De Leeuw S. 2006. A statistical-mechanical theory of fibril formation in dilute protein solutions. *Biophysical Journal* **90**:3134–3145.

Gras S. 2007. Amyloid fibrils: From disease to design. New biomaterial applications for self-assembling cross-β fibrils. *Australian Journal of Chemistry* **60**:333–342.

Healy J, Wong K, Roux C, Domigan L, Sunde M, Sawyer E, Gras S, Gerrard J, Vadudevamurthy M. 2012. Polymorphism and higher ordered structures of protein nanofibers from crude mixtures of fish lens crystallins: Towards useful materials. *Biopolymers*:Accepted.

Humblet-Hua N, Sagis L, van der Linden E. 2008. Effects of flow on hen egg white lysozyme (HEWL) fibril formation: length distribution, flexibility, and kinetics. *Journal of Agricultural and Food Chemistry* **56**:11875–11882.

Jansen R, Dzwolak W, Winter R. 2005. Amyloidogenic self-assembly of insulin aggregates probed by high resolution atomic force microscopy. *Biophysical Journal* **88**:1344–1353.

Jimenez J, Nettleton E, Bouchard M, Robinson C, Dobson C, Saibil H. 2002. The protofilament structure of insulin amyloid fibrils. *Proceedings of the National Academy of Sciences of the United States of America* **99**:9196–9201.

Khurana R, Ionescu-Zanetti C, Pope M, Li J, Nielson L, Ramírez-Alvarado M, Regan L, Fink A, Carter S. 2003. A general model for amyloid fibril assembly based on morphological studies using atomic force microscopy. *Biophysical Journal* **85**:1135–1144.

Krebs M, MacPhee C, Miller A, Dunlop I, Dobson C, Donald A. 2004. The formation of spherulites by amyloid fibrils of bovine insulin. *Proceedings of the National Academy of Sciences of the United States of America* **101**:14420–14424.

Langkilde A, Vestergaard B. 2009. Methods for structural characterization of prefibrillar intermediates and amyloid fibrils. *FEBS Letters* **583**:2600–26091.

Mauro M, Craparo E, Podesta A, Bulone D, Carrotta R, Martorana V, Tiana G, San Biagio P. 2007. Kinetics of different processes in human insulin amyloid formation. *Journal of Molecular Biology* **366**:258–274.

Naiki H, Higuchi K, Hosokawa M, Takeda T. 1989. Fluorometric determination of amyloid fibrils in vitro using the fluorescent dye, thioflavin T. *Analytical Biochemistry* **177**:244–249.

Nielsen L, Frokjaer S, Carpenter J, Brange J. 2001a. Studies of the structure of insulin fibrils by Fourier transform infrared (FTIR) spectroscopy and electron microscopy. *Journal of Pharmaceutical Sciences* **90**:29–37.

Nielsen L, Khurana R, Coats A, Frokjaer S, Brange J, Vyas S, Uversky V, Fink A. 2001b. Effect of environmental factors on the kinetics of insulin fibril formation: elucidation of the molecular mechanism. *Biochemistry* **40**:6036–6046.

Petkova A, Leapman R, Guo Z, Yau W-M, Mattson M, Tycko R. 2005. Self-propagating, molecular-level polymorphism in Alzheimer's β-amyloid fibrils. *Science* **307**:262–265.

van Raaij M, van Gestel J, Segers-Nolten I, de Leeuw S, Subramaniam V. 2008. Concentration dependence of α-synuclein fibril length assessed by quantitative atomic force microscopy and statistical-mechanical theory. *Biophysical Journal* **95**:4871–4878.

Rao S. 2008. Amyloid fibrils in bionanomaterials. PhD Thesis; University of Canterbury.

Raynes J. 2012. Immobilising biomolecules on amyloid fibrils for bionanotechnological applications. PhD Thesis; University of Canterbury.

Rogers S, Venema P, van der Ploeg J, Sagis L, Donald A, van der Linden E. 2005a. Electric birefringence study of an amyloid fibril system: The short end of the length distribution. *European Physical Journal* **18**:207–217.

Rogers S, Venema P, Sagis L, van der Linden E, Donald A. 2005b. Measuring the length distribution of a fibril system: A flow birefringence technique applied to amyloid fibrils. *Macromolecules* **38**:2948–2958.

Sabaté R, Lascu I, Saupe S. 2008. On the binding of thioflavin-T to HET-s amyloid fibrils assembled at pH 2. *Journal of Structural Biology* **162**:387–396.

Thirumalai D, Klimov D, Dima R. 2003. Emerging ideas on the molecular basis of protein and peptide aggregation. *Current Opinion in Structural Biology* **13**:146–159.

Waterhouse S, Gerrard J. 2004. Amyloid fibrils in bionanotechnology. *Australian Journal of Chemistry* **57**:519–523.

Waugh D. 1946. A fibrous modification of insulin. I. The heat precipitate of insulin. *Journal of the American Chemical Society* **68**:247–250.

Waugh D. 1957. A mechanism for the formation of fibrils from protein molecules. *Journal of Cellular and Comparative Physiology* **49**:145–164.

Whittingham J, Scott D, Chance K, Wilson A, Finch J, Brange J, Dodson G. 2002. Insulin at pH 2: Structural analysis of the conditions promoting insulin fibre formation. *Journal of Molecular Biology* **318**:479–490.

Xue W, Hellewell A, Gosal W, Homans S, Hewitt E, Radford S. 2009a. Fibril fragmentation enhances amyloid cytotoxicity. *Journal of Biological Chemistry* **284**:34272–34282.

Xue W, Homans S, Radford S. 2009b. Amyloid fibril length distribution quantified by atomic force microscopy single-particle image analysis. *Protein Engineering, Design and Selection* **22**:489–496.

4. Chapter Four

Electrical properties and manipulation of amyloid fibrils

4.1. Introduction

The electrical properties of unmodified amyloid fibrils formed from bovine insulin, fish eye crystallins, and fungal hydrophobins had not been previously investigated. Network measurements are commonly used for investigation into the conductive properties of fibres (Liu *et al*., 2009; Malvankar *et al*., 2011; del Mercato *et al*., 2007), and for this study, methods based upon those of del Mercato *et al*. were initially used. del Mercato *et al*. used interdigitated electrodes to study the electrical conduction of "amyloid-like" fibrils formed from the elastin-related polypeptide, poly(ValGlyGlyLeuGly), finding that they were weak conductors. This chapter presents electrical characterisation, via network measurements, for all three aforementioned fibril systems.

As many biological nanowires are seen to have low conductivity in their unmodified state (Storm *et al*., 2001), biological structures have been used as a scaffold for the formation of more highly conductive nanowires, via modification with metals (Bai *et al*., 2009; Braun *et al*., 1998; Ford *et al*., 2001; Patolsky *et al*., 2002; Patolsky *et al*., 2004), or, as is the case in this study, conducting polymers (Hamedi *et al*., 2008; Herland *et al*., 2008; Nickels *et al*., 2004; Niu *et al*., 2007a; Niu *et al*., 2007b). This chapter also assesses the level to which modification of bovine insulin amyloid fibrils by the conducting polymers, polypyrrole and polyaniline, increases conductivity.

In addition to network measurements, it is also desirable to carry out electrical characterisation on single or small numbers of isolated fibrils (Castillo *et al*., 2008). The technique of dielectrophoresis was used to isolate small numbers of crystallin amyloid fibrils between electrode pairs. Once immobilised, electrical properties of the crystallin amyloid fibrils were able to be examined, and these measurements compared to network measurements, as well as theoretical calculations of conductivity.

4.2. Conductive properties of amyloid fibril networks

The conductive properties of amyloid fibril networks formed from a) bovine insulin, b) fish eye crystallins, and c) fungal hydrophobins, were examined by deposition of amyloid fibrils onto gold interdigitated electrodes that were fabricated by photolithography, and subsequent measurement of the current-voltage (I-V) characteristics of the networks.

4.3. Fabrication of microelectrodes

The microelectrodes used to examine the conductive properties of amyloid fibril networks were fabricated via the process of optical lithography. Lithography is defined as “the process of transferring patterns of geometric shapes on a mask to a thin layer of radiation-sensitive material (called resist) covering the surface of a semi-conductor wafer” (Sze, 2002). To then produce permanent features on a semi-conductor wafer, in this case, an array of gold microelectrodes, these resist patterns must be transferred again to the layers comprising the device, and this is accomplished by selectively removing unmasked portions of a layer. Optical lithography involves the use of ultraviolet (UV) light.

4.3.1. Mask design and fabrication

The first step in mask making is to use a computer-aided design (CAD) system to completely describe the desired circuit pattern. The CAD system then drives the pattern generation, an optical or electron beam lithographic system that transfers patterns to the electron-sensitised mask (Sze, 2002). Photomasks can be either positive or negative masks, meaning that the pattern on the mask is either the pattern desired on the substrate or the inverse, respectively.

A positive photomask was created for the fabrication of the microelectodes, with nine different electrode designs transferred to the mask (Section 7.11.1). The nine designs had variation in electrode width (EW), electrode gap size (EG), spacing between electrode pairs (ES), and number of electrode pairs (EP) (**Table 4.1**). Each interdigitated electrode layout also required a landing space (LS) of sufficient size to enable the needles of the probe station to make contact with the electrodes, this was 200 μm^2 in all designs. In all designs the electrodes were 400 μm in length.

Table 4.1. *Detail of the nine electrode designs (A-I) transferred to the photomask for the fabrication of interdigitated microelectrodes. The designs vary in electrode width (EW), gap size (EG), spacing between electrode pairs (ES), and number of pairs (EP).*

Design	EW (μm)	EG (μm)	ES (μm)	EP (μm)
A	3	3	3	16
B	3	2	2	19
C	3	5	5	12
D	6	3	3	16
E	3	3	3	4
F	6	3	N/A	1
G	6	3	18	6
H	3	3	21	6
I	3	4	4	13

The process for the transfer of the mask design to the mask is shown schematically in **Figure 4.1**. The mask material used consisted of soda lime glass coated with low reflective chrome onto which a layer of positive photoresist was applied (**Figure 4.1**, A). The designs detailed in **Table 4.1** were transferred to the layer of positive photoresist using a mask-writer, with the exposed portions of photoresist removed using developer. The unprotected chrome region is then removed via etching, and the remainder of the photoresist then removed with acetone (**Figure 4.1**, B). This process results in the creation of a positive photomask.

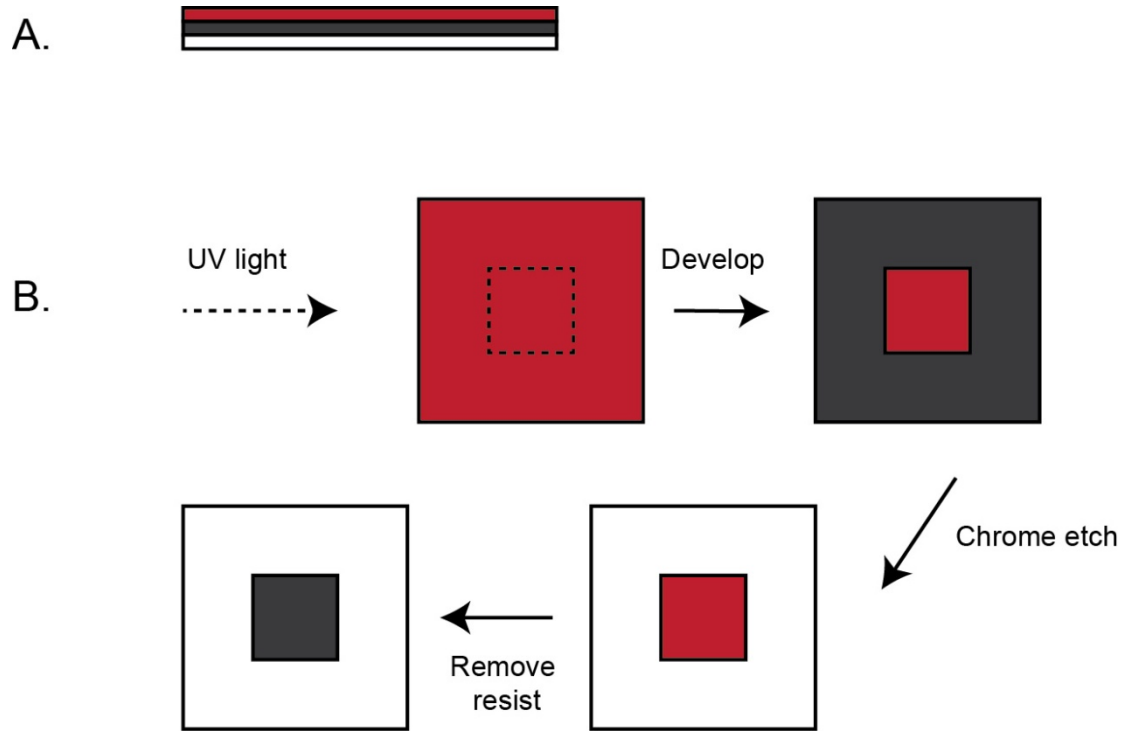

Figure 4.1. *Schematic showing the procedure for mask manufacture. The mask material (A), consists of soda lime glass (white) coated with low reflective chrome (dark grey), over which a layer of positive photoresist is applied (maroon). The desired pattern is transferred to the mask via the procedure shown in B. Firstly, a mask-writer transfers the desired pattern onto the photoresist using UV light, which is then removed using developer. The chrome is then removed using chrome etch, and lastly, the remainder of the photoresist is removed using acetone.*

4.3.2. Pattern transfer

In order to create an array of gold interdigitated electrodes, a layer of gold, with a nichrome adhesion layer, was deposited via evaporation onto a silicon oxide wafer (Section 7.11.2). To this wafer, a layer of positive photoresist is then applied, and the patterns from the mask fabricated in Section 4.3.1 were then transferred using a mask aligner (Section 7.11.3). The exposed photoresist was then removed with developer and the exposed gold and nichrome removed via etching. The final result was a microchip containing arrays of interdigitated gold electrodes on an insulating silicon oxide wafer as shown in **Figure 4.2**. The photolithography process described above is shown schematically in **Figure 4.3**.

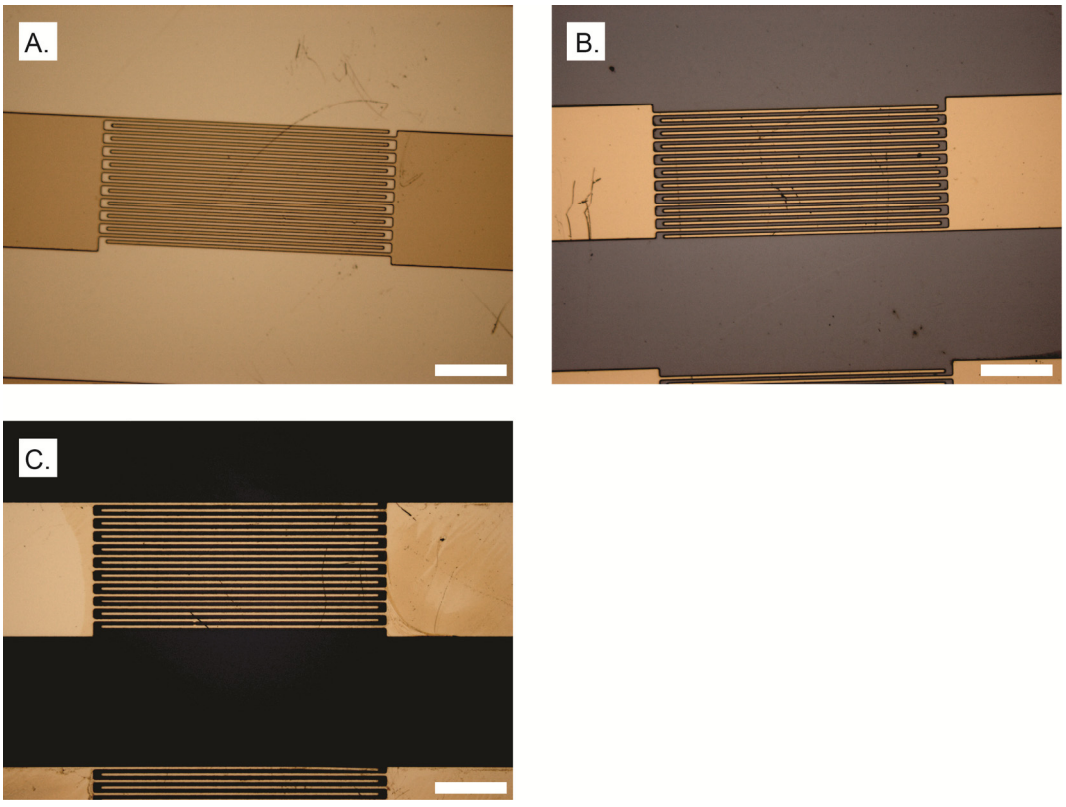

Figure 4.2. *Optical microscopy images of interdigitated gold electrodes fabricated by optical lithography shown after the development of photoresist (A), after the removal of gold by etching (B), and finally, after the removal of the nichrome adhesion layer by etching (C). Scale bars are 100 μm..*

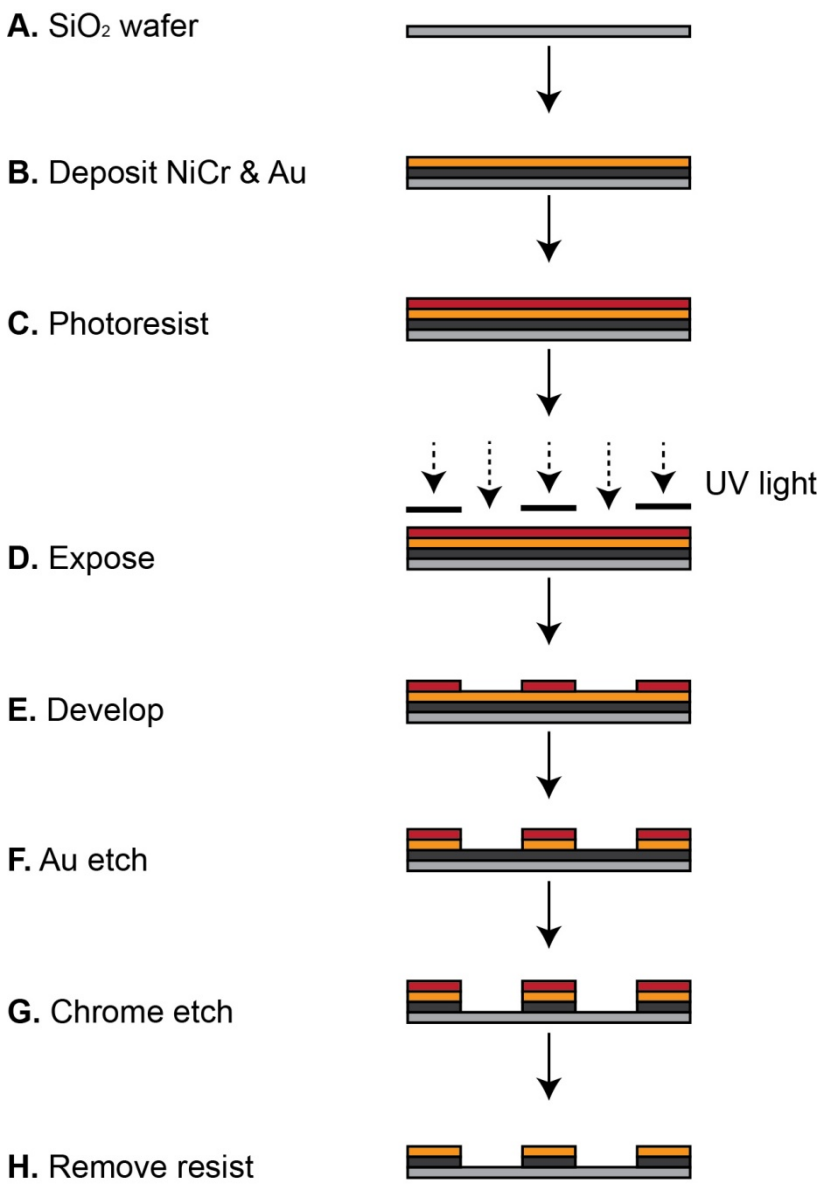

Figure 4.3. *Schematic showing the photolithographic process used for the fabrication of gold microelectrodes. A) A silicon oxide wafer. B) Gold and nichrome are deposited onto the silicon oxide wafer via evaporation. C) A layer of positive photoresist is spun onto the wafer. D) The pattern from the mask is transferred to the photoresist using a mask aligner, with UV light exposing the portions photoresist not masked. E) The exposed photoresist is removed with developer. F) and G) The gold and nichrome are removed via etching. H) The remaining photoresist is removed.*

4.4. Bovine insulin fibrils

For conductivity measurements, bovine insulin amyloid fibrils were formed under the conditions at which the average length of fibrils reached a maximum, with the exception of the removal of salt (Section 7.12). Bovine insulin amyloid fibrils formed under these conditions are shown in **Figure 4.4**. For these experiments it was desirable to have long fibrils, as even though the amyloid fibrils exist in a network environment as opposed to isolated fibrils, the existence of amyloid fibrils of maximum length increases the likelihood of good contacts between the interdigitated electrodes. The importance of good protein-electrode contacts has been previously noted (del Mercato *et al*., 2007).

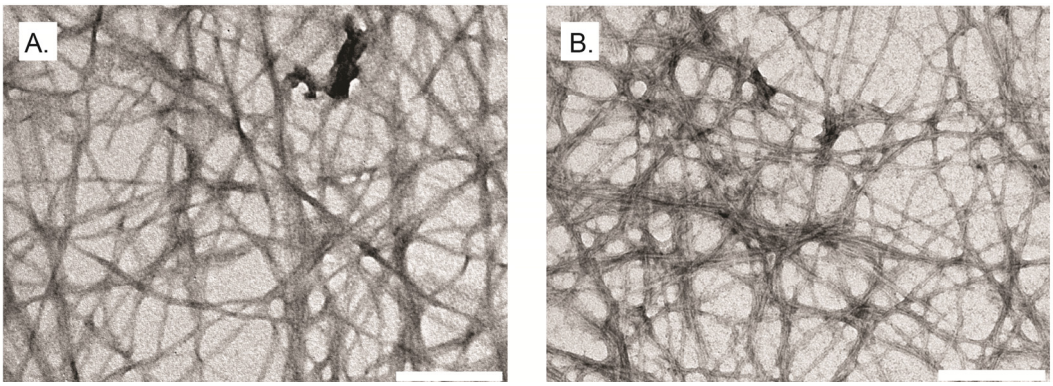

Figure 4.4. *TEM images showing bovine insulin amyloid fibrils formed under the conditions that were found in Chapter 3 to give the maximum average fibril length (A), and fibrils formed under this same condition with the exception of the removal of salt (B). Scale bar is 0.2 μm.*

Salt was removed in order to eliminate its potential impact on conductivity measurements, which meant fibrils were formed in pH adjusted nanopure water, which would have only had very low salt present from the protein and pH adjustment. This was seen to have minimal effect on fibril growth or morphology (**Figure 4.4**, A), as compared to those grown under the same conditions with salt present (**Figure 4.4**, B). A similar length distribution is also seen for those fibrils grown in the absence of salt as shown in **Figure 4.5**, with the average fibril length 1.19 μm, as compared to 1.33 μm for those growth with salt present (**Table 4.2**) In the experiments of del Mercato *et al*., fibrils were also formed in nanopure water (del Mercato *et al*., 2007).

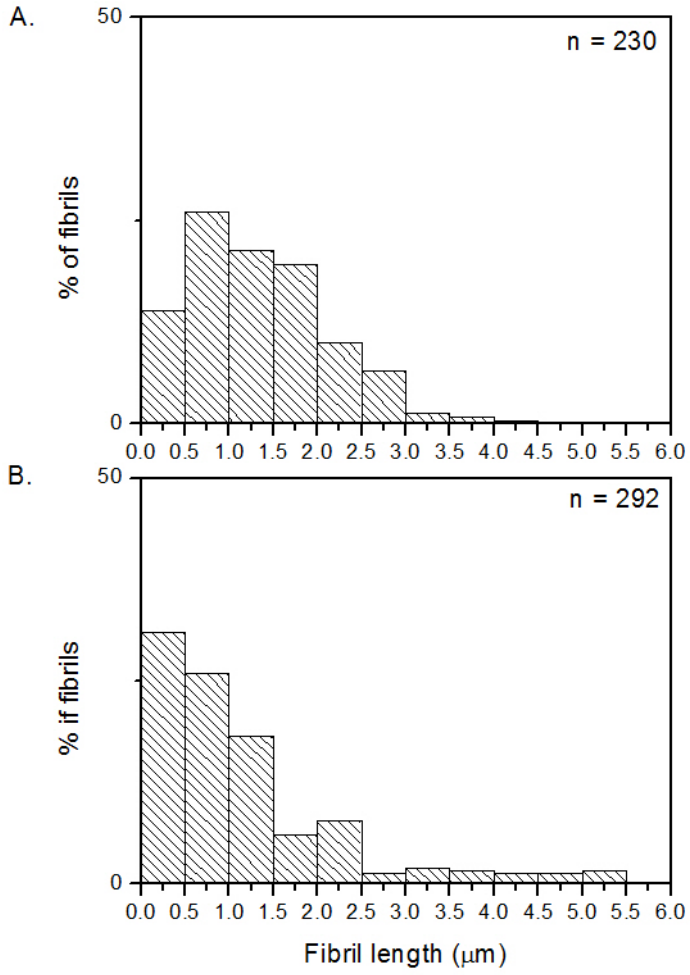

Figure 4.5. *Length distribution of bovine insulin amyloid fibrils formed in the presence (A), and absence (B), of salt.*

Table 4.2. *Average fibril length and range for bovine insulin fibrils formed in the presence and absence of salt.*

Growth conditions	Sample size (n)	Average fibril length (μm)	Range (μm)
Salt present in growth buffer	230	1.33	0.19-4.21
No salt in growth buffer	292	1.19	0.08-5.47

For unmodified amyloid fibrils formed from bovine insulin, current values in the range of 10^{-9} to 10^{-8} A were recorded for bias voltages in the range of 0 – 2 V (**Figure 4.6**) (Section 7.12), with the different curves reflecting the fact that the fibrils exist as a network, with different numbers of fibrils bridging the electrodes at different points. Control experiments carried out on empty devices and in the presence of fibril buffer revealed low current values in the range of 10^{-12} A (**Figure 4.6,** insets A and B).

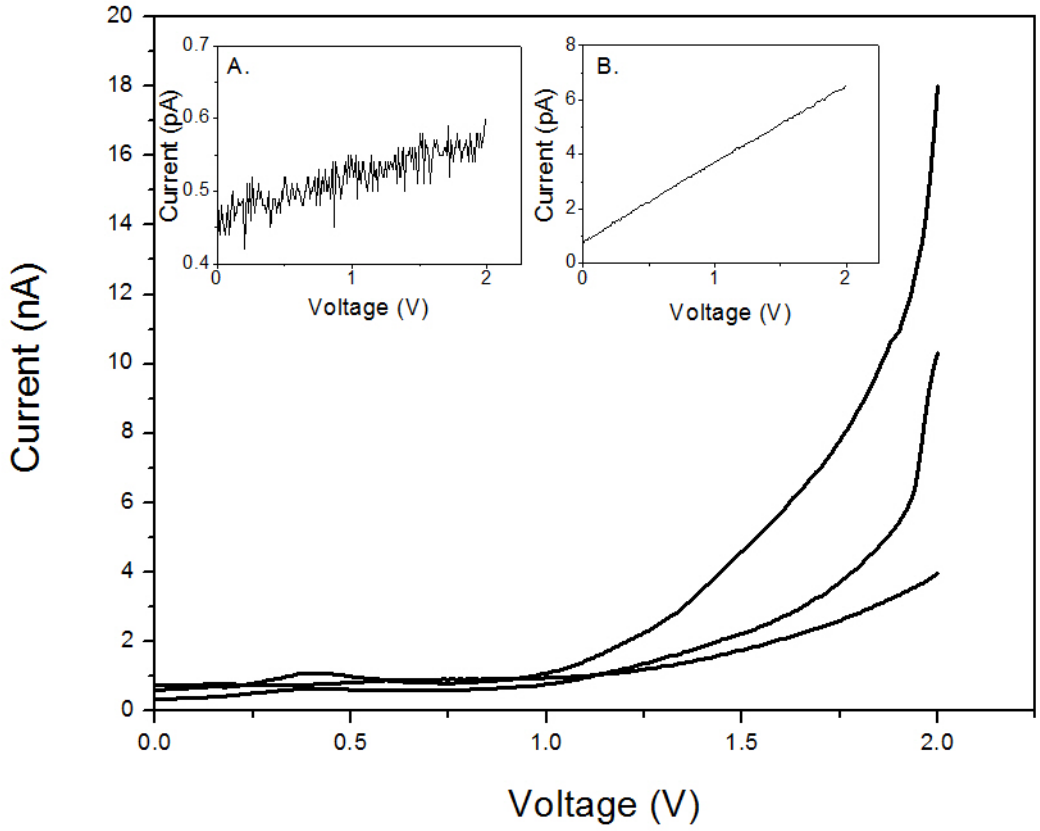

Figure 4.6. *Typical current-voltage (I-V) curves observed for networks formed from bovine insulin amyloid fibrils on three different samples. Inset: A) Blank device and B) Control with insulin fibril buffer only.*[1]

When fibrils are formed from bovine insulin, as with other proteins, non-fibrillar species are often present, either in the form of soluble precursors which have not been converted to fibrils or amorphous aggregate (Zurdo *et al*., 2001). These non-fibrillar species can be removed using pepsin (Section 7.13), a protease which has activity at low pH, which will digest non-fibrillar species, whilst leaving amyloid fibrils intact (Zurdo *et al*., 2001). I-V curves were also measured for networks of bovine insulin amyloid fibrils that were treated with pepsin, in order to ascertain that the observed electrical characteristics could be attributed to the fibril structure. As an additional control, I-V curves were also measured after deposition of native insulin in solution.

[1] This work is published in (Domigan *et al*., 2011)

TEM images taken before and after treatment with pepsin (Section 7.5), show the fibrillar structure of bovine insulin amyloid fibrils to still be intact, with no change to fibril morphology (**Figure 4.7**). A clearer TEM image is produced after pepsin treatment, likely due to the removal of any non-fibrillar protein from the background, which may have affected the contrast achieved with negative staining.

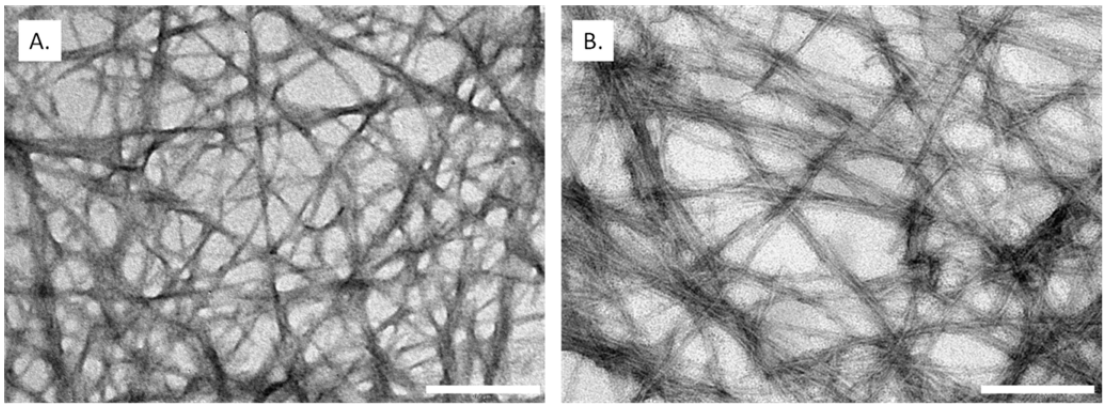

Figure 4.7. *TEM images of bovine insulin amyloid fibrils before (A) and after (B) digestion with pepsin. Scale bar is 0.2 µm.*

I-V curves for the digested insulin fibril samples showed a slight decrease in conductivity, with current values in the range of 10^{-10} A recorded for bias voltages in the range of 0–2 Volts (**Figure 4.8**). Control measurements are the same as those shown in **Figure 4.6**, A and B. This decrease in observed current values could be due to the removal of amorphous aggregate or native insulin protein that was in some way contributing to the observed current, or could be due to a decrease in the concentration of insulin fibrils, resulting from the removal of the pepsin by centrifugation prior to deposition of the protease-treated network onto electrodes. To further investigate this, I-V curves were also constructed for native insulin protein deposited onto interdigitated electrodes.

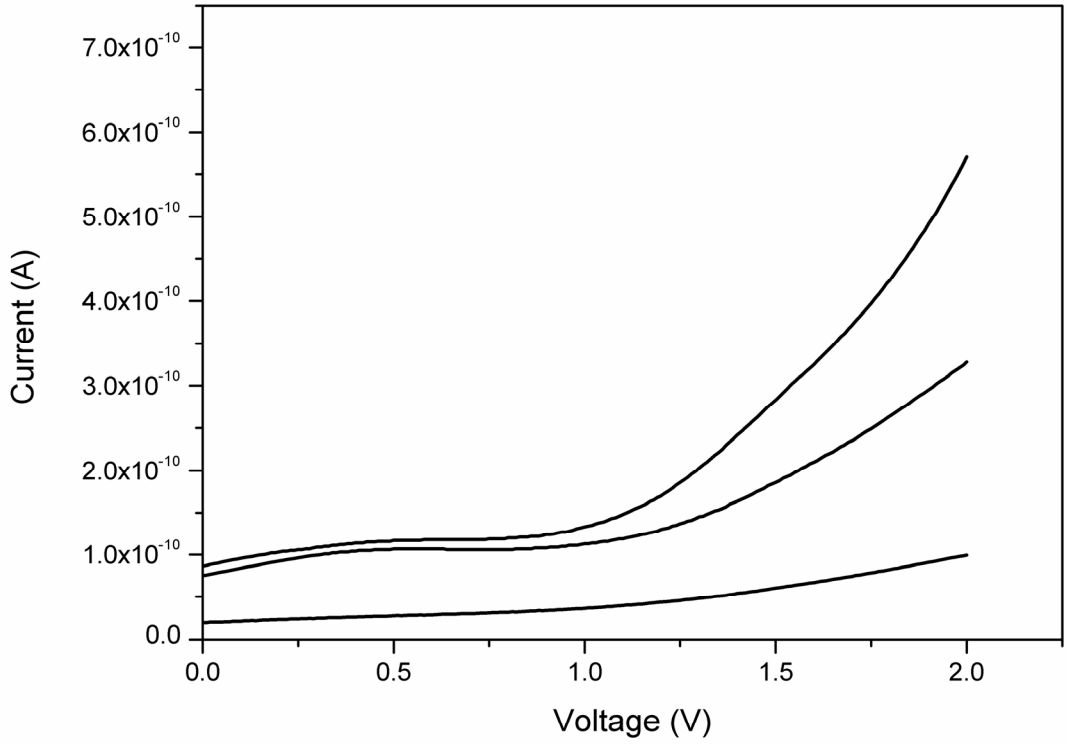

Figure 4.8. *Typical current-voltage (I-V) curves recorded for networks of insulin fibrils after treatment with pepsin on three different samples.*

I-V curves for native bovine insulin protein deposited onto interdigitated electrodes (**Figure 4.9**) were similar to those obtained with blank electrodes, or the buffer control (**Figure 4.6**, A and B). This suggests that the observed current values in **Figure 4.6** can indeed be attributed to the fibril structure, and that the discrepancies seen in conductivity before and after pepsin treatment are most likely due to a decrease in the concentration of fibrils, meaning a reduced density of the network, and therefore fewer fibrils bridging electrodes. These additional controls of protease treated fibrils and native protein were not carried out in the investigation of del Mercato *et al*., although images of the poly(ValGlyGlyLeuGly) show little unfibrilised protein (del Mercato *et al*., 2007).

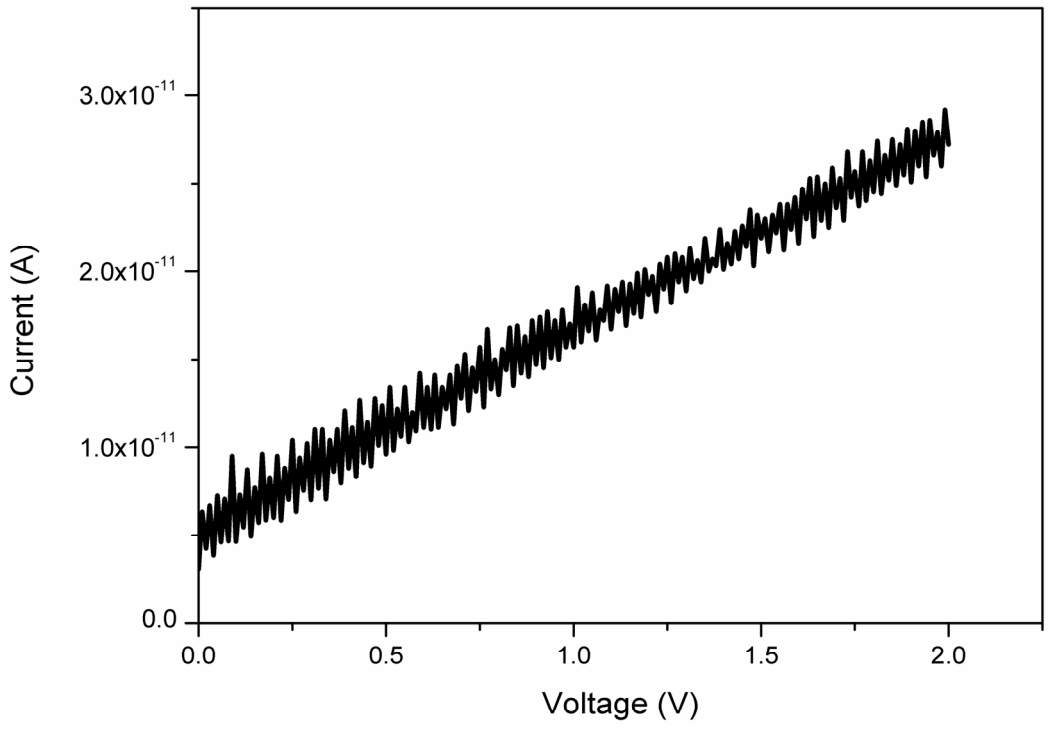

Figure 4.9. *Typical current-voltage (I-V) curve for native bovine insulin deposited onto interdigitated electrodes.*

The bovine insulin used throughout was obtained commercially (Sigma Chemicals (Lot 054K1375)), and is stated to contain 0.5 % zinc. As stated previously in Chapter 3, in solution, insulin exists as an equilibrium mixture of monomers, dimers, tetramers, hexamers, and possibly higher associated states (Nielsen *et al*., 2001). Hexameric porcine insulin has been shown to contain two zinc ions per hexamer, 17 Å apart on the threefold symmetry axis, which traverses the central cavity of the hexamer (Harding *et al*., 1966). Each zinc ion is co-ordinated to three imidazoyl nitrogen atoms from His-B10 and three water molecules (Adams *et al*., 1969). Hexameric bovine insulin has been shown to be structurally identical to porcine insulin (Smith *et al*., 2005), with the zinc ions existing with the same stoichiometry and arrangement (**Figure 4.10**).

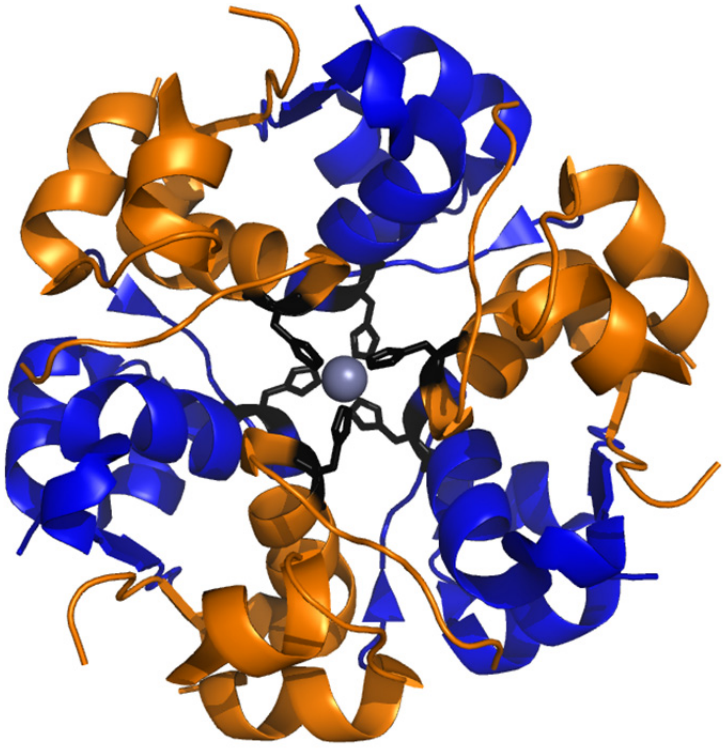

Figure 4.10. *PyMOL image showing hexameric bovine insulin complexed with two zinc ions. Both zinc ions lie on the threefold symmetry axis and so the second zinc ion is not visible in this image. The monomers are shown in alternating blue and orange, with the histidine residues involved in zinc binding shown in stick representation in black. Water molecules also involved in zinc binding have been omitted from this image for clarity. Constructed using PyMOL (Delano, 2002), from PDB file 2ZP6 (Jaimohan et al., 2008).*

As amyloid fibrils were formed directly from dissolved bovine insulin powder, it was assumed that the zinc ions may have been present in the fibril structure. In order to investigate the possibility of a role of the zinc ions in the conductivity of bovine insulin fibrils, EDTA was used to remove zinc from the bovine insulin powder prior to fibril formation (Section 7.14). No great morphological differences were observed by TEM in the "minus-zinc" bovine insulin fibrils, although the presence of zinc is thought to perhaps influence uranyl acetate staining (**Figure 4.11**).

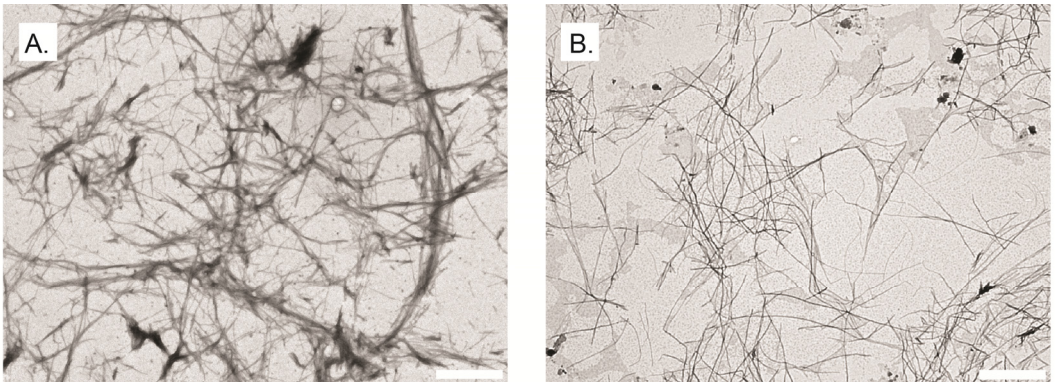

Figure 4.11. *TEM images of bovine insulin amyloid fibrils formed with (A), and without (B), zinc. Scale bar is 1 μm.*

I-V curves for bovine insulin amyloid fibrils formed in the absence of zinc were very similar to those recorded for insulin fibrils with zinc present, with current values in the range of 10^{-9} A recorded for bias voltages in the range of 0–2 Volts (**Figure 4.12**). Control measurements are the same as those shown in **Figure 4.6**, A and B. As there was no large difference observed in the conductivity of insulin fibrils with and without zinc present it appears that the zinc ions do not play a major role in charge transfer within the fibril structure.

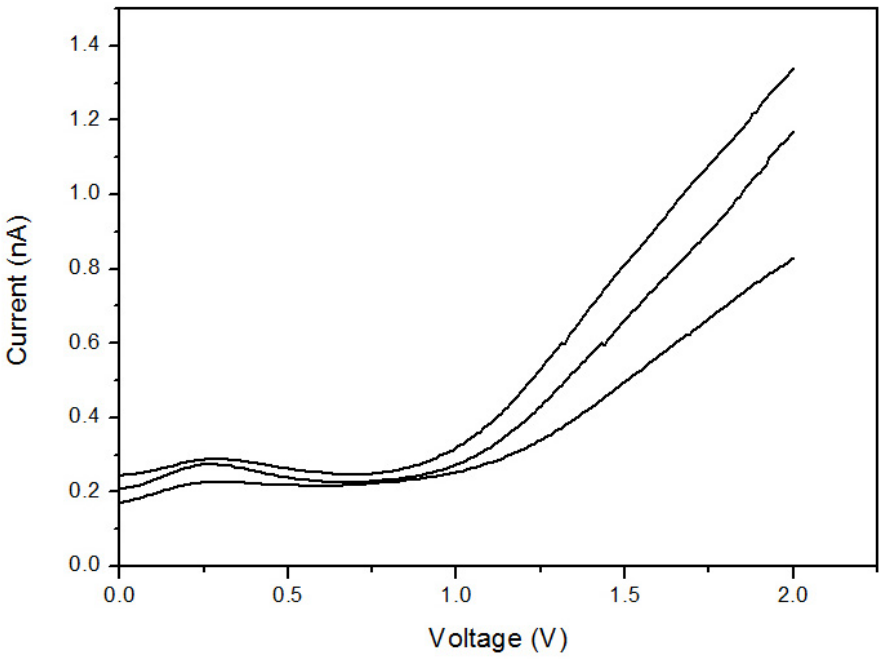

Figure 4.12. *Typical current-voltage (I-V) curve for bovine insulin fibrils formed in the absence of zinc deposited onto interdigitated electrodes on three different samples.*

4.5. Fish eye crystallins fibrils

Conductivity measurements were also carried out on networks of crystallin fibrils formed from crude fish eye protein. Crystallin fibrils were formed using the standard in house conditions (Section 7.4.2) (**Figure 4.13**), as the fibrils formed from crystallin proteins are much longer than those formed from insulin and so adequate bridging of electrodes was not of concern. Length distributions of crystallin amyloid fibrils are shown in Section 4.10.2.

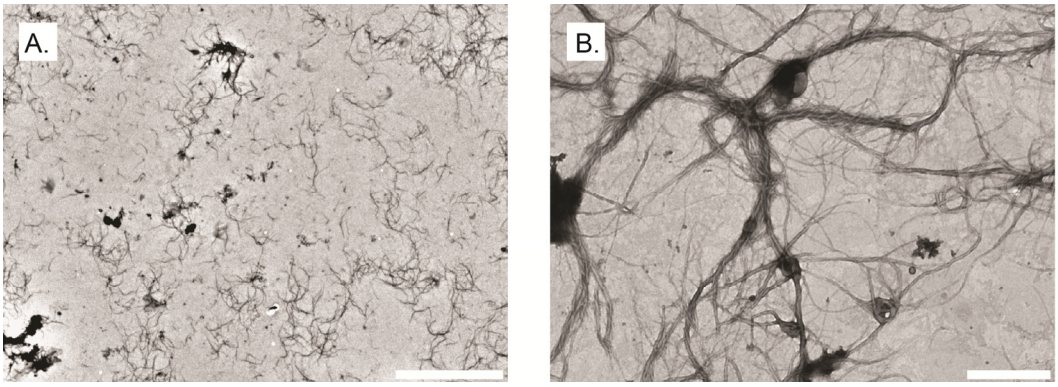

Figure 4.13. *TEM images of crude crystallin fibril sample used for conductivity measurements of fibril networks. Scale bars are 10 μm (A) and 1 μm (B).*

For amyloid fibrils formed from crude fish eye crystallin proteins, current values in the range of 10^{-10} to 10^{-11} A were recorded for bias voltages in the range of 0–2 V (**Figure 4.14**) (Section 7.12). Control experiments carried out on empty devices (**Figure 4.6**, A), and in the presence of fibril buffer revealed low current values in the range of 10^{-12} A (**Figure 4.14**, insert). I-V curves for crude crystallin proteins in the native state deposited onto interdigitated electrodes were similar to those for the buffer control (**Figure 4.15**); this is the same as was observed for native insulin. Crystallin fibrils were not subjected to protease treatment, as preliminary experiments showed this to degrade the fibrils, and the fibril formation process for crude crystallins has also been optimised to eliminate the presence of amorphous aggregate.

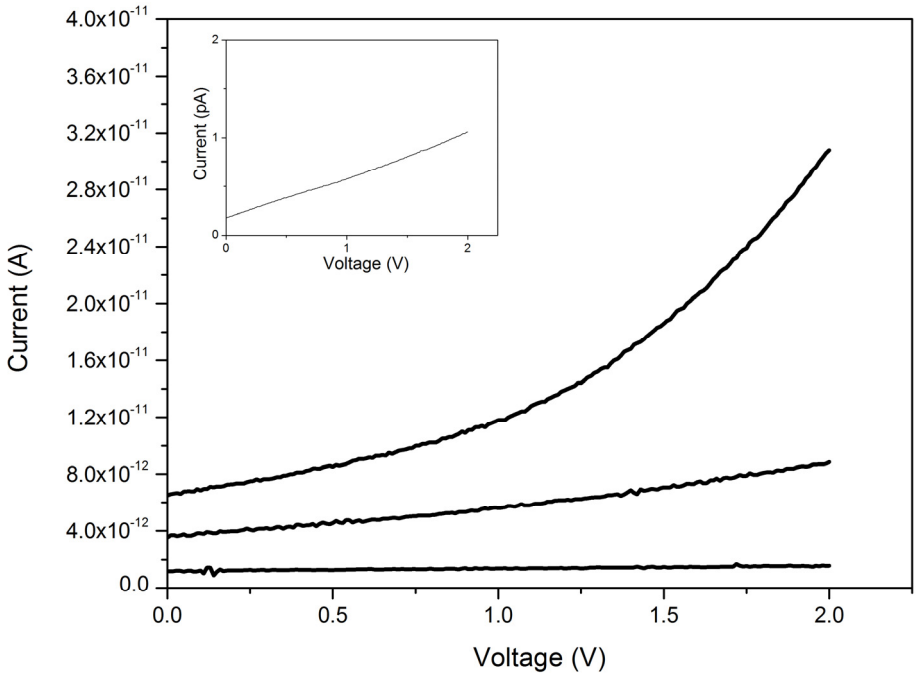

Figure 4.14. *Typical current-voltage (I-V) curve for crude crystallin fibrils deposited onto interdigitated electrodes on three different samples. Inset shows crystallin fibril buffer control.*

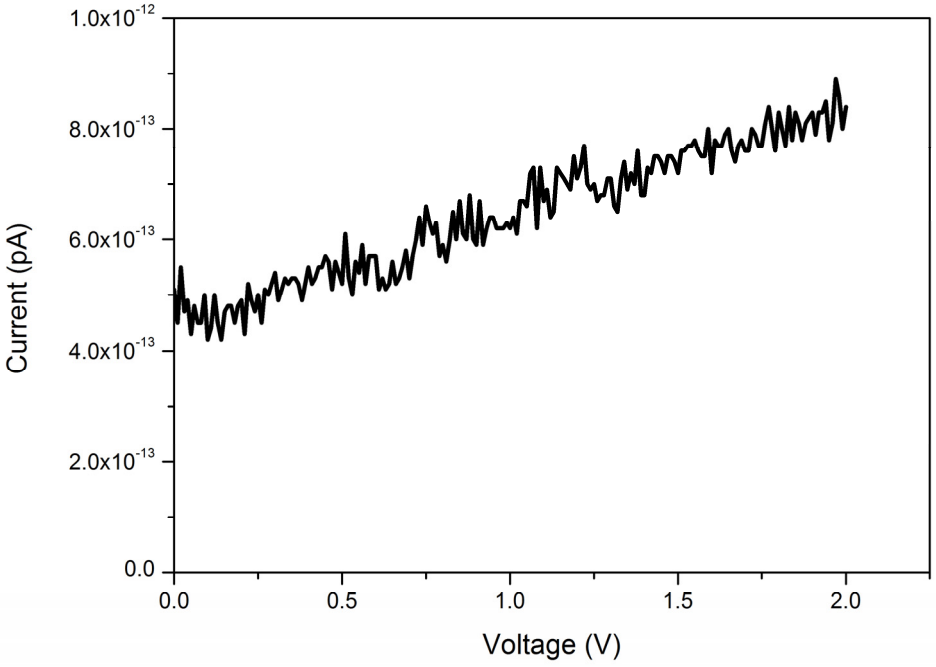

Figure 4.15. *Typical current-voltage (I-V) curve for native crude crystallins deposited onto interdigitated electrodes on three different samples.*

4.6. Fungal hydrophobins rodlets

Conductivity measurements were also carried out for networks of fibrils formed from fungal hydrophobins (Section 7.12). The amyloid fibrils formed from this protein source give rise to a distinct network structure compared to that observed for insulin and crystallin fibrils. Hydrophobin rodlets form an ordered, regular network as opposed to a random one, as shown in **Figure 4.16**. This regular structure has been observed on fungal spores, as well as with *in vitro* formation of rodlets on a surface (Sunde *et al*., 2008). The rodlet network is a monolayer which is approximately 1.3–2.8 nm thick, depending on preparation conditions (Paananen *et al*., 2003; Szilvay *et al*., 2007). It has also been shown that the monolayer lacks interwoven structures (Beever *et al*., 1979; Beever and Dempsey, 1978; Dempsey and Beever, 1979), making it an interesting network to study in terms of charge transfer.

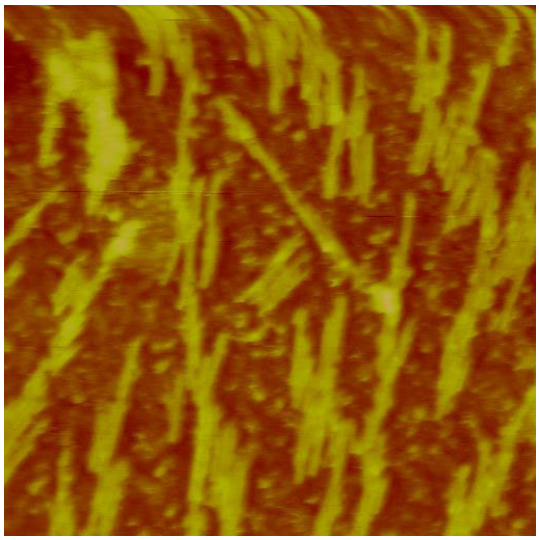

Figure 4.16. *Representative tapping-mode AFM image of fungal hydrophobin rodlets Rodlets were formed onto a silicon wafer. Scan size 2 μm*^{2}.

Hydrophobin networks were deposited onto interdigitated electrodes and current values in the range of 10^{-10} A were recorded for bias voltages in the range of 0–2 Volts (**Figure 4.17**). Control experiments carried out on both empty devices (**Figure 4.6**, inset A), and in the presence of hydrophobin rodlet buffer (**Figure 4.17**, inset) showed low current values in the range of 10^{-12} A. As hydrophobins form rodlets spontaneously in the presence of a solid/water interface, it was not possible to obtain current values for native hydrophobins.

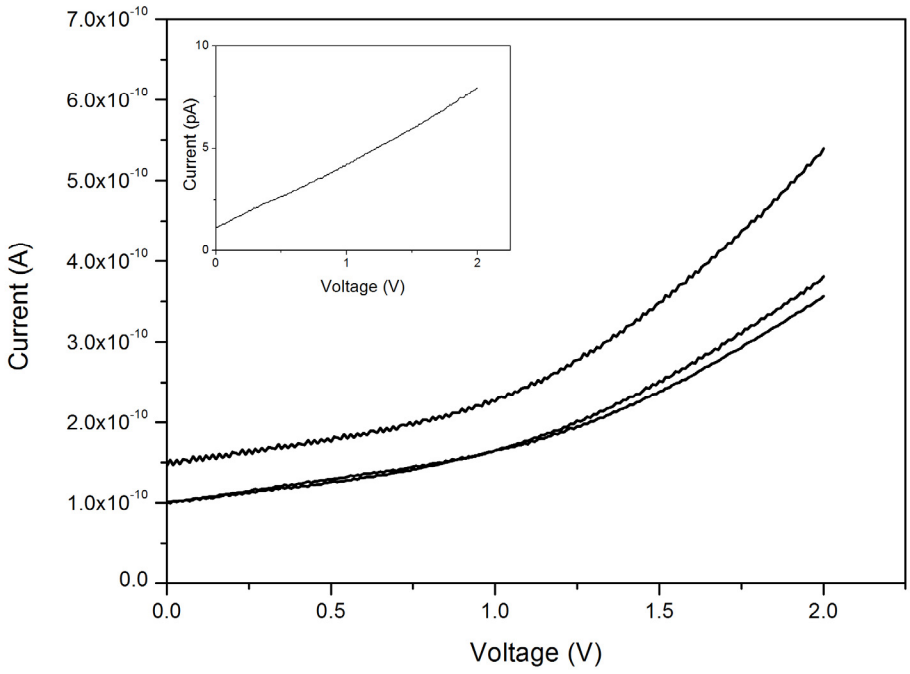

Figure 4.17. *Typical current-voltage (I-V) curves recorded for networks of fungal hydrophobin rodlets on three different samples.*

4.7. Summary of conductive properties of amyloid fibril networks

It was observed that networks of amyloid fibrils formed from bovine insulin, fish eye crystallins, and fungal hydrophobins all had fairly similar conductive properties, with networks from all three fibril systems having low current values in the range of 10^{-8} to 10^{-10} A recorded for bias voltages in the range of 0-2 V (**Table 4.3**). As these current values fall within a narrow range it is therefore likely that the generic fibril structure is playing a role in influencing conductivity, as the native protein gives much lower current values, but with differences seen due to amino acid composition. Further studies, such as mutagenesis of charged residues, would be necessary to confirm this hypothesis.

Table 4.3. *Summary of conductive properties of amyloid fibril networks deposited onto interdigitated electrodes.*

Network components	**Current values (A) recorded (for bias voltages 0-2 V)**
Bovine insulin amyloid fibrils	10^{-9} to 10^{-8}
Bovine insulin amyloid fibrils – after digest with pepsin	10^{-10}
Bovine insulin amyloid fibrils – in the absence of zinc	10^{-9}
Fish eye crude crystallin amyloid fibrils	10^{-10}
Fungal hydrophobin rodlets	10^{-10}
Poly(ValGlyGlyLeuGly) amyloid-like fibrils (del Mercato *et al*., 2007)	10^{-9}

The observed current values for the three fibril systems in this study are similar to those previously recorded by del Mercato *et al*. in their study on the conductivity of "amyloid-like" fibrils formed from an elastin-related polypeptide, which formed fibrils with diameters ranging from 20 to 250 nm – much larger structures than the amyloid fibrils employed here (del Mercato *et al*., 2007). They recorded current values typically in the range of several nanoAmps, and suggested the presence of charge-transfer pathways in the fibrillar structures, with particular emphasis on an important role of water molecules. It can be speculated that a similar mode of charge-transfer is in place for the range of fibrils used in this study. It is interesting that although these four amyloid fibril systems are significantly different, for example they range from fibrils formed from an engineered peptide (del Mercato *et al*., 2007), through to those formed from a crude protein mixture, the observed electrical behaviour is very similar, with low current values consistently recorded (**Table 4.3**).

These results are in agreement with the findings of Schiebel *et al*. that in the unmodified state, amyloid fibrils are insulators (Scheibel *et al*., 2003). This was not an altogether surprising result, considering that most biological nanofibres and nanotubes have been found to have low conductivity (Storm *et al*., 2001). For example, although DNA has had varying conductivities reported, depending on sequence and environmental conditions, the conductivities are in the range of 2 S/cm down to 10^{-16} S/cm (Bockrath *et al*., 2002; Gomez-Navarro *et al*., 2002; Tran *et al*., 2000), with the majority of reports finding DNA to be insulating.

In conclusion, amyloid fibrils formed from bovine insulin, fish eye crystallins, and fungal hydrophobins all have low conductivity, and if they are to be utilised in an application where good ability to sustain electrical charge is necessary, they should be used as a scaffold or template for the formation of more highly conductive nanowires.

4.8. Modification of amyloid fibrils with conducting polymers

Amyloid fibrils from bovine insulin were modified using the conducting polymers polypyrrole (PPY, **Figure 4.18**, C) and polyaniline (PANI, **Figure 4.18**, D). This modification process was carried out by collaborators, Cosmin Laslau and Jadranka Travas-Sejdic from the Polymer Electronics Research Group at Auckland University.

Since the discovery of the electrically conductive properties of doped polyacetylene in 1977 (Chiang *et al*., 1977), conducting polymers have been the focus of much scientific attention due to their wide applicability, such as in electronic circuitry, organic LEDs and solar cells, and in sensing devices (Gerard *et al*., 2002; Inzelt *et al*., 2000). Both PPY and PANI are polyheterocyclics, a class of aromatic conducting polymers recognised as having good stability, conductivity, and ease of synthesis (Guimard *et al*., 2007).

Both PPY and PANI can be easily synthesised by either chemical oxidation or electrochemical polymerization of pyrrole and aniline respectively, under relatively mild conditions (Chandrasekhar, 1999; Genies *et al*., 1990; MacDiarmid *et al*., 1987), with advantages and disadvantages recognised for each type of synthesis (Ateh *et al*., 2006). For this study, the polymerisation reactions were carried out using chemical oxidation by ammonium persulfate in the presence of the insulin fibrils.

PANI is environmentally stable, with electronic characteristics that are controllable through a simple acid-doping/base-redoping pathway (Jang, 2006). Due to these characteristics, PANI can be used in a range of applications, such as sensing (Huang *et al*., 2003), field emission displays (Wang *et al*., 2001), and electronic circuitry (Drury *et al*., 1998). Of all the conducting polymers, PPY has been the most extensively studied for biological and medical applications, such as biosensors and tissue engineering scaffolds (Guimard *et al*., 2007), due to its high biocompatibility.

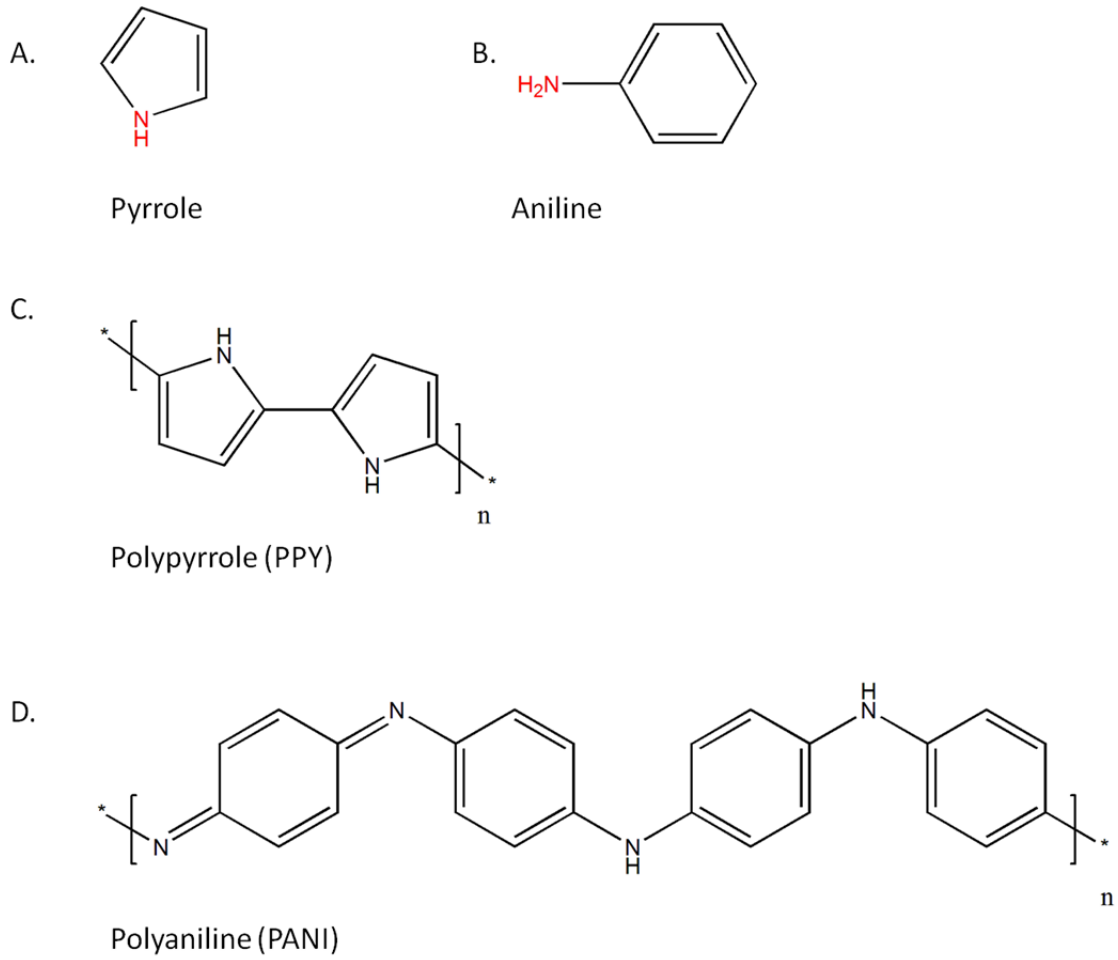

Figure 4.18. *Structures of the monomers A) Pyrrole, and B) Aniline, with amino groups shown in red, and the conducting polymers C) Polypyrrole (PPY), and D) Polyaniline (PANI). Adapted from Martin (1995).*

Nanostructured conducting polymers, such as PANI and PPY, are of high interest, as nanoforms of these polymers offer new properties and superior performance (Li *et al*., 2008; Li *et al*., 2009; Tran *et al*., 2009). 1-D conducting polymer structures were first produced in the 1970s, with the formation of films of polyacetylene nanofibres (Shirakawa *et al*., 1977). Since then, conducting polymer nanowires have been formed by a variety of different techniques such as electrospinning (MacDiarmid *et al*., 2001; Pinto *et al*., 2003), mechanical stretching (He *et al*., 2001), post-synthetic self assembly via deposition onto solid supports (Carswell *et al*., 2003; Malik and Nandi, 2002), and solution-phase synthesis, which has the advantage of being able to produce bulk quantities of nanowires (Tran *et al*., 2009).

Solution-phase synthesis of conducting polymer nanowires can be either template or non-template directed. When a template is used, this may either be a "soft"-template, for example, a surfactant that can guide the growth of the polymer in or around self-assembled micelles, or a "hard"-template (Tran *et al*., 2009). A hard-template is one with pre-formed nanoscale features. The template is often removed, although this can be a difficult procedure, such as in the case where the conducting polymer is synthesised using the inside pores of a membrane as a template (Martin, 1995).

A range of different templates have been used for the seeding or templating of conducting polymer nanowires, ranging from the inorganic to the biological (Lu *et al*., 2010). Biological templates that have been used include TMV molecules (Niu *et al*., 2006; Niu *et al*., 2007a; Niu *et al*., 2007b), DNA (Ma *et al*., 2004; Moon *et al*., 2010; Nickels *et al*., 2004), RNA (Fan *et al*., 2007), polysaccharides (Numata *et al*., 2004; Shi *et al*., 2006), and amyloid fibrils - which were modified with the conducting polymers PEDOT-S, PTAA, and PPF (Hamedi *et al*., 2008; Herland *et al*., 2007; Herland *et al*., 2008; Tanaka *et al*., 2008),

PANI and PPY nanofibres have previously been synthesised in solution (Huang *et al*., 2003; Huang and Kaner, 2004). TMV molecules have also been used for the formation of both PANI (Niu *et al*., 2006; Niu *et al*., 2007a), and PPY nanofibres (Niu *et al*., 2007b), with the polymerisation carried out by chemical oxidation in both cases. To date, amyloid fibrils have not been used as templates for the formation of PANI or PPY nanofibres.

Bovine insulin amyloid fibrils were used as a scaffold for the formation of amyloid-PPY and amyloid-PANI conjugate nanowires. In both cases, the polymerisation reaction was carried out in the presence of amyloid fibrils, resulting in the amyloid fibrils being coated with the conducting polymer, as shown in **Figure 4.19**. It can be seen in **Figure 4.19** that the insulin fibril structure is still intact, an important observation as DNA was previously shown to be degraded by ammonium persulfate, causing visible breaks in the wires (Nickels *et al*., 2004). It was also seen that the two different conducting polymers give different coating morphologies, with the amyloid-PANI showing a "webbed" morphology (**Figure 4.19**, B), while the amyloid-PPY shows a "beaded" morphology (**Figure 4.19**, C). This change in morphology was also observed by Hamedi *et al.,* who saw an increased diameter of fibrils and a webbed morphology upon coating insulin fibrils with the conducting polymer PEDOT-S (Hamedi *et al*., 2008). It should be noted that Niu *et al*. managed to shift from the propensity to form a webbed morphology towards the formation of individual unbranched fibres in their studies on TMV-PANI, by changing the polymerisation conditions, namely with the addition of poly(sulfonated styrene) (PSS).

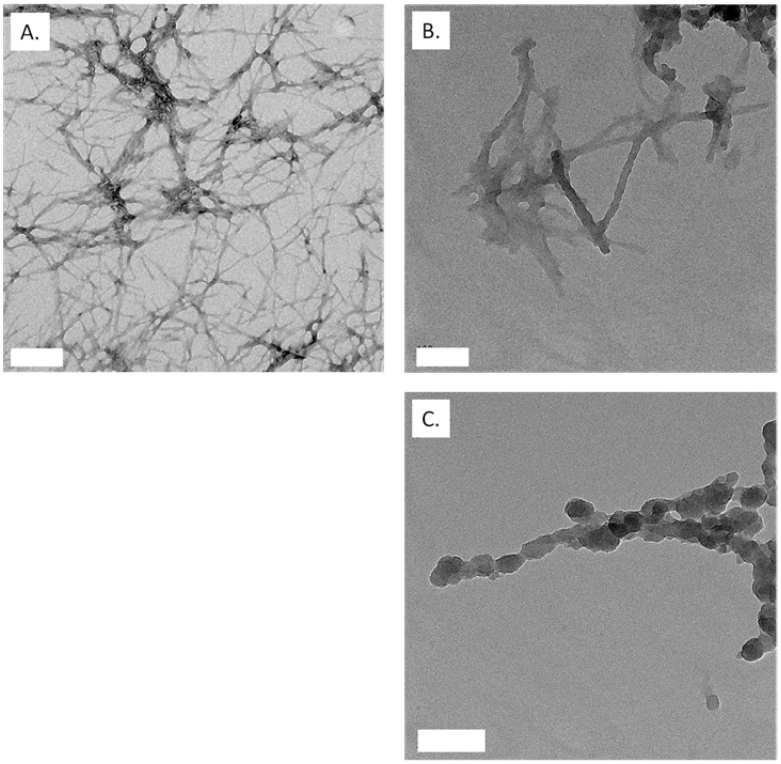

Figure 4.19. *TEM images of: A) Bovine insulin amyloid fibrils prior to modification. Scale bar 200 nm. B) Amyloid fibrils modified with PANI. Scale bar 100 nm. C) Amyloid fibrils modified with PPY. Scale bar 100 nm.*

As to the mechanism of the polymer coating onto the fibrils, a similar mechanism to that proposed for the coating of TMV molecules is suggested. That is that the negatively charged surface residues "bind" the amino group (shown in red, **Figure 4.18**) of the monomers, pyrrole or aniline (**Figure 4.18**, A and B respectively), through electrostatic interactions or hydrogen bonding (Li *et al*., 2008). This causes accumulation of monomers on the surface of the fibrils, with *in situ* polymerisation of absorbed monomers causing a thin layer of polymer on the surface.

The diameter of PANI nanofibres has been shown to vary depending on the reaction conditions, specifically the acid used for polymerisation, with nanofibres formed of diameters ranging from 30 to 120 nm (Li *et al*., 2008). In the studies by Niu *et al*., using TMV as a template, they saw diameters increase from 18 nm in the native TMV structure, to 22 nm for TMV-PPY (Niu *et al*., 2007c), and 40 nm to 1-2 μm for TMV-PANI, depending on the pH at which the polymerisation was carried out at (Niu *et al*., 2007a). In this study, the conducting polymer coating saw an increase in diameter from 7-10 nm to approximately 20 nm for the amyloid-PANI fibres, and approximately 30 nm for the amyloid-PPY fibres (**Figure 4.19**). Alteration of the polymerisation conditions, as mentioned above, could be utilised in future work to achieve a more uniform coating, and to control the thickness of the coating.

4.9. Conductive properties of modified amyloid fibril networks

The conductive properties of both the amyloid-PPY and amyloid-PANI networks were examined by the same method as was used for the unmodified fibrils (Section 7.12). It was seen that for amyloid-PPY networks, current values in the range of 10^{-5} to 10^{-4} A were recorded for bias voltages in the range of 0–2 V (**Figure 4.20**). Investigation into the conductive properties of amyloid-PANI networks saw that current values in the range of 10^{-8} to 10^{-7} A were recorded for bias voltages in the range of 0 – 2 V (**Figure 4.21**). Control measurements on blank electrodes were the same as for previous experiments (**Figure 4.6**, A).

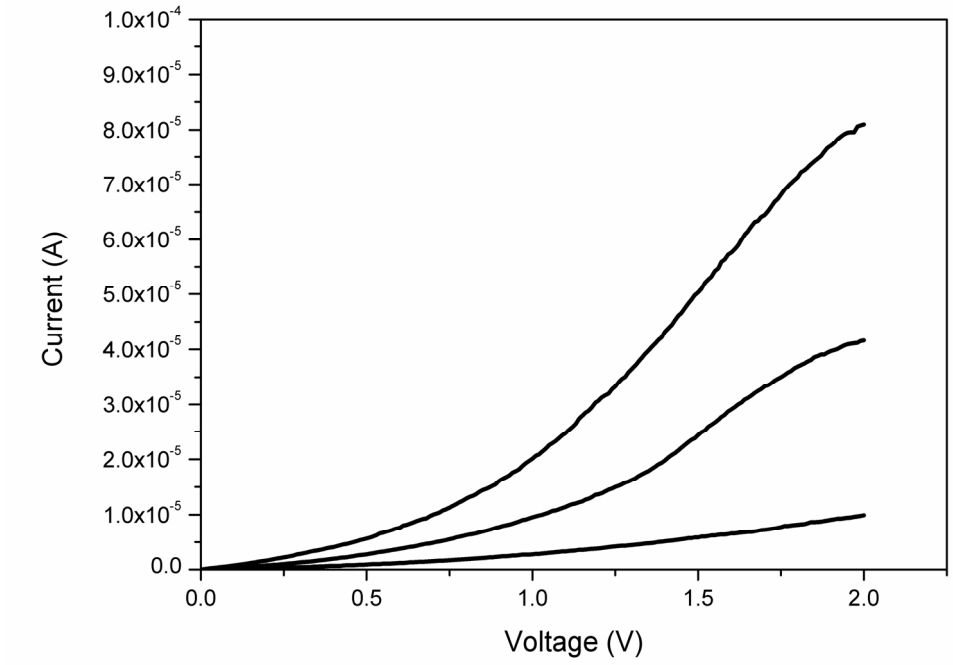

Figure 4.20. *Typical current-voltage (I-V) curves for networks of bovine insulin amyloid fibrils modified with polypyrrole (PPY) on three different samples.*

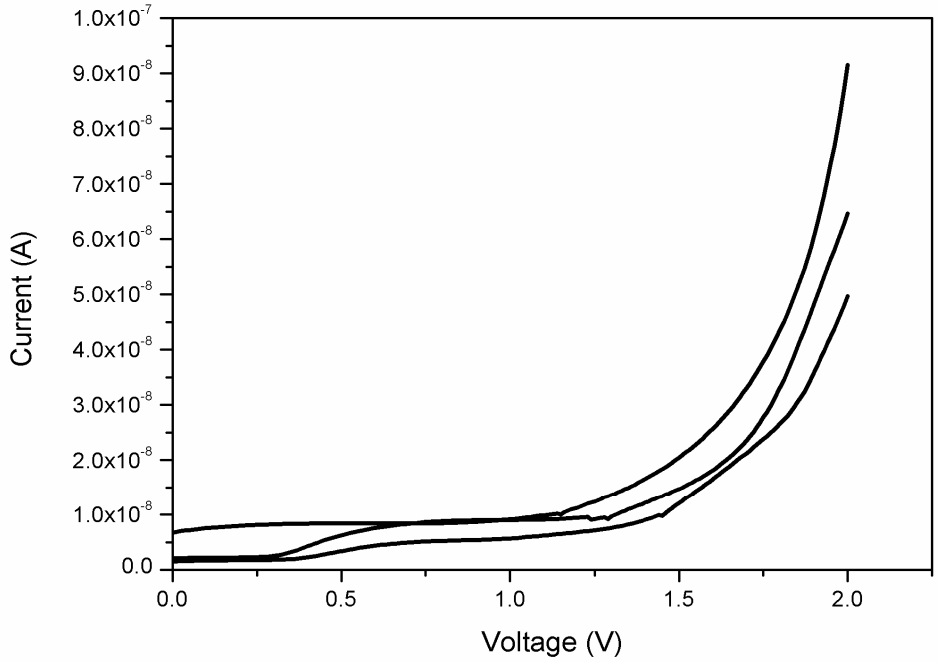

Figure 4.21. *Typical current-voltage (I-V) curves for networks of bovine insulin amyloid fibrils modified with polyaniline (PANI) on three different samples.*

As shown in **Table 4.4**, modification of bovine insulin amyloid fibrils with the conducting polymers PPY and PANI causes an increase in conductivity of the amyloid fibril network by four and one orders of magnitude respectively. Doping of amyloid-PANI nanowires carried out with HCl was unsuccessful, with no improved conductance. This was also the case for DNA-PANI nanowires (Nickels *et al*., 2004).

Table 4.4. *Summary of current values recorded for unmodified and modified bovine insulin amyloid fibril networks.*

Network components	**Current values recorded (for bias voltages 0-2V)**
Bovine insulin amyloid fibrils	10^{-9} to 10^{-8} A
Bovine insulin amyloid fibrils + PPY	10^{-5} to 10^{-4} A
Bovine insulin amyloid fibrils + PANI	10^{-8} to 10^{-7} A

4.10. Manipulation and immobilisation of amyloid fibrils by DEP

Dielectrophoresis (DEP) is a non-destructive, non-invasive electrokinetic mechanism, that is defined as the motion of a polarisable particle in a non-uniform electric field (Lapizco-Encinas and Rito-Palomares, 2007). DEP has been used extensively on biological particles, for analysis and separation of particles such as cells (Kang *et al*., 2008), micro-organisms (Moncada-Hernandez *et al*., 2011), DNA (Kuzyk *et al*., 2008), RNA (Giraud *et al*., 2011), protein particles (Lapizco-Encinas *et al*., 2008), and more relevant to this project, for the manipulation and isolation of biological nanotubes (Castillo *et al*., 2008), in order to probe electrical properties. At the nanoscale, DEP is most commonly used for controlled positioning of individual objects on a chip (Kuzyk, 2011).

4.10.1. Theory of DEP

DEP was first discovered by Pohl in 1951, and refers to the movement of particles induced by polarisation effects in non-uniform electric fields (Lapizco-Encinas and Rito-Palomares, 2007; Pohl, 1951). If a dielectric particle, that is, a particle that is polarisable, is suspended in an electric field, the particle will polarise. The magnitude and direction of this induced dipole depends on a number of factors: the frequency and magnitude of the applied electric field, and also the dielectric properties of both the particle and the medium. These dielectric properties are *conductivity*, the ease with which charge can move through a material, and *permittivity*, which is how much resistance is encountered when forming an electric field (Dimaki, 2009).

In a uniform electric field, the force on either side of the particle is the same, so there is no net force pulling the particle anywhere and the particle will not move, unless the particle carries a net charge and the field frequency is close or equal to zero. In a non-uniform electric field, as is the case with DEP, the field lines are denser on one side of the particle than the other, meaning that the electric field is stronger on one side than the other and the particle will move (Dimaki, 2009). If the particle is more polarisable than the medium, then the particle will move towards the strongest field, which is called positive DEP. If the particle is less polarisable than the medium you will get negative DEP, where the particle moves towards the weakest field. This is shown schematically in **Figure 4.22**.

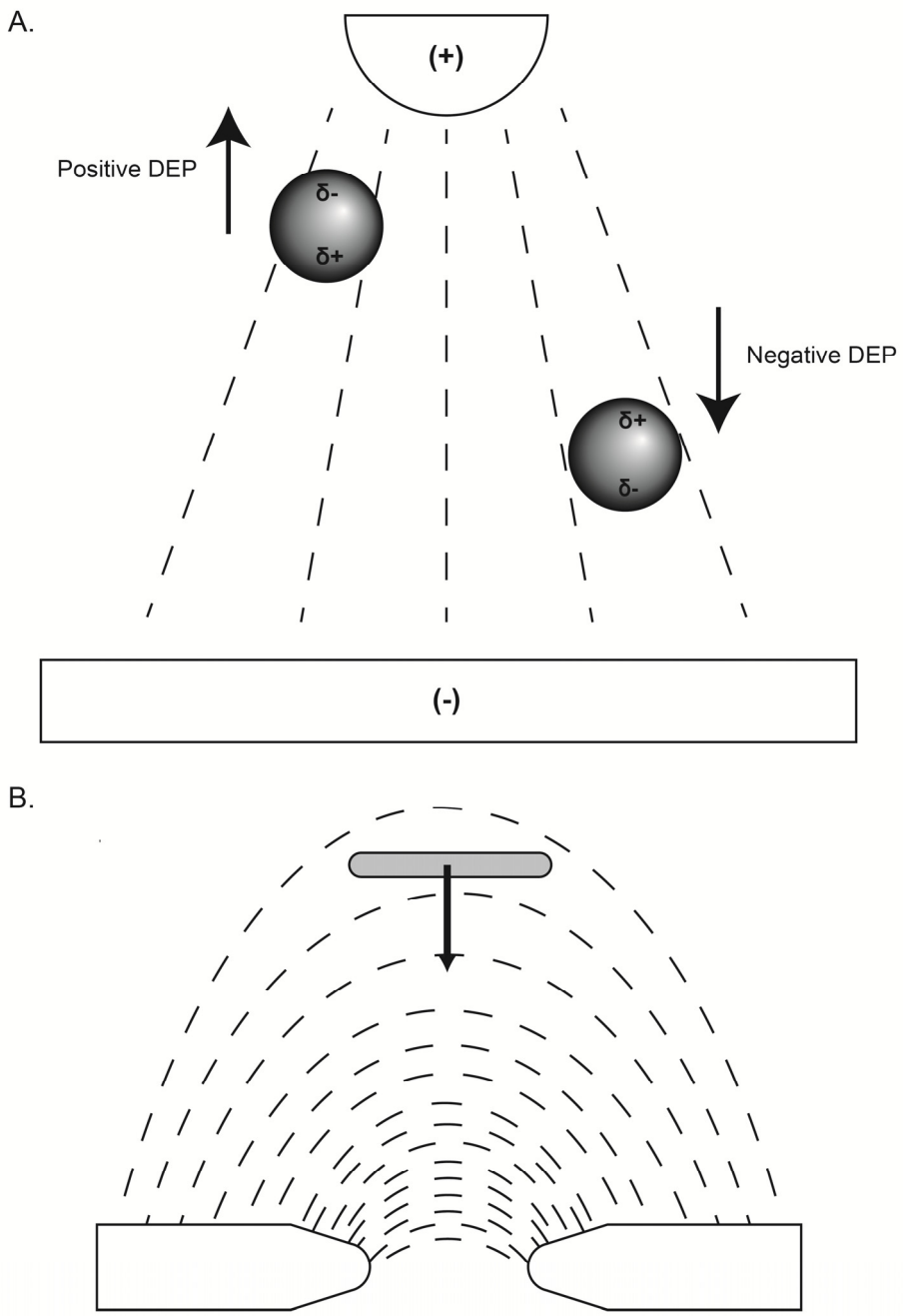

Figure 4.22. *A) Schematic showing positive and negative DEP. Positive DEP occurs when the particle is more polarisable than the medium, and so moves towards the strongest point of the electric field. Negative DEP is where the reverse occurs, the particle is less polarisable than the medium and so movement is in the direction of the weakest field. B) For this study, the aim is to immobilise crystallin fibrils between an electrode pair using positive DEP.*

There are two ways of generating non-uniform electric fields: electrode-based DEP, which involves applying a voltage across an electrode array, and insulator-based DEP, where insulating structures are placed between a pair of electrodes (Gonzalez and Remcho, 2005). This study used electrode-based DEP.

4.10.2. Governing equations

The force (F) exerted by an electric field, E, on a dipole with dipole moment, p, is given by the following equation (Dimaki and Bøggild, 2005; Kuzyk, 2011):

$$F = (p.\nabla)E \tag{4.1}$$

Where ∇ is the mathematical "del" operator. Here the higher order terms of the force are omitted. Therefore, the expression is only accurate if the magnitude of the electric field does not vary significantly across the dipole (Dimaki and Bøggild, 2005). In an AC-field the time-averaged force on a particle will be given by:

$$F_{DEP} = \Gamma.\varepsilon_m.\varepsilon_0.\mathrm{Re}\left\{K_f\right\}.\nabla\left|E^2\right| \tag{4.2}$$

Where Γ is a factor depending on the particle geometry, ε_m is the relative permittivity of the suspending medium, ε_0 is the permittivity of the vacuum, and E is the applied electric field (amplitude and not root mean square). The factor K_f depends on the complex permittivities of both the particle and the medium, plus the particle geometry.

As alluded to above, particle geometry is an important factor in dielectrophoresis. The geometry of crystallin fibrils was assumed to be that of a prolate ellipsoid (**Figure 4.23**), where $\alpha_1 >> \alpha_2 = \alpha_3$. This geometry was used as it had been previously used for structures of a similar geometry to crystallin fibrils: FF nanotubes (Castillo *et al*., 2008), and SWNT (Lin *et al*., 2007).

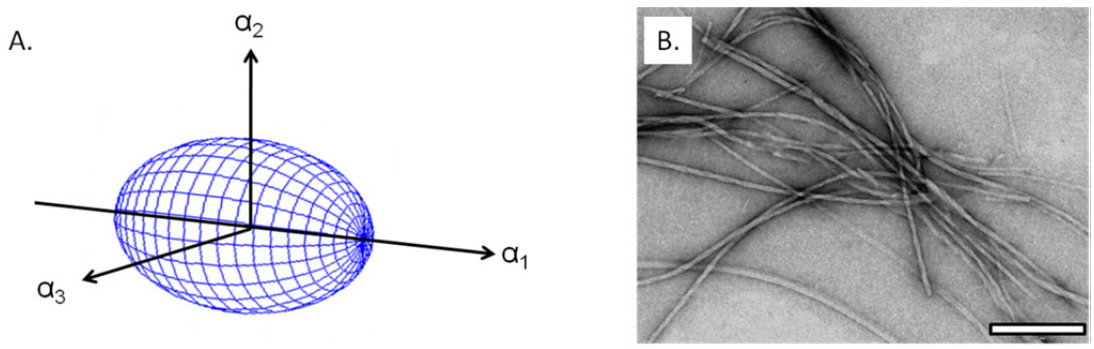

Figure 4.23. *The geometry of crystallin fibrils (B), was assumed to be that of a prolate ellipsoid, where* $\alpha_1 >> \alpha_2 = \alpha_3$.

The length distribution of crystallin fibrils was measured from TEM images of the fibril sample used for the DEP experiments (**Figure 4.24**), with an average length of 4.92 µm calculated (n = 207) (Section 7.10.2). The average diameter of crystallin fibrils was measured from AFM images of the same fibril sample, and was 16.3 ± 5.6 nm (Section 7.10.3).

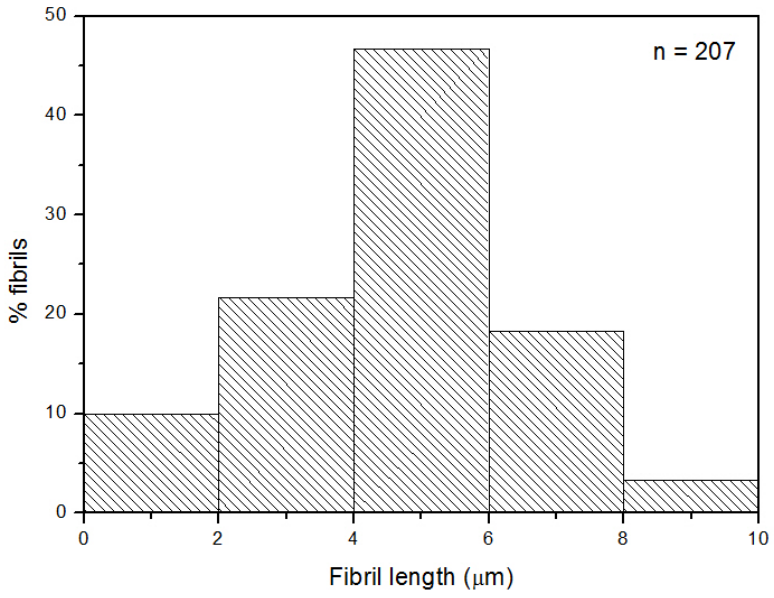

Figure 4.24. *Histogram showing length distribution of crystallin fibril preparation that was used for DEP experiments.*

In the case of the prolate ellipsoid, the factor K_f is now different for each principal axis n (n = 1, 2 and 3), and is given by:

$$K_f^n = \frac{\varepsilon_p - \varepsilon_m}{\varepsilon_m + A_n.(\varepsilon_p - \varepsilon_m)} \tag{4.3}$$

Where ε_p and ε_m are the relative permittivities of the particle and the medium respectively, and A_n is the depolarising factor for the axis n. In the case of a prolate ellipsoid where $\alpha_1 >> \alpha_2 = \alpha_3$, as is the case with crystallin fibrils (**Figure 4.23**), and assuming that the major axis of the particle, axis 1 in this case, is aligned with the field (**Figure 4.22**, B), the depolarising factor is given by:

$$A_1 = -\frac{1-e^2}{2e^2}\left[2e - \ln\left(\frac{1+e}{1-e}\right)\right] \tag{4.4}$$

Where e is the eccentricity of the particle, which is given by:

$$e = \sqrt{1 - \left(\frac{\alpha_2}{\alpha_1}\right)^2} \tag{4.5}$$

That the particle geometry has been assumed to be a prolate ellipsoid also influences the geometry factor Γ (from Equation 4.2). The geometry factor Γ for a prolate ellipsoid is given by:

$$\Gamma = \frac{3}{4}V_p \xrightarrow{ellipsoid} \Gamma = \pi.\alpha_1.\alpha_2.\alpha_3 \tag{4.6}$$

Equation 4.2 shows that the dielectrophoretic force is dependent on the real part of K_f. If the real part is positive, then the DEP force is in the direction of increasing electric field, which gives positive DEP as described previously, and vice versa. The frequency at which the behaviour of the particle in the electric field changes from positive to negative DEP is called the turnover frequency, f_{to}, and for a prolate ellipsoid, this is given by:

$$f_{to} = \frac{1}{2\pi.\varepsilon_0}\sqrt{-\frac{\sigma_p - \sigma_m}{\varepsilon_p - \varepsilon_m}.\frac{\sigma_p + \alpha.\sigma_m}{\varepsilon_p + \alpha.\varepsilon_m}}, \alpha = \frac{1}{A_n} - L \tag{4.7}$$

4.10.3. Manipulation and immobilisation of crystallin amyloid fibrils

A DEP microchip, that was custom designed and fabricated by collaborators at Denmark Technical University, with 5 electrode pairs with a 5 µm gap was used in experiments to attempt to immobilise crystallin amyloid fibrils between electodes, with the aim of further electrical characterisation once fibrils were isolated. The methods for design and fabrication of the DEP microchip are laid out in Section 7.15.1, along with images of the microchip design in **Figure 4.25**.

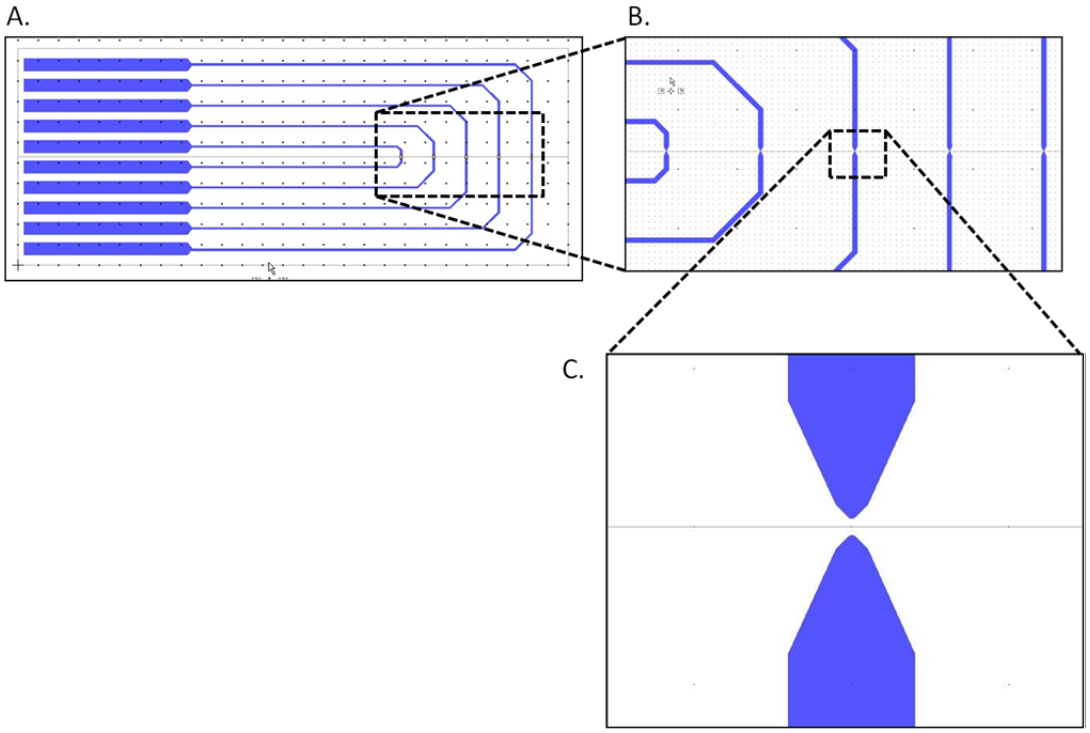

Figure 4.25 *Design of the DEP microchip. The DEP microchip consisted of 5 pairs of electrodes, with large landing spaces located at the end of the chip for contact with the chip holder (A). A closer view of these electrodes (B and C), shows that each electrode pair is spaced 5 µm apart.*

As described in Section 7.15.1, a range of parameter combinations, varying voltage frequencies ranging from 1 kHz to 1 MHz , and voltage amplitudes of 10 and 20 V peak-peak were investigated in order to get the optimal values to manipulate the amyloid fibrils using positive DEP. Positive DEP was required as previously performed simulations of the electric field had shown the electric field was to be strongest around the tips of the electrodes (Castillo *et al*., 2008), the point where fibril immobilisation was desirable.

Positive DEP was only seen at a voltage of 20 V peak-peak (Vpp), and at frequencies from 50 – 100 kHz. Results of the DEP experiments, showing the percentage of instances of positive DEP from ten samples per parameter combination are summarised in **Table 4.5**. From the result of these experiments the turnover frequency, defined in Section 4.10.2, can be estimated to be 100 kHz.

Table 4.5. *Summary of the percentage of instances of positive DEP from ten samples per parameter combination*

Voltage (Vpp)	Frequency (kHz)	Percentage of electrode pairs at which positive DEP occurred
20	50	80
20	75	25
20	100	10
20	125	0
20	150	0

Control electrodes, where crystallin fibrils were deposited but no DEP forces applied, showed no immobilisation of crystallin fibrils (**Figure 4.26**, B), as compared to electrodes where immobilisation of crystallin fibrils by DEP was successful. Representative SEM images of crystallin fibrils immobilised on electrode pairs are shown in **Figure 4.26** (Section 7.15.2).

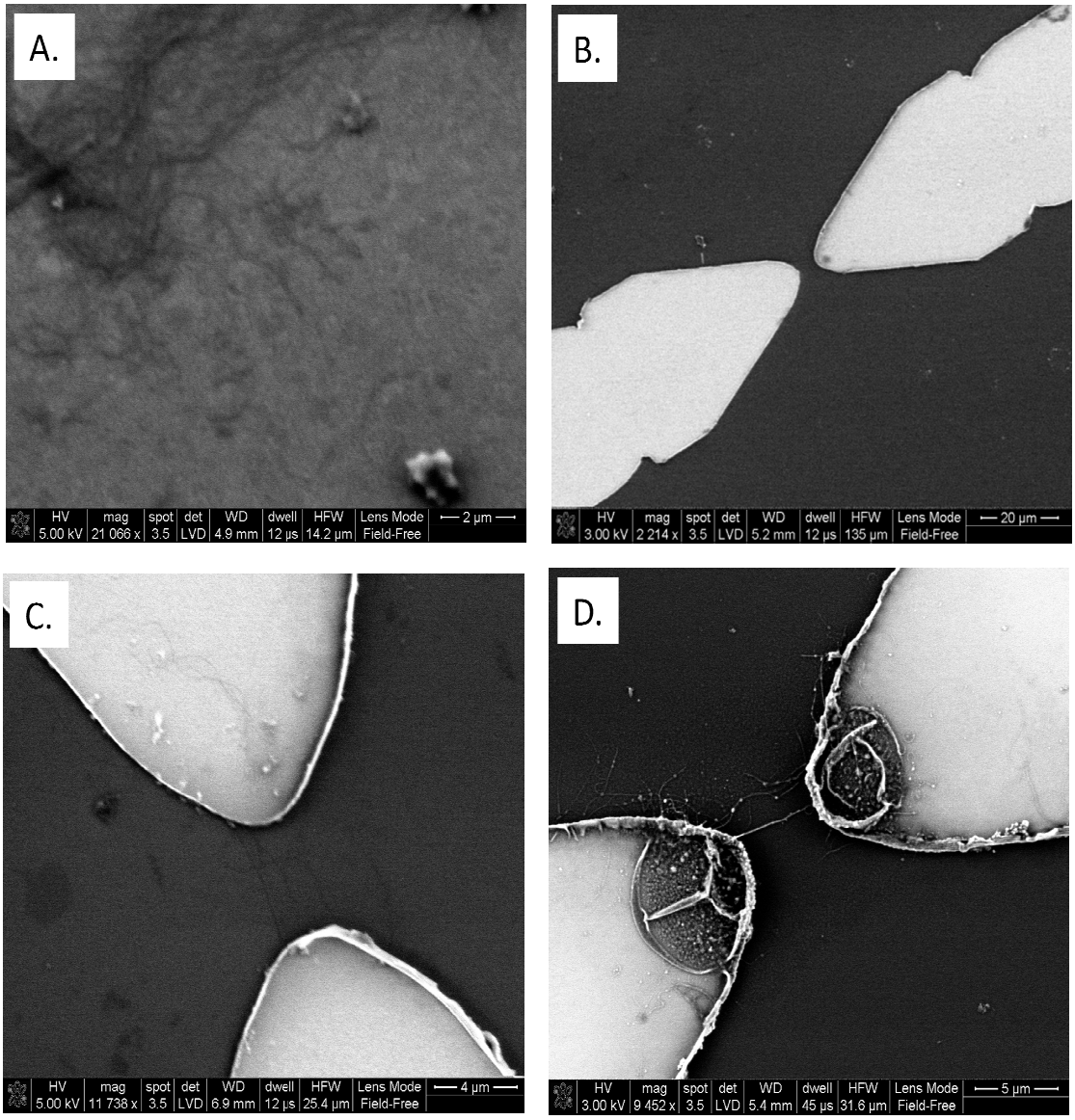

Figure 4.26. *SEM images showing A) Crystallin amyloid fibrils deposited on Au substrate, B) Control electrode pair, where crystallin fibrils were deposited but no DEP forces applied, and C) and D), representative images of where DEP forces applied resulted in successful immobilisation of crystallin fibrils between electrode pairs.*

As shown in **Figure 4.26**, D, when voltages of 20 Vpp at 100 kHz were applied to electrodes, as well as crystallin fibrils being immobilised, there was an unusual deposition of material at the tips of electrodes. By comparison to previously observed samples (**Figure 4.27**), and also by energy-dispersive X-ray spectroscopy (EDX) (Appendix C) it was ascertained that the gold was still intact, but at this point it is unknown what phenomena is occurring.

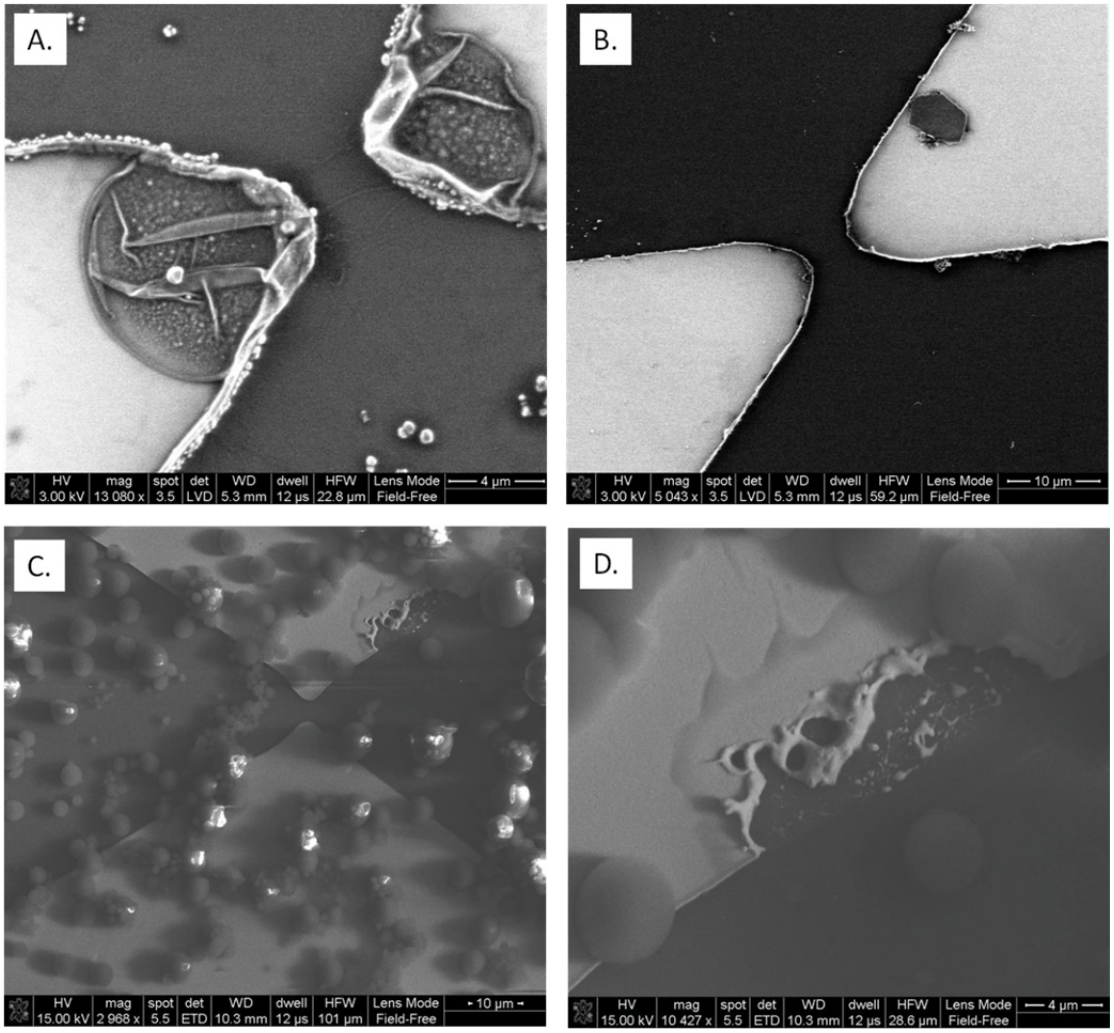

Figure 4.27. *SEM images of DEP electrodes showing unusual deposition, A) at the electrode tip, scale bar 4 µm, and B) at other places on the electrode, scale bar 10 µm. C) and D) are comparison SEM images of instances where the deposited gold layer has been known to be removed. Scale bars are 10 µm and 4 µm respectively.*

4.11. Conductive properties of immobilised crystallin fibrils

As mentioned previously, DEP can be used as a means of immobilising particles, in order that different properties, such as conductivity in this case, may be investigated. The turnover frequency of a particle can also be used to reveal some information about conductive properties. In this section, the conductive properties of immobilised crystallin fibrils will be discussed, firstly, as approximated by turnover frequency, and also as determined experimentally.

4.11.1. Conductivity estimated by turnover frequency

From Equation 4.7, the estimated turnover frequency can be used to give some approximation of the conductivity of crystallin fibrils.

The turnover frequency (f_{to}) was determined experimentally to be approximately 100 kHz (**Table 4.6**, A), as it was above this frequency that positive dielectrophoresis was no longer observed (**Table 4.5**).

Another important variable is permittivity, also referred to as the dielectric constant. The permittivity of free space (ε_0), is a fundamental constant and is given by $\varepsilon_0 = 8.85 \times 10^{-12}$ C/Vm (**Table 4.6**, B). The permittivity of a material reflects the sum total of the polarisation response of the matter plus the residual electric field (Kirby, 2010). The permittivity of the medium (ε_m) was calculated from literature values for the permittivities of the components of the buffer mixture in which the crystallin fibrils are suspended, 25% *n*-propanol (**Table 4.6**, C) (Kirby, 2010). The permittivity of the particle, in this case, the crystallin fibrils, was assumed to be equivalent to the permittivity of protein, which is accepted to be between 10 and 35 (**Table 4.6**, D) (Simonson and Brooks III, 1996).

The conductivity of the medium was measured using a digital conductivity meter. The medium is the buffer (25% *n*-propanol), and this had a conductivity of 2 μS/cm (**Table 4.6**, E).

From the variables described above, it is possible to very approximately calculate the theoretical conductivity of the particle (a crystallin fibril), as being in the range of 10^{-4} S/m (Calculated by Maria Dimaki using MATLAB, *personal communication*).

***Table 4.6**. Summary of the variables required to calculate the conductivity of a particle from turnover frequency.*

Variable	Value	
A) Turnover frequency (f_{to})	100 kHz	Estimated from DEP experiments (see **Table 4.5**)
B) Permittivity of vacuum (ε_0)	$\varepsilon_0 = 8.85 \times 10^{-12}$ C/Vm	Fundamental constant
C) Permittivity of medium (ε_m)	$\varepsilon_m = \frac{1}{4}.20 + \frac{3}{4}.80 = 65$	Calculated from buffer mixture (25% *n*-propanol) $\varepsilon_m = \frac{1}{4}.\varepsilon_{n-propanol} + \frac{3}{4}.\varepsilon_{water}$
D) Permittivity of particle (ε_p)	10-35	Assumed to be that of protein
E) Conductivity of medium (σ_m)	2 μS/cm	Measured
F) Conductivity of particle (σ_p)	~ 9×10^{-4} S/m	Unknown – calculated from Equation 7

4.11.2. Conductivity measured experimentally by I-V curves

As was shown in Section 4.10.3, crystallin fibrils were successfully immobilised between electrode pairs using DEP. This allowed for investigation into the electrical properties of the immobilised fibrils, and in this case, an investigation into the I-V characteristics of a smaller, and more specific number of fibrils than were observed for the network measurements (Section 4.5). I-V curves were constructed for the pairs of DEP electrodes using a probe station and parameter analyser (Section 7.15.3), as was used for the network measurements.

I-V curves were able to be obtained for three pairs of electrodes, with current values in the range of 10^{-10} A recorded for bias voltages in the range of 0–2 V (**Figure 4.28**). Other electrode pairs failed to give I-V curves above that observed for a blank electrode pair (**Figure 4.28**, insert), suggesting that in these cases although fibrils were immobilised between electrodes, there was not good contact between the gold electrodes and the fibrils.

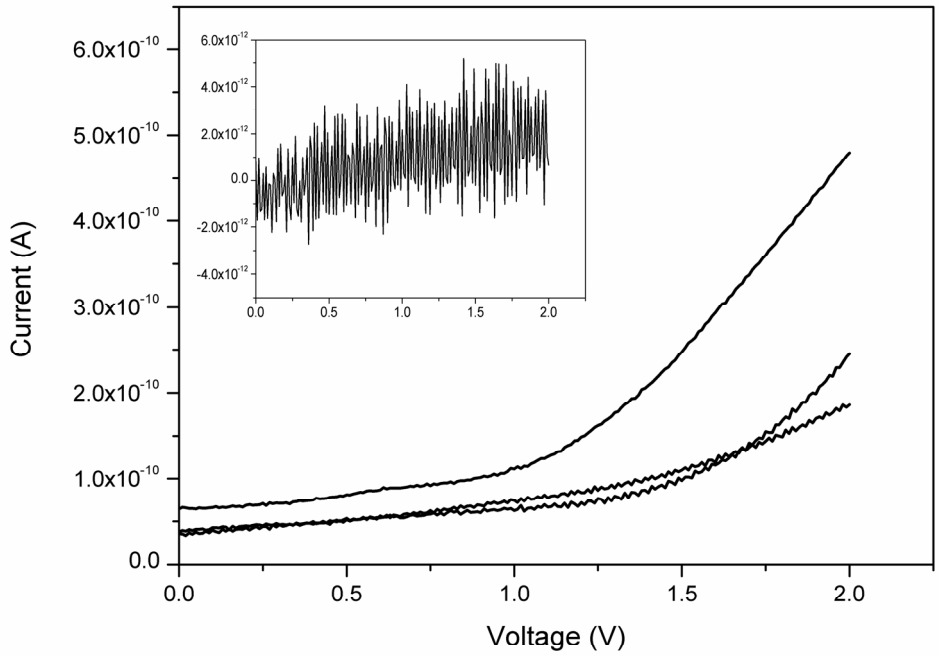

Figure 4.28. *Typical current-voltage (I-V) curves recorded for crystallin amyloid fibrils immobilised between electrode pairs by DEP for three different samples. Insert shows blank electrode pair.*

After I-V measurements were performed, the electrodes were covered with a thin layer of gold and it was verified by SEM that crystallin fibrils were immobilised between these electrodes. Clear SEM images were obtained for one pair of electrodes (**Figure 4.29**), and it can be seen that there are a number of fibrils present between the electrode pair.

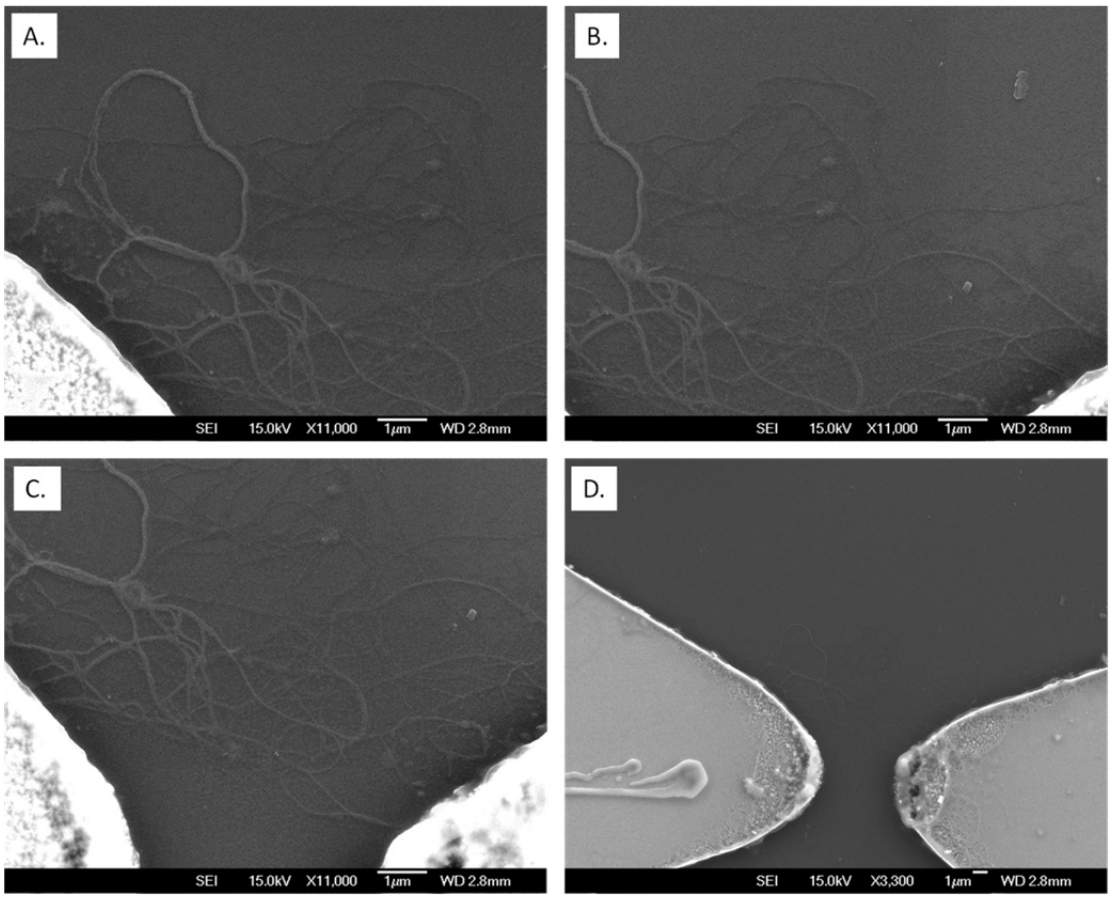

Figure 4.29. *A), B), and C) SEM images of electrode pair which gave the highest current values. D) SEM image of electrode pair used for blank measurements. Scale bar is 1 μm in all images.*

From the I-V curves obtained and the SEM images it is possible to obtain an approximate value in S/cm for the conductivity of the crystallin fibrils. For the DEP chip for which the SEM images in **Figure 4.29** were obtained, the current value at 2 V was 5 x 10^{-10} A, which gives a resistance value of 4 x 10^{8} Ω. From the SEM images (**Figure 4.29**), it can be approximated that there are 20 fibrils of average length 6 μm between the two electrodes. From these values, the conductivity of the crystallin amyloid fibrils can be approximated to be in the range of 10^{-6} S/m. Given that a number of approximations have been made in the calculation of this conductivity value as well as the theoretical one based on turnover frequency, no detailed comparison can be made between these two values. However, it is worth noting that the conductivity of small bundles of crystallin fibrils does correlate well to what was seen in the network measurements in Section 4.5.

4.12. Summary

Investigation into the conductive properties of amyloid fibril networks revealed amyloid fibrils formed from bovine insulin, fungal hydrophobins, and crude fish crystallins to all have low conductivity in the unmodified state, with typical current values in the nA to pA range achieved. These unmodified fibrils can then be treated as a nanowire scaffold, where their conductivity is increased through modification, or used unmodified in other applications. The modification of bovine insulin amyloid fibrils with the conductive polymers polyaniline and polypyrrole resulted in increased conductivity: by approximately two and four orders of magnitude respectively.

Amyloid fibrils formed from crude fish crystallin proteins were able to be manipulated on a microchip using DEP. DEP was used to immobilise small bundles of fibrils between pairs of gold electrodes, which allowed the conductive properties of small numbers of crystallin fibrils to be examined, and these were seen to correlate well with the level of conductivity observed in network measurements.

4.13. References

Adams M, Blundell T, Dodson E, Dodson G, Vijayan M, Baker E, Harding M, Hodgkin D, Rimmer B, Sheat S. 1969. Structure of rhombohedral 2 zinc insulin crystals. *Nature* **224**:491–495.

Ateh D, Navsaria H, Vadgama P. 2006. Polypyrrole-based conducting polymers and interactions with biological tissues. *Journal of the Royal Society Interface* **3**:741.

Bai H, Xu F, Anjia L, Matsui H. 2009. Low temperature synthesis of ZnO nanowires by using a genetically-modified collagen-like triple helix as a catalytic template. *Soft Matter* **5**:966–969.

Beever R, Dempsey G. 1978. Function of rodlets on the surface of fungal spores. *Nature* **272**:608–610.

Beever R, Redgwell R, Dempsey G. 1979. Purification and chemical characterization of the rodlet layer of Neurospora crassa conidia. *Journal of Bacteriology* **140**:1063.

Bockrath M, Markovic N, Shepard A, Tinkham M, Gurevich L, Kouwenhoven L, Wu M, Sohn L. 2002. Scanned conductance microscopy of carbon nanotubes and łambda-DNA. *Nano Letters* **2**:187–190.

Braun E, Eichen Y, Sivan U, Ben-Yoseph G. 1998. DNA-templated assembly and electrode attachment of a conducting silver wire. *Nature* **391**:775–778.

Carswell A., Edgar A, Grady B. 2003. Adsorbed surfactants as templates for the synthesis of morphologically controlled polyaniline and polypyrrole nanostructures on flat surfaces: from spheres to wires to flat films. *Journal of the American Chemical Society* **125**:14793–14800.

Castillo J, Tanzi S, Dimaki M, Svendsen W. 2008. Manipulation of self-assembly amyloid peptide nanotubes by dielectrophoresis. *Electrophoresis* **29**:5026–5032.

Chandrasekhar P. 1999. Conducting polymers, fundamentals and applications: a practical approach. Springer Netherlands.

Chiang C, Fincher Jr C, Park Y, Heeger A, Shirakawa H, Louis E, Gau S, MacDiarmid A. 1977. Electrical conductivity in doped polyacetylene. *Physical Review Letters* **39**:1098–1101.

Delano W. 2002. The PyMOL Molecular Graphics System.

Dempsey G, Beever R. 1979. Electron microscopy of the rodlet layer of Neurospora crassa conidia. *Journal of Bacteriology* **140**:1050.

Dimaki M. 2009. Dielectrophoresis: A simple introduction. Technical University of Denmark.

Dimaki M, Bøggild P. 2005. Frequency dependence of the structure and electrical behaviour of carbon nanotube networks assembled by dielectrophoresis. *Nanotechnology* **16**:759–763.

Domigan L, Healy J, Meade S, Blaikie R, Gerrard J. 2011. Controlling the dimensions of amyloid fibrils: Towards homogenous components for bionanotechnology. *Biopolymers* **97**:123–133.

Drury C, Mutsaers C, Hart C, Matters M, De Leeuw D. 1998. Low-cost all-polymer integrated circuits. *Applied Physics Letters* **73**:108–110.

Fan Y, Chen X, Trigg A, Tung C, Kong J, Gao Z. 2007. Detection of microRNAs using target-guided formation of conducting polymer nanowires in nanogaps. *Journal of the American Chemical Society* **129**:5437–5443.

Ford W, Harnack O, Yasuda A, Wessels J. 2001. Platinated DNA as precursors to templated chains of metal nanoparticles. *Advanced Materials* **13**:1793–1797.

Genies E, Boyle A, Lapkowski M, Tsintavis C. 1990. Polyaniline: a historical survey. *Synthetic Metals* **36**:139–182.

Gerard M, Chaubey A, Malhotra B. 2002. Application of conducting polymers to biosensors. *Biosensors and Bioelectronics* **17**:345–359.

Giraud G, Pethig R, Schulze H, Henihan G, Terry J, Menachery A, Ciani I, Corrigan D, Campbell C, Mount A. 2011. Dielectrophoretic manipulation of ribosomal RNA. *Biomicrofluidics* **5**:024116.

Gomez-Navarro C, Moreno-Herrero F, De Pablo P, Colchero J, Gomez-Herrero J, Baro A. 2002. Contactless experiments on individual DNA molecules show no evidence for molecular wire behavior. *Proceedings of the National Academy of Sciences of the United States of America* **99**:8484.

Gonzalez C, Remcho V. 2005. Harnessing dielectric forces for separations of cells, fine particles and macromolecules. *Journal of Chromatography A* **1079**:59–68.

Guimard N, Gomez N, Schmidt C. 2007. Conducting polymers in biomedical engineering. *Progress in Polymer Science* **32**:876–921.

Hamedi M, Herland A, Karlsson R, Inganas O. 2008. Electrochemical devices made from conducting nanowire networks self-assembled from amyloid fibrils and alkoxysulfonate PEDOT. *Nano Letters* **8**:1736–1740.

Harding M, Hodgkin D, Kennedy A, O'Connor A, Weitzmann P. 1966. The crystal structure of insulin II. An investigation of rhombohedral zinc insulin crystals and a report of other crystalline forms. *Journal of Molecular Biology* **16**:212–226.

He H, Li C, Tao N. 2001. Conductance of polymer nanowires fabricated by a combined electrodeposition and mechanical break junction method. *Applied Physics Letters* **78**:811.

Herland A, Thomsson D, Mirzov O, Scheblykin I, Inganäs O. 2008. Decoration of amyloid fibrils with luminescent conjugated polymers. *Journal of Materials Chemistry* **18**:126–132.

Herland A, Björk P, Hania P, Scheblykin I, Inganäs O. 2007. Alignment of a conjugated polymer onto amyloid-like protein fibrils. *Small* **3**:318–25.

Huang J, Kaner R. 2004. Nanofiber formation in the chemical polymerization of aniline: A mechanistic study. *Angewandte Chemie* **116**:5941–5945.

Huang J, Virji S, Weiller B, Kaner R. 2003. Polyaniline nanofibers: facile synthesis and chemical sensors. *Journal of the American Chemical Society* **125**:314–315.

Inzelt G, Pineri M, Schultze J, Vorotyntsev M. 2000. Electron and proton conducting polymers: recent developments and prospects. *Electrochimica Acta* **45**:2403–2421.

Jaimohan S, Naresh M, Mandal A. 2008. Crystal structure of bovine insulin (hexameric form). *DOI: 10.2210/pdb 2zp6/pdb*.

Jang J. 2006. Conducting polymer nanomaterials and their applications. *Emissive Materials Nanomaterials*:189–260.

Kang Y, Li D, Kalams S, Eid J. 2008. DC-Dielectrophoretic separation of biological cells by size. *Biomedical Microdevices* **10**:243–249.

Kirby B. 2010. Micro- and nanoscale fluid mechanics : transport in microfluidic devices. Cambridge: Cambridge University Press.

Kuzyk A. 2011. Dielectrophoresis at the nanoscale. *Electrophoresis* **32**:2307–2313.

Kuzyk A, Yurke B, Toppari J, Linko V, Törmä P. 2008. Dielectrophoretic trapping of DNA origami. *Small* **4**:447–450.

Lapizco-Encinas B, Ozuna-Chacón S, Rito-Palomares M. 2008. Protein manipulation with insulator-based dielectrophoresis and direct current electric fields. *Journal of Chromatography A* **1206**:45–51.

Lapizco-Encinas B, Rito-Palomares M. 2007. Dielectrophoresis for the manipulation of nanobioparticles. *Electrophoresis* **28**:4521–4538.

Li C, Bai H, Shi G. 2009. Conducting polymer nanomaterials: electrosynthesis and applications. *Chemical Society Reviews* **38**:2397–2409.

Li D, Huang J, Kaner R. 2008. Polyaniline nanofibers: a unique polymer nanostructure for versatile applications. *Accounts of Chemical Research* **42**:135–145.

Lin Y, Shiomi J, Maruyama S, Amberg G. 2007. Electrothermal flow in dielectrophoresis of single-walled carbon nanotubes. *Physical Review B* **76**:045419.

Liu J, Cai Z, Koley G. 2009. Charge transport and trapping in InN nanowires investigated by scanning probe microscopy. *Journal of Applied Physics* **106**:124907–124907.

Lu X, Zhang W, Wang C, Wen TC, Wei Y. 2010. One-dimensional conducting polymer nanocomposites: Synthesis, properties and applications. *Progress in Polymer Science* **36**:671–712.

Ma Y, Zhang J, Zhang G, He H. 2004. Polyaniline nanowires on Si surfaces fabricated with DNA templates. *Journal of the American Chemical Society* **126**:7097–7101.

MacDiarmid A, Chiang J, Richter A, Epstein A. 1987. Polyaniline: A new concept in conducting polymers. *Synthetic Metals* **18**:285–290.

MacDiarmid A, Jones W, Norris I, Gao J, Johnson A, Pinto N, Hone J, Han B, Ko F, Okuzaki H. 2001. Electrostatically-generated nanofibers of electronic polymers. *Synthetic Metals* **119**:27–30.

Malik S, Nandi A. 2002. Crystallization mechanism of regioregular poly (3-alkyl thiophene). *Journal of Polymer Science Part B: Polymer Physics* **40**:2073–2085.

Malvankar N, Vargas M, Nevin K, Franks A, Leang C, Kim B, Inoue K, Mester T, Covalla S, Johnson J. 2011. Tunable metallic-like conductivity in microbial nanowire networks. *Nature Nanotechnology* **6**:573–579.

Martin C. 1995. Template synthesis of electronically conductive polymer nanostructures. *Accounts of Chemical Research* **28**:61–68.

del Mercato L, Pompa P, Maruccio G, Torre A, Sabella S, Tamburro A, Cingolani R, Rinaldi R. 2007. Charge transport and intrinsic fluorescence in amyloid-like fibrils. *Proceedings of the National Academy of Sciences of the United States of America* **104**:18019–18024.

Moncada-Hernandez H, Baylon-Cardiel J, Pérez-González V, Lapizco-Encinas B. 2011. Insulator-based dielectrophoresis of microorganisms: theoretical and experimental results. *Electrophoresis* **32**:2502–2511.

Moon H, Kim H, Kim N, Roh Y. 2010. Fabrication of highly uniform conductive polypyrrole nanowires with DNA template. *Journal of Nanoscience and Nanotechnology* **10**:3180–3184.

Nickels P, Dittmer W, Beyer S, Kotthaus J, Simmel F. 2004. Polyaniline nanowire synthesis templated by DNA. *Nanotechnology* **15**:1524.

Nielsen L, Khurana R, Coats A, Frokjaer S, Brange J, Vyas S, Uversky V, Fink A. 2001. Effect of environmental factors on the kinetics of insulin fibril formation: Elucidation of the molecular mechanism. *Biochemistry* **40**:6036–6046.

Niu Z, Bruckman MA, Li S, Lee LA, Lee B, Pingali SV, Thiyagarajan P, Wang Q. 2007a. Assembly of tobacco mosaic virus into fibrous and macroscopic bundled arrays mediated by surface aniline polymerization. *Langmuir* **23**:6719–6724.

Niu Z, Bruckman M, Kotakadi V, He J, Emrick T, Russell T, Yang L, Wang Q. 2006. Study and characterization of tobacco mosaic virus head-to-tail assembly assisted by aniline polymerization. *Chemical Communications*:3019–3021.

Niu Z, Liu J, Lee L, Bruckman M, Zhao D, Koley G, Wang Q. 2007b. Biological templated synthesis of water-soluble conductive polymeric nanowires. *Nano Letters* **7**:3729–3733.

Numata M, Hasegawa T, Fujisawa T, Sakurai K, Shinkai S. 2004. Beta-1, 3-glucan (schizophyllan) can act as a one-dimensional host for creation of novel poly (aniline) nanofiber structures. *Organic Letters* **6**:4447–4450.

Paananen A, Vuorimaa E, Torkkeli M, Penttilä M, Kauranen M, Ikkala O, Lemmetyinen H, Serimaa R, Linder MB. 2003. Structural hierarchy in molecular films of two class II hydrophobins. *Biochemistry* **42**:5253–5258.

Patolsky F, Weizmann Y, Lioubashevski O, Willner I. 2002. Au-nanoparticle nanowires based on DNA and polylysine templates. *Angewandte Chemie - International Edition* **41**:2323–2327.

Patolsky F, Weizmann Y, Willner I. 2004. Actin-based metallic nanowires as bio-nanotransporters. *Nature Materials* **3**:692–695.

Pinto N, Johnson Jr A, MacDiarmid A, Mueller C, Theofylaktos N, Robinson D, Miranda F. 2003. Electrospun polyaniline/polyethylene oxide nanofiber field-effect transistor. *Applied Physics Letters* **83**:4244.

Pohl H. 1951. The motion and precipitation of suspensoids in divergent electric fields. *Journal of Applied Physics* **22**:869–871.

Scheibel T, Parthasarathy R, Sawicki G, Lin X-M, Jaeger H, Lindquist S. 2003. Conducting nanowires built by controlled self-assembly of amyloid fibers and selective metal deposition. *Proceedings of the National Academy of Sciences of the United States of America* **100**:4527–4532.

Shi W, Ge D, Wang J, Jiang Z, Ren L, Zhang Q. 2006. Heparin-controlled growth of polypyrrole nanowires. *Macromolecular Rapid Communications* **27**:926–930.

Shirakawa H, Louis E, MacDiarmid A, Chiang C, Heeger A. 1977. Synthesis of electrically conducting organic polymers: halogen derivatives of polyacetylene. *Journal of the American Chemical Society*:578–580.

Simonson T, Brooks III C. 1996. Charge screening and the dielectric constant of proteins: insights from molecular dynamics. *Journal of the American Chemical Society* **118**:8452–8458.

Smith G, Pangborn W, Blessing R. 2005. The structure of T6 bovine insulin. *Acta Crystallographica Section D: Biological Crystallography* **61**:1476–1482.

Storm A, van Noort J, de Vries S, Dekker C. 2001. Insulating behavior for DNA molecules between nanoelectrodes at the 100 nm length scale. *Applied Physics Letters* **79**:3881–3883.

Sunde M, Kwan A., Templeton M, Beever R, Mackay J. 2008. Structural analysis of hydrophobins. *Micron* **39**:773–784.

Sze S. 2002. Lithography and etching. In: . *Semiconductor devices: physics and technology* 2nd ed. Wiley, pp. 404–451.

Szilvay G, Paananen A, Laurikainen K, Vuorimaa E, Lemmetyinen H, Peltonen J, Linder M. 2007. Self-assembled hydrophobin protein films at the air-water interface: structural analysis and molecular engineering. *Biochemistry* **46**:2345–2354.

Tanaka H, Herland A, Lindgren L, Tsutsui T, Andersson M. 2008. Enhanced current efficiency from bio-organic light-emitting diodes using decorated amyloid fibrils with conjugated polymer. *Nano Letters* **8**:2858–2861.

Tran H, Li D, Kaner R. 2009. One-Dimensional Conducting Polymer Nanostructures: Bulk Synthesis and Applications. *Advanced Materials* **21**:1487–1499.

Tran P, Alavi B, Gruner G. 2000. Charge transport along the lambda-DNA double helix. *Physical Review Letters* **85**:1564–1567.

Wang C, Wang Z, Li M, Li H. 2001. Well-aligned polyaniline nano-fibril array membrane and its field emission property. *Chemical Physics Letters* **341**:431–434.

Zurdo J, Guijarro J, Dobson C. 2001. Preparation and characterization of purified amyloid fibrils. *Journal of the American Chemical Society* **123**:8141.

5. Chapter Five

A model application: glucose sensing

5.1. Introduction

The model nanowire application chosen was the creation of a glucose sensor, *via* immobilisation of glucose oxidase (GOx) to the amyloid fibril scaffold, and modification of electrodes with this now active scaffold. GOx was used in this study as it is used in a range of industrial processes, including in glucose sensing (Wong *et al*., 2008). Also, the relatively low cost and good stability of GOx make the glucose/GOx system a convenient model for method development, particularly in the area of biosensing (Raba and Mottola, 1995).

Conventional methods for enzyme immobilisation on the electrode surfaces include adsorption, cross-linking, electrochemical co-polymerisation, covalent attachment, and entrapment in polymeric gels or carbon paste (Yemini *et al*., 2006). Some of the limitations of these methods are low quantities of attached enzymes, partial loss of enzyme activity, low stability, non-biocompatible immobilisation compounds, and time consuming immobilisation processes (Wang, 1991). Using biomaterials such as lipids, proteins, and peptides can overcome some of these shortcomings (Deng *et al*., 2004).

There are a few previously reported cases of PNT/PNFs being used in this way, beginning with FF peptides (Yemini *et al*., 2005a). Electrodes modified with FF peptides were shown to have H_2O_2 and NADH sensing capabilities (Yemini *et al*., 2005b), and those modified with GOx functionalised FF peptides showed an amperometric response to glucose (Yemini *et al*., 2005b). A collagen-like peptide and the ionic complementary peptide EFK16-11 have also been used in this way (Qian *et al*., 2009; Yemini *et al*., 2006).

This chapter describes the formation of GOx functionalised amyloid fibrils, and the glucose sensing capabilities of gold electrodes modified with these fibrils.

5.2. Glucose oxidase (GOx)

Since it was first discovered by Muller in *Aspergillus niger* extracts (Müller, 1928), glucose oxidase (β-D-glucose:oxygen 1-oxidoreductase, GOx) has been found to be produced naturally in a range of fungi and insects (Wong *et al*., 2008). The function of GOx *in vivo* is as an antibacterial and antifungal agent, *via* the production of hydrogen peroxide (Wong *et al*., 2008). GOx is used in many industrial applications, such as food preservation, baking, dry egg production, wine production, gluconic acid production, glucose sensing, and potentially in fuel cell applications (Wong *et al*., 2008). GOx has been purified from a range of fungal sources (Bankar *et al*., 2009), with *A. niger* most commonly used for GOx production (Pluschkell *et al*., 1996), and this was used in this study.

GOx is a flavoprotein which catalyzes the oxidation of β-D-glucose by molecular oxygen to glucono-δ-lactone, which spontaneously hydrolyzes to form gluconic acid, with hydrogen peroxide also produced (Leskovac *et al*., 2005). Subsequently the flavin adenine dinucleotide (FAD) cofactor of GOx is reduced to $FADH_2$. The overall reaction scheme is shown in **Figure 5.1**.

GOx from *A. niger* has a molecular weight of approximately 160 kDa, and is a dimeric glycoprotein, with two identical polypeptide chain subunits covalently linked *via* disulfide bonds (Hecht *et al*., 1993). Each subunit contains one molecules of non-covalently linked FAD as a cofactor, which functions by acting as an electron carrier during catalysis (Wilson and Turner, 1992; Wong *et al*., 2008). The structure of GOx is shown in **Figure 5.2**.

GOx is widely used in glucose sensing, due to its high specificity for glucose, and broad temperature (20-50 °C) and pH (4-7) range (Bankar *et al*., 2009).

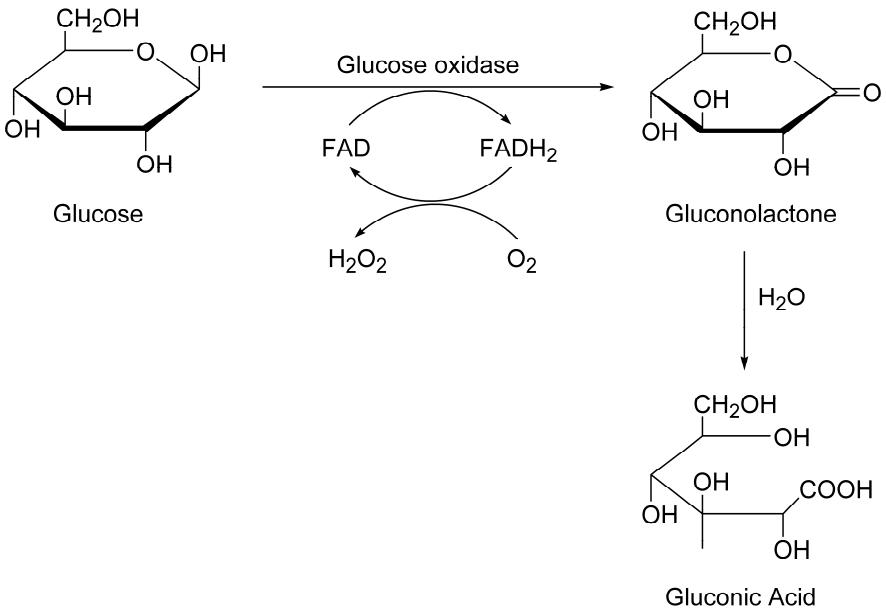

Figure 5.1. *Schematic of the overall reaction catalyzed by GOx. The reaction involves oxidation of glucose to gluconolactone, which spontaneously hydrolyzes to form gluconic acid. Consequently, the FAD cofactor of GOx is reduced to* $FADH_2$*, and molecular oxygen to reduced to* H_2O_2*, the production of which leads to the reoxidation of the cofactor. Adapted from Leskovac et al. (2005).*

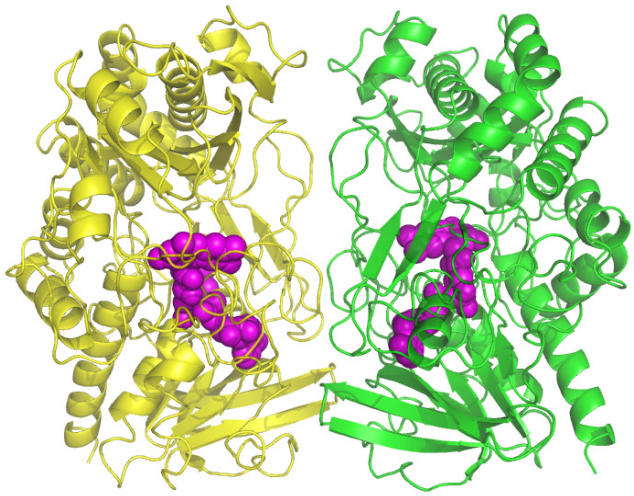

Figure 5.2. *PyMOL image of the GOx dimer (Delano, 2002), with the two subunits shown in yellow and green. The FAD cofactors are shown in magenta. Image was constructed using PDB file 1GAL (Hecht et al., 1993)*

5.3. Amplex® red assay to determine GOx activity

GOx activity was determined using the Amplex® red assay (Section 7.17.1). A simplified mechanism for this assay is shown in

Figure 5.3. When GOx converts glucose to gluconolactone, H_2O_2 is produced (**Figure 5.1**). In the presence of horseradish peroxidase (HRP), Amplex® red (10-acetyl-3,7-dihydroxyphenoxazine) reacts with H_2O_2 in 1:1 reaction stoichiometry to produce the red-fluorescent oxidation product resorufin. The fluorescence of resorufin is detected at excitation/emission of approximately 570/585 nm.

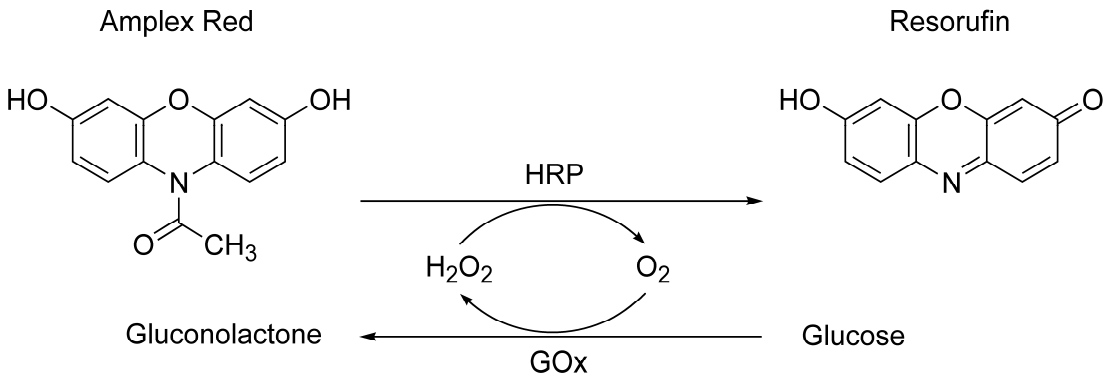

Figure 5.3. *A simplified mechanism of the Amplex® red assay for glucose oxidase activity. The Amplex® red assay works by coupling the GOx and HRP mediated reactions. The H_2O_2 produced by the GOx catalysed reaction reacts with Amplex® red in the HRP catalysed reaction to produce the fluorescent compound resorufin.*

A standard curve for the Amplex® red assay was constructed using GOx concentrations ranging from 1-7 mU/mL (**Figure 5.4**), with one unit defined as the amount that will oxidase one micromole of β-D-glucose to D-gluconolactone and H_2O_2 per minute at pH 5.1 and 30 °C (Section 7.17.2).

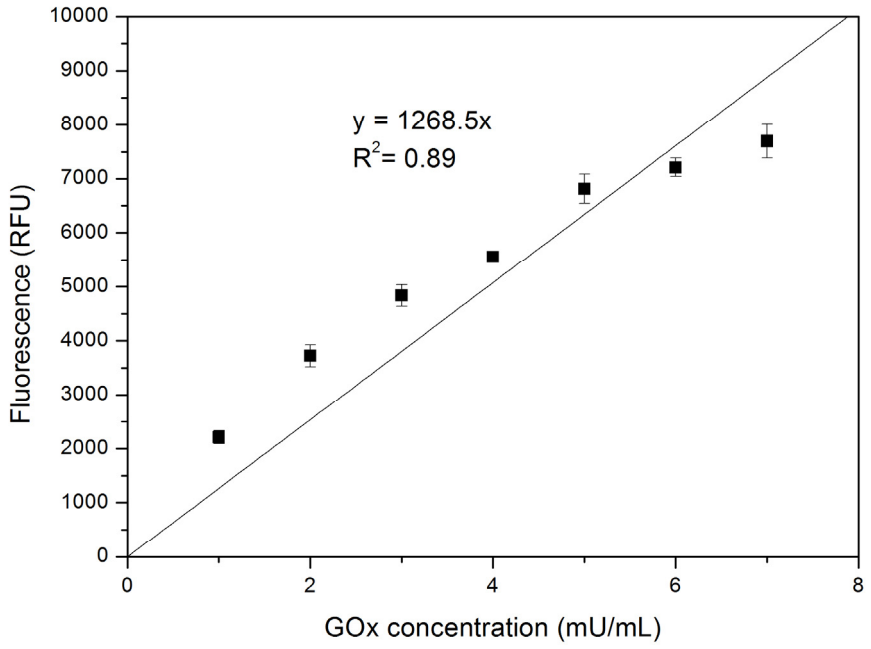

Figure 5.4. *GOx standard curve constructed using the Amplex® red assay for GOx concentrations from 1-7 mU/mL. One unit is defined as the amount that will oxidase 1.0 µmol of β-D-glucose to D-gluconolactone and H_2O_2 per minute at pH 5.1 and 30°C (Invitrogen, 2006).*

5.4. Immobilisation of GOx to insulin amyloid fibrils

GOx was immobilised to the insulin amyloid fibril scaffold using glutaraldehyde and SDS-PAGE was used to assess the degree of cross-linking. After immobilisation, the activity of the cross-linked samples was examined using the Amplex® red assay, to confirm that GOx was still active once immobilised.

5.4.1. Glutaraldehyde cross-linking of GOx to insulin fibrils

Using the methods previously established in our lab (Pilkington *et al*., 2010), GOx was immobilised onto insulin fibrils using the cross-linking molecule glutaraldehyde (GA) (**Figure 5.5**). GA forms imine bonds between the free amine groups of surface lysine residues on proteins and the aldehyde groups of GA.

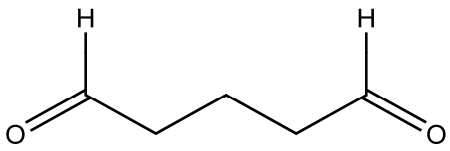

Figure 5.5*. Structure of the cross-linking molecule glutaraldehyde (GA) (Hermanson, 1996).*

Dimeric glycosylated GOx has 30 lysine residues in its sequence, of which 24 of these are located on the surface of the protein, as shown in **Figure 5.6**. Of these surface lysines, five are available for cross-linking, as was shown by covalently reacting the residues with N-hydroxysuccinimde (Baszkin *et al*., 1997; Frederick *et al*., 1990; Kriechbaum *et al*., 1989).

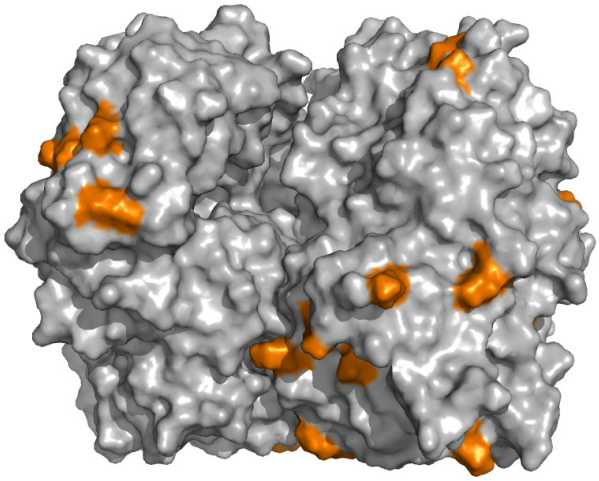

Figure 5.6. *Surface representation of the GOx dimer showing surface lysines residues in orange. Image was created using PyMOL from PDB file 1GAL (Delano, 2002; Hecht et al., 1993)*

The number of available lysine residues on the surface of insulin fibrils is unknown, due to insufficient structural information about the arrangement of native insulin within a fibril. However, it is thought that insulin fibrils form from association between monomers (Brange *et al*., 1997), and there is one lysine residue per monomer as shown in **Figure 5.7**. There are also two N-terminal amino groups available per insulin monomer.

A chain

G I V E Q C C A S V C S L Y Q L E N Y C N
1 10 20

B chain

F V N Q H L C G S H L V E A L Y L V C G E R G F F Y T P K A
1 10 20 30

Figure 5.7. Primary sequence of bovine insulin showing lysine residue in red.

The cross-linking protocol followed the previously established methods (Pilkington *et al*., 2010), with the exception of the reaction order. In order to try to minimize fibril-fibril cross-linking, and thus maintain the maximum possible surface area for immobilisation of GOx, GOx and GA were incubated first, and then fibrils added (Section 7.16).

SDS-PAGE, which denatures proteins using the detergent SDS and separates proteins based on molecular weight, was used to confirm cross-linking had occurred (Section 7.1). Amyloid fibrils are too large to enter the gel, and so remain in the well at the top of the gel. If GOx has been successfully immobilised to the amyloid fibrils then that too will remain in the well. If GOx has not been immobilised to the amyloid fibrils then it is free to move into the gel. The SDS-PAGE gel in **Figure 5.8** confirms that immobilisation of GOx to insulin fibrils was successful. Native GOx resulted in a single band at approximately 80 kDa (Lane 1), which corresponds to the molecular weight of monomeric GOx, due to the dimer being denatured by SDS. Insulin fibrils show no band, as they remain in the well (Lane 2). When GOx is incubated with insulin fibrils with no cross-linking molecule there appears to be some association with the fibrils, as shown by the decrease in intensity of the monomeric GOx band at 80 kDa (Lane 3). Cross-linking GOx alone using GA produces a very weak band at 80 kDa, and a band at 160 kDa, which corresponds to the stabilisation of the dimer by cross-linking (Lane 4). Lane 5 shows insulin fibrils cross-linked to themselves, with again no band due to the fibrils remaining in the well. When GOx is immobilised to insulin fibrils using GA there is no GOx band on the gel, due to the GOx remaining in the well with the insulin fibrils (Lane 6).

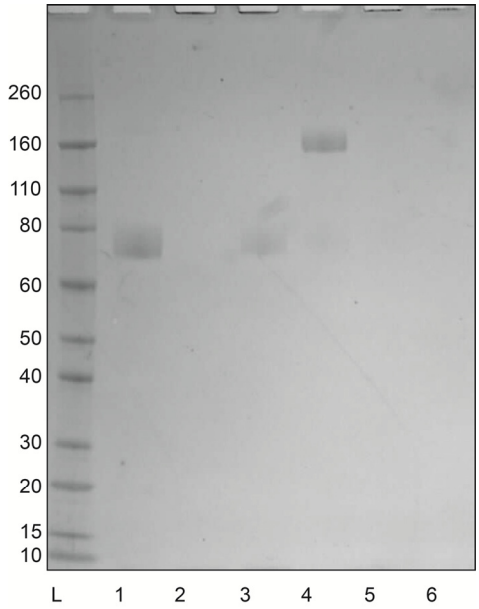

Figure 5.8. *SDS-PAGE gel of GA cross-linking of GOx to insulin fibrils. L = ladder (molecular weights in kDa on left hand side), 1 = GOx, 2 = insulin fibrils, 3 = GOx + insulin fibrils, 4 = GOx + GA, 5 = insulin fibrils + GA, and 6 = insulin fibrils + GA + GOx.*

The structures and morphologies of GOx-functionalised insulin fibrils (GOx:IF) were observed by TEM (Section 7.5), and representative images are shown in **Figure 5.9**. Under TEM, GOx gives a cloudy pattern (**Figure 5.9**, A and B), as grid assembly and staining is likely to cause the GOx dimer to be in a denatured anhydrous state. When GA is added to GOx, there is an increase in the density of the observed GOx (**Figure 5.9**, C and D), which is consistent with the presence of intermolecular cross-links. When GOx is added to insulin fibrils, without any cross-linker, there is still some association, and this is seen under TEM (**Figure 5.9**, E and F). The sample with GOx covalently cross-linked to insulin fibrils shows an increase in this association, as expected (**Figure 5.9**, G and H). It is also worth noting that not all GOx is immobilised to the fibrils, as cloudy structures similar to those observed in the GOx only sample are visible, and also that there is some inter-fibril cross-linking occurring, as evidenced by the increased density of the insulin fibril network. Further optimisation of the cross-linking method used in order to minimize these undesirable effects would be beneficial.

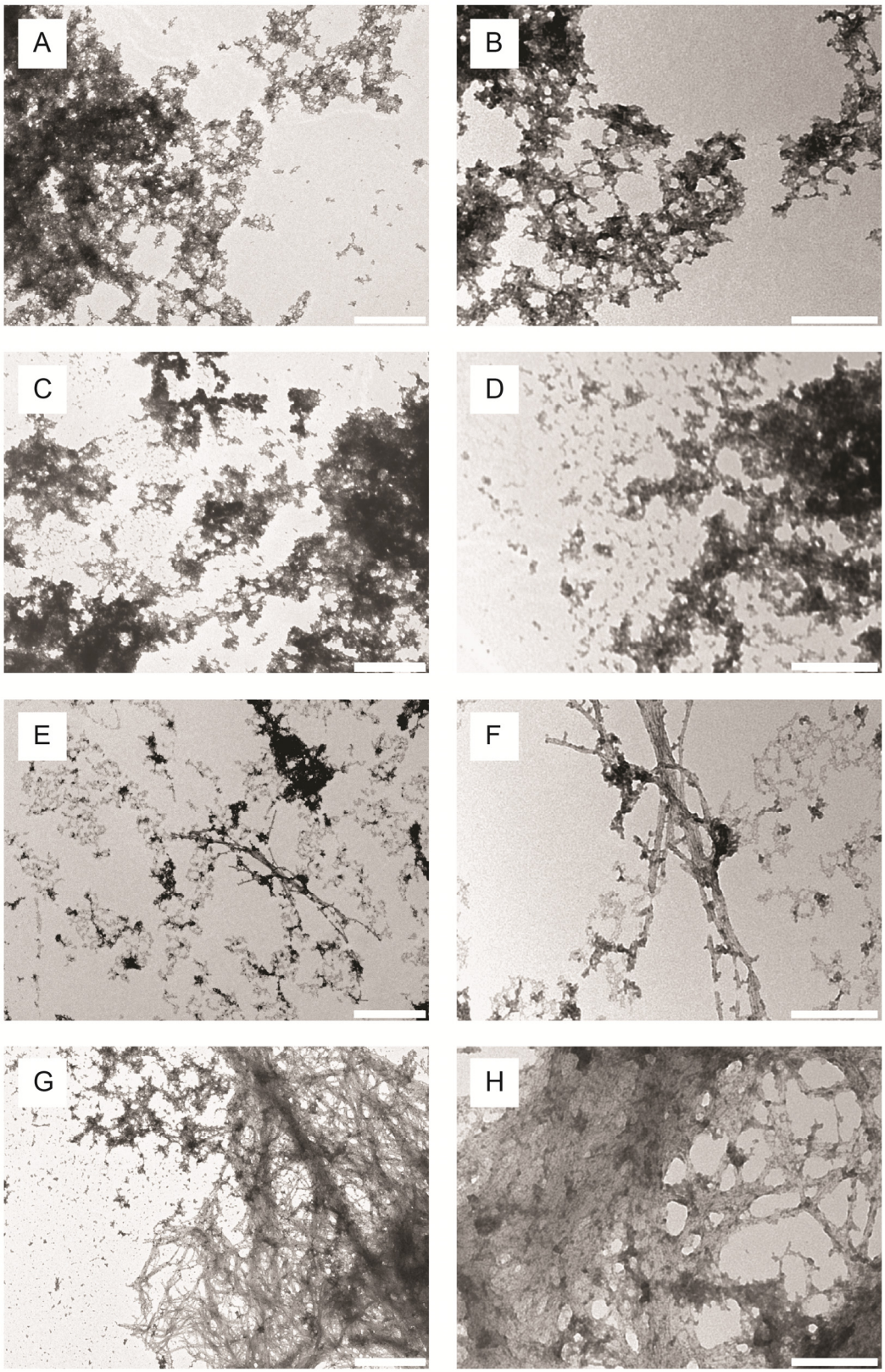

Figure 5.9. *Representative TEM images of GOx (A & B), GOx + GA (C & D), GOx + IF (E & F), and GOx + GA + IF (G & H). Scale bars are 0.5 μm (A, C, E, G) and 0.2 μm (B, D, F, H).*

5.4.2. Activity of cross-linked samples

The activity of cross-linked samples was assayed using the Amplex® red assay (Section 5.2.1). Firstly, the activity of all samples was tested in solution, and then in order to test the effectiveness of the cross-linker, the insulin fibrils were collected using centrifugation, and the activity of the supernatant tested. The amount of GOx activity remaining in the supernatant was indicative of the degree of immobilisation of GOx to the insulin fibrils that was achieved (Section 7.17.3).

Upon incubation of GOx with insulin fibrils, there was a slight decrease in activity compared to the GOx only control, with activity decreasing to 87 % as shown in **Figure 5.10**, suggesting that the presence of fibrils interferes with the reaction in some way, possibly due to some association of GOx with the insulin fibrils. No activity is lost when GOx alone is crosslinked. When GOx is crosslinked to the insulin fibrils there is also a slight drop in activity to 91 % of the GOx only control, this is expected as immobilisation of enzymes often results in some loss of activity. Upon comparison of the activity of the supernatant of the samples containing GOx and insulin fibrils, with and without the presence of glutaraldehyde, the sample with glutaraldehyde present has significantly less activity in the supernatant, 6 % as compared to 62 %, which demonstrates the effectiveness of the immobilisation.

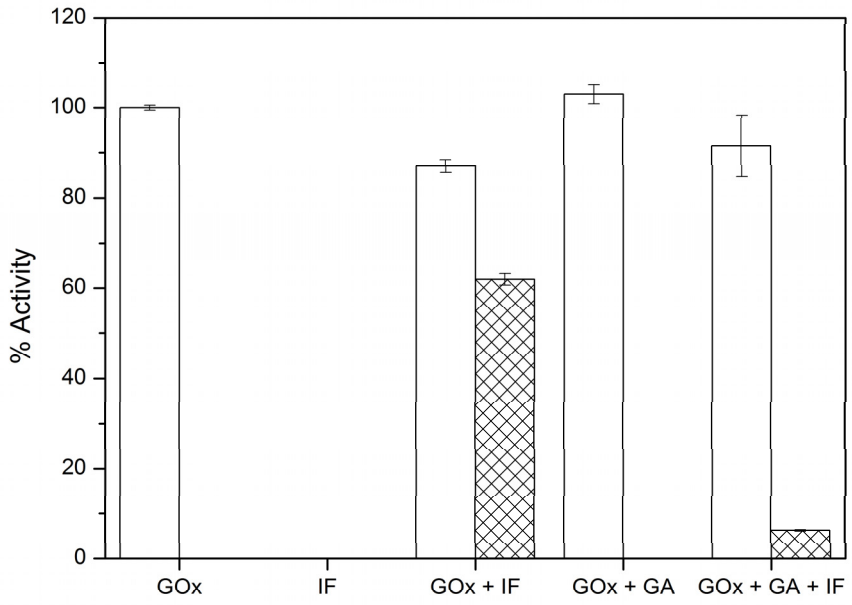

Figure 5.10. *Graph showing % GOx activity, standardised against the GOx only control, of samples containing insulin fibrils (IF), GOx + IF, GOx + glutaraldehyde (GA), and GOx + GA + IF (white bars). The samples GOx + IF and GOx + GA + IF were then centrifuged to collect the insulin fibrils and the activity of the supernatant tested to ascertain the effectiveness of the cross-linker (cross-hatched bars). Each value represents the average of three replicates, with error bars representing the standard deviation.*

5.5. Immobilisation of GOx to crystallin amyloid fibrils

The use of crystallin amyloid fibrils as a scaffold for enzyme immobilisation was also investigated, *via* the immobilisation of GOx to crystallin fibrils. Methods involving the use of GA, as well as an alternative cross-linking molecule, methylglyoxal (MG), were examined, with no successful immobilisation of GOx to the crystallin fibril scaffold. In order to resolve this issue the lysine availability of crystallin fibrils was analysed and the possibility of post-translational modification of fish crystallin proteins was investigated.

5.5.1. Cross-linking of GOx to crystallin fibrils

It was first attempted to immobilise GOx to crystallin fibrils using the methods established for the immobilisation of GOx to insulin fibrils *via* GA cross-linking (Pilkington *et al*., 2010). The degree of cross-linking was assessed by SDS-PAGE (**Figure 5.11**) (Section 7.1). Native GOx resulted in a band at approximately 80 kDa (Lane 1), which corresponds to the molecular weight of monomeric GOx, due to the dimer being denatured by SDS. There is also a slight band at approximately 160 kDa, indicating that the dimer was not completely denatured. Crude crystallin fibrils show no band, as they remain in the well (Lane 2). When GOx is incubated with crystallin fibrils with no cross-linking molecule the same bands appear as for GOx only (Lane 3). Cross-linking GOx alone using GA produces a very weak band at 80 kDa, and a band at 160 kDa, which corresponds to the stabilisation of the dimer by cross-linking, there is also a faint high molecular band, which corresponds to the presence of a higher order GOx species (Lane 4). When GOx is immobilised to crystallin fibrils using GA there is no decrease in the intensity of the GOx band on the gel, which indicates that no GOx was immobilised to the crystallin fibrils (Lane 5).

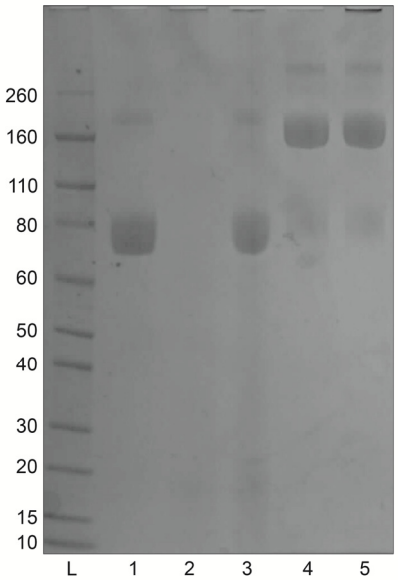

Figure 5.11. *SDS-PAGE gel of GA cross-linking of GOx to crude crystallin fibrils. L = ladder (molecular weights in kDa on left hand side), 1 = GOx, 2 = crude crystallin fibrils, 3 = GOx + crude crystallin fibrils, 4 = GOx + GA, 5 = crude crystallin fibrils + GA.*

As the established method did not result in successful immobilisation of GOx to crystallin fibrils, a number of alternate methods were tried, which involved altering various variables, including the total cross-linking reaction time, time of pre-incubation of the cross-linking molecule with the fibrils, the reaction temperature, the reaction order, and the concentrations of the cross-linker, GOx, and the fibrils (Section 7.20). The different conditions tried are summarised in **Table 5.1**.

Table 5.1. *Details of different conditions attempted for immobilisation of GOx to crude crystallin fibrils (GOx=glucose oxidase, CF=crystallin fibrils, and X=cross-linker).*

Variable	**Different conditions tried**
Reaction order	GOx+CF→X, GOx+X→CF, CF+X→GOx, GOx→CF→X, GOx→X→CF, GOx→CF→X,
Total reaction time (min)	30-120
Pre-incubation time (min) (GOx+CF/GOx+X/CF+X)	5-20
Reaction temperature (°C)	25, 37
Cross-linker	GA, MG, GA+MG
Cross-linker concentration	GA (10-150 mM), MG (1-4 %)
Crystallin fibril concentration (mg/mL)*	1.0–10.0
GOx concentration (mg/mL)	0.5–2.0

*This value is approximate. Fibrils were formed using the standard in-house conditions and then concentration by centrifugation.

An alternative cross-linking molecule was also used, methylglyoxal (MG) (**Figure 5.12).** MG is an α-dicarbonyl compound, and forms protein-protein cross-links by reacting with lysine and arginine residues, preferentially reacting with arginine residues (Miller *et al*., 2003). None of the cross-linking conditions detailed in **Table 5.1** were successful, with all resulting with levels of immobilisation similar to that seen in **Figure 5.11**.

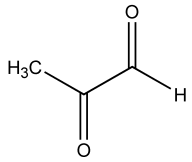

Figure 5.12. *The structure of methylglyoxal (MG) (Miller et al., 2003).*

5.6. Assessment of amino group availability of crystallin fibrils

In order to investigate the lack of cross-linking *via* glutaraldehyde for crystallin fibrils, the amino group availability of crystallin fibrils was assessed. Two alternate assays were used to determine amino group availability: the *o*-phthaldialdehyde (OPA) assay, and the ninhydrin assay.

5.6.1. OPA assay to determine amino group availability

The OPA assay functions *via* the reaction of OPA with primary amines, in the presence a reducing agent, for example 2-mercaptoethanol, to form a fluorescent product, a 1-alkylthio-2-substituted isoindole, the absorbance of which can be detected at 340 nm (**Figure 5.13**) (Roth, 1971). This assay will therefore detect lysine residues, as well as N-terminal amines, in protein samples. The OPA assay was carried out according to in-house methods (Roth, 1971) (Section 7.18), with a standard curve created using lysine concentrations ranging from 0.2–2.0 mM (**Figure 5.14**) (Section 7.18.1).

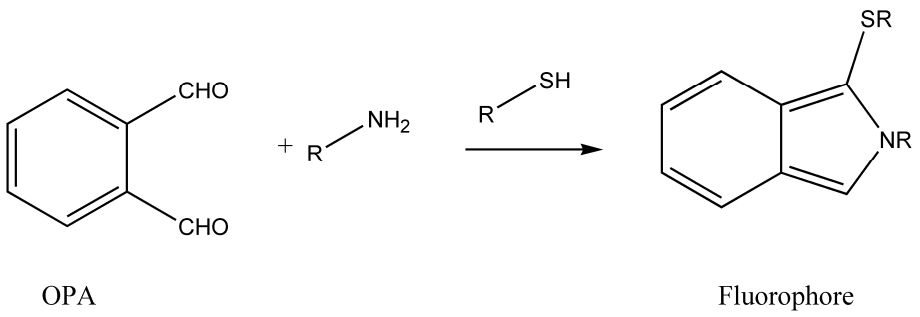

Figure 5.13. *OPA reacts with primary amines, in the presence of a reducing agent, to produce a fluorescent product that can be detected at 340 nm (Roth, 1971).*

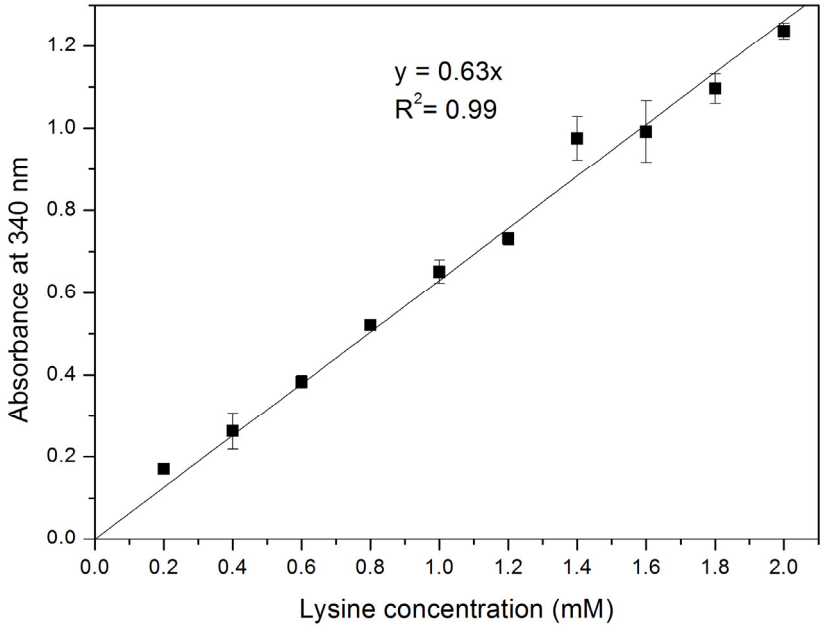

Figure 5.14. *OPA standard curve showing absorbance at 340 nm for lysine concentrations ranging from 0.2-2.0 mM. Error bars represent the standard deviation of three replicates.*

5.6.2. Ninhydrin assay to determine amino group availability

The ninhydrin assay functions by reaction of ninhydrin solution (triketohydrindene hydrate), with ε-amino groups and N-terminal amines, to produce a purple coloured compound diketohydrindylidenediketohydrindamine (Ruhemann's purple) which can be detected at 570 nm (Friedman, 2004) (**Figure 5.15**). The ninhydrin assay was carried out according to in-house methods (Friedman *et al*., 1984) (Section 7.19), with a standard curve constructed using lysine concentrations from 0.2 to 2.0 mM (**Figure 5.16**) (Section 7.19.1).

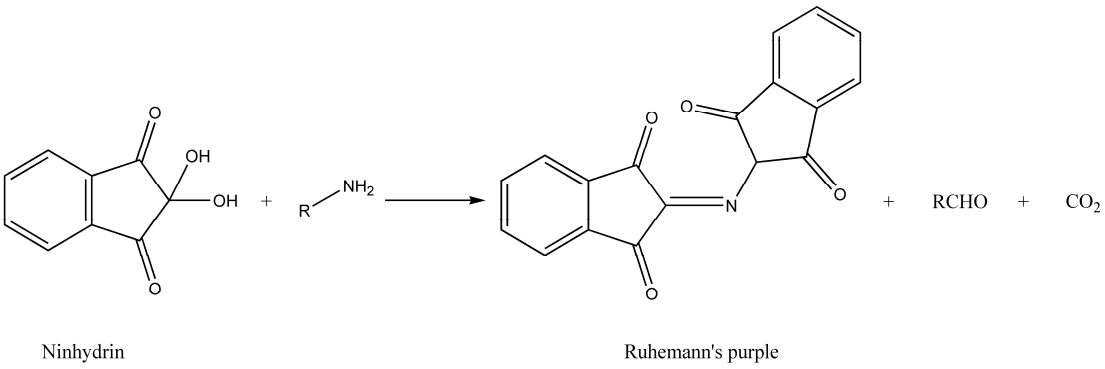

Figure 5.15. *Ninhydrin reacts with primary amines to produce a fluorescent product, Ruhemann's purple, that can be detected at 570 nm (Friedman, 2004).*

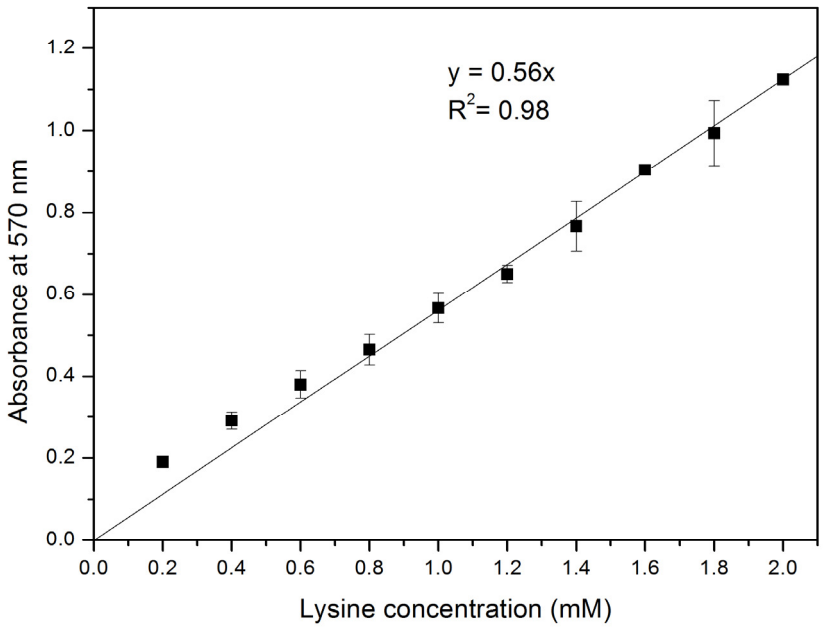

Figure 5.16. *Ninhydrin standard curve showing absorbance at 570 nm for lysine concentrations ranging from 0.2-2.0 mM. Error bars represent the standard deviation of three replicates.*

5.6.3. Amino group availability of insulin fibrils

Determining the amino group availability of amyloid fibrils is more complicated than for native proteins. Neither the number of native monomers per fibril, nor solvent accessibility of particular residues is known, therefore, it is impossible to calculate a theoretical amino group concentration in order to validate the use of a fluorescent amino group assay. There are also additional complicating factors associated with crystallin amyloid fibrils:

1) The crystallin amyloid fibrils used in this study are formed from mixtures of crude crystallin proteins.

2) The fibril formation process involves a step where amorphous aggregate is removed by centrifugation, meaning that even if the initial concentration of native protein is known, there is uncertainty in the concentration of native protein that becomes incorporated in the fibril structure.

Because of this, the two assays described above were first used to determine the amino group availability of both native bovine insulin (1.0 mg/mL) and insulin amyloid fibrils (formed from 1.0 mg/mL native bovine insulin), in order to validate the use of these assays. The results of these assays are summarised in **Table 5.2**.

By comparison with the theoretical amino group concentration of bovine insulin, the amino group availability as ascertained by each of the two assays indicates that approximately two out of three of the amino groups are accessible (**Table 5.2**). There was very good correlation between the two assays, indicating that both are suitable for determining the available amino groups in amyloid fibrils. Interestingly, there was not a great reduction in the available lysine in bovine insulin amyloid fibrils as compared to that in native bovine insulin. Further studies, assaying the availability of a range of different amino acids in the native and fibrilised form, could provide further insight into the arrangement of the native polypeptide chain within the fibril structure.

Table 5.2. *Summary of both calculated (using the OPA and ninhydrin assays), and theoretical amino group availabilities of native bovine insulin and bovine insulin amyloid fibrils.*

Sample	Amino group concentration (μM) calculated from standard curve*		Theoretical amino group concentration (μM)**
	OPA assay	Ninhydrin assay	
Native bovine insulin (1.0 mg/mL)	368 ± 20	366 ± 14	517
Bovine insulin fibrils (formed from 1.0 mg/mL native bovine insulin)	314 ± 13	324 ± 1	N/A

* The standard curve was constructed using lysine, therefore values were multiplied by two to obtain amino group concentration

** Determined from bovine insulin sequence (**Figure 5.7**)

5.6.4. Amino group availability of crude crystallin fibrils

The OPA and ninhydrin assays were then used to assess the amino group availability of amyloid fibrils formed from crude crystallin proteins. The samples used were crystallin fibrils that were formed from 10 mg/mL native crystallin proteins, however, the concentration of protein in the fibrils is unknown due the removal of some as amorphous aggregate. The results of these assays are summarised in **Table 5.3**. The theoretical amino group concentration is unknown, but based upon the relative abundances of α, β, and γ crystallins found in Section 2.6.1, and sequence information for these proteins from *D.rerio*, the amino group concentration of crystallin fibrils should be greater than that of insulin amyloid fibrils. However, based on the results of the OPA and ninhydrin assays, there are some available amino groups, and therefore cross-linking *via* amino groups should have been successful, indicating the presence of some other interference.

Table 5.3. *Summary of calculated (using the OPA and ninhydrin assays) amino group availability of crude crystallin amyloid fibrils.*

Sample	Lysine concentration (μM) calculated from standard curve	
	OPA assay	**Ninhydrin assay**
Crude crystallin fibrils (formed from 10 mg/mL native crystallin proteins)	214 ± 7	258 ± 10

5.7. Post-translational modification of crystallin proteins

As crystallin proteins are long-lived, they are often used to understand the chemical processes associated with aging, such as post-translational modifications (Harding *et al*., 1976). Crystallin proteins, from a range of species, have been observed to undergo a number of different post-translational modifications, such as; phosphorylation, truncation, deamidation, glycosylation, glycation, racemisation, isomerisation, deoxidation, acetylation, and carbamylation (Hanson *et al*., 1998; Kiss *et al*., 2010; Lapko *et al*., 2001; Miesbauer *et al*., 1994; Smith *et al*., 1992). The post-translational modification of crystallins is thought to have implications for cataract formation (Harding, 1991; Smith *et al*., 1992); however, of more interest to this study is the possibility of these types of modifications having an effect on the ability to target specific amino acid residues for immobilisation of GOx. Lysine is the site of a number of post-translational modifications, such as acetylation, carbamylation, and glycation (Cloos and Christgau, 2004). Due to time constraints, a full examination of lysine modification could not be performed; however, preliminary experiments have been carried out to investigate whether the crude crystallin proteins contain carbohydrates.

Carbohydrates can be incorporated into proteins both enzymatically (glycosylation), and non-enzymatically (glycation) (Hermanson, 1996). Glycosylation of proteins involves either N-linked, *via* asparagine, or O-linked, *via* threonine, serine, and hydroxylysine, sugar modification (Thotakura and Bahl, 1987). Although the amine groups of lysine residues are not directly targeted here, the attachment of carbohydrates could hinder access to lysine if it was located near an attachment site. Lysine residues are directly targeted in glycation, which adds a carbohydrate to a protein *via* reaction between reducing sugars and amine groups of proteins (Sojar and Bahl, 1987). The aldehyde group of a reducing sugar first forms a Schiff base linkage with the amine group, and then this bond can undergo an Amadori rearrangement to form a stable ketoamine derivative (**Figure 5.17**). This results in a blocked amine containing a sugar derivative (Hermanson, 1996).

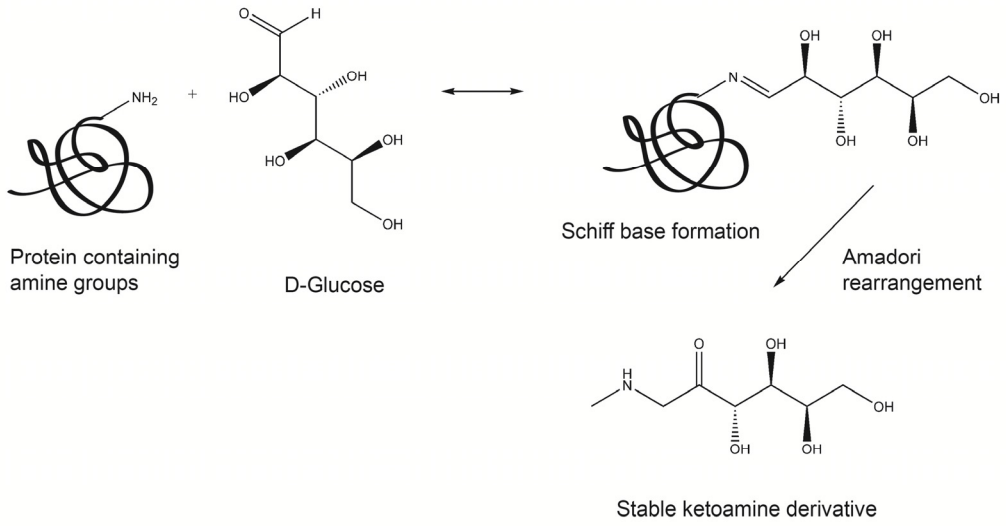

Figure 5.17. *A reducing sugar may modify protein amine groups, such as those on lysine residues, through Schiff base formation followed by an Amadori rearrangement to give a stable ketoamine product. Schematic adapted from Hermanson, (1996).*

The presence of carbohydrates in crystallin proteins was investigated by staining SDS-PAGE gels with Pro-Q Emerald 300 staining solution (Molecular Probes, Invitrogen) (Section 7.21), which reacts with periodate-oxidised carbohydrate groups, creating a fluorescent signal on glycoproteins (Molecular Probes, 2007). Crude crystallin proteins, along with the fractions separated in Chapter 2, Section 2.12.1, were run on an SDS-PAGE gel. GOx was also run as a positive glycoprotein control, as the GOx used is known to possess a carbohydrate shell (Leskovac *et al*., 2005) (Section 5.2). A representative SDS-PAGE gel is shown in **Figure 5.18**, with the image on the left the gel stained with the protein stain Coomassie Blue, and on the right, the same gel stained with Pro-Q Emerald 300. Positive staining for glycoproteins was seen for the GOx control (Lane 9), and also for bands containing both mixtures of crude crystallin proteins, and the fractions corresponding to semi-purified α, β, and γ crystallins (Lanes 10-16). Although it is difficult to assign this to individual crystallin subunits due to the similarities in size, it can be confirmed that fish crystallin proteins do contain carbohydrates, which would at least contribute to the difficulty encountered with GOx immobilisation techniques.

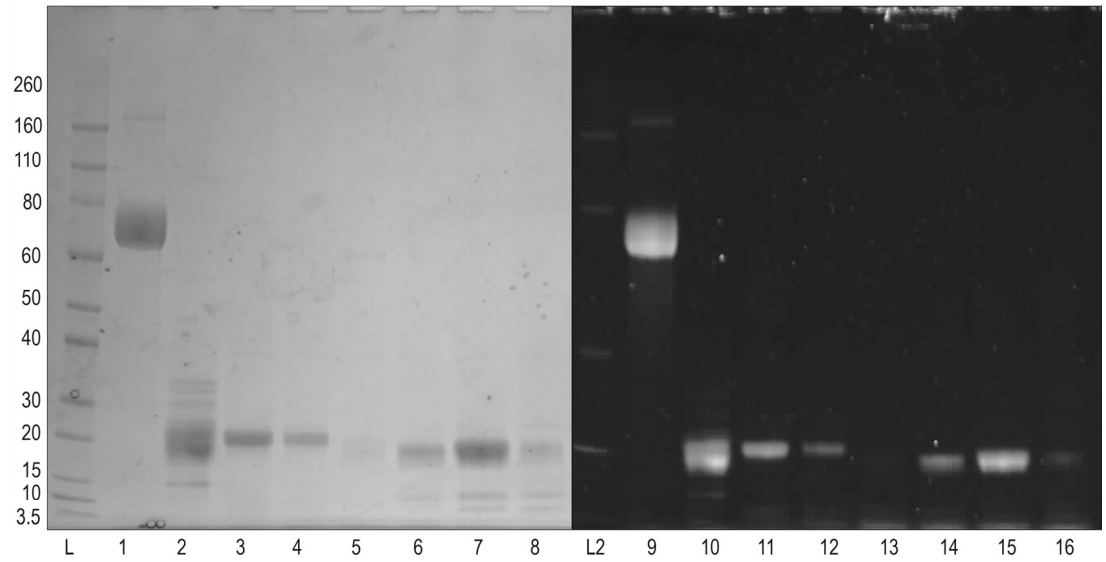

Figure 5.18. *SDS-PAGE gel of crystallin proteins stained for proteins (left-hand image), and glycoproteins (right-hand image). L & L2 = ladder (molecular weights in kDa are indicated to the left of the ladder), 1 & 9 = GOx (glycoprotein positive control), 2 & 10 = crude crystallin proteins, 3 & 11 = αT_1, 4 & 12 = αT_2, 5 & 13 = βT_1, 6 & 14 = βT_2, 7 & 15 = γT_1, and 8 & 16 = γT_2.*

Going forward, there are a number of different methods that could be utilised in order to achieve immobilisation of GOx, and other enzymes, to crude crystallin proteins:

1) Coupling through polysaccharide chains. This involves mild sodium periodate oxidate, which cleaves adjacent hydroxyl groups in sugar residues to create highly reactive aldehyde groups. Immobilisation *via* this method could help preserve enzymatic activity as reactions are not taking place near the active site or other critical residues in the polypeptide chain (Hermanson, 1996).

2) Removal of the carbohydrates, either chemically or enzymatically (Sojar and Bahl, 1987; Thotakura and Bahl, 1987).

3) Immobilisation *via* other amino acid residues. Amine (lysine, arginine, histidine), carboxylic (aspartic acid, glutamic acid), sulfhydryl (cysteine), and hydroxyl (tyrosine) moieties can all be targeted for cross-linking (Hermanson, 1996).

For this work, remaining experiments were carried out with insulin amyloid fibrils.

5.8. Development of a glucose sensing device

In the development of a glucose sensing device the activity of the functionalised fibrils needed to be taken into account; both the long-term activity, and the activity when the fibrils are on a surface as opposed to in solution. The electrochemical behaviour of insulin amyloid fibrils was also investigated.

5.8.1. Time-course of activity of GOx functionalised fibrils

The long-term activity of GOx:IF was investigated using the Amplex® red assay, with the activity of samples assayed over a 40 day period, during which samples were stored at 4 °C (Section 7.22.1). The results of this assay for samples containing GOx only, GOx and GA, GOx and insulin fibrils, and GOx:IF, are shown in **Figure 5.19**. It was seen that all of the four samples showed an initial drop in activity over the first two days, with activity loss ranging from approximately 20–30 % (**Figure 5.19**). The activity then reaches a plateau, with overall activity losses of approximately 25 % (GOx only), 35 % (GOx and GA), 45 % (GOx and insulin fibrils), and 20 % (GOx:IF). Immobilisation of GOx onto insulin fibrils resulted in increased stability, something which is commonly observed with enzyme immobilisation (Polizzi *et al*., 2007). These results also indicate that GOx:IF may be used in applications for at least 40 days without any loss in activity or inconsistency in results.

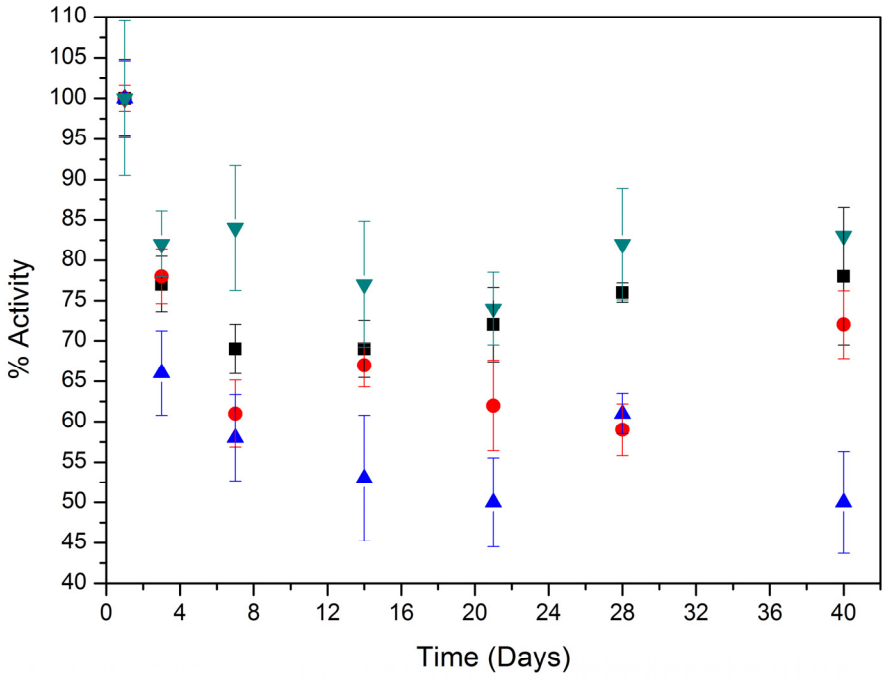

Figure 5.19. *Timecourse of % activity of samples stored at 4 °C. Black square = GOx, red circle = GOx + GA, blue triangle = GOx + IF, green triangle = GOx + GA + IF. Data points represent the mean of three replicates, with error bars showing the standard deviation.*

5.8.2. Surface activity of GOx functionalised fibrils

It was also important to ensure that the functionalised fibrils retained activity when deposited on a surface, as this is the state that they would be in on an electrode. The activity of functionalised fibrils on a surface was investigated qualitatively, by depositing the functionalised fibrils on to a silicon oxide wafer, and removal of excess solvent by evaporation. A droplet of the Amplex® red assay reaction mix was then deposited on top of the fibrils, and the colour change observed (Section 7.22.2). Control samples containing insulin fibrils only and GOx only were also assayed in this way. An image of the results of this qualitative assay is shown in **Figure 5.20**.

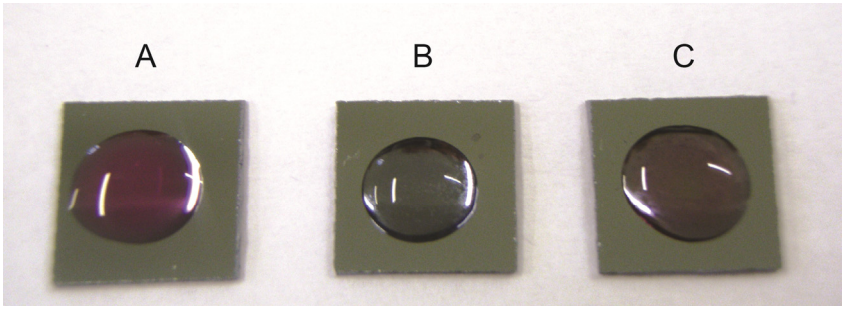

Figure 5.20. *Qualitative assay using Amplex® red of GOx activity of samples deposited onto silicon substrates. A = GOx control, B = insulin fibril control, and C = GOx + GA + insulin fibrils.*

GOx only control displayed a vibrant pink colour (**Figure 5.20**, A), consistent with the formation of large amount of resorufin, which is indicative of the presence of GOx activity (**Figure 5.3**, A). The insulin fibril only control showed no colour change, as would be expected (**Figure 5.20**, B). The sample containing the functionalised fibrils (GOx, GA, and insulin fibrils) showed pink coloration (**Figure 5.20**, C), although not as vibrantly as the GOx only control. This is consistent with in solution activity assays, where the GOx activity of functionalised fibrils was approximately 90 % of that of the GOx only control (**Figure 5.10**). This indicates that the functionalised fibrils retain activity when deposited on a surface.

5.8.3. Electrochemical behaviour of insulin amyloid fibrils

The electrochemical behaviour of insulin amyloid fibrils was examined by deposition of fibrils onto gold electrodes, with excess solvent removed by evaporation. For these initial experiments, screen-printed electrodes were used (Dropsens), with a gold working electrode (4 mm diameter), a gold counter electrode, and a silver reference electrode (Section 7.22.3).

The electrochemical behaviour of insulin amyloid fibrils was examined using cyclic voltammetry in the presence of the mediator FcOH (1.5 mM in phosphate buffer, pH 7.4). At higher concentrations of fibrils there was a marked decrease in the current response. This is because at high concentrations there are a large number of insulin fibrils, which then block the conductive electrode surface. In order to allow sufficient electron transfer, the concentration of insulin fibrils was kept at 0.21 mg/mL (diluted from fibrils formed at 1.9 mg/mL) for subsequent experiments. This blocking behaviour has also been observed for FF peptide nanotubes (Sasso *et al*., 2012).

Figure 5.21 shows comparative cyclic voltammetry of a screen-printed gold electrodes response to 1.5 mM FcOH without (top), and with (bottom) modification with insulin amyloids at a range of scan rates. The responses observed are not dramatically different, likely due to the low concentration of fibrils deposited. However, when the electrode is modified with fibrils there is a larger background current, due to capacitance resulting from the protein charges on the surface. There is also an observed shift in peak potential, E_{pa} = 98 mV for a fibril modified electrode versus E_{pa} = 137 mV for a bare electrode. This is likely due to the negative charge of the protein stabilising the ferrocene oxidation product.

No significant changes in the peak current were found after the potential was swept from -0.1 to +0.4 V and back at a scan rate of 50 mV/s for 50 cycles. This indicates that the insulin fibrils are well adhered to the gold electrode surface.

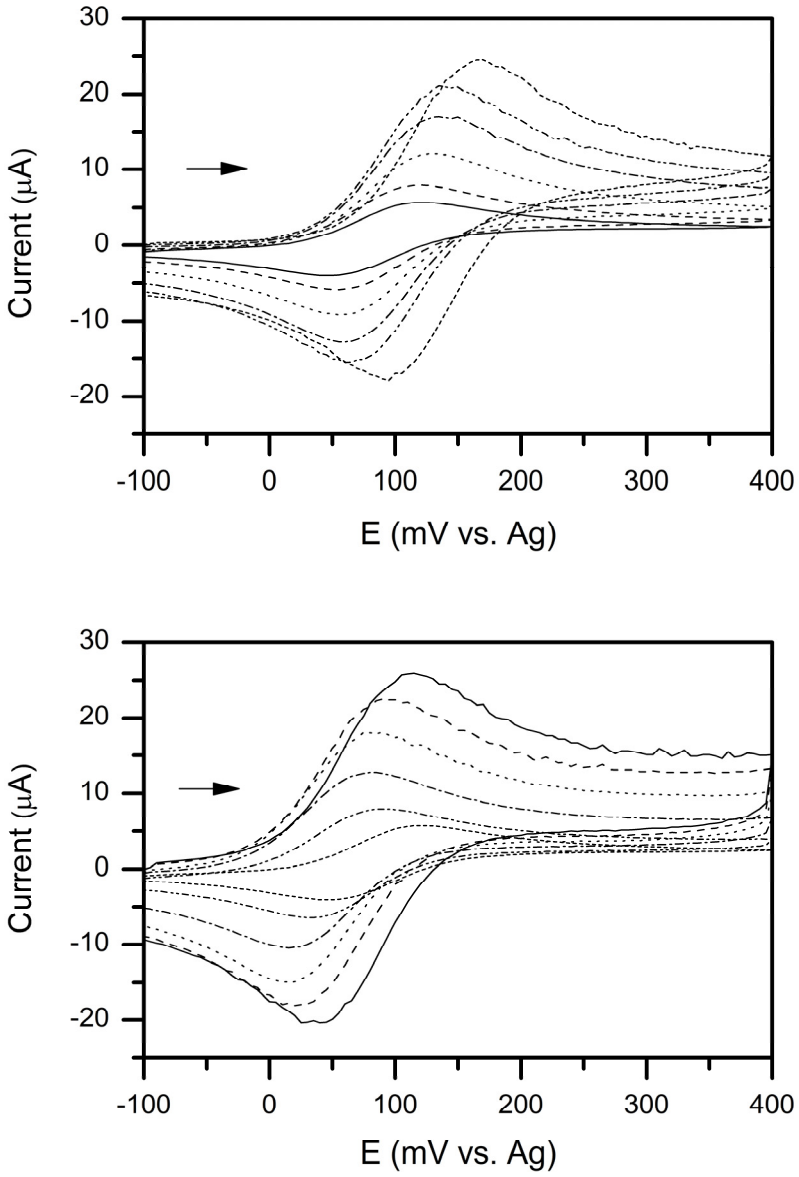

Figure 5.21. *Comparative cyclic voltammetry of a screen-printed electrode response to 1.5 mM FeOH with (bottom) and without (top) modification with insulin amyloid fibrils at different scan rates (from inner to outer): 5, 10, 25, 50, 75, 100 mV/s. The arrow indicates the initial scan direction.*

5.9. Glucose sensing

Under normal circumstances, direct electron transfer between the active site of reduced GOx and a metal electrode takes place slowly or not at all because the gap between the active site and the electrode surfaces is too large for electron transfer (Leskovac *et al*., 2005). The use of electron transfer mediators can overcome this problem, and can be used in a number of ways, such as in solution where the mediator can diffuse freely between the enzyme and electrode (Leskovac *et al*., 2005).

One electron acceptor mediators are usually used, and derivatives of ferrocene are the largest class of one electron oxidants (Leskovac *et al*., 2005). Ferrocene derivatives are also good because ferrocene is small enough to penetrate the active site of GOx (Alvarez-Icaza *et al*., 1995).

Gold electrodes were modified with GOx:IF and their response to glucose examined by cyclic voltammetry in the presence of the mediator ferrocene methanol (FeOH).

5.9.1. Modification of gold electrodes with GOx functionalised fibrils

Gold electrodes were prepared by evaporating an 8 mm diameter circle of gold onto a 10 mm^2 silicon oxide wafer, using a custom made sample holder (**Figure 5.22**, A) (Section 7.23.1). GOx:IF were then deposited onto the gold electrode, and the excess solvent evaporated by incubating the electrodes for one hour at 37 °C (Section 7.23.2). Modified electrodes were prepared fresh before each experiment for consistency.

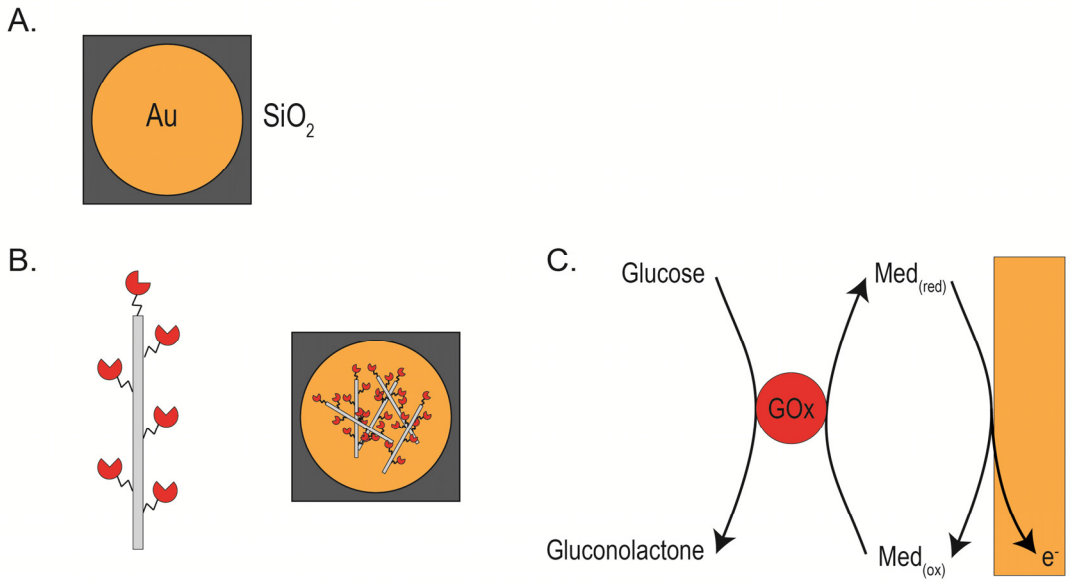

***Figure 5.22**. Schematic representations of: A) Gold electrodes on a silicon oxide wafer which were fabricated for glucose sensing experiments. B) Modification of gold electrodes with GOx:IF C) Schematic of the mechanism of electron transfer to the Au electrode. Glucose is oxidized to gluconolactone, and electron transfer from reduced GOx then occurs via the mediator molecule.*

Other studies have needed to incorporate thiol groups into peptides in order to maintain contact with the gold surface (Yemini *et al*., 2005a); however, one of the advantages of using amyloid fibrils formed from a full protein, as opposed to a peptide, is that there is a greater range of functional groups present. **Figure 5.22**, B, showed a very simplified schematic of the modified gold electrodes. The amyloid fibrils interact with the gold surface *via* thiol groups, and GOx is in turn covalently bound to the amyloid fibril, *via* the GA cross-linker. **Figure 5.23** shows representative AFM images of unmodified (A), and GOx:IF modified (B) gold electrodes.

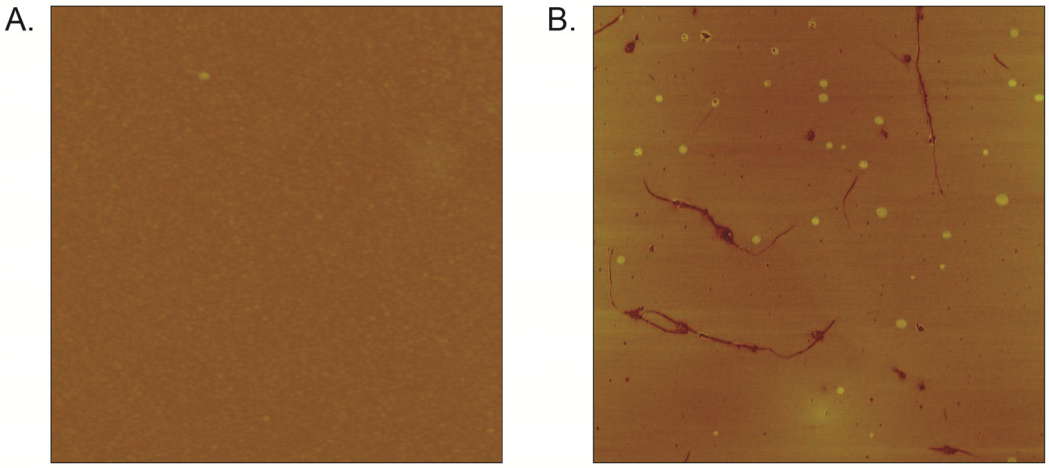

Figure 5.23. *Representative AFM images of gold electrode before (A), and after (B), modification with GOx:IF. Scan size is 5 μm*^{2}.

5.9.2. Response of modified electrode to glucose

The catalytic activity of the GOx:IF modified electrodes was quantified in the presence of excess glucose, using FcOH as a mediator in solution (Section 7.23.3). **Figure 5.22**, C, shows a schematic of the mechanism of response of the modified electrode to glucose. As glucose oxidase is present, when glucose is present in the solution being examined, this is oxidised to gluconolactone. Electron transfer from the reduced enzyme to the gold electrode then occurs *via* the mediator molecule present, in this case FcOH. As glucose/gluconolactone and $FADH_2$/FAD couples are two electron and two proton systems, and ferrocenes are one electron oxidizing systems, two equivalents of ferrocene and ferrocenium are involved in the reaction (Leskovac *et al*., 2005).

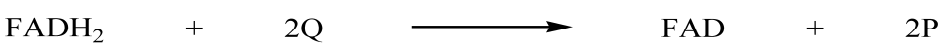

Figure 5.24. *Global representation of the oxidative half reaction of GOx. The oxidation of $FADH_2$ to FAD involves the reduction of two equivalents of ferrocene (Q) to ferrocenium (P) (Leskovac et al., 2005).*

As shown in **Figure 5.25**, A, in the absence of glucose (solid trace), a chemically reversible, diffusion-controlled response is obtained for the $FcOH^{+/0}$ redox couple at the GOx:IF modified electrode. In the presence of glucose (dotted trace), the anodic current in amplified due the catalytic oxidation of glucose by GOx, mediatied by FcOH. This shows that this very simple device based upon GOx:IF is able to electrochemically detect glucose. Washing and repeated use of the modified electrode resulted in little reduction in the observed response, indicating that the fibrils are well adhered to the gold electrode and the device is reusable.

The catalytic activity of the GOx:IF modified electrode can be expressed as the current amplification (CA), defined by:

$$CA = (i_{FcOH\ +\ Glu} - i_{FcOH}) \,/\, i_{FcOH}$$

where i_{FcOH} is the anodic peak current recorded at the electrode in the absence of glucose, and $i_{FcOH\ +\ Glu}$ is the anodic peak current recorded in the presence of glucose (**Figure 5.25**, A) (Lehr *et al*., 2010).

The influence of the presence of the GOx:IF on current amplification was examined by comparing the average current amplification in the presence of excess (400 mM) glucose for gold only electrodes, GOx only modified gold electrodes, and the GOx:IF modified gold electrodes. The GOx only control was created by the same methods as detailed in Section 5.9.1, with the exception that GOx only was deposited. The GOx sample used was diluted in phosphate buffer to have the same activity in solution, as ascertained by the Amplex® red assay, as the GOx:IF sample used. The average CA in the presence of 400 mM glucose for for each of these three samples are shown in **Figure 5.25**, B. The Au only electrode showed no CA, as would be expected. The GOx only electrode and the GOx:IF electrode had CA values within error of each other, although it should be noted that there was quite high error for the GOx:IF electrode due to the heterogeneity of the fibrils in solution due to fibril-fibril cross-linking.

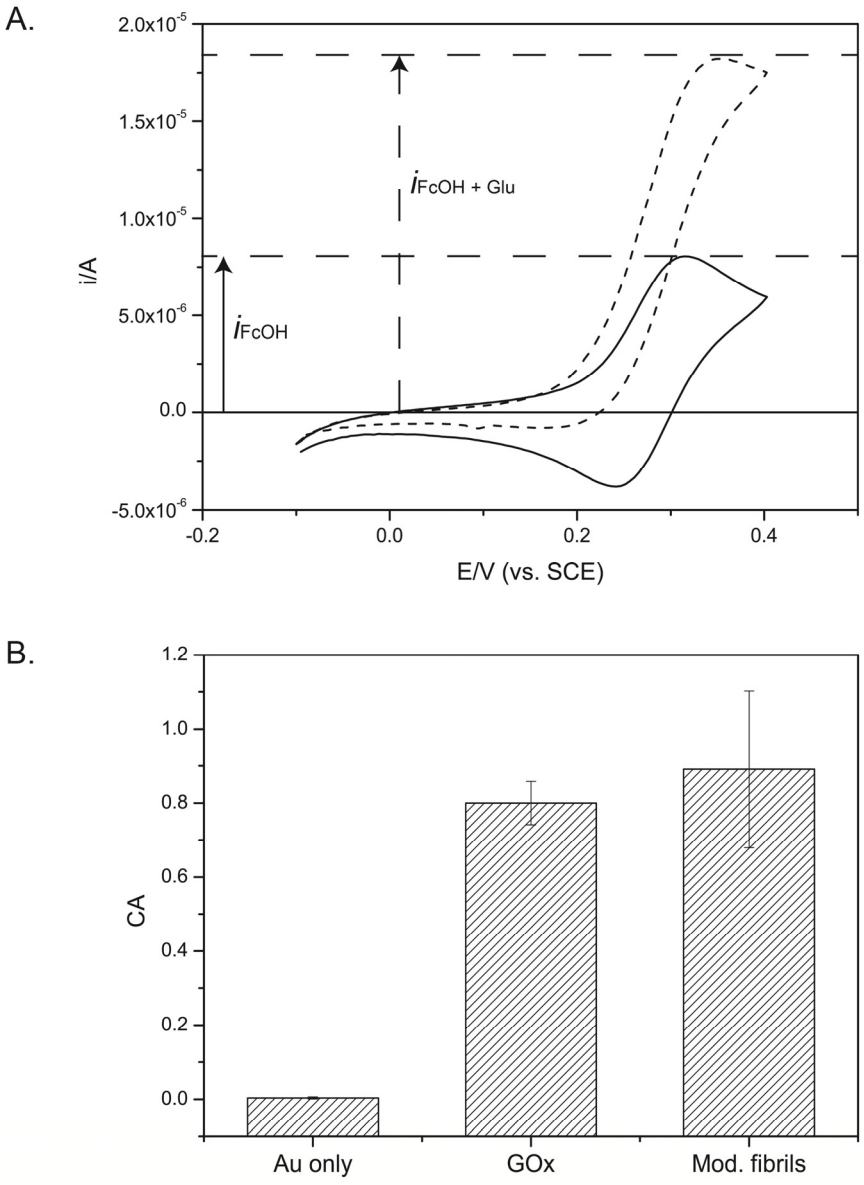

***Figure 5.25**. A) Representative cyclic voltammagram (scan rate = 5 mV) recorded in 1.5 mM FcOH PB solution, pH 7.4, for a functionalised fibril modified Au electrode in the absence (solid trace), and presence (dotted trace), of 400 mM glucose (SCE = saturated calomel electrode). B) Average current amplification (CA) for Au only electrodes, GOx modified Au electrodes, and Au electrodes modified with functionalised fibrils. Each value represents the average of five replicates, with error bars representing the standard deviation of the mean.*

This result suggests that the presence of fibrils is not increasing the CA of the electrode. This is very likely to be due to the fact that the GOx:IF have to be significantly diluted before deposition onto the electrode, due to the blocking behaviour of high concentrations of insulin fibrils (Section 5.8.3). This means that the benefit of the increased surface area available for enzyme attachment due to the presence of the fibrils is not being fully realised.

5.10. Towards single-molecule sensors

Preliminary experiments were carried out on the use of GOx:IF as single-molecule sensors, similar to those described in Section 1.8. As manipulation and isolation of individual insulin fibrils is not yet achievable, these experiments used the same experimental set-up as used in Section 4.2. Networks of GOx:IF were deposited onto interdigitated gold electrodes, which were fabricated as per Section 7.11 (**Figure 5.26**).

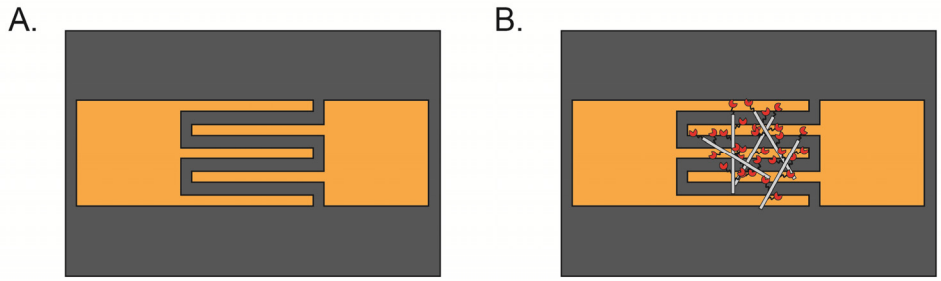

Figure 5.26. *A) Schematic representation of interdigitated gold electrodes fabricated on a silicon oxide wafer. B) Networks of GOx:IF were deposited onto these interdigitated electrodes.*

I-V curves were constructed using a probe station and parameter analyser for networks of GOx:IF (**Figure 5.27**), showing current values in the range of 10^{-11} A recorded for bias voltages of 0-2 V. This is a decrease in conductivity compared to insulin fibrils only (Section 4.4). This was also seen when GOx was immobilised to the surface of CNTs, with the reasoning being that GOx immobilisation decreased the capacitance of the tube (Besteman *et al*., 2003).

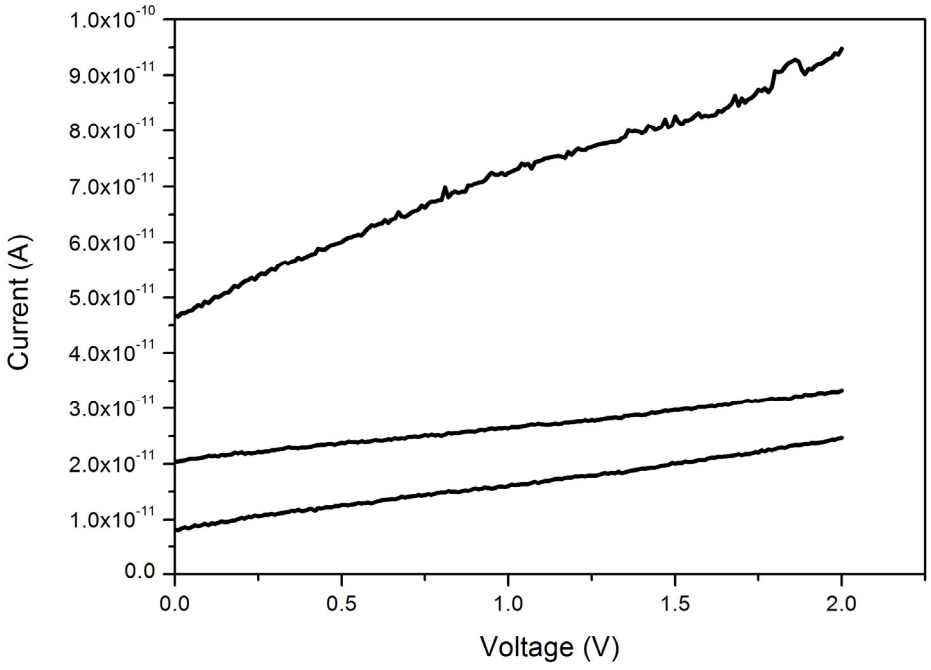

Figure 5.27. *Typical I-V curves obtained for networks of GOx:IF taken from three different samples.*

I-V measurements were also taken in the presence of 0.2 mM glucose. An increase in current was observed, indicating that the GOx:IF showed glucose sensitivity. **Figure 5.28** shows a comparison of the current at 2 V for networks of insulin fibrils, GOx:IF, and both of these networks upon addition of glucose. Some increase in current is seen upon addition of glucose to insulin fibril networks, this is likely due to the conductivity of fibrils increasing upon hydration, as was observed by del Mercato *et al*. (2007).

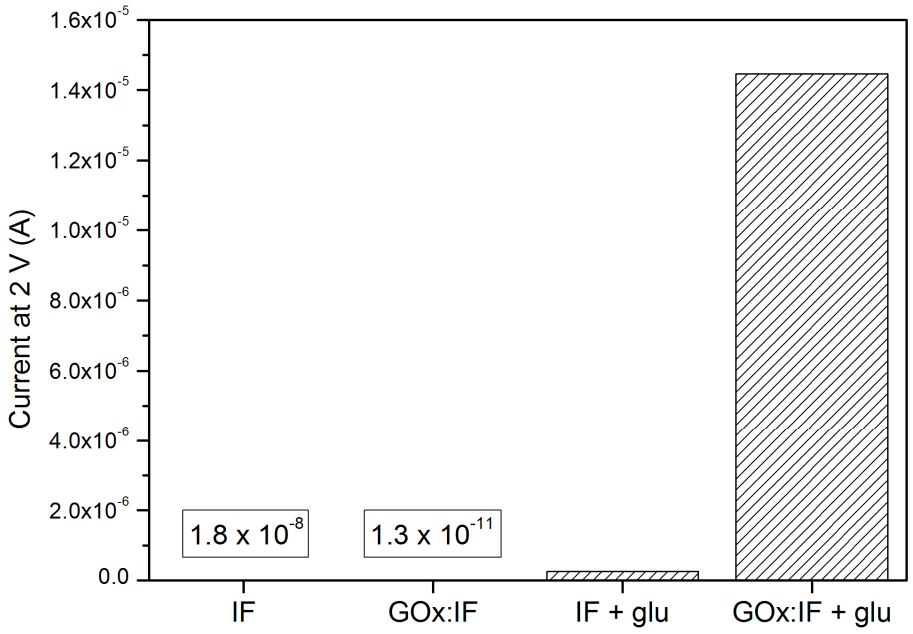

Figure 5.28. *Preliminary results showing the current recorded at 2 V for networks of insulin fibrils (IF), networks of GOx modified insulin fibrils (GOx:IF), and these two networks upon addition of 0.2 mM glucose.*

The large increase in current seen when glucose is added to GOx:IF indicates that it is GOx activity that is responsible for the increase in current. Besteman *et al*. (2003) observed similar results with a single-molecule sensor consisting of a GOx modified CNT. In their study they identified the need for further experiments to unambiguously identify which of the processes associated with the GOx catalysed reaction (conformational change, changed charge state of amino acids, conversion of oxygen to hydrogen peroxide) is responsible for the measured conductance change, and the same applies to this study. Nonetheless, these are promising initial results towards the formation of an amyloid fibril based single-molecule glucose sensor, with the much lower background current of the insulin fibrils, as compared to CNTs, potentially offering higher sensitivity.

5.11. Summary

This chapter has investigated the use of amyloid fibrils in a model nanowire application: the creation of a glucose sensor. GOx was covalently immobilised to insulin fibrils using the cross-linker GA, with the functionalised fibrils showing GOx activity, and stability over a long time period. Attempts were also made to immobilise GOx to crystallin fibrils; however, these were unsuccessful. This is likely to be due to post-translational modification to fish crystallin proteins, such carbohydrate modification, which may be blocking access to key surface functional groups. Deglycosylation and alternative immobilisation techniques could be explored to overcome this problem.

The modification of gold electrodes with GOx:IF resulted in a simple device that showed a response to glucose, as investigated by cyclic voltammetry. However, due to the blocking behaviour of insulin fibrils, the electrode was only able to be modified with low concentrations of GOx:IF, meaning that the full benefits of the increased surface area provided by the fibril scaffold were not realised. Preliminary investigations in the use of GOx:IF as single-molecule sensors showed the conductivity of GOx:IF networks to be glucose sensitive. This was a promising initial result towards the creation of a conductance-based glucose sensing device.

5.12. References

Alvarez-Icaza M, Kalisz H, Hecht H, Aumann K, Schomburg D, Schmid R. 1995. The design of enzyme sensors based on the enzyme structure. *Biosensors and Bioelectronics* **10**:735–742.

Bankar S, Bule M, Singhal R, Ananthanarayan L. 2009. Glucose oxidase - an overview. *Biotechnology Advances* **27**:489–501.

Baszkin A, Boissonnade M, Rosilio V, Kamyshny A, Magdassi S. 1997. Adsorption of hydrophobized glucose oxidase at solution/air interface. *Journal of Colloid and Interface Science* **190**:313–317.

Besteman K, Lee J-O, Wiertz F, Heering H, Dekker C. 2003. Enzyme-coated carbon nanotubes as single-molecule biosensors. *Nano Letters* **3**:727–730.

Brange J, Andersen L, Laursen E, Meyn G, Rasmussen E. 1997. Toward understanding insulin fibrillation. *Journal of Pharmaceutical Sciences* **86**:517–525.

Cloos P, Christgau S. 2004. Post-translational modifications of proteins: implications for aging, antigen recognition, and autoimmunity. *Biogerontology* **5**:139–58.

Delano W. 2002. The PyMOL Molecular Graphics System.

Deng T, Wang H, Li J, Hu S, Shen G, Yu R. 2004. A novel immunosensor based on self-assembled chitosan/alginate multilayers for the detection of factor B. *Sensors and Actuators B: Chemical* **99**:123–129.

Frederick K, Tung J, Emerick R, Masiarz F, Chamberlain S, Vasavada A, Rosenberg S, Chakraborty S, Schopfer L, Schopter L. 1990. Glucose oxidase from Aspergillus niger. Cloning, gene sequence, secretion from *Saccharomyces cerevisiae* and kinetic analysis of a yeast-derived enzyme. *Journal of Biological Chemistry* **265**:3793.

Friedman M. 2004. Applications of the ninhydrin reaction for analysis of amino acids, peptides, and proteins to agricultural and biomedical sciences. *Journal of Agricultural and Food Chemistry* **52**:385–406.

Friedman M, Pang J, Smith G. 1984. Ninhydrin-reactive lysine in food proteins. *Journal of Food Science* **49**:10–13.

Hanson S, Smith D, Smith J. 1998. Deamidation and disulfide bonding in human lens [gamma]-crystallins. *Experimental Eye Research* **67**:301–312.

Harding J. 1991. Cataract: biochemistry, epidemiology and pharmacology. Chapman and Hall London.

Harding J, Dilley K. 1976. Structural proteins of the mammalian lens: a review with emphasis on changes in development, aging and cataract. *Experimental Eye Research* **22**:1.

Hecht H, Kalisz H, Hendle J, Schmid R, Schomburg D. 1993. Crystal structure of glucose oxidase from *Aspergillus niger* refined at 2.3 Å resolution. *Journal of Molecular Biology* **229**:153–172.

Hermanson G. 1996. Bioconjugate techniques. USA: Academic Press.

Invitrogen. 2006. Amplex red glucose/glucose oxidase assay kit. Molecular Probes, Inc.

Kiss A, Devries A, Morgan-Kiss R. 2010. Comparative analysis of crystallins and lipids from the lens of Antarctic toothfish and cow. *Journal of Comparative Physiology B: Biochemical, Systemic, and Environmental Physiology* **180**:1019–1032.

Kriechbaum M, Heilmann H, Wientjes F, Hahn M, Jany K, Gassen H, Sharif F, Alaeddinoglu G. 1989. Cloning and DNA sequence analysis of the glucose oxidase gene from *Aspergillus niger* NRRL-3. *FEBS Letters* **255**:63–66.

Lapko V, Smith D, Smith J. 2001. *In vivo* carbamylation and acetylation of water-soluble human lens alphaB-crystallin lysine 92. *Protein Science* **10**:1130–1136.

Lehr J, Williamson B, Barrière F, Downard A. 2010. Dependence of catalytic activity and long-term stability of enzyme hydrogel films on curing time. *Bioelectrochemistry* **79**:142–146.

Leskovac V, Trivic S, Wohlfahrt G, Kandrac J, Pericin D. 2005. Glucose oxidase from *Aspergillus niger*: the mechanism of action with molecular oxygen, quinones, and one-electron acceptors. *The International Journal of Biochemistry & Cell Biology* **37**:731–750.

del Mercato L, Pompa P, Maruccio G, Torre A, Sabella S, Tamburro A, Cingolani R, Rinaldi R. 2007. Charge transport and intrinsic fluorescence in amyloid-like fibrils. *Proceedings of the National Academy of Sciences of the United States of America* **104**:18019–18024.

Miesbauer L, Zhou X, Yang Z, Sun Y, Smith D, Smith J. 1994. Post-translational modifications of water-soluble human lens crystallins from young adults. *Journal of Biological Chemistry* **269**:12494.

Miller A, Meade S, Gerrard J. 2003. New insights into protein crosslinking via the Maillard reaction: structural requirements, the effect on enzyme function, and predicted efficacy of crosslinking inhibitors as anti-ageing therapeutics. *Bioorganic & Medicinal Chemistry* **11**:843–852.

Molecular Probes. 2007. Pro-Q Emerald 300 glycoprotein gel and blot stain kit - product information.

Müller D. 1928. Oxidation von Glukose mit Extrakten aus *Aspergillus niger* (Oxidation of glucose with the extracts from *Aspergillus niger*). *Biochemistry Z* **199**:36.

Pilkington S, Roberts S, Meade S, Gerrard J. 2010. Amyloid fibrils as a nanoscaffold for enzyme immobilisation. *Biotechnology Progress* **26**:93–100.

Pluschkell S, Hellmuth K, Rinas U. 1996. Kinetics of glucose oxidase excretion by recombinant *Aspergillus niger*. *Biotechnology and Bioengineering* **51**:215–220.

Polizzi K, Bommarius A, Broering J, Chaparro-Riggers J. 2007. Stability of biocatalysts. *Current Opinion in Chemical Biology* **11**:220–225.

Qian Z, Khan M, Mikkelsen S, Chen P. 2009. Improved enzyme immobilization on an ionic-complementary peptide-modified electrode for biomolecular sensing. *Langmuir* **26**:2176–2180.

Raba J, Mottola H. 1995. Glucose oxidase as an analytical reagent. *Critical Reviews in Analytical Chemistry* **25**:1–42.

Roth M. 1971. Fluorescence reaction for amino acids. *Analytical Chemistry* **43**:880–&.

Sasso L, Vedarethinam I, Emneus J, Svendsen W, Castillo J. 2012. Self-assembled dipheylalanine nanowires for cellular studies and sensor applications. *Journal of Nanoscience and Nanotechnology*:Accepted.

Smith J, Sun Y, Smith D, Green B. 1992. Identification of the posttranslational modifications of bovine lens alpha B-crystallins by mass spectrometry. *Protein Science* **1**:601–608.

Sojar H, Bahl O. 1987. Chemical deglycosylation of glycoproteins. *Methods in Enzymology* **138**:341–350.

Thotakura N, Bahl O. 1987. Enzymatic deglycosylation of glycoproteins. *Methods in Enzymology* **138**:350–359.

Wang J. 1991. Modified electrodes for electrochemical sensors. *Electroanalysis* **3**:255–259.

Wilson R, Turner A. 1992. Glucose oxidase: an ideal enzyme. *Biosensors and Bioelectronics* **7**:165–185.

Wong C, Wong K, Chen X. 2008. Glucose oxidase: natural occurrence, function, properties and industrial applications. *Applied Microbiology and Biotechnology* **78**:927–938.

Yemini M, Reches M, Gazit E, Rishpon J. 2005a. Peptide nanotube-modified electrodes for enzyme-biosensor applications. *Analytical Chemistry* **77**:5155–5159.

Yemini M, Reches M, Rishpon J, Gazit E. 2005b. Novel electrochemical biosensing platform using self-assembled peptide nanotubes. *Nano Letters* **5**:183–186.

Yemini M, Xu P, Kaplan D, Rishpon J. 2006. Collagen-like peptide as a matrix for enzyme immobilization in electrochemical biosensors. *Electroanalysis* **18**:2049–2054.

6. Chapter Six

Conclusions and suggestions for future work

Amyloid fibrils have been recognised in the literature as being among a number of biomolecules and biomolecular assemblies that show potential to be used as nanomaterials (Gras, 2007; Waterhouse and Gerrard, 2004). This thesis aimed to investigate the use of amyloid fibrils as nanowires, a role suited to their size and morphology. A number of other protein nanotubes/nanofibres have also been identified for this role, although they are typically formed from purified proteins and engineered peptides (Gazit, 2007). Amyloid fibrils have the novelty of being forming from a large number of protein and peptide solutions (Dobson, 2003) and if they are to be used successfully in bionanotechnology, there is a need for a cheap and readily available protein source (Waterhouse and Gerrard, 2004). Crude crystallin proteins have been identified as meeting these requirements (Garvey *et al*., 2009), and so fibrils from this protein source were the major focus of this thesis, with an emphasis on their suitability as nanomaterials. Bovine insulin and fungal hydrophobins were also used. The use of amyloid fibrils as nanowires was investigated by examining the ability to control their dimensions and arrangement, as well as an evaluation of stability and conductivity. Functionalisation of fibrils enabled an investigation into their use in glucose sensing, chosen as a model nanowire application.

Initially, fibrils were formed from each of the three protein sources, and the resulting fibrils were characterised by the ThT assay and TEM. Amyloid fibrils were readily formed from bovine insulin, validating its selection as the model amyloid forming protein for this thesis. Hydrophobin rodlets were also formed as per the literature (Kwan *et al*., 2006) with further investigation showing that the provision of additional air/water and solid/water interfaces increased the rate of fibrillation. Mixtures of crude fish crystallin proteins formed fibrillar structures, which were characterised both structurally, and in terms of their applicability to bionanotechnological applications.

X-ray fibre diffraction was used to examine the intermolecular structure of amyloid fibrils from crude fish crystallins for the first time. The resulting diffraction pattern showed isotropic reflections at 4.6 Å and 10.3 Å, which confirm the presence of the characteristic cross-β amyloid structure (Pauling and Corey, 1951; Serpell *et al*., 1999). The ability of all three classes (α, β, and γ) of fish crystallin proteins to form fibrils was also examined, with SEC used to successfully semi-purify the crystallin proteins. All three classes of crystallin proteins were shown to form fibrils under the same conditions used to form fibrils from crude mixtures of crystallins, with no noticeable differences in morphology. This result confirmed that all classes of crystallins are able to form amyloid fibrils (Garvey *et al*., 2009), as well as validating the use of a crude protein mixture, as further purification did not appear to improve fibril morphology or yield.

Crystallin amyloid fibrils were shown to be stable across a wide pH range, as well as in water, phosphate buffer, ethanol, isopropanol, and methanol. Previous work had investigated the stability in solution of FF nanotubes (Andersen *et al*., 2011), a widely used PNT, and these showed considerably less stability than crystallin amyloid fibrils. Of the solvents tested, only acetonitrile dissolved crystallin amyloid fibrils and, interestingly, reduced concentrations of acetonitrile resulted in a change in fibril morphology, with the formation of circular assemblies. This result supports the use of crystallin fibrils as nanomaterials, particularly in applications requiring prolonged solvent contact, such as biosensing.

A systematic study investigating the effect of growth and storage conditions on the dimensions of bovine insulin fibrils achieved a range of length distributions, although increased homogeneity would still be desirable. Fibril length increased with decreasing native protein concentration, with fibrils formed at 0.5 mg/mL existing up to 6 μm in length. This is likely due to the impact of protein concentration on the kinetics of nucleation and elongation (Brange *et al*., 1997; Mauro *et al*., 2007; Waugh, 1946).

The affect of storage conditions was also examined, with the most noticeable effect on fibril length resulting from freeze/thaw cycles, which saw the fragmentation of fibrils into much shorter species. Throughout these processes, no change was seen to fibril diameter. The ability to form fibrils of varied lengths is important for potential applications, where control over dimensions is desirable. For this thesis, the ability to grow long fibrils was also needed in order to carry out conductivity measurements, as fibrils were needed to be long enough to bridge electrodes.

The conditions that gave the shortest and longest fibrils, namely, freeze-thaw cycles and low concentration respectively, were then applied to the crystallin fibril system, to investigate whether the same trend in fibril length was observed. Results indicated that it is unlikely to be possible to apply the same "length-controlling" conditions to different fibril systems, although previous work has shown that crystallin fibrils can be produced in a range of sizes (Healy *et al*., 2012; Raynes, 2012). A greater understanding of the mechanism of fibril formation from crude crystallin proteins along with optimisation of specific "length-controlling" conditions for this protein system would result in increased control over these structures.

The conductivity of networks of amyloid fibrils formed from bovine insulin, fungal hydrophobins, and crude crystallin proteins was investigated *via* methods based upon those of del Mercato *et al*. (2007). A microchip with interdigitated gold electrodes was fabricated by optical lithography and etching, and networks of amyloid fibrils were deposited onto the microelectrodes. Amyloid fibrils from all three protein sources had low conductivity, with current values falling in the range of 10^{-8}-10^{-10} A for applied bias voltages of 0-2 V. This narrow range of conductivity suggests a role of the generic fibril structure in determining conductivity, which is supported by the even lower current values observed for native protein (10^{-12} A). Further investigation involving mutation of charged residues could be used to fully elucidate the mode of conduction. This finding that amyloid fibrils are insulating is in agreement with previous work regarding the conductivity of biomolecules such as amyloid-like fibrils (Scheibel *et al*., 2003); peptide nanotubes (Castillo *et al*., 2008); and DNA (Storm *et al*., 2001).

Although amyloid fibrils are insulating, they can be used as scaffolds or templates for the formation of conductive nanowires. Insulin amyloid fibrils were modified with the conducting polymers PPY and PANI. This modification saw an increase in the conductivity of insulin fibril networks by four and one orders of magnitude respectively. Although amyloid fibrils have been previously modified with the conducting polymers PEDOT-S, PTAA, and PPF (Hamedi *et al*., 2008; Herland *et al*., 2007; Herland *et al*., 2008; Tanaka *et al*., 2008), this was the first use of PPY and PANI. Future work optimising the modification process would be useful in order to achieve more uniform coatings, as well as an investigation into whether crude crystallin fibrils can also be used as a successful nanowire scaffold.

DEP was used to manipulate crystallin amyloid fibrils on a microchip, in order to probe the electrical properties of small numbers of fibrils. This has previously been done with FF peptides and CNTs (Castillo *et al*., 2008; Dimaki and Bøggild, 2005). DEP was shown to be a successful tool for manipulating and immobilising bundles of crystallin fibrils between electrode pairs in a controlled manner. Once immobilised, fibrils were imaged by SEM. Investigation into the conductivity of immobilised bundles showed low current values, similar to those seen in network studies. Continuing research focusing on the use of DEP as a tool to integrate these structures into biosensing and bioelectronics devices would be useful. Microfluidics could also be incorporated into the DEP chip to improve the orientation of immobilised fibrils, as flow has previously been shown to be effective in alignment of fibrils (Adachi *et al*., 2007).

Amyloid fibrils can also be used as a scaffold for enzyme immobilisation, with amyloid fibrils acting as a high surface area support. GOx was successfully immobilised to insulin fibrils with GA as per the methods of Pilkington *et al*. (2010), although further work would be beneficial to optimise this process to minimise fibril-fibril cross-linking, and maintain maximal surface area for GOx immobilisation. GOx activity was shown to be maintained and localised on the amyloid fibrils, with immobilisation also increasing stability.

Attempts were made to immobilise GOx to crystallin fibrils using both GA and MG, although these were unfortunately unsuccessful, despite the use of a range of cross-linking conditions. Post-translational modifications are thought to be the reason for this, and preliminary experiments involving carbohydrate-specific staining of SDS-PAGE gels showed crude crystallin proteins to be highly glycosylated. In order to use crystallin amyloid fibrils for enzyme immobilisation future work is needed exploring alternate immobilisation methods, relying on different surface chemistry and/or removal of carbohydrates.

A very basic glucose sensing device was then made by modifying gold electrodes with the GOx functionalised insulin fibrils. Prior to glucose sensing experiments, the electrochemical behaviour of insulin fibrils was investigated and as high concentrations of fibrils were seen to block the conductive electrode surface, low concentrations of GOx functionalised fibrils were used in future experiments. The catalytic activity of the modified electrodes was quantified in the presence of excess glucose, using FcOH as a mediator in solution. The anodic current was seen to be amplified in the presence of glucose, which showed that this very simple device was able to be used to electrochemically detect glucose. Washing and repeated use of the modified electrode resulted in little reduction in the observed response, indicating that the fibrils are well adhered to the gold electrode and the device is reusable. Other PNT/PNFs such as FF PNTs have also been used in this way (Yemini *et al*., 2005), although it has subsequently been shown that they have poor stability in phosphate buffer (Andersen *et al*., 2011), in which they were immersed for glucose sensing experiments, raising doubts over their effectiveness and certainly the reusability of a sensing device based around them.

Comparison of current amplification achieved with GOx:IF modified electrodes was compared to a GOx only modified electrode, where the GOx sample used was diluted in phosphate buffer to have the same activity in solution as the GOx:IF sample used. The GOx:IF and GOx only modified electrodes show very similar current amplifications, which suggests that the presence of fibrils is not increasing the current amplification of the electrode. The role of the fibrils was to increase the available surface area to which GOx could be immobilised, and as fibrils had to be used at low concentrations due to their blocking behaviour, this benefit was not fully realised. It would be interesting to co-functionalise insulin fibrils with both conducting polymer and GOx, as increased fibril conductivity would overcome this blocking behaviour, meaning that fibrils could be fully utilised as a high surface area support for biosensing.

Preliminary investigations towards the use of GOx:IF as single-molecule sensors showed the conductivity of GOx:IF networks to be glucose sensitive. This was a promising initial result towards the creation of a conductance-based glucose sensing device. Future work involving a full characterisation of this system's capability would help realise this goal, particularly if insulin fibrils were able to be manipulated and immobilised by DEP in the same way that crystallin fibrils were.

This study has confirmed a role for amyloid fibrils in bionanotechnology. The use of amyloid fibrils formed from crude crystallin proteins in this area would add value to a low cost waste product. Work on these fibrils and those formed from the other protein sources used in this thesis show amyloid fibrils to have potential as novel nanoscaffolds, with a number of desirable properties. Modification of these nanoscaffolds either to increase conductivity or add functionality would allow their use in a variety of nanowire applications, such as biosensing and bioelectronics.

6.1. References

Adachi R, Yamaguchi K, Yagi H, Sakurai K, Naiki H, Goto Y. 2007. Flow-induced alignment of amyloid protofilaments revealed by linear dichroism. *Journal of Biological Chemistry* **282**:8978–8983.

Andersen K, Castillo-Leon J, Hedström M, Svendsen W. 2011. Stability of diphenylalanine peptide nanotubes in solution. *Nanoscale* **3**:994–998.

Brange J, Andersen L, Laursen E, Meyn G, Rasmussen E. 1997. Toward understanding insulin fibrillation. *Journal of Pharmaceutical Sciences* **86**:517–525.

Castillo J, Tanzi S, Dimaki M, Svendsen W. 2008. Manipulation of self-assembly amyloid peptide nanotubes by dielectrophoresis. *Electrophoresis* **29**:5026–5032.

Dimaki M, Bøggild P. 2005. Frequency dependence of the structure and electrical behaviour of carbon nanotube networks assembled by dielectrophoresis. *Nanotechnology* **16**:759–763.

Dobson C. 2003. Protein folding and misfolding. *Nature* **426**:884–890.

Garvey M, Gras S, Meehan S, Meade S, Carver J, Gerrard J. 2009. Protein nanofibres of defined morphology prepared from mixtures of crude crystallins. *International Journal of Nanotechnology* **6**:258–273.

Gazit E. 2007. Use of biomolecular templates for the fabrication of metal nanowires. *FEBS Journal* **274**:317–322.

Gras S. 2007. Amyloid fibrils: From disease to design. New biomaterial applications for self-assembling cross-β fibrils. *Australian Journal of Chemistry* **60**:333–342.

Hamedi M, Herland A, Karlsson R, Inganas O. 2008. Electrochemical devices made from conducting nanowire networks self-assembled from amyloid fibrils and alkoxysulfonate PEDOT. *Nano Letters* **8**:1736–1740.

Healy J, Wong K, Roux C, Domigan L, Sunde M, Sawyer E, Gras S, Gerrard J, Vadudevamurthy M. 2012. Polymorphism and higher ordered structures of protein nanofibers from crude mixtures of fish lens crystallins: Towards useful materials. *Biopolymers*:Accepted.

Herland A, Thomsson D, Mirzov O, Scheblykin I, Inganäs O. 2008. Decoration of amyloid fibrils with luminescent conjugated polymers. *Journal of Materials Chemistry* **18**:126–132.

Herland A, Björk P, Hania P, Scheblykin I, Inganäs O. 2007. Alignment of a conjugated polymer onto amyloid-like protein fibrils. *Small* **3**:318–25.

Kwan A, Winefield R, Sunde M, Matthews J, Haverkamp R, Templeton M, Mackay J. 2006. Structural basis for rodlet assembly in fungal hydrophobins. *Proceedings of the National Academy of Sciences of the United States of America* **103**:3621–3626.

Mauro M, Craparo E, Podesta A, Bulone D, Carrotta R, Martorana V, Tiana G, San Biagio P. 2007. Kinetics of different processes in human insulin amyloid formation. *Journal of Molecular Biology* **366**:258–274.

del Mercato L, Pompa P, Maruccio G, Torre A, Sabella S, Tamburro A, Cingolani R, Rinaldi R. 2007. Charge transport and intrinsic fluorescence in amyloid-like fibrils. *Proceedings of the National Academy of Sciences of the United States of America* **104**:18019–18024.

Pauling L, Corey R. 1951. Configuration of polypeptide chains. *Nature* **168**:550–551.

Pilkington S, Roberts S, Meade S, Gerrard J. 2010. Amyloid fibrils as a nanoscaffold for enzyme immobilisation. *Biotechnology Progress* **26**:93–100.

Raynes J. 2012. Immobilising biomolecules on amyloid fibrils for bionanotechnological applications. PhD Thesis; University of Canterbury.

Scheibel T, Parthasarathy R, Sawicki G, Lin X-M, Jaeger H, Lindquist S. 2003. Conducting nanowires built by controlled self-assembly of amyloid fibers and selective metal deposition. *Proceedings of the National Academy of Sciences of the United States of America* **100**:4527–4532.

Serpell L, Fraser P, Sunde M. 1999. X-ray fiber diffraction of amyloid fibrils. *Amyloids, Prions, and other Protein Aggregates* **309**:526–536.

Storm A, van Noort J, de Vries S, Dekker C. 2001. Insulating behavior for DNA molecules between nanoelectrodes at the 100 nm length scale. *Applied Physics Letters* **79**:3881–3883.

Tanaka H, Herland A, Lindgren L, Tsutsui T, Andersson M. 2008. Enhanced current efficiency from bio-organic light-emitting diodes using decorated amyloid fibrils with conjugated polymer. *Nano Letters* **8**:2858–2861.

Waterhouse S, Gerrard J. 2004. Amyloid fibrils in bionanotechnology. *Australian Journal of Chemistry* **57**:519–523.

Waugh D. 1946. A fibrous modification of insulin. I. The heat precipitate of insulin. *Journal of the American Chemical Society* **68**:247–250.

Yemini M, Reches M, Rishpon J, Gazit E. 2005. Novel electrochemical biosensing platform using self-assembled peptide nanotubes. *Nano Letters* **5**:183–186.

7. Chapter Seven

Experimental

7.1. General materials and methods

Unless otherwise stated, all chemicals, reagents, and solvents were obtained from Sigma Chemical Co., BDH Laboratory Supplies or Invitrogen, and were of analytical grade.

Fish heads were supplied by the local fish market, with eye lenses extracted in the lab.

pH measurements were carried out using an UltraBasic UB10 pH meter, purchased from Denver Instrument Co. and fitted with a high-performance glass body pH/Tris electrode. The electrode was calibrated against standard buffers at pH 4.0, 7.0, and 9.0, purchased from BDH Laboratory Supplies.

Sodium dodecyl sulfate polyacrylamide gel electrophoresis (SDS-PAGE) was run using a NuPAGE system gel electrophoresis box, with precast 10 well NuPAGE Novex® 4-12 % Bis-Tris gradient gels 1.0 mm (Invitrogen). Samples were prepared by mixing with lithium dodecyl sulfate (LDS) 4 x sample buffer, and reducing agent, and then heating at 90 °C for 5 minutes to aid the reduction of disulfide bonds. An Invitrogen Novex® Sharp Pre-stained Wide-Range Protein Standard ladder was also run for each gel. Electrophoresis was carried out at a constant voltage of 200 V in 3-(*N*-morpholino)ethanesulfonic acid (MOPS)-SDS running buffer (**Table 7.1**) at room temperature for 50 minutes. Gels were stained with Coomassie R-250 (**Table 7.1**) for 30 minutes, and then destained with destaining solution (**Table 7.1**) for at least three hours. Gel images were captured using a BioImaging System (Syngene).

Protein concentrations of unknown solutions were measured on a Thermo Scientific NanoDrop ND-1000 Spectrophotometer (A_{280}) (Thermo Fischer Scientific), unless stated otherwise. Measurements of three replicates were averaged and corrected for a blank of the sample buffer.

Table 7.1. *SDS-PAGE gel solutions*

Solution	Contents
(MOPS)-SDS running buffer	50 mM MOPS
	50 mM tris base
	0.1 % SDS
	1 mM ethylenediaminetetraacetic acid (EDTA)
	pH 7.4
Coomassie R-250	2.5 ng/L Coomassie R-250
	10 % (v/v) glacial acetic acid
	45 % (v/v) methanol
	45 % (v/v) dH_2O
Destaining solution	30 % (v/v) methanol
	10 % (v/v) acetic acid
	60 % (v/v) dH_2O

Freeze drying of samples was carried out in a Thermo Savant Supermodulyo 230 freeze drier.

Images of protein structures were constructed using PyMOL (The PyMOL Molecular Graphics System, Version 1.3, Schrodinger, LLC), from the appropriate PDB file.

Alignments of protein sequences were performed using ClustalW (Larkin *et al*., 2007), on the server at the EMBL-EBI (Goujon *et al*., 2010), using the default alignment settings. Phylogenetic trees were constructed using FigTree (Version 1.3.1, BEAST Software).

Optical microscopy images were taken using a Olympus BX60 Transmitted-Reflected Light Microscope fitted with a Leica DFC320 Digital Camera.

7.2. Procedures for bovine insulin amyloid fibril formation and ThT assay

Insulin amyloid fibrils were prepared by in-house methods adapted from the literature (Nielsen *et al*., 2001), using bovine insulin obtained commercially (Sigma Chemicals (Lot 054K1375)). Fibrils were analysed by the ThT fluorescence assay (LeVine III, 1993).

7.2.1. Formation of fibrils from bovine insulin

Unless stated otherwise, solutions of insulin were prepared in duplicate to 5.8 mg/mL, in insulin fibril buffer (**Table 7.2**). Samples were aliquoted (1 mL) into sealed Eppendorf tubes and placed in a heating block set at 60 °C for 24 hours. Insulin control samples were prepared and immediately placed in the freezer. The presence of fibrils was confirmed using the ThT assay and TEM imaging.

Table 7.2. *Components of insulin fibril formation buffer.*

Solution	Contents
Insulin fibril buffer	100 mM NaCl 25 mM HCl, pH 1.6 with HCl

7.2.2. ThT assay on insulin fibrils

The ThT assay was carried out according to in-house methods. ThT solution was prepared fresh before each use by dissolving 2.5 mM ThT in ThT buffer (**Table 7.3**), and then filtering the solution with a syringe filter. ThT assay solutions (**Table 7.3**) were aliquoted into 96 well, clear bottomed Nunc^{TM} fluorescence well plates. The following controls were also prepared: 1) Insulin fibrils without ThT, 2) No insulin fibril solution. The well plates were sealed with Nunc^{TM} 236707 sealing tape, to minimise evaporation. ThT fluorescence emission intensity was measured using excitation/emission filters of 450 and 485 nm respectively. Measurements were recorded by a BMG Labtech FLUOstar OPTIMA Platereader (Alphatech Systems Ltd). Fluorescence was measured for at least three replicates.

Table 7.3. *Details of ThT assay components*

Solution	Contents
ThT buffer	50 mM tris 100 mM NaCl pH 7.5
ThT assay solution – regular (contents per well)	100 µL ThT buffer 66 µL nanopure water 30 µL unknown sample 4 µL ThT solution
ThT assay solution – real time (contents per well)	12.5 µM ThT Unknown sample (final volume 200 µL)

Where fibril formation was monitored using the ThT assay in real-time, the protocol differed from that described above and is detailed in **Table 7.3**. Fluorescence was measured every five minutes for 240 minutes, with the platereader incubating the sample at the desired temperature for the duration of the assay.

7.3. Procedures for hydrophobin rodlet formation and ThT assay

Unless stated otherwise, hydrophobins were prepared by in-house methods from the Sunde lab (Kwan *et al*., 2008). Hydrophobin rodlets were formed using the hydrophobin protein EAS, kindly provided by Margie Sunde from the University of Sydney. Rodlets were analysed by the ThT fluorescence assay (LeVine III, 1993).

7.3.1. Formation of hydrophobin rodlets

Hydrophobins were dissolved in nanopure H_2O at a concentration of 1 mg/mL, and rodlets then formed by vortexing the sample for two minutes (Kwan *et al*., 2008).

7.3.2. ThT assay on hydrophobin rodlets

The ThT assay was carried out as per Section 7.2.2, with the exception that only 10 μL of protein sample was used per 200 μL assay volume. Where fibril formation was monitored using the ThT assay in real-time, the method described in Section 7.2.2 was followed, with the exception that fluorescence was measured every two minutes for three hours.

7.4. Procedures for crystallin amyloid fibril formation and ThT assay

Crystallin proteins were extracted from fish eye lenses and amyloid fibrils formed from this crude mixture by in-house methods adapted from Garvey *et al*. (2009). Fibril formation was confirmed by the ThT fluorescence assay (LeVine III, 1993), and TEM imaging.

7.4.1. Extraction of crystallin proteins

The crystallin protein extraction method was adapted from Garvey *et al*. (2009). Fish eye lenses were homogenised in extraction buffer, with 2 mL buffer used per lens. Homogenisation was carried out for 20 minutes using a IKA® Ultra Turrax® Tube Disperser fitted with tube ST-20. The homogenate was centrifuged at 10,000 rpm for 30 minutes at 20 °C in an Eppendorf® MiniSpin® Plus bench-top centrifuge. The supernatant was removed and analysed for protein concentration using the Nanodrop (A_{280}) (Section 0). The crude crystallin stock solution was then either used fresh for fibril formation or kept at 4 °C until use.

Table 7.4. *Details for solutions needed for extraction of crystallin proteins*

Solution	Contents
Extraction buffer	50 mM Tris 5 mM EDTA 1 mM DTT pH 7.0

7.4.2. Formation of fibrils from crude crystallins

Amyloid fibrils were formed directly from crude mixtures of fish eye lens proteins using methods adapted from the literature (Garvey *et al*., 2009). The crude crystallin stock solution was diluted to 10 mg/mL into 25 % *n*-propanol, pH 3.8 that was preheated to 80 °C, to give a total volume of 1 mL. The sample was incubated for 1 hour at 80 °C in a heating block and then centrifuged at 10,000 rpm for 1 min. The supernatant was then removed and returned to the heating block, where it was incubated at 80 °C for 24 hours. The sample was then incubated at room temperature for at least 3 days. The presence of fibrils was confirmed using the ThT assay and TEM imaging.

7.4.3. ThT assay on crystallin fibrils

The ThT assay on crystallin fibrils was carried out as described in Section 7.2.2. Control measurements were also carried out on a sample that was taken from the supernatant that fibrils were formed from (Section 7.3.2), prior to incubation.

7.5. TEM imaging of amyloid fibrils

Insulin, crystallin, and hydrophobin fibril formation and morphology were assessed by TEM using negative staining, as described in the literature (Nilsson, 2004). TEM samples were prepared using Formvar-coated copper TEM grids (200 mesh). Grids were first washed with 3 μL nanopure water. 3 μL of protein fibril sample was placed on the grid and left for 1.5 min, with excess removed with filter paper. The grid was then stained with 2 μL uranyl acetate (2% w/v) and left for 45 sec, with excess removed with filter paper. Grids were then rinsed with another aliquot of nanopure water, and left to air dry. For TEM imaging of hydrophobin rodlets the grid was floated on a 3 μL droplet of hydrophobin solution for 5 minutes, which allowed rodlets to form on the TEM grid. Samples were then stained as described. The micrographs were taken using a Morgagni 268D TEM (FEI Company, Oregan, USA) operating at 80 kV and fitted with a 40 μm objective aperture.

7.6. AFM imaging of amyloid fibrils

Amyloid fibril samples were diluted to 0.01 mg/mL in pH 1.6 nanopure water, and 10 μL of solution deposited onto silicon oxide wafers and dried by evaporation. For AFM imaging of hydrophobin rodlets the wafer was floated on a 400 μL droplet of hydrophobin solution for 5 minutes, which allowed rodlets to form on the wafer.

Tapping-mode AFM images were obtained with a Digital Instruments Dimension 3100 AFM, imaging in air. General purpose silicon probes with aluminium reflex coating (Tap300Al-G; Budget Sensors, Innovative Solutions Bulgaria Ltd) were used, with a force constant of 40 N/m and a resonance frequency of 300 kHz. Images were collected (512 samples/line) at scan speeds of 0.5-1.0 Hz. The images were flattened and analysed using NanoScope (R) III (Version 5.31 R1, Digital Instruments).

7.7. X-ray fibre diffraction of crude crystallin fibrils

X-ray fibre diffraction was carried at the University of Sydney by in-house methods, based on those of Serpell *et al*., (1999). Crude crystallin fibrils were concentrated using centrifugation (30 min at 13,500 rpm) and the pellet resuspended in minimal milliQ water. Aliquots of crude crystallin fibrils (10-20 μL) were suspended between two waxed-filled capillary ends, and the sample air-dried. The small stalk of protein obtained was placed in an X-ray beam and diffraction data were obtained using a CuK_{α} Rigaku rotating anode source (wavelength 1.5418 Å) equipped with a MARresearch image plate detector. The sample to detector distance was 175 mm and the exposure time was 20 min. Images were examined and relections were measured using marView.

7.8. Procedures for the formation of amyloid fibrils from semi-purified crystallins.

Mixtures of crude crystallin proteins were semi-purified into the three classes, α, β, and γ, using size exclusion chromatography (SEC), with amyloid fibrils then formed from the semi-purifed fractions (Garvey *et al*., 2009).

7.8.1. Separation of crystallin proteins using size exclusion chromatography.

Crude crystallin proteins were prepared as described in Section 7.4.1 and purified by SEC on a HiLoad 16/60 Superdex 200 prep grade column (Garvey *et al*., 2009). The elution speed was 0.5 mL/min, with 20 mM Tris (pH 8.0) at 4 °C. The absorbance at 280 nm was monitored, and 0.5 mL fractions were collected. This separation process was carried out multiple times, and achieved a typical elution profile with high reproducibility. Samples were run on an SDS-PAGE gel (Section 0) to assess purity.

7.8.2. Formation of fibrils from purified crystallin proteins

After separation (Section 7.8.1), fractions containing each of the various classes of crystallin proteins were pooled, and the protein concentrated by freeze drying (Section 0). The freeze dried protein was then resuspended in minimal nanopure H_2O, and the concentration determined by NanoDrop (Section 0). Amyloid fibril formation was then carried out as described in Section 7.4.2.

7.9. Procedures to test crystallin fibril stability in various solvents

The procedures to test crystallin fibril stability in the presence of various solvents were based on those of (Andersen *et al*., 2011). Fibrils formed from crude crystallins (Section 7.4.2) were collected by centrifugation at 10,000 rpm for 2 min, and resuspended in various solvents (**Table 7.5**). Presence of fibrils was assessed by the ThT assay (Section 7.4.3) immediately and also after 3 hours of incubation at room temperature. Samples were analysed by TEM after 3 hours of incubation.

Table 7.5. *Details of the different solvents used to test crystallin stability*

Solutions	Contents
Crystallin fibril buffer	25 % *n*-propanol, pH 3.8
Crystallin fibril buffer – pH 7.0	Crystallin fibril buffer adjusted to pH 7.0
Water	Nanopure H_2O
Phosphate buffer	100 mM sodium phosphate buffer, pH 7.4
Ethanol	100 % ethanol
Isopropanol	100 % isopropanol
Methanol	100 % methanol
Acetonitrile	100 % acetonitrile

7.10. Procedures to assess the effect of growth and storage conditions on insulin amyloid fibril dimensions

The effect of various growth and storage conditions on the dimensions of insulin amyloid fibrils were determined by the formation of fibrils at various combinations of conditions, followed by analysis of dimension using TEM and AFM imaging.

7.10.1. Insulin fibril formation

Fibrils were formed from adapted in-house methods. Bovine insulin was dissolved at varying concentrations (0.5, 1.0, 2.0, 3.0, 4.0, 5.0, and 5.8 mg/mL) in 100 mM NaCl adjusted to a various pH values (pH 1.0, 1.5, 2.0 and 2.5) with HCl. This preparation was then subjected to elevated temperature (30, 40, 50 and 60 °C) for periods of time ranging from 24 hours up to 7 days. The effect of storage condition was also investigated, with fibrils being stored at room temperature, under refrigeration, and frozen. A full description of the different combinations of conditions is detailed in **Table 7.6**. The presence of amyloid fibrils was confirmed using the ThT assay (Section 7.2.2.). As we were interested in the resulting dimensions of fibrils we accounted for any discrepancies in the time taken for nuclei to form by making length and diameter measurements once all samples had reached similar ThT values.

Table 7.6. *Detail of the different growth and storage conditions used for the insulin amyloid fibril samples.*

Sample number	Growth concentration (mg/mL)	Growth temperature (°C)	Buffer		Growth time	Storage conditions
			pH	Salt		
1	5.8	Room temp.	1.5	100 mM NaCl	24 hrs	Room temp.
2		30				
3		40				
4		50				
5		60				
6	5.8	60	1.0	100 mM NaCl	24 hrs	Room temp.
7			2.0			
8			2.5			
9	0.5	60	1.5	100 mM NaCl	24 hrs	Room temp.
10	1.0					
11	2.0					
12	3.0					
13	4.0					
14	5.0					
15	5.8	60	1.5	100 mM NaCl	24 hrs	Refrigeration
16						Freeze/thaw x1
17						Freeze/thaw x2

7.10.2. TEM imaging of fibril length and data acquisition

TEM imaging (Section 7.5) was used to assess the effect of growth and storage condition on insulin fibril length. Images of fibrils were captured randomly on the grids and their lengths were measured to construct a length distribution. To obtain reliable statistics, at least 200 fibrils were analysed for each sample. Only fibrils that could be clearly distinguished with both ends visible within the image were analysed (Humblet-Hua *et al*., 2008).

7.10.3. AFM imaging of fibril diameter and data acquisition

AFM imaging (Section 7.6) was used to assess the effect of growth and storage condition on insulin fibril diameter. Diameter data were collected from a representative AFM image for 20 fibrils per sample, as the average of three measurements along the length of the fibril.

7.11. Procedures for fabrication of microelectrodes by optical lithography

In order to test the conductivity of amyloid fibril networks, interdigitated gold microelectrodes were fabricated using standard photolithographic techniques, based upon those of del Mercato *et al*., (2007).

7.11.1. Mask design and fabrication

Mask designs were created using the CAD system L-Edit Layout Editor v. 12.6 (Tanner EDA). The mask material used consisted of 10 cm^2 soda lime glass coated with low reflective chrome, onto which a layer of positive photoresist was applied using a Headway Research Inc. Spinner (Model PWM32). The designs were transferred to the mask material using a Heidelberg μPG 101 micropattern generator (Heidelberg Instruments, Germany). Following pattern transfer, the photoresist was removed using MIF 300 (metal ion free) developer, the active ingredient of which is TMAH (tetramethyl ammonium hydroxide). The chrome was then removed using chrome etch (consisting of ceric ammonium hydroxide), and lastly the remainder of the photoresist was removed using acetone.

7.11.2. Wafer preparation

Using a Balzers evaporator, fitted with a Sigma Instruments SQM-160 rate/thickness monitor, a 100 nm Au layer and a 10 nm NiCr adhesion layer were deposited onto a SiO_2 wafer, which was washed successively with acetone, methanol, and isopropanol, and then baked at 100 °C to remove solvent traces prior to this. The thickness of the layers was confirmed using a Veeco Dektak 150 Surface Profilometer. Following the evaporation process, the wafer was cut into 1 cm^2 chips using a diamond scriber. Prior to pattern transfer by optical lithography, the chips were cleaned *via* successive washing with acetone, methanol, and isopropanol, with the chips dried with a stream of nitrogen between washes. Following cleaning, the chips were baked at 100 °C for 15 minutes to ensure all solvent traces had been removed.

7.11.3. Pattern transfer by optical lithography

A layer of HDMS was applied to the chip using a Headway Research Inc. Spinner (Model PWM32), with 1 drop deposited and spun on for one minute at 4000 rpm. Two drops of AZ1518 (general use positive photoresist) were then applied and spun for one minute at 4000 rpm. The chip was then baked for 90 seconds at 100 °C.

The mask pattern was then transferred to the substrate using a Karl Suss MA6 mask aligner, operating in vacuum contact mode, with an alignment gap of 100 μm, and an exposure time of 25 seconds.

Following exposure, the photoresist was developed by being placed in AZ MIF 300 positive resist developer for 17 seconds and then into de-ionized water to stop the reaction. The chip was blown dry with nitrogen and baked for 60 seconds at 100 °C. The chip was placed in gold etch for 5-10 second intervals, until the gold layer was confirmed to be removed by optical microscopy. The nichrome layer was removed in the same way using chrome etch. Finally, the remaining photoresist was removed using acetone and the chip blown dry with nitrogen.

7.12. Conductivity measurements of amyloid fibril networks

Conductivity measurements on amyloid fibril networks were carried out as per the methods of del Mercato *et al*., (2007). For insulin, both unmodified and modified, and crystallins, amyloid fibril samples of 10 μL were deposited onto gold interdigitated electrodes, and solvent removed *via* evaporation. For hydrophobin amyloid fibril samples, the chip was floated on a 400 μL droplet containing hydrophobins for five minutes, with excess solvent then removed by evaporation. The sample current was measured by means of a probe station (Micromanipulator 1800) combined with a parameter analyser (Hewlett-Packard HP 4155A).

In order to remove the presence of salt as a complicating factor, the insulin fibril samples used for conductivity measurements were grown in the absence of salt after ensuring that this had no effect on dimensions of fibrils formed. Dimensions were analysed from TEM images as per Section 7.10.2

7.13. Protease treatment of insulin fibrils

Insulin amyloid fibrils were treated with the protease pepsin, to remove any non-fibrillar species present (Zurdo *et al*., 2001). Pepsin was added to insulin amyloid fibrils at a ratio of 1:200 w/w pepsin:fibrils and the sample incubated at 37 °C for at least 1 hour. The sample was centrifuged at 14,500 rpm for 3 minutes using an Eppendorf® Minispin® Plus benchtop centrifuge. The supernatant was removed and the fibrils resuspended in insulin fibril buffer (**Table 7.2**).

7.14. Formation of "minus-zinc" bovine insulin fibrils

Prior to fibril formation, zinc was removed from bovine insulin powder. The desired concentration of bovine insulin was dissolved in nanopure water pH 1.6 with 5 mM EDTA and the sample incubated for 1 hour. The sample was run on a desalting column to remove EDTA. Following the removal of zinc, fibrils were formed as usual.

7.15. Procedures for manipulation and immobilisation of amyloid fibrils by dielectrophoresis

The following work was carried out during a visit to Denmark Technical University, Copenhagen. Crystallin amyloid fibrils were immobilised between electrodes on a microchip by DEP (Castillo *et al*., 2008). Immobilisation of fibrils was confirmed using SEM, and conductivity of the immobilised fibrils then investigated.

7.15.1. Manipulation of crystallin amyloid fibrils by DEP

A DEP microchip, consisting of 5 gold electrode pairs with a 5 μm gap on a silicon oxide wafer, was custom designed and fabricated using standard photolithographic techniques by collaborators at Denmark Technical University (Dimaki and Bøggild, 2005). An aliquot of 10 μL of crystallin amyloid fibrils, as prepared by the methods outlined in Section 7.4.2, was placed on top of the microelectrodes. The alternating current was then turned on and the different parameters were applied: frequency, potential magnitude, and time. Voltage amplitudes from 10 to 20 Vpp, frequencies from 1 kHz to 1 MHz, and times up to 5 min were applied on the electrodes for the DEP experiment. After the chosen time was finished and the voltage turned off, excess solvent was removed from the chip using a stream of nitrogen (Castillo *et al*., 2008). Each parameter combination was carried out for ten samples.

7.15.2. SEM imaging of DEP microchips

SEM imaging of DEP microchips was carried out with a LEO 1550 Scanning Electron Microscope with EDX.

7.15.3. Conductivity measurements

The sample current of crystallin amyloid fibrils that had been immobilised between electrode pairs by DEP was measured by means of a probe station (Micromanipulator 1800) combined with a parameter analyser (Hewlett-Packard HP 4155A) (Castillo *et al*., 2008).

7.16. Procedures for immobilisation of GOx to insulin amyloid fibrils using glutaraldehyde

Methods used for the cross-linking of glucose oxidase to bovine insulin amyloid fibrils were based on the protocol established by (Pilkington *et al*., 2010). The cross-linking reaction involved 1.9 mg/mL insulin amyloid fibrils, 150 mM glutaraldehyde, and 0.6 mg/mL glucose oxidase in 100 mM phosphate buffer at pH 7.4, at a ratio of 1:1:1. The insulin amyloid fibrils were first mixed by inversion with glutaraldehyde, and preincubated for 5 min, after which the glucose oxidase was added and the sample mixed by inversion again. The sample was incubated for 1 hour at 25 °C, after which the reaction was quenched by 100 mM Tris-HCl, pH 8.0, with the samples then immediately placed on ice. Samples were run on an SDS-PAGE gel to ensure that cross-linking had occurred (Section 0). "Active" amyloid fibrils were then collected by centrifuging the sample for two minutes at 14,000 rpm in a Eppendorf® Minispin® Plus benchtop centrifuge, with the fibrils then resuspended in 100 mM phosphate buffer, pH 7.4, and stored at 4 °C.

7.17. Procedures to determine glucose oxidase activity

Glucose oxidase activity was measured using the Invitrogen Amplex® red/Glucose oxidase assay kit (Zhou *et al*., 1997).

7.17.1. The Amplex® red assay

Samples containing glucose oxidase were incubated with Amplex® red reaction mixture (**Table 7.1**), for 30 minutes at room temperature, taking care that the samples were protected from light. Fluorescence was measured with a Labtech FLUOstar OPTIMA plate reader using excitation at 530 nm and fluorescence detection at 590 nm. Background fluorescence, as determined for a control sample with no glucose oxidase present, was subtracted from each value.

Table 7.7. *Components of Amplex® red reaction mixture*

Solution	Contents
Amplex® red reaction mixture	50 µm Amplex® red reagent 0.1 U/mL horseradish peroxidise (HRP) 50 mM glucose 100 mM sodium phosphate buffer, pH 7.4

7.17.2. GOx standard curve

A standard curve for the Amplex® red assay was created using GOx concentrations from 0 – 10 mU, where one unit is defined as the amount that will oxidize 1.0 µmole of β-D-glucose to D-gluconolactone and H_2O_2 per minute at pH 5.1 and 30 °C.

7.17.3. GOx activity of samples

GOx activity of samples was determined using the Amplex® red assay as described in Section 7.18, with the exception that samples were first diluted 1/10,000 in 100 mM phosphate buffer, pH 7.4. A control sample containing the fibril formation buffer was also assayed. All samples were assayed in triplicate.

7.18. The OPA assay

The OPA assay was carried out using in-house methods, based on those of Roth (1971). OPA solution was prepared as per **Table 7.8**. OPA solution (1 mL) was added to 50 µL of the sample of interest, and shaken by inversion for two minutes. The absorbance of the sample was then read at 340 nm using a BioRad SmartSpec Plus Spectrophotometer.

Table 7.8. *Details of OPA solution components*

Solution	Contents
OPA solution	25 mL sodium borate (0.1 M)
	2.5 mL SDS (20 % (w/w))
	40 mg OPA, dissolved in 1 mL methanol
	100 µL 2-mercaptoethanol
	Final volume adjusted to 50 mL with dH_2O

7.18.1. OPA standard curve

A standard curve for the OPA assay was created using lysine, dissolved in nanopure H_2O at concentrations from 0 – 200 µM, using the protocol described in Section 7.18. All samples were assayed in triplicate.

7.18.2. OPA assay of samples

The OPA assay was carried out on samples containing either native protein or amyloid fibrils using the protocol described in Section 7.18. A control sample containing the fibril formation buffer was also assayed. All samples were assayed in triplicate.

7.19. The ninhydrin assay

The ninhydrin assay was carried out using in-house methods, based on those of (Friedman *et al*., 1984). Ninhydrin buffer was prepared by a 1:3 mixture of lithium acetate buffer and ninhydrin solution (**Table 7.9**), and stored, covered with foil, at 2-8 °C. The ninhydrin buffer was added to diluted protein samples in a 1:1 ratio, along with a sample blank. The samples were heated in a water bath at 100 °C for ten minutes, vortexing after five minutes. The samples were then cooled on ice. 300 µL of 95 % (v/v) ethanol was then added to 300 µL of each sample and vortexed. The absorbance of the sample was then read at 570 nm using a BioRad SmartSpec Plus Spectrophotometer. If the A_{570} exceeded 1.0, the samples were further diluted with 95 % ethanol.

Table 7.9. *Details of ninhydrin buffer components*

Solution	Contents
Lithium acetate buffer	4 M lithium acetate
	pH 5.2 with acetic acid
Ninhydrin solution	0.01 M ninhydrin
	0.01 M hydridantin
	75 % (v/v) DMSO

7.19.1. Ninhydrin standard curve

A standard curve for the ninhydrin assay was created using lysine, dissolved in nanopure H_2O at concentrations from 0 – 200 μM, using the protocol described in Section 7.19. All samples were assayed in triplicate.

7.19.2. Ninhydrin assay of samples

The ninhydrin assay was carried out on samples containing either native protein or amyloid fibrils using the protocol described in Section 7.19. Samples were diluted with 95 % ethanol when needed to obtain an A_{570} below 1.0. A control sample containing the fibril formation buffer was also assayed. All samples were assayed in triplicate.

7.20. Procedures for immobilisation of GOx to crystallin amyloid fibrils

Attempts were made to immobilise GOx to crystallin amyloid fibrils using the methods in Section 7.16, and following this, attempts were made by varying the reaction conditions, including using the cross-linker methylglyoxal. Details of the different reaction conditions used are detailed in **Table 7.10**.

Crystallin fibrils were concentrated where desired by centrifugation and resuspension in minimal crystallin fibril buffer (Section 7.4.2). GOx, crystallin fibrils, and the cross-linking molecule (GA or MG), were combined in a ratio of 1:1:1 in various orders, with pre-incubation of two components where desired. This reaction mixture was then incubated at either 25 or 37 °C for the specified reaction time, after which the reaction was quenched by the addition of 100 mM Tris-HCl, pH 8.0, with the samples immediately placed on ice. The degree of cross-linking was then assessed by SDS-PAGE (Section 0).

Table 7.10. *Details of different conditions attempted for immobilisation of GOx to crude crystallin fibrils (GOx=glucose oxidase, CF=crystallin fibrils, and X=cross-linker).*

Variable	**Different conditions tried**
Reaction order	GOx+CF→X, GOx+X→CF, CF+X→GOx, GOx→CF→X, GOx→X→CF, GOx→CF→X,
Total reaction time (min)	30 - 120
Pre-incubation time (min)	5 - 20
(GOx+CF/GOx+X/CF+X)	
Reaction temperature (°C)	25, 37
Cross-linker	GA, MG, GA+MG
Cross-linker concentration	GA (10-150 mM), MG (1-4 %)
Crystallin fibril concentration (mg/mL)*	1.0 – 10.0
GOx concentration (mg/mL)	0.5 – 2.0

* This value is approximate.

7.21. Glycoprotein gel protocol

Glycoprotein gels were run using the Molecular Probes Pro-Q Emerald 300 Glycoprotein Gel and Blot Stain Kit (Invitrogen). Proteins were first separated by standard SDS-PAGE (Section 0). The gel was then fixed by immersing the gel in approximately 100 mL of fix solution (**Table 7.11**), and incubating at room temperature with gentle agitation for 45 minutes. This step was repeated to ensure the SDS was fully washed out of the gel. The gel was incubated in approximately 100 mL of wash solution (**Table 7.11**), with gentle agitation for 10-20 minutes. This step was also repeated. The carbohydrates were oxidized by incubating the gel in 25 mL of oxidizing solution (**Table 7.11**), with gentle agitation for 30 minutes. The gel was washed in approximately 100 mL of wash solution with gentle agitation for 10-20 minutes, and this step was carried out three times. The gel was stained by incubating in the dark in 25 mL of Pro-Q Emerald 300 staining solution (**Table 7.11**), while gently agitating for 90-120 minutes. The gel was washed by incubation for 15-20 minutes in 100 mL wash solution with gentle incubation. The stained gel was visualised using a 300 nm UV transilluminator, and gel images captured using a BioImaging System (Syngene).

Table 7.11. *Details of glycoprotein gel solutions*

Solution	**Components**
Pro-Q Emerald 300 Stock Solution	Pro-Q Emerald 300 reagent dissolved in 6 mL *N,N*-Dimethylformamide (DMF)
Fix solution	50 % methanol 5 % glacial acetic acid dH_2O
Wash solution	3 % glacial acetic acid
Oxidising solution	2.5 g periodic acid 250 mL 3 % glacial acetic acid
Pro-Q Emerald 300 Staining Solution	Pro-Q Emerald 300 Stock Solution diluted 50-fold into Pro-Q Emerald 300 Staining Buffer (this was prepared fresh before each use)

7.22. Development of a glucose sensing device

A glucose sensing device was developed using the GOx:IF that were formed as per Section 7.16.

7.22.1. Time-course of GOx:insulin amyloid fibril activity

The stability of the GOx:insulin amyloid fibrils, formed as per Section 7.16, was examined by testing the activity of samples stored at 4 °C, using the Amplex® red assay (Section 7.17.3). Activity was assayed in samples over a 40 day period. Controls of GOx only, GOx and GA, and GOx and insulin fibrils were also included. All samples were assayed in triplicate.

7.22.2. Qualitative assay of GOx activity

In order to ensure that GOx:IF were active when deposited on a surface, a qualitative assay of GOx activity was carried out. A 20 μL droplet of GOx:insulin fibrils, formed as per Section 7.16, was deposited onto 10 mm^2 silicon substrates, and excess solvent removed by evaporation. A droplet of Amplex® red reaction mixture was then deposited onto the substrate, and the colour change observed. Positive and negative controls of GOx only and insulin fibrils only respectively were also included.

7.22.3. Electrochemical characterisation of insulin fibrils

Electrochemical characterisation of insulin fibrils was carried out using DropSens screen-printed electrodes (DRT-C220AT, DropSens, Spain), which have dimensions of 3.4 x 1.0 x 0.05 cm (length x width x height), and consist of a 4 mm gold working electrode, a gold counter electrode, and a silver reference electrode. 20 μL of insulin fibril solution, at various concentrations diluted from fibrils formed at 1.9 mg/mL were deposited onto the electrode, and excess solvent removed by evaporation for one hour at 37 °C. Cyclic voltammetry was carried out in the presence of 1.5 mM FcOH in phosphate buffer, pH 7.4 (scan rate 5 mV/s) using a Uniscan Instruments PG581 potentiostat-galvanostat with a Dropsens connector DRP-CAC to connect the screen-printed electrode to the potentiostat. Once the optimum fibril concentration was established, cyclic voltammetry was carried out on both blank and fibril modified electrodes at scan rates from 5 to 100 mV.

7.23. Glucose sensing

The potential for GOx:IF to be used in a glucose sensing device was investigated by the modification of gold electrodes with GOx:IF followed by electrochemical detection of glucose in solution.

7.23.1. Formation of gold electrodes

A large silicon oxide wafer coated with a protective resist layer and then diced into 10 mm^2 wafers using a diamond scriber, and the resulting wafers washed successively with acetone, methanol, and isopropanol, and then baked at 100 °C to remove any solvent traces. The wafers were then mounted in a custom made sample holder which only reveals a 8 mm diameter circle in the centre of the wafer, and a 100 nm Au layer with a 10 nm NiCr adhesion layer deposited by evaporation using a Balzers evaporator fitted with a Sigma Instruments SQM – 160 rate/thickness monitor. Post evaporation, the wafers were again cleaned with acetone, methoanol, and isopropanol, and baked at 100 °C for 15 minutes.

7.23.2. Modification of gold electrodes

Gold electrodes were modified with GOx functionalised insulin fibrils by methods based upon those of Qian *et al*., (2009). 10 μL of GOx:IF sample was deposited onto the gold electrode, and excess solvent removed by evaporation, with the electrode incubated at 37 °C for one hour.

7.23.3. Electrochemical detection of glucose

The electrochemical detection of glucose was carried out by methods based on those of Lehr *et al*., (2010). Electrochemical measurements were performed using a computer-controlled EG & G PAR model 362 potentiostat. The GOx:IF modified electrodes (Section 7.23.2) were mounted on an insulated metal stage under a glass cell secured with four springs. A hole in the cell bottom was centred over the electrode and sealed with an O-ring. The area of the working electrode was 4 mm diameter. Electrical contact was maintained with a copper strip externally connected to the sample. The counter electrode was Pt wire and the reference electrode was silver/silver chloride.

The catalytic activity of the GOx:IF modified electrode was quantified *via* cyclic voltammograms in the absence and presence of excess glucose (400 mM), using 1.5 mM FcOH in 100 mM phosphate buffer, pH 7.4 as a mediator in solution. Voltammograms were obtained by cycling between -0.1 and +0.4 V at a scan rate of 5 mV/s. Controls experiments were carried out on unmodified electrodes, and on electrodes with GOx, which had been diluted in 100 mM phosphate buffer, pH 7.4 to have the same activity in solution as the GOx:IF sample, as ascertained by the Amplex® red assay (Section 7.17.3).

7.23.4. GOx:IF network sensors

The glucose sensing capabilities of GOx:IF networks was investigated. I-V characterisation of GOx:IF was carried out as per Section 7.12, with additional I-V measurements taken after the deposition of a droplet of 0.2 mM glucose (in 100 mM phosphate buffer, pH 7.4) on top of the GOx:IF network. Control experiments were also carried out with deposition of glucose on to insulin fibril networks.

7.24. qNano characterisation of crystallin amyloid fibrils

Methods for the characterisation of crystallin amyloid fibrils using the qNano were based upon those of Vogel *et al*. (2011), with all components obtained from IZON Science (New Zealand). Tunable nanopores were mounted on the q-Nano, and stretched open until the desired pore size was reached. Standard electrolyte buffer (SEB) was placed in both fluid cells which contain one electrode each, above and below the membrane. Current pulse signals were collected using IZON propriety software. Crystallin fibril samples run on the qNano were first diluted 100 x into SEB, and then placed in a sonicating water bath for 10 minutes.

7.25. References

Andersen K, Castillo-Leon J, Hedström M, Svendsen W. 2011. Stability of diphenylalanine peptide nanotubes in solution. *Nanoscale* **3**:994–998.

Castillo J, Tanzi S, Dimaki M, Svendsen W. 2008. Manipulation of self-assembly amyloid peptide nanotubes by dielectrophoresis. *Electrophoresis* **29**:5026–5032.

Dimaki M, Bøggild P. 2005. Frequency dependence of the structure and electrical behaviour of carbon nanotube networks assembled by dielectrophoresis. *Nanotechnology* **16**:759–763.

Friedman M, Pang J, Smith G. 1984. Ninhydrin-reactive lysine in food proteins. *Journal of Food Science* **49**:10–13.

Garvey M, Gras S, Meehan S, Meade S, Carver J, Gerrard J. 2009. Protein nanofibres of defined morphology prepared from mixtures of crude crystallins. *International Journal of Nanotechnology* **6**:258–273.

Goujon M, McWilliam H, Li W, Valentin F, Paern J, Lopez R. 2010. A new bioinformatics analysis tools framework at EMBL-EBI. *Nucleic Acids Research* **38**:Suppl W695–9.

Humblet-Hua N, Sagis L, van der Linden E. 2008. Effects of flow on hen egg white lysozyme (HEWL) fibril formation: length distribution, flexibility, and kinetics. *Journal of Agricultural and Food Chemistry* **56**:11875–11882.

Kwan A, Macindoe I, Vukasin P, Morris V, Kass I, Gupte R, Mark A, Templeton M, Mackay J, Sunde M. 2008. The Cys3-Cys4 loop of the hydrophobin EAS is not required for rodlet formation and surface activity. *Journal of Molecular Biology* **382**:708–720.

Larkin M, Blackshields G, Brown N, Chenna R, McGettigan P, McWilliam H, Valentin I, Wallace I, Wilm A, Lopez R, Thompson J, Gibson T, Higgins D. 2007. ClustalW and ClustalX version 2. *Bioinformatics* **23**:2947–2948.

Lehr J, Williamson B, Barrière F, Downard A. 2010. Dependence of catalytic activity and long-term stability of enzyme hydrogel films on curing time. *Bioelectrochemistry* **79**:142–146.

LeVine III H. 1993. Thioflavin T interaction with synthetic Alzheimer's disease β-amyloid peptides: Detection of amyloid aggregation in solution. *Protein Science* **2**:404–410.

del Mercato L, Pompa P, Maruccio G, Torre A, Sabella S, Tamburro A, Cingolani R, Rinaldi R. 2007. Charge transport and intrinsic fluorescence in amyloid-like fibrils. *Proceedings of the National Academy of Sciences of the United States of America* **104**:18019–18024.

Nielsen L, Khurana R, Coats A, Frokjaer S, Brange J, Vyas S, Uversky V, Fink A. 2001. Effect of environmental factors on the kinetics of insulin fibril formation: elucidation of the molecular mechanism. *Biochemistry* **40**:6036–6046.

Nilsson M. 2004. Techniques to study amyloid fibril formation in vitro. *Methods* **34**:151–160.

Pilkington S, Roberts S, Meade S, Gerrard J. 2010. Amyloid fibrils as a nanoscaffold for enzyme imobilization. *Biotechnology Progress* **26**:93–100.

Qian Z, Khan M, Mikkelsen S, Chen P. 2009. Improved enzyme immobilization on an ionic-complementary peptide-modified electrode for biomolecular sensing. *Langmuir* **26**:2176–2180.

Roth M. 1971. Fluorescence reaction for amino acids. *Analytical Chemistry* **43**:880–&.

Serpell L, Fraser P, Sunde M. 1999. X-ray fiber diffraction of amyloid fibrils. *Amyloids, Prions, and other Protein Aggregates* **309**:526–536.

Vogel R, Willmott G, Kozak D, Roberts G, Anderson W, Groenewegen L, Glossop B, Barnett A, Turner A, Trau M. 2011. Quantitative sizing of nano/microparticles with a tunable elastomeric pore sensor. *Analytical Chemistry* **83**:3499–3506.

Willmott G, Broom M, Jansen M, Young R, Arnold W. 2011. Tunable elastomeric nanopores. *Molecular and Nano-Tubes*:209.

Zhou M, Diwu Z, Panchuk-Voloshina N, Haugland R. 1997. A stable nonfluorescent derivative of resorufin for the fluorometric determination of trace hydrogen peroxide: applications in detecting the activity of phagocyte NADPH oxidase and other oxidases. *Analytical Biochemistry* **253**:162–168.

Zurdo J, Guijarro J, Dobson C. 2001. Preparation and characterization of purified amyloid fibrils. *Journal of the American Chemical Society* **123**:8141.

A. Appendix A

Sequence alignments of crystallin proteins

In Chapter 2, PyMOL images are shown of some examples of crystallin protein structures. Where possible, the structure shown was that from *Danio rerio* (zebrafish), as this is the only fish for which full crystallin sequence information is available. If no structure from *D. rerio* was available, the structure shown was that of the PDB files available, that had the highest sequence similarity to *D. rerio*. Sequence alignments were carried out using ClustalW. Details of the structures chosen, with justification, are shown in **Table A.1**, with the various sequence alignments shown in **Figure A.1** (αB-crystallin), **Figure A.2** (βA4-crystallin), **Figure A.3** (βB2-crystallin), and **Figure A.4** (γB-crystallin).

Table A.1. *Details of crystallin sequence information and representative structures chosen.*

Protein	sequence ID (*D. rerio*)	Structures available	Sequence ID	Alignment score * (%)	Structure used **	PDB ID
αA-crystallin	AAK61363.1	*D. rerio****	AAK61363.1	N/A	*D. rerio*	3N3E
αB-crystallin	AAD49096.1	*H. sapiens*	ACP18852.1	58.0	*H. sapiens*	3L1G
βA4-crystallin	NP_001018135.1	*H. sapiens*	NP_001877.1	68.0	*H. sapiens*	3LWK
βB2-crystallin	NP_001018138.1	*B. taurus*	NP_777232.1	71.0	*H. sapiens*	1YTQ
		M. musculus	NP_031799.1	71.0		
		R. norvegicus	NP_037069.1	71.0		
		H. sapiens	NP_00487.1	72.0		
γB-crystallin	NP_001012390.1	*H. sapiens*	NP_005201.2	59.0	*B. taurus*	1AMM
		B. taurus	NP_001013612.1	64.0		

*This is the pairwise alignment score (%) upon alignment with the *D. rerio* sequence.

**The structure used was that with the highest sequence similarity (based on alignment score) with the *D. rerio* sequence.

*** If the *D. rerio* structure was available then this was used.

```
Daniorerio-alphaB       MEISIQHPWYRRPLFPGFFPYRIFDQYFGEHLSDSD--PFSPFYTMFYYR-PYLWRFPSW 57
Homosapiens-alphaB      MDIAIHHPWIHRPFFPFHSPSRLFDQFFGEHLLESDLFPTSTSLSPFYLRPPSFLRAPSW 60
                        *:*:*:*** :**:** . * *:***:***** :**  * *.  : ** * * : * ***

Daniorerio-alphaB       WDSGMSEMRQDRDRFVINLDVKHFSPDELTVKVNEDFIEIHGKHDERQDDHGIVAREFFR 117
Homosapiens-alphaB      FDTGLSEMRLEKDRFSVNLDVKHFSPEELKVKVLGDVIEVHGKHEERQDEHGFISREFHR 120
                        :*:*:**** ::*** :*********:**.*** *.**:****:****:**:::***.*

Daniorerio-alphaB       KYKIPAGVDPGAITSSLSSDGVLTINTLRHQLDILERSIPIICGEKPPAQK---- 168
Homosapiens-alphaB      KYRIPADVDPLTITSSLSSDGVLTVNGPRKQVSGPERTIPITREEKPAVTAAPKK 175
                        **:***.*** :************:*  *:*:.  **:***   ***..
```

Figure A.1. *Sequence alignment of αB-crystallin proteins from* D. rerio *and* H. sapiens.

```
Daniorerio-betaA4       MTHHCTKFSGHWKIIVYDEECFQQRHHEFTSECCNVMEFGFESVRSLRVESGAWVGYEHA 60
Homosapiens-betaA4      MTLQCTKSAGPWKMVVWDEDGFQQRRHEFTAECPSVLELGFETVRSLKVLSGAWVGFEHA 60
                        ** :*** :* **::*:**: ****:****:** .*:*:***:****:* ******:***

Daniorerio-betaA4       SYQGHQFVLERGEYPQCDSFGGSNAYHIERMTSFRPISCANHRECRMTIYERENYLGRKG 120
Homosapiens-betaA4      GFQGQQYILERGEYPSWDAWGGNTAYPAERLTSFRPAACANHRDSRLTIFEQENFLGKKG 120
                        .:**:*::*******. *::**..**  **:***** :*****:.*:**:*:**:**:**

Daniorerio-betaA4       ELSDDYPSLQAMGWCNNEVGSLRVQSGAFVCYQFPGYRGYQYIMECDRHCGEYKQFREFG 180
Homosapiens-betaA4      ELSDDYPSLQAMGWEGNEVGSFHVHSGAWVCSQFPGYRGFQYVLECDHHSGDYKHFREWG 180
                        ************** .*****::*:***:** *******:**::***:*.*:**:***:*

Daniorerio-betaA4       SHSQTPQIQSIRRIQQ 196
Homosapiens-betaA4      SHAPTFQVQSIRRIQQ 196
                        **: * *:********
```

Figure A.2. *Sequence alignment of βA4-crystallin proteins from* D. rerio *and* H. sapiens.

```
Musmusculus-betaB2          MASDHQTQAGKP-QPLNP--KIIIFEQENFQGHSHELSGPCPNLKETGME 47
Rattusnorvegicus-betaB2     MASDHQTQAGKP-QPLNP--KIIIFEQENFQGHSHELSGPCPNLKETGME 47
Homosapiens-betaB2          MASDHQTQAGKP-QSLNP--KIIIFEQENFQGHSHELNGPCPNLKETGVE 47
Bostaurus-betaB2            MASDHQTQAGKP-QPLNP--KIIIFEQENFQGHSHELNGPCPNLKETGVE 47
Daniorerio-betaB2           MATDHQNPAIKQKQPVASAFKLVIYEQENFQGRCHELTGPCNNLQEAGVE 50
                            **:***. * *  *.: .  *::*:*******:.***.*** **:*:*:*

Musmusculus-betaB2          KAGSVLVQAGPWVGYEQANCKGEQFVFEKGEYPRWDSWTSSRRTDSLSSL 97
Rattusnorvegicus-betaB2     KAGSVLVQAGPWVGYEQANCKGEQFVFEKGEYPRWDSWTSSRRTDSLSSL 97
Homosapiens-betaB2          KAGSVLVQAGPWVGYEQANCKGEQFVFEKGEYPRWDSWTSSRRTDSLSSL 97
Bostaurus-betaB2            KAGSVLVQAGPWVGYEQANCKGEQFVFEKGEYPRWDSWTSSRRTDSLSSL 97
Daniorerio-betaB2           KVGSVLVQCGPWVGFEQPGCKGEQYVFEKGEYPRWDSWTNSRRSDCIVAF 100
                            *.******.*****:**..*****:**************.***:*.: ::

Musmusculus-betaB2          RPIKVDSQEHKIILYENPNFTGKKMEIVDDDVPSFHAHGYQEKVSSVRVQ 147
Rattusnorvegicus-betaB2     RPIKVDSQEHKIILYENPNFTGKKMEIVDDDVPSFHAHGYQEKVSSVRVQ 147
Homosapiens-betaB2          RPIKVDSQEHKIILYENPNFTGKKMEIIDDDVPSFHAHGYQEKVSSVRVQ 147
Bostaurus-betaB2            RPIKVDSQEHKITLYENPNFTGKKMEVIDDDVPSFHAHGYQEKVSSVRVQ 147
Daniorerio-betaB2           RPIKVDSQEHKIVLYENPSFTGKKIEIIDDDVPSFHAHGYHEKVSSVRVQ 150
                            ************ *****.*****:*::************:*********

Musmusculus-betaB2          SGTWVGYQYPGYRGLQYLLEKGDYKDNSDFGAPHPQVQSVRRIRDMQWHQ 197
Rattusnorvegicus-betaB2     SGTWVGYQYPGYRGLQYLLEKGDYKDNSDFGAPHPQVQSVRRIRDMQWHQ 197
Homosapiens-betaB2          SGTWVGYQYPGYRGLQYLLEKGDYKDSSDFGAPHPQVQSVRRIRDMQWHQ 197
Bostaurus-betaB2            SGTWVGYQYPGYRGLQYLLEKGDYKDSGDFGAPQPQVQSVRRIRDMQWHQ 197
Daniorerio-betaB2           SGTWVGYQYPGYRGFQYLFEKGEFKECSEFGAALPQIQSVRRIRDMQYHP 200
                            **************:***:***::*: .:***. **:***********:*

Musmusculus-betaB2          RGAFHPSS 205
Rattusnorvegicus-betaB2     RGAFHPSS 205
Homosapiens-betaB2          RGAFHPSN 205
Bostaurus-betaB2            RGAFHPSS 205
Daniorerio-betaB2           RGAFQATS 208
                            ****:.:.
```

Figure A.3. *Sequence alignment of βB2-crystallin proteins from* M. musculus*,* R. norvegicus*,* H. sapiens*,* B. Taurus*, and* D. rerio*.*

```
Homosapiens-gammaB      ---------MGKITFYEDRAFQGRSYECTTDCPNLQPYFSRCNSIRVESGCWMIYERPNY 51
Bostaurus-gammaB        ---------MGKITFYEDRGFQGHCYECSSDCPNLQPYFSRCNSIRVDSGCWMLYERPNY 51
Daniorerio-gammaB       MKLAKNMDRMGKIVFYEDRNFQGRSFECSLDCPELSSHFTRCNSIRVENGAWVLYERPNY 60
                                 ****.***** ***:.:**: ***:*..:*:********:.*.*::******

Homosapiens-gammaB      QGHQYFLRRGEYPDYQQWMGLSDSIRSCCLIPPHSGAYRMKIYDRDELRGQMSELTDDCI 111
Bostaurus-gammaB        QGHQYFLRRGDYPDYQQWMGFNDSIRSCRLIPQHTGTFRMRIYERDDFRGQMSEITDDCP 111
Daniorerio-gammaB       MGFQYILTRGEYPDYQRWMGYNDTIRSCRMVRNHTGSFRIRLYERPDFQGQIMESSEDWP 120
                         *.**:* **:*****:*** .*:**** ::  *:*::*:::*:* :::**  * ::*

Homosapiens-gammaB      SVQDRFHLTEIHSLNVLEGSWILYEMPNYRGRQYLLRPGEYRRFLDWGAPNAKVGSLRRV 171
Bostaurus-gammaB        SLQDRFHLTEVHSLNVLEGSWVLYEMPSYRGRQYLLRPGEYRRYLDWGAMNAKVGSLRRV 171
Daniorerio-gammaB       SLYDRFRQREVHSCNVLDGAWIFFEHPNYRGRQYLLEKGEYRCFTDWNAMHPTVGSIRRI 180
                        *: ***:  *:** ***:*:*:::* *.********. **** : **.* :..***:**:

Homosapiens-gammaB      MDLY 175
Bostaurus-gammaB        MDFY 175
Daniorerio-gammaB       QDF- 183
                         *:
```

Figure A.4. *Sequence alignment of γB-crystallin proteins from* H. sapiens, B. taurus, *and* D. rerio.

B. Appendix B

Characterisation of crystallin fibrils using the qNano

The qNano particle analyzer (Izon, New Zealand) was investigated as an alternative method for the characterization of crystallin fibrils. The qNano consists of a resizable nanopore, which is embedded in a thermoplastic polyurethane (TPU) membrane, which is in turn, situated in a fluid cell. The fluid cell contains an electrolyte solution, and when a voltage is applied across this membrane, a stable current, which may be attributed to the electrolyte solution, is observed. The instrument operates by detecting the change in resistance or ionic current caused by the passage of particles through the sensing channel or pore (Willmott *et al*., 2011; Willmott and Moore, 2008). This is shown schematically in **Figure B.1**.

Crystallin amyloid fibrils were lightly sonicated, using a sonicating water bath, prior to being introduced into the upper fluid cell. This was in done in order to reduce the number of large fibrillar aggregates, to increase the likelihood of visualising single-molecule translocation events. The fibrils were confirmed to be still intact by TEM (**Figure B.2**) and not fragmented to the degree seen with heavy sonication (Chapter 3, Section 3.5).

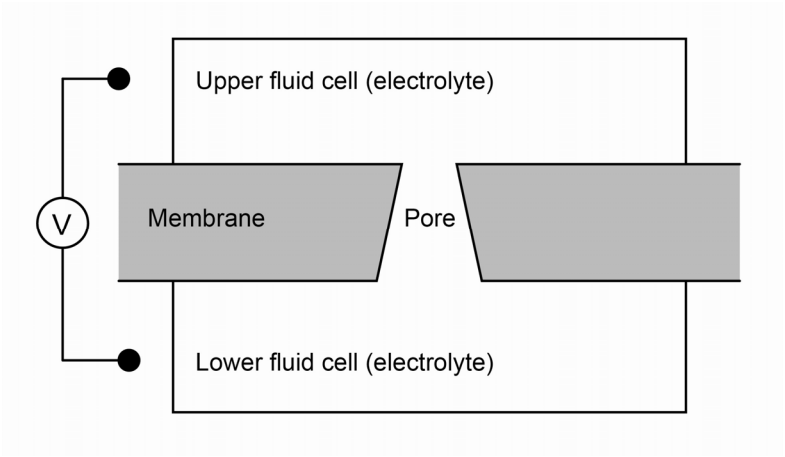

Figure B.1. *Schematic of the nanopore system utilised by the qNano. The nanopore system consists of a resizable nanopore which is embedded in a membrane. On either side of the membrane is an electrolyte solution which is contained in a fluid cell. A voltage is applied across this membrane, and so when a particle traverses the membrane via the nanopore, a fluctuation in current is observed, also known as a blockade event.*

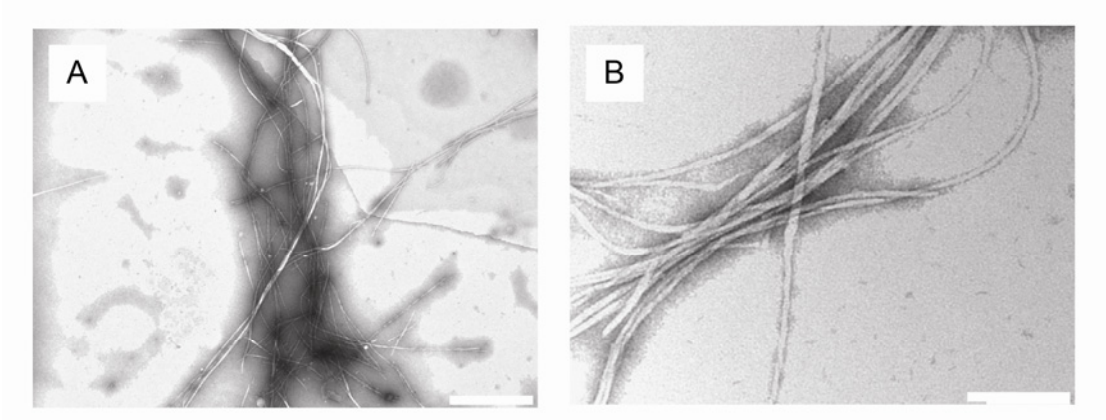

Figure B.2 *Representaitve TEM images of crystallin fibrils that were resuspended into SEB and then placed in a sonicating water bath for 10 minutes. Scale bars are 1 μm (A), and 0.2 μm (B).*

As crystallin fibrils are insulating (Chapter 4), when they pass through the pore they reduce/block the ionic current in a manner that reflects both their size and conformation. Each single-molecule translocation can be characterised by two parameters; the average blockade height (nA), and the duration of the blockade, that is, the time taken for the molecule to completely traverse the pore. **Figure B.3** shows a scatter plot of these two parameters for 64 events, along with examples of some of the current-time traces observed for translocation events. It is tempting to speculate that an event in which there is an increased blockade for a short time (**Figure B.3**, B, i) is due to the fibril being folded over on itself, in contrast to a long blockade duration where the fibril is stretched out (**Figure B.3**, B, ii). This was observed for DNA molecules passing through a graphene nanopore (Garaj *et al*., 2010); however, further investigation is required to establish if this is occurring with the fibrils in this study.

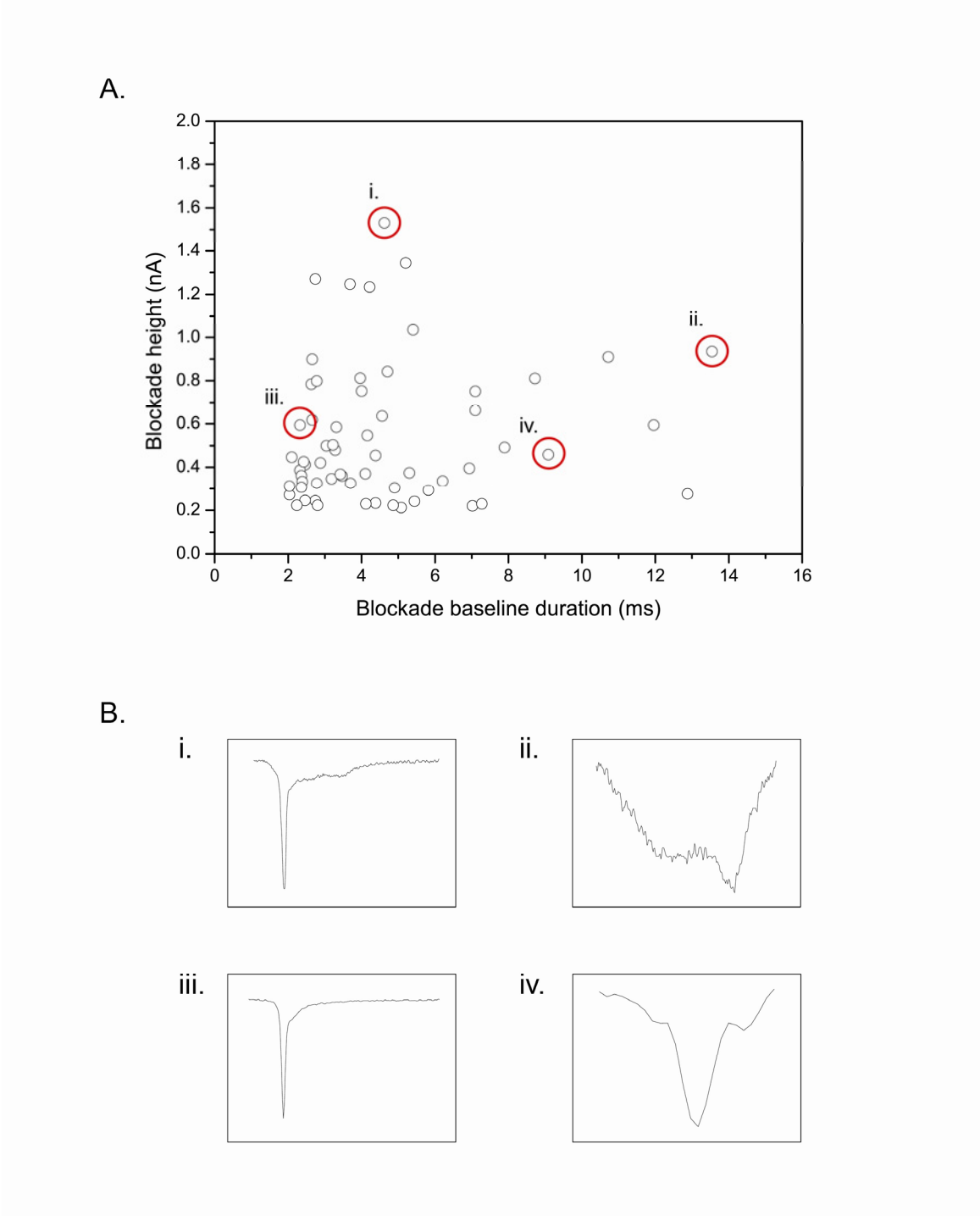

Figure B.3. *A) Scatter plot of blockade baseline duration versus blockade height, and B), examples of individual blockade traces, which correspond to the red circled events in the scatter plot.*

The qNano is able to be using for the gathering information on the size distribution of sample, by relating the blockade height to the size of the particle. Standard particles are used in order to generate data corresponding to the absolute size of particles. However, to date, the standard particles used are spherical, and so the absolute size distribution of crystallin fibrils was not able to be established from these. **Figure B.4** shows the distribution of average blockade heights (nA) of single-molecule translocation events for crystallin amyloid fibrils. Although absolute sizes of fibrils cannot be obtained from this, the existence of a large population of small fibrils is seen, similar to what was observed in the length characterisation of insulin fibrils in this thesis, and also in other studies in the literature. The development of a rod-shaped standard particle would allow a more meaningful analysis of the size distribution of amyloid fibrils.

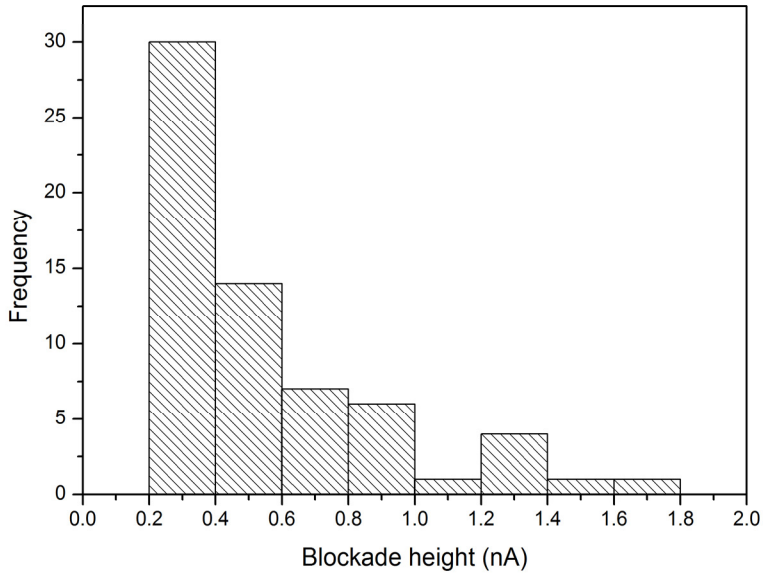

Figure B.4. *Distribution of average blockade heights (nA) of single-molecule translocation events for crystallin amyloid fibrils.*

A major problem encountered during this work was the clogging of the nanopore by the crystallin fibrils. This resulted in difficulty in achieving large sample sizes, as data were only able to be collected for approximately five minutes before the pore clogged. It also complicates the analysis of the parameters detailed in **Figure B.3**, as a long translocation event could be due to membrane-fibril interactions. Previous work, using a synthetic nanopore, overcame this problem by coating the nanopore with a fluid bilayer (Yusko *et al*., 2011). This coating eliminated non-specific interactions, meaning that translocation events of molecules that aggregate and have a tendency to clog nanopores were able to be analysed. This coating allowed analysis of translocation events of αβ-amyloid fibrils for 40 minutes at a time; however, no size data was gathered. A coating of this type on the TPU membranes used in the qNano would allow full characterisation of these type of molecules.

References

Garaj S, Hubbard W, Reina A, Kong J, Branton D, Golovchenko J. 2010. Graphene as a subnanometre trans-electrode membrane. *Nature* **467**:190–193.

Willmott G, Broom M, Jansen M, Young R, Arnold W. 2011. Tunable elastomeric nanopores. *Molecular and Nano-Tubes*:209.

Willmott G, Moore P. 2008. Reversible mechanical actuation of elastomeric nanopores. *Nanotechnology* **19**:475504.

Yusko E, Johnson J, Majd S, Prangkio P, Rollings R, Li J, Yang J, Mayer M. 2011. Controlling protein translocation through nanopores with bio-inspired fluid walls. *Nature Nanotechnology* **6**:253–260.

C. Appendix C

EDX analysis of DEP electrodes

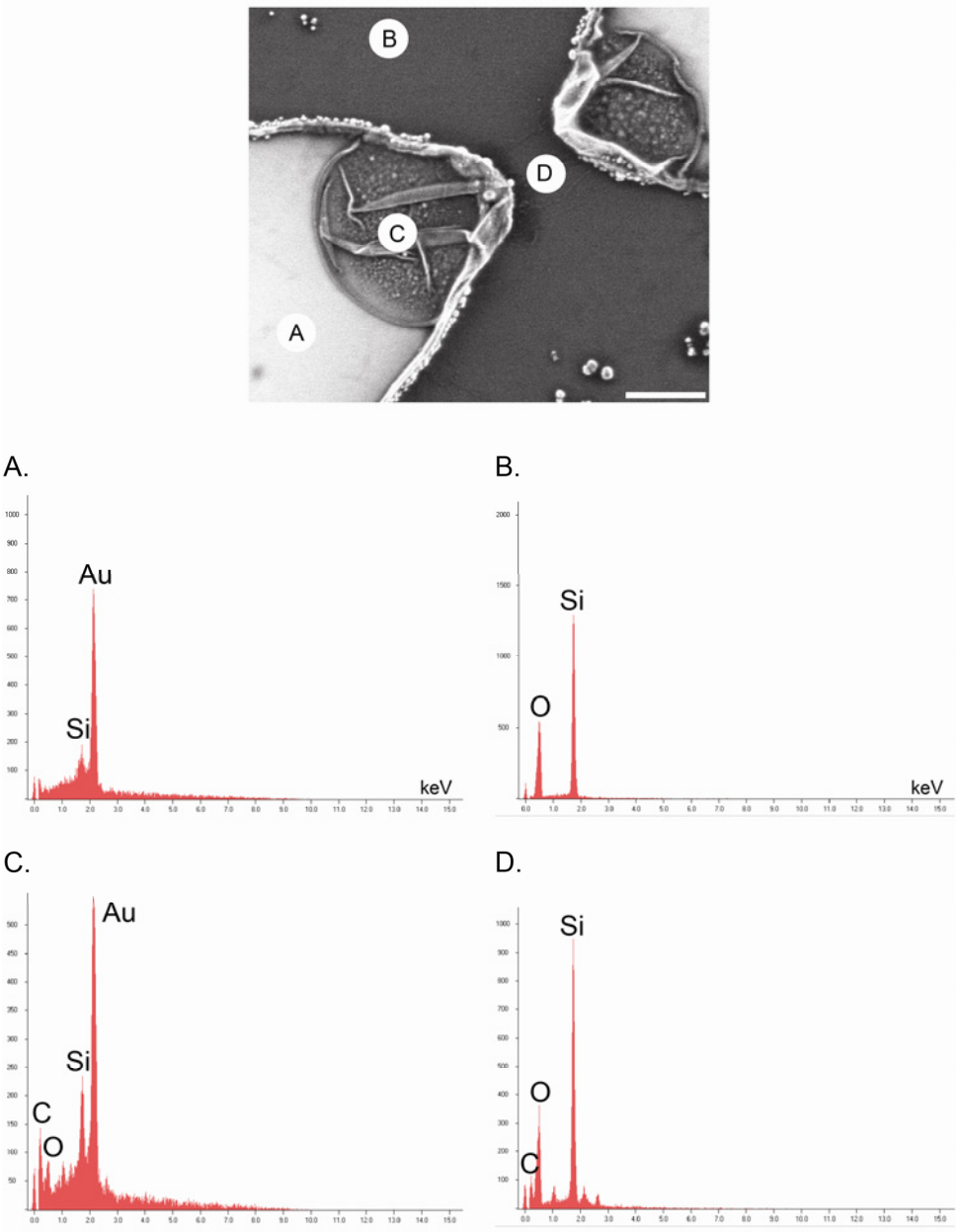

Figure C.1. *EDX analysis of electrode pairs after immobilisation of crystallin fibrils by DEP. Top: SEM image of electrode pairs and sites of EDX analysis. Bottom: EDX spectra with assigned peaks for A) Gold electrode, B) Silicon oxide wafer, C) Electrode tip, and D) Middle of electrode pair.*